Triggering on Leptons for Beyond the Standard Model Searches at ATLAS

Matthew Cleary Tamsett

Department of Physics

Royal Holloway, University of London

A thesis submitted to the University of London for the Degree of Doctor of Philosophy

September 2010

Declaration

I confirm that the work presented in this thesis is my own. Where information has been derived from other sources, I confirm that this has been indicated in the document.

Matthew Cleary Tamsett

Abstract

This thesis presents a study of leptonic signals of possible extensions to the Standard Model at the LHC and the ability of the ATLAS detector to trigger on these. In particular, this work focuses on the effects of lepton isolation on the electron trigger at ATLAS.

Monte Carlo simulations of supersymmetric processes at benchmark points and top quark decays are studied as well as dileptonic decays of Z-bosons. Differences are observed in the efficiency of the leptonic trigger between “busy” events, such as SUSY and top samples, and the events containing well isolated leptons commonly used to evaluate trigger efficiencies. It is shown that these differences can be explained in terms of the main kinematic properties and isolation of leptons and that a data driven efficiency measurement can be obtained using the Z-boson resonance. This method is applied across scans of supersymmetric parameter space as a weighted average, and it is shown that trigger efficiencies are high and consistent for the wide variety of models considered.

Further studies examine the highly energetic electrons expected to be produced in the decays of hypothesised new heavy neutral resonances. It is shown, due to the shower structure of very energetic electrons, that isolated triggers are unsuitable for such signatures. Moreover, a data driven measurement of the electron’s properties in terms of their main kinematic properties is shown to be sufficient to explain the observed efficiencies for non-isolated triggers.

Finally, an initial study of the very first electrons produced in LHC collisions is presented, which displays good agreement between the data and the Monte Carlo prediction for the main kinematical variables and electromagnetic shower shapes. The efficiency of the lowest energy threshold electron trigger is measured and seen to be high and consistent with the MC prediction.

Acknowledgements

There are a large number of people without whom this thesis would never have been possible. Firstly I'd like to thank my supervisor Antonella De Santo for her guidance and support, and for pushing me to achieve all I can. Without a supervisor as talented as you both this thesis, and my research skills would have been greatly diminished. I'd also like to thank Christina Potter, Teresa Fonseca Martín, Pedro Teixeira-Dias and Glen Cowan for helping me through the many problems I encountered over these last four years.

Most of all I'd like to thank my friends and family. You are the reason I pursued an academic path and why I managed to get to where I am today. The friends who helped me are too many to list, so I won't try in case someone gets left out. That said, I once promised Baris that I'd mention his name if he helped me to help write some decent code for once. The rest of you know who you are. Without my family I would have struggled to be able to go to University in the first place, let alone stay there for so many years. Thanks to Mum, for choosing a good university, and to you, Fergus, Nan and Grandad for supporting me while I was there. To Dave for the guidance to choose a PhD, and to Patrick, Helen, Nathan and Daniel for being the best family anyone could ask for.

This work was funded by the Science and Technology Facilities Council and undertaken at Royal Holloway, University of London.

There is no use trying, said Alice; one can’t believe impossible things.

I dare say you haven’t had much practice, said the Queen. When I was your age, I always did it for half an hour a day. Why, sometimes I’ve believed as many as six impossible things before breakfast.

Through the Looking Glass, and What Alice Found There,
Lewis Carroll (1871).

Alice and the Red Queen,
Mervyn Peake (1946).

Contents

Preface

In December 2009 the Large Hadron Collider (LHC) at CERN collided beams of protons for the first time. This moment marked the beginning of a long search for new particles, forces and dimensions in an energy regime never previously explored at any experiment. Positioned at the beam collision points around the LHC ring are four large, complex detectors. These are designed to record and analyse the glimpses of the unknown high energy world provided by LHC collisions. These experiments will test the current theoretical framework of particle physics, the Standard Model (SM), to new levels of precision, and will search for the tell-tail signatures of new, Beyond the Standard Model (BSM) physics.

The rate at which the LHC will produce collisions is 10^5 times higher than the technologically imposed upper limit at which the detectors are able to record data. The choice of which collisions to record and which to discard is achieved via the use of trigger systems. It is these which control which physical processes it is possible to study and which it is not. One tried and tested method for the selection of interesting collisions is via the identification of energetic leptons. This thesis presents a study of the ability of one LHC detector, ATLAS, to select leptons (in particular, electrons) produced in the decays of BSM particles. Particular attention is paid to those leptons produced by the decays of supersymmetric particles and new neutral heavy resonances.

This thesis is organised in the following way:

- Chapter 1 provides a short overview of the Standard Model of particle physics, and the theoretical motivations for its extension, including an introduction to supersymmetry; the main topic of this thesis, and to some BSM neutral resonances.
- Chapter 2 will then discuss the ATLAS experiment at the LHC, the tool with which experimental particle physicists hope to discover evidence for BSM physics.
- Chapter 3 presents an overview of the ATLAS trigger system, with particular attention paid

to the electron and muon trigger systems.

- Chapter 4 introduces the Monte Carlo simulation methods used at ATLAS, and the prescription by which particle objects and kinematical variables are reconstructed within the ATLAS detector. This chapter provides the final piece of introductory material needed before discussion of the author's own work can begin.

- Chapter 5 presents the results of studies of the efficiency of the ATLAS trigger to select individual, well isolated electrons in simulated events of single electrons and the Z$\rightarrow e^+e^-$ process. This chapter includes a discussion of a method for the extraction of trigger efficiencies directly from collision data.

- Chapter 6 expands the work of the previous chapter to study the electron trigger efficiency in the complex, hadron rich environments expected to be produced via the decays of supersymmetric particles and jet rich SM events. This chapter describes a new method for the expansion of data driven efficiency measurements to determine efficiency in these "busy" events. A discussion of "fake" electrons, their effects on trigger efficiencies and their origins is also presented.

- Chapter 7 utilises the results of Chapter 6 to extract a measure of the performance of both the electron and muon triggers in supersymmetric models across a wide range of phenomenologically motivated scenarios.

- Chapter 8 moves away from supersymmetry, to study the efficiency of the electron trigger, and the effects of the electron isolation thereof, in the selection of the very energetic electrons characteristic of the decay of heavy BSM neutral resonances. This chapter, again, includes a prescription for the determination of this efficiency from data.

- Chapter 9, the final chapter, presents a preliminary analysis of electrons produced in the very first collisions produced at ATLAS by the LHC. This includes an extraction of the efficiency of the most inclusive electron trigger used in the very early stages of data taking.

Chapters 6, 7 and 8 are the author's original work. The work in Chapters 5 and 9 was conducted by the author in collaboration with members of the relevant physics and performance working groups of the ATLAS collaboration. All the figures shown in these chapters were produced by the author.

Chapter 1

Theory and Motivation

This chapter presents a brief overview of the Standard Model, the current theoretical framework of fundamental particle physics, along with a discussion of some of its limitations, omissions and possible extensions.

1.1 The Standard Model of Particle Physics

The Standard Model (SM) of particle physics is a model of the dynamics of fundamental particle interactions set within the mechanical formalism of Quantum Field Theory [1, 2]. Particles are the quanta of the underlying fields and all fundamental interactions arise from the general principle of local gauge invariance.

Observed particles, as characterised by the SM, fall into two distinct categories: matter particles, which are spin-$\frac{1}{2}$ fermions (f), and force carriers, which are spin-1 bosons. Fermions can further be subdivided into particles that feel the strong force; the quarks, and particles that do not; the leptons. The full assembly of known fundamental particles is presented in Figure 1.1.

Quarks come in six types or flavours and are arranged into three distinct families, also known as generations. The first generation is comprised of the *up* quark, and the slightly heavier *down* quark. These have charges (Q) (in units of the charge of the electron e) of $+\frac{2}{3}$ and $-\frac{1}{3}$ respectively. The two following generations are successively more massive and likewise consist of a doublet of an up-type quark and a down-type quark. The second generation consists of the enigmatically named *charm* and *strange* quarks, while the third generation includes the *top* and *bottom* quarks. Each quark carries a quantum number called colour, which can be either *red*, *green* or *blue*. Free quarks have never been observed directly, instead they are confined inside composite systems known as hadrons. The most commonplace hadrons are the proton and the neutron, three-quark systems made up of the lightest two quarks, up and down.

	Fermions			*Bosons*
Quarks	$\begin{pmatrix} u \\ d \end{pmatrix}$	$\begin{pmatrix} c \\ s \end{pmatrix}$	$\begin{pmatrix} t \\ b \end{pmatrix}$	γ Z W^+
Leptons	$\begin{pmatrix} e \\ \nu_e \end{pmatrix}$	$\begin{pmatrix} \mu \\ \nu_\mu \end{pmatrix}$	$\begin{pmatrix} \tau \\ \nu_\tau \end{pmatrix}$	W^- g
	I	II	III	
		Generation		

Figure 1.1: The known particle content of the Standard Model of particle physics.

Similarly, there exist six leptons which are also classified into three families: the familiar *electron*-type leptons, the *muon*-type and the *tau*-type. Each lepton family consists of a doublet including a charged lepton and its corresponding neutral neutrino. The mass of the charged leptons increases from one generation to the next, as it does for the quarks. In the simplest version of the SM, neutrinos are considered massless. However, recent observations of neutrino flavour oscillations has shown that at least two neutrinos must have small masses [3, 4].

To each matter particle there exists a corresponding anti-particle with the same mass but opposite charge. These are usually denoted with a bar or with a superscript indicating opposite charge. Some properties of the SM fermions are summarised in Table 1.1.

Interactions between fermions are mediated by the emission and absorption of gauge bosons. The SM describes three of the four known fundamental forces of nature: the electromagnetic (EM), the strong and the weak forces. The type of exchanged boson determines the type of interaction. The EM force is mediated by the massless photon, the strong force is mediated by eight massless, coloured gluons, and the weak force is mediated by the massive $W^{\pm}$ and Z bosons. These forces couple to electric charge, colour and weak isospin, respectively. Table 1.2 shows the pertinent masses and the relative coupling strength of each force at low energies.

The simplest version of the SM also includes a neutral, spin-0 Higgs boson, which is involved in the generation of particle masses [6]. The Higgs boson has yet to be observed experimentally.

The fourth fundamental force, gravity, is conspicuously absent from the SM. In principle gravitational interactions should also be describable in terms of the exchange of a graviton gauge boson. However attempts to create a satisfactory quantum field theory of gravity and incorporate this into the SM have so far failed.

Table 1.1: The masses and charges of the fermions [5].

Fermion	Symbol	Mass	Q/e
up	u	1.5-3.3 MeV	
charm	c	1.27 GeV	$\frac{2}{3}$
top	t	171.3 GeV	
down	d	3.5-6 MeV	
strange	s	105 MeV	$-\frac{1}{3}$
bottom	b	4.2 GeV	
electron	e^-	0.511 MeV	
muon	μ^-	105.7 MeV	-1
tau	τ^-	1.78 GeV	
electron neutrino	ν_e	< 2 eV	
muon neutrino	ν_μ	< 0.19 MeV	0
tau neutrino	ν_τ	< 18.2 MeV	

Table 1.2: The masses and properties of the bosons [5] .

Boson	Symbol	Mass [GeV]	Q/e	Typical coupling
photon	γ	0	0	$\frac{1}{137}$
gluon	g	0	0	1
Z	Z	91.189	0	10^{-6}
$W^{\pm}$	$W^{\pm}$	80.398	±1	10^{-6}

The SM is an exceptionally successful theory and contemporary experimental particle physics is the study of the successes and, more notably, the omissions of the SM. To understand the SM it is necessary to understand the forces it describes. The following sections will describe each of these forces in turn, then the unification of the EM and weak forces, and finally the Higgs mechanism.

1.1.1 Quantum Electrodynamics

With the exception of gravity, electromagnetism is probably the force most familiar to us in our everyday lives. This is the force responsible for electricity, light, friction, chemical bonding and the vast majority of everyday phenomena. Perhaps as a consequence, the theory of electromagnetism, or Quantum Electrodynamics (QED), is the oldest and most successful of the dynamical theories that were eventually brought together to form the SM.

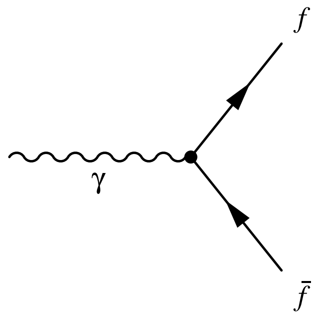

Figure 1.2: The basic interaction vertex of QED. In this diagram, and all subsequent diagrams, time runs from left to right.

All QED can be represented simply with interactions of the form of Figure 1.2. This shows the interaction of a charged fermion with a quantum of the electomagnetic field, a photon, and can describe both the emission and absorption of photons and the creation and annihilation of particle-antiparticle pairs. The strength of any interaction is characterised by a coupling constant associated with each vertex. The EM force couples to electric charge, so the strength of EM interactions is related to the charge of the fermions involved. Physical processes can be understood by combining primitive vertices into complete diagrams, known as Feynman diagrams. Such diagrams are an elegant representation of a process, with the external lines telling the nature of the process and the internal lines describing the mechanism involved. More complicated diagrams, with multiple vertices are generically referred to as *higher order* diagrams. Any given process is described by the sum over all possible internal states, that is to say the combination of all possible Feynman diagrams of all orders. Two examples of Feynman diagrams of QED processes are shown in Figure 1.3.

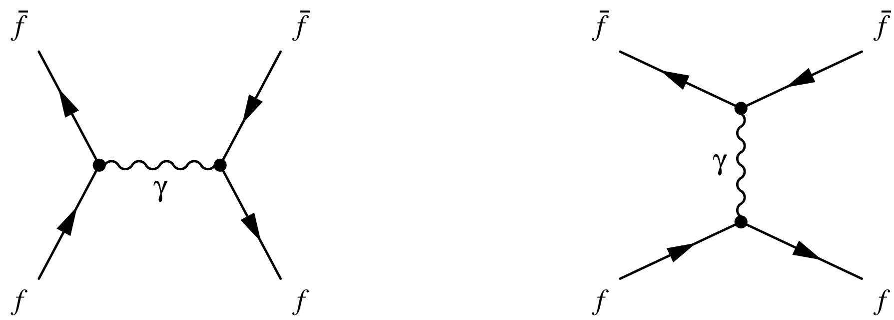

Figure 1.3: Two QED Feynman Diagrams for the process $f\bar{f} \rightarrow f\bar{f}$.

A general framework for theories involving the exchange of vector bosons, or *local gauge* theories, was proposed by Yang and Mills in 1954 [7]. QED is an example of such a theory. The dynamics of non-interacting massive fermion fields are described by the Dirac equation [8]. Interaction terms are added to this by requiring that the appropriate Lagrangian remain invariant under a local phase transformation, namely under the rotation of the fermion field through an arbitrary phase that is also a function of position. To preserve the invariance of the Lagrangian it is necessary to introduce a new massless vector field, identified with the photon field which must transform appropriately under a local gauge transformation. In other words, the Lagrangian does not change if the fermion field is altered by an arbitrary phase factor, as long the photon field is consistently altered. The final Lagrangian that satisfies the above requirements is then the Lagrangian which describes QED. This is observed to contain terms interpreted as an interaction of the form shown in Figure 1.2, where a charged fermion interacts with a massless photon. The imposition that the physical system remains invariant under this interaction results in the conservation of electric charge as required by experimental observations.

The local gauge transformation performed in QED can be thought of as a transformation under the symmetry group of U(1) unitary matrices of dimensions 1×1, where charged fermions interact with a single massless field. Similarly to QED, the theories describing the strong and weak forces are constructed via the extension of the principle of local gauge invariance to other symmetry groups. These will be the subject of the following sections.

1.1.2 Quantum Chromodynamics

Quantum Chromodynamics (QCD) is the quantum field theory that describes strong interactions. The strong force is responsible, for example, for the binding of nuclei. In analogy to the EM force and its relationship to the electric charge, the strong force is said to couple to colour charge. Thus only the coloured particles, quarks and gluons, can partake in strong interactions. In QCD the local gauge group is SU(3) and fields transform in the vector space of colour. To preserve local gauge invariance, eight massless vector fields are introduced, the quanta of which are the eight gluons.

The fundamental interaction vertex of the strong force is shown in Figure 1.4 as the interaction of quarks with a gluon field. The group SU(3) is said to be *non-Abelian*, referring to the fact that not all of the group generators commute. This feature leads to the inclusion of self-interaction terms of the fields in the Lagrangian, the likes of which are not present in QED, and therefore to the inclusion of triple and quartic gluon vertices as shown in Figure 1.5. In physical terms this arises as the gluons themselves possess colour and so are able to self-couple. In QED the photon

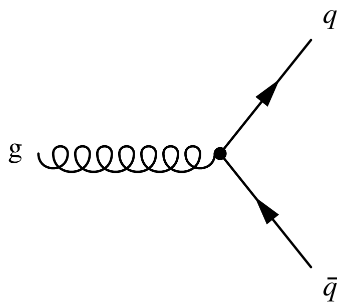

Figure 1.4: The basic interaction vertex of QCD.

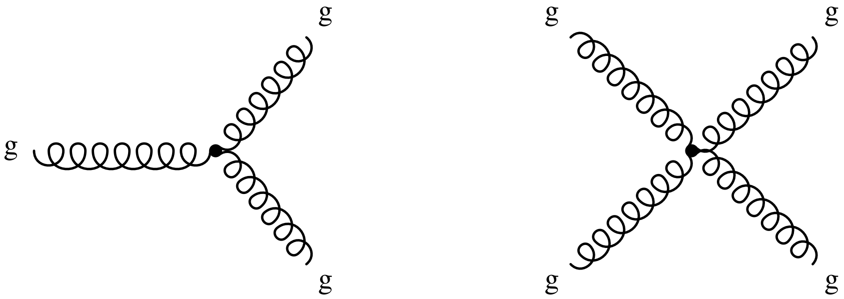

Figure 1.5: The gluon self interaction vertices.

was electrically neutral and therefore not able to self interact.

The strong interaction preserves electric charge, colour and quark flavour. Other interesting and peculiar features of QCD include *asymptotic freedom* and *colour confinement*, both discussed below.

Asymptotic freedom relates to the decrease of the strength of the strong coupling constant with decreasing distance. This can be understood by considering higher order loop corrections to given processes. A QED example of this is shown in Figure 1.6 as a fermion loop in the interactions between two electrons. The virtual pair contribute to the energy dependence of this process resulting in a net decrease of the effective coupling at low energies or long ranges.

In QCD, loop corrections are provided by quark-anti-quark and gluon-gluon loops, as shown in Figure 1.7. The quark-anti-quark loops have a similar effect to charged fermion loops in QED and serve to reduce the coupling strength of the strong force at long ranges. Gluon loops, on the other hand, contribute to the energy dependence with the opposite sign and lead to a net increase in coupling at large ranges. Due to the balance in the number of quark flavours and the number of colours, the gluon-gluon effect is dominant and the coupling of the strong force increases at

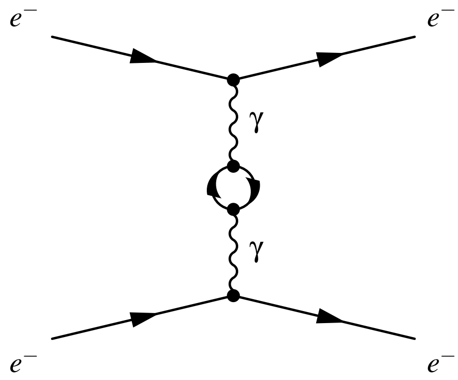

Figure 1.6: Loop corrections in EM interactions. Such interactions are responsible for the decrease in the effective strength of the EM interaction at low energies. In addition to the one loop correction shown, higher order terms with two or more loops are also important.

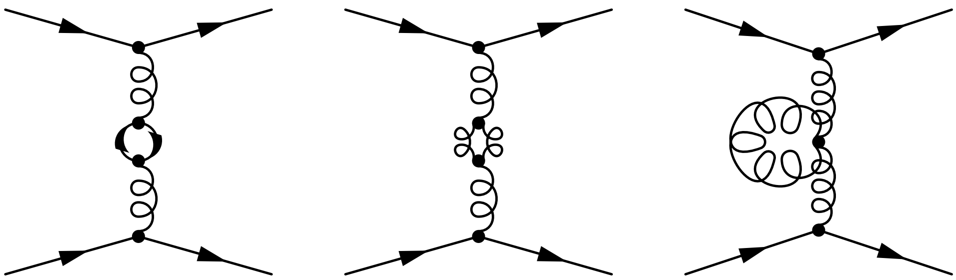

Figure 1.7: Loop corrections in strong interactions.

long range and decreases at short distances. This leads to the phenomenon of quark confinement, whereby isolated quarks are never observed. Confinement has important consequences for the phenomenology of collider signatures where energetic quarks or gluons are produced, resulting in the production of collimated jets of hadrons in the final state.

The final distinction between QCD and QED is that whilst free particles with net electric charge are observed in nature, no particles with net colour have ever been observed. Coloured particles are confined to colourless bound states. Such colourless states can be constructed either as three quark systems containing red, green and blue quarks (or anti-red, anti-green and anti-blue) or as two quark states containing a coloured and an anti-coloured quark. The three-quark states are collectively know as baryons, of which the proton and the neutron are familiar examples. Two-quark systems are known as mesons, the most common example being the pion, which consists of up and down type quarks and anti-quarks, and comes in charged and neutral varieties.

1.1.3 The Weak Force and Electroweak Unification

The third force incorporated into the SM is the weak force. This is the force responsible, for example, for nuclear beta decay and which also plays an important role in fusion mechanisms in stars. Like QED and QCD, the theory of the weak force is arrived at by the requirement that the appropriate Lagrangian remain locally gauge invariant. In this case it is required that the Lagrangian describing the interactions of left-handed fermion doublets is invariant under SU(2)$_L$ transformations in the vector space of weak isospin, I. Glashow, Weinberg and Salam [9, 10, 11] extended this theory by the expansion of the gauge group to SU(2)$_L$ $\times$ U(1)$_Y$, such that the weak and EM forces became two facets of the same *Electroweak* (EW) force and are unified at high energies. Here the gauge group U(1)$_Y$ of *weak hyper-charge* Y is defined by:

$$Q = Y + I_3, \tag{1.1}$$

where Q is the electric charge and I_3 is the third component of weak isospin. In order to retain local gauge invariance, four fields are introduced, $W_\mu^{1,2,3}$ and B_0. The EW vector bosons γ, Z, and W$^\pm$, are then the quanta of the mixing of these four fields [1].

In the EW theory, right handed fermions now transform under U(1)$_Y$ only, whilst left handed fermions transform under SU(2)$_L$ $\times$ U(1)$_Y$. By treating left and right handed fermions differently, the weak force maximally violates parity. Like QCD, this theory is non-Abelian, so it also includes self-interaction terms in the Lagrangian.

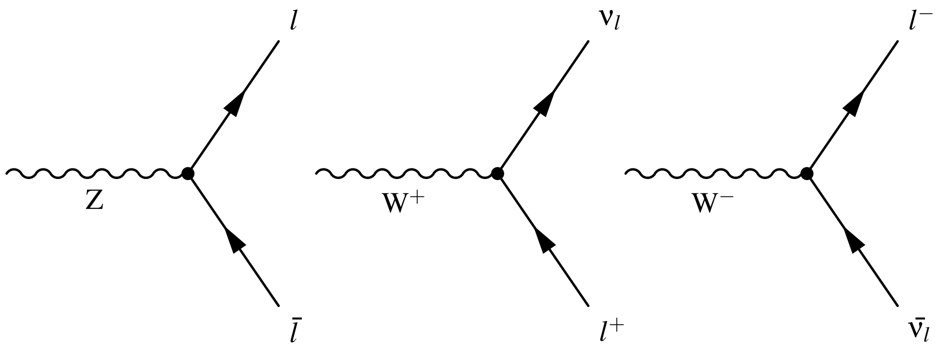

Figure 1.8: The interaction vertex of weak gauge bosons and leptons.

Weak processes involving leptons consist of the fundamental vertex shown in Figure 1.8 and can involve either the charged W-bosons (charged-current interactions), or the neutral Z-boson (neutral-current interactions). Charged-current interactions must involve the conversion of charged leptons into the corresponding lepton neutrino in order to preserve charge. The resultant lepton

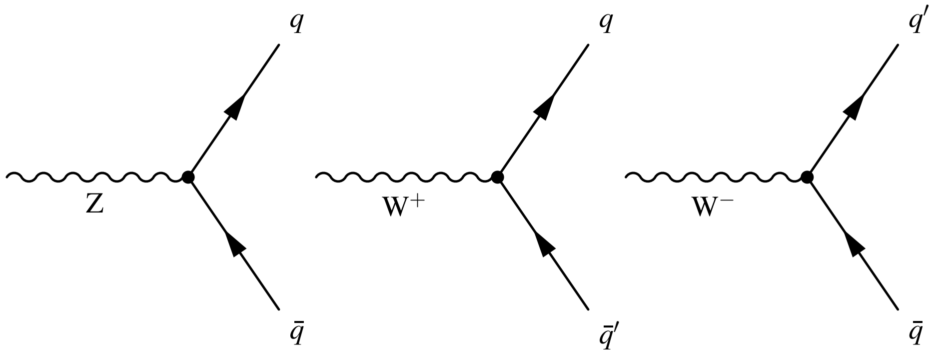

Figure 1.9: The interaction vertex of weak gauge bosons and quarks. Unlike leptons the weak eigenstates of quarks are not the mass eigenstates, this can result in FCCC, where by a up or down type quark is produced in conjunction with a down or up type quark of a different generation.

is of the same generation (i.e, no vertex exists where a muon transforms into an electron or tau neutrino), so *lepton number* remains conserved.

Weak vertices involving quarks are shown in Figure 1.9. Rather than coupling to the mass eigenstates of down type quarks (d,s,b) the weak force instead couples to weak gauge eigenstates d', s' and b'. These are formed of linear combinations of the mass eigenstates of down-type quarks as described by the CKM matrix [12]. This generational mixing allows for so-called flavour-changing charged-currents (FCCC), whereby quarks of different flavours are involved at a single weak vertex. Cross generational FCCC are suppressed with respect to inter-generational processes and likewise doubly cross generational reactions are doubly suppressed. Flavour-changing neutral-currents (FCNC) are not allowed in the SM. As in EM and strong interactions, weak interactions preserve charge, colour and weak isospin.

1.1.4 Mass Generation and the Higgs Boson

The theories of the strong and EW interactions can be combined into a single Lagrangian which is invariant under $\mathrm{SU}(3)_C \times \mathrm{SU}(2)_L \times \mathrm{U}(1)_Y$ transformations. Such a theory describes all three forces but is missing a crucial piece. The $\mathrm{W}^{\pm}$ and Z bosons, unlike photons and gluons, are massive, and the procedure used so far does not include a prescription for the inclusion of their masses. In fact, in order to retain the local gauge invariance of the Lagrangian, the masses of the gauge fields must explicitly be set to zero. In 1971 it was shown by 't Hooft that in order for a theory to be *renormalisable*, and produce meaningful predictions, then the theory must retain local gauge invariance [13]. Therefore, in order to obtain a successful, predictive theory, the Lagrangian should be constructed in such a way that mass terms are included yet local gauge invariance is retained. One proposed methodology that does just this is the Higgs mechanism [6].

The Higgs mechanism involves the generation of mass terms via the use of a spontaneously broken symmetry. This is done by the introduction of a potential to the Lagrangian which contains both quadratic and quartic functions of the associated fields. Such potentials can be chosen such that the symmetry of the overall system is preserved but the lowest energy state of the system is no longer at zero. Instead a new minimum must be *spontaneously* chosen to be the ground state of the system. As this new ground state will not be at zero, the symmetry of the system is now broken. This results in the inclusion of mass terms in the Lagrangian whilst retaining its local gauge invariance. The mass terms are *generated* or revealed by the choice of the new ground state.

Applying this procedure to the SM Lagrangian leads to the creation of four new scalar fields with non-zero values of hyper-charge, isospin and charge. Three of these fields are associated with massless scalar bosons and one with a massive scalar boson. The three massless *Goldstone* bosons are used to give masses to the weak gauge bosons and hence break the symmetry of the EW interaction. The fourth boson remains in the theory as the elusive Higgs boson. The non-zero ground state or vacuum expectation value of the system results in the vacuum everywhere gaining the ability to emit or absorb neutral colourless Higgs bosons that carry isospin and hyper-charge. Therefore fermions and weak gauge bosons that can couple to this new boson acquire mass, but the gluon and photon, which cannot, remain massless. The additional couplings between the Higgs boson and the SM fermions are termed *Yukawa* couplings. Thus the Higgs mechanism allows masses to be generated in a way that does not violate local gauge invariance, while the theory remains renormalisable.

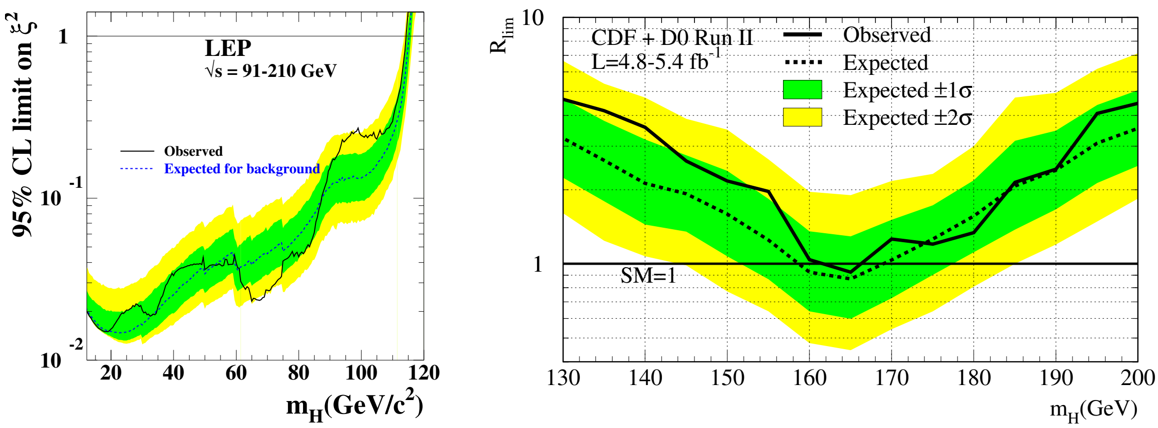

Figure 1.10: Experimental search limits on the mass of a SM Higgs boson from (left) the $H \rightarrow ZZ$ channel at LEP [14] and (right) the $H \rightarrow WW$ channel at the Tevatron [15].

The Higgs boson remains unobserved and as such the SM remains incomplete. Figure 1.10 shows the current experimentally excluded mass region for the Higgs boson, from LEP [14] and Tevatron searches [15]. Unless current Higgs theories are severely wrong then a SM Higgs boson should be observable at the LHC.

The Higgs mechanism is not without its caveats. The mass of the Higgs boson m_H, is required by EW unitarity to be of order of a few hundred MeV. Yet it is subject to large corrections δm_H to its bare mass m_0, proportional to the square of the masses of each particle in the theory [16]:

$$m_H^2 = m_0^2 + \delta m_H^2, \tag{1.2}$$

where

$$\delta m_H^2 = \frac{\lambda_s}{16\pi^2}[\Lambda_{UV}^2 - 2\, m_s^2\, ln(\frac{\Lambda_{UV}}{m_s}) + ...] - \frac{|\lambda_f|^2}{8\pi^2}[\Lambda_{UV}^2 - 3\, m_f^2\, ln(\frac{\Lambda_{UV}}{m_f}) + ...]. \tag{1.3}$$

The first term in Equation 1.3 defines the correction due to scalars of mass m_s and the second term is the equivalent for fermions of mass m_f. Here λ_f, λ_s are the couplings between the Higgs and these particles and Λ_{UV} is the energy cut-off scale to which the theory is valid or, equivalently, the mass of the heaviest particle in the theory. The Higgs mass is therefore disturbingly sensitive to the scale of any high mass physics. This would not be an issue were the SM an exhaustive description of the universe but, as previously stated, this cannot be the case. Quantum gravity, at the very least, is lacking a description within the SM and effects of this are believed to become important around the Planck Mass (M_P) $\sim 10^{19}$ GeV. If Λ_{UV} is identified with M_P then both terms in 1.3 will add extremely large corrections to the Higgs mass, such that fine tuning of parameters is required to some thirty orders of magnitude to keep the Higgs boson light. This is considered *unnatural*, and is known as the hierarchy problem.

1.1.5 Beyond the Standard Model

Despite its numerous successes, the SM remains an incomplete picture. Aside from the obvious omission of gravity and the infamous hierarchy problem, the SM also fails to offer an explanation of cold dark matter.

For some time evidence has been mounting based on astronomical observations requiring the existence of cold dark matter [17]. The measured rotation velocities of both stars within galaxies and galaxies within clusters strongly indicate that the matter density of the universe must greatly exceed that of the visible luminous matter. Stringent constraints on the densities of both matter and baryons have been obtained via observations of cosmic microwave background anisotropies by the WMAP collaboration [18]. These indicate that not only is the amount of observed matter far below that required, but that the missing "dark" matter matter must be non-baryonic. Furthermore, if the dark matter density is to be within the required range, then its self-annihilation cross section should be at the weak scale and hence dark matter itself should interact via the weak force. None of the existing SM particles provide a suitable dark matter candidate, hence any explanation will require the extension of the SM.

Attempts to reconcile the SM with these omissions have led to a wide variety of new models, generically referred to as Beyond the Standard Model physics (BSM). This thesis will focus on a small selection of these models which predict new phenomenology in the TeV region and are particularly interesting to study at the LHC. Further details of these will be included in the following sections.

1.2 Supersymmetry

A proposed extension to the SM, supersymmetry (SUSY) [19, 20], postulates the existence of a new kind of fundamental symmetry involving the transformation of bosonic fields into fermionic fields, and similarly fermionic into bosonic fields. Every particle in the theory is grouped into a *supermultiplet*, where two states belong to the same supermultiplet if one can be generated from the other by some combination of the SUSY generators plus some space-time translation or rotation. SUSY requires every fermion to have a scalar bosonic super-partner, and every boson to have a fermionic super-partner, and that these new super-partners, or *sparticles*, should have identical hyper-charge, isospin, and colour. As no SM particles fit the criteria to be suitable super-partners of any other SM particle, SUSY theories hypothesises a large number of additional particles. In this way SUSY provides an elegant solution to the hierarchy problem, a possible dark matter candidate and a stepping stone towards the unification of the EW and strong forces.

That SUSY offers a solution to the hierarchy problem is evident upon inspection of Equation 1.3, where it can be seen that the fermionic and scalar terms provide similar but opposite sign corrections. The nature of the SUSY generators requires the introduction of an additional complex scalar for each SM fermion and an additional fermion for every scalar. This provides exactly the necessary particle content to ensure the exact cancellation of the divergent corrections to the Higgs mass.

An interesting implication of SUSY is that the interaction of the sparticles with the gauge fields alters the behaviour of loop corrections as shown in Figures 1.6 and 1.7. The resultant modification to the dependence of coupling constants with energy scale leads to couplings which unify at high energies, as shown in Figure 1.11. A feature that was absent in the SM. This can be interpreted as an indication that the strong and EW forces may in fact be two facets of the same theory. In much the same way that the weak and EM forces were unified above the weak scale, now all three forces can be unified above the grand unification (GUT) scale of around 10^{16} GeV. While in itself this is not a motivation for SUSY it is a pleasant aesthetic side effect.

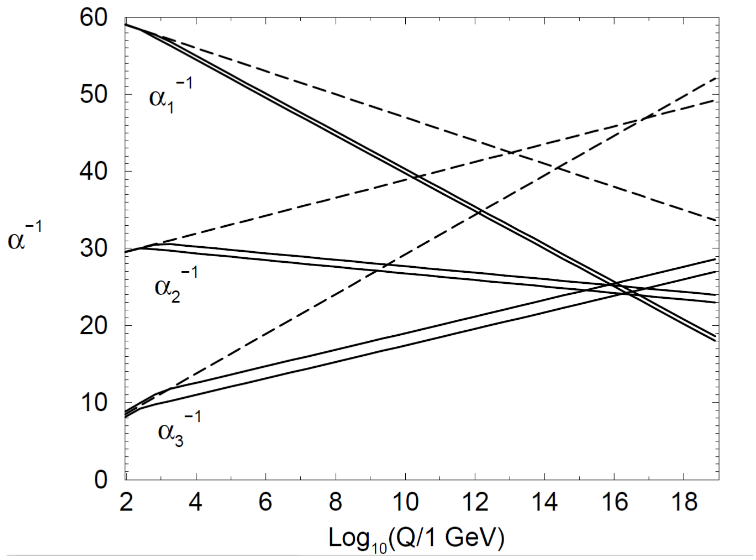

Figure 1.11: The running of the inverse coupling constants of the gauge couplings with energy (Q), where α_1,α_2 and α_3 are the gauge couplings for EM, weak and strong forces respectively. The dashed lines show the SM only prediction and the solid lines the Minimal Supersymmetric Standard Model (MSSM), see text. The widths represent theoretical uncertainties, (from [20]).

1.2.1 The Minimal Supersymmetric Standard Model

The model described in this thesis is the minimally phenomenologically viable extension of the SM, meaning the minimum extra particle content has been introduced. This is the so called Minimal Supersymmetric Standard Model (MSSM). The MSSM incorporates the SM fermions into *chiral* supermultiplets along with a further complex scalar, and the SM gauge bosons into *gauge* supermultiplets along with an additional Majorana fermion[1]. Super-partners to SM fermions are named for their SM equivalent with the addition of an *s* (for scalar) prefix. Therefore quarks superpartners are generically referred to as *squarks* (such as the *sup* and the *sdown*), and the leptonic super partners are known as sleptons (such as the *selectron* and the *sneutrino*).

In order to give mass to all the sparticles, the SM Higgs sector must be extended into two Higgs doublets, comprised of four complex scalar fields with eight degrees of freedom. Three of these are absorbed in EW symmetry breaking, and the remainder manifest as five physical Higgs bosons, three neutral, h^0, A^0, H^0, and two charged H^+ and H^-. These SM Higgs fields are then classified into chiral supermultiplets with a total of four fermionic superpartners.

The super-partners to the Higgs and gauge bosons are fermions and are suffixed with *ino* and collectively referred to as *gauginos*. The EW and Higgsino gauge states mix to form mass eigenstates: four neutral, the *neutralinos*; and two charged, the *charginos*.

The symbols for SUSY particles are generally over-lined with a tilde. In addition, antisparticles will be super-scripted with a star. The sparticle content of the MSSM is summarised

[1]Instead of having distinct antiparticles, Majorana fermions are their own antiparticles.

Table 1.3: The sparticle content of the MSSM.

Name	Spin	Gauge eigenstates	Mass eigenstates
squarks	0	$\tilde{u}_L$ $\tilde{u}_R$ $\tilde{d}_L$ $\tilde{d}_R$	(same)
		$\tilde{s}_L$ $\tilde{s}_R$ $\tilde{c}_L$ $\tilde{c}_R$	(same)
		$\tilde{t}_L$ $\tilde{t}_R$ $\tilde{b}_L$ $\tilde{b}_R$	$\tilde{t}_1$ $\tilde{t}_2$ $\tilde{b}_1$ $\tilde{b}_2$
sleptons	0	$\tilde{e}_L$ $\tilde{e}_R$ $\tilde{\nu}_e$	(same)
		$\tilde{\mu}_L$ $\tilde{\mu}_R$ $\tilde{\nu}_\mu$	(same)
		$\tilde{\tau}_L$ $\tilde{\tau}_R$ $\tilde{\nu}_\tau$	$\tilde{\tau}_1$ $\tilde{\tau}_2$ $\tilde{\nu}_\tau$
neutralinos	$\frac{1}{2}$	$\tilde{B}^0$ $\tilde{W}^0$ $\tilde{H}_u^0$ $\tilde{H}_d^0$	$\tilde{\chi}_1^0$ $\tilde{\chi}_2^0$ $\tilde{\chi}_3^0$ $\tilde{\chi}_4^0$
charginos	$\frac{1}{2}$	$\tilde{W}^\pm$ $\tilde{H}_u^+$ $\tilde{H}_d^-$	$\tilde{\chi}_1^\pm$ $\tilde{\chi}_2^\pm$
gluino	$\frac{1}{2}$	$\tilde{g}$	(same)

in Table 1.3.

R-Parity

The most general form of the MSSM includes terms that violate both lepton and baryon number, allowing for phenomena such as proton decay within $\sim 10^{-2}$ s by processes such as that shown in Figure 1.12. Current experimental limits place the minimum proton lifetime at around 1.6×10^{33} years [21], which strongly excludes this form of the MSSM.

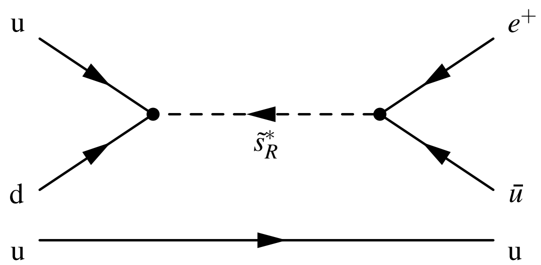

Figure 1.12: Proton decay to π^0 and e^+ via intermediary supersymmetric strange squark. This process is allowed in the general form of the MSSM and requires the violation of conservation of both lepton and baryon numbers.

To avoid unacceptably fast proton decay, an additional symmetry is introduced called *R-parity*, R. This is defined as:

$$R = (-1)^{3(B-L)+2S}, \tag{1.4}$$

where B is the baryon number, L is the lepton number and S is the spin. All SM particles have R of +1 and all SUSY particles have R of -1. In R-parity conserving models, R is an exactly conserved, multiplicative quantum number, meaning that fast proton decay is excluded, there can be no mixing between SM and SUSY particles and that every interaction vertex must contain an even number of sparticles. R-parity conservation has some profound consequences for the phenomenology of the MSSM. Sparticles must be produced in pairs in interactions of SM particles; every sparticle must decay to an odd number of sparticles; and the lightest SUSY particle (LSP) will be stable. In many MSSM models the LSP is the lightest neutralino, which is neutral, massive and weakly interacting which makes it an excellent candidate for the absent cold dark matter particle. It should be noted that models without R-parity conservation can be constructed in which proton decay is adequately suppressed, however this thesis will only consider R-parity conserving models.

1.2.2 SUSY Breaking and Supergravity

If SUSY was realised in nature as an unbroken symmetry then the super-partner particles would have identical mass to their SM counterparts. This is evidently not the case, as such particles would be trivial to observe. Therefore, if it exists, SUSY must be a broken symmetry.

The MSSM Lagrangian introduces 106 extra free parameters to the SM and can be expressed as the sum of the terms:

$$\mathcal{L}_{MSSM} = \mathcal{L}_{SUSY} + \mathcal{L}_{soft}, \tag{1.5}$$

where $\mathcal{L}_{SUSY}$ contains the terms invariant under SUSY transforms and $\mathcal{L}_{soft}$ contains the SUSY breaking parameters. Within this Lagrangian only a single parameter, the SUSY mass scale, is involved in $\mathcal{L}_{SUSY}$, with the remaining 105 contained within $\mathcal{L}_{soft}$. Fortunately, the majority of these parameters are tightly constrained in order not to introduce experimentally excluded flavour mixings or CP violating processes. The remainder are restricted by the mechanism of SUSY breaking.

In order to break SUSY yet preserve the solution to the hierarchy problem, breaking must occur in such a way that the couplings of super partners remains unaffected. The residual Higgs mass corrections are then only proportional to the difference in mass scale between SUSY and the SM. In the most viable models the SUSY mass must therefore be around the 1 TeV range.

The mechanism by which SUSY is broken is a hotly debated topic. Any spontaneous SUSY breaking requires the extension of the MSSM. The most common approach is to assume breaking takes place via a flavour-blind interaction with a *hidden sector* that only couples very weakly to the so called *visible sector* via a messenger particle. Two well studied examples of this are supergravity (SUGRA) [22], where breaking is mediated via gravitational interactions, and gauge mediated symmetry breaking (GMSB) [23], where the familiar gauge interactions are responsible for symmetry breaking and the soft terms in the MSSM Lagrangian come from loop diagrams including messenger particles.

This thesis will consider benchmark scenarios in the minimal supergravity, or mSUGRA model. In mSUGRA the MSSM parameter space is significantly reduced by a particular choice of potential such that the 106 free parameters of the MSSM are reduced to only five:

$$m_0,\ m_{\frac{1}{2}},\ A_0,\ \tan\beta,\ sign(\mu). \quad (1.6)$$

Three of these are defined at the GUT mass, $M_{GUT} \approx 2 \times 10^{16}$ GeV, where the masses of the various sparticles unify: m_0 is the universal scalar mass; $m_{\frac{1}{2}}$ is the universal fermion mass; and A_0 is the universal trilinear coupling. Low energy effective masses and couplings are obtained from the GUT values via the renormalisation group equations. The two remaining parameters are: $\tan\beta$, the ratio of the Higgs vacuum expectation values; and the sign of μ, the supersymmetric Higgs mass parameter. Whilst the assumptions that go into the construction of mSUGRA may not be realised in nature, the reduction in the number of parameters enable the exploration of the rich phenomenology of SUSY without the need to investigate a daunting 106 dimensional parameter space.

1.2.3 Phenomenology of SUSY

R-parity conserving mSUGRA models extend the allowed SM interaction vertices via the inclusion of the new SUSY particles. The couplings of these SUSY vertices are determined by the SM EW, Yukawa and QCD coupling strengths.

The vertices involving neutralinos are shown in Figure 1.13, and similarly for charginos in Figure 1.14. Each gaugino mass eigenstate contains a mixture of bino, wino and higgsino components, therefore they are able to decay to slepton/lepton squark/quark pairs, or any lighter neutralino/chargino and a Higgs or EW gauge boson. The couplings of each vertex will depend on the precise gaugino mixture. For instance, gauginos with a large higgsino component will have enhanced couplings to third family quark-squark pairs due to the large top-quark Yukawa coupling and those with large wino components will favour decays into left-handed sfermions.

Figure 1.15 shows the allowed slepton vertices and similarly Figure 1.16 shows the allowed squark and gluino vertices.

The precise phenomenology of a given mSUGRA model will strongly depend on the particular choice of model parameters. It is these which determine the makeup and masses of the mass

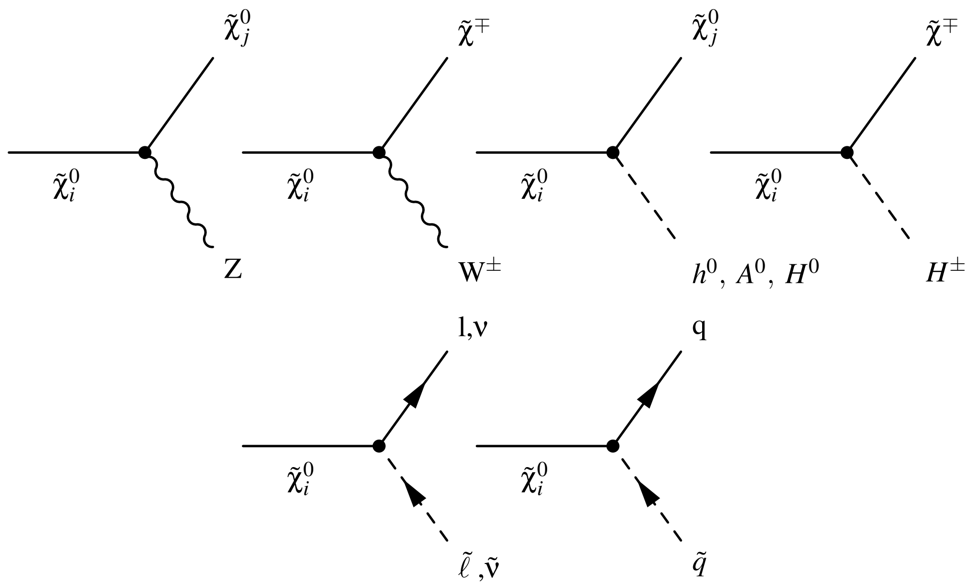

Figure 1.13: The interaction vertices of neutralinos.

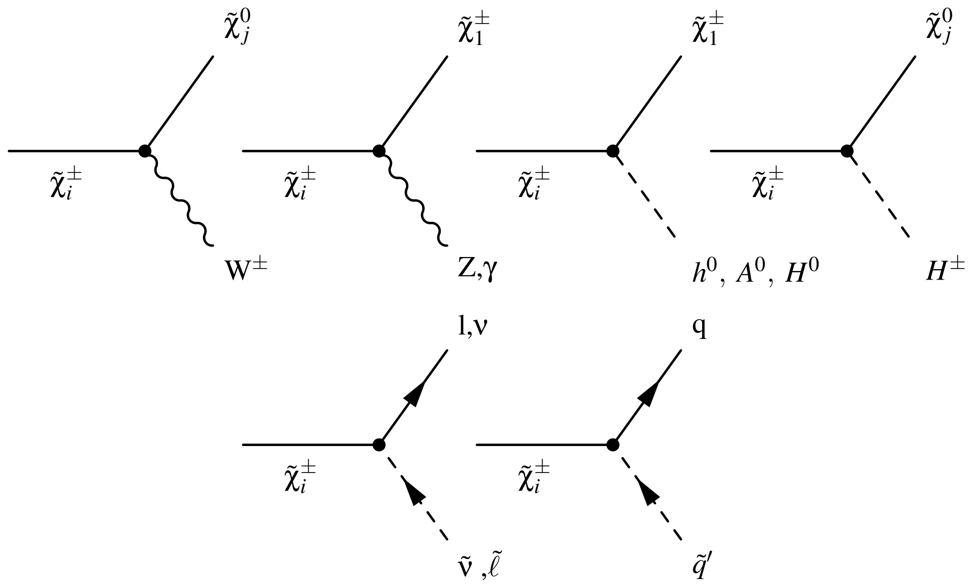

Figure 1.14: The interaction vertices of charginos.

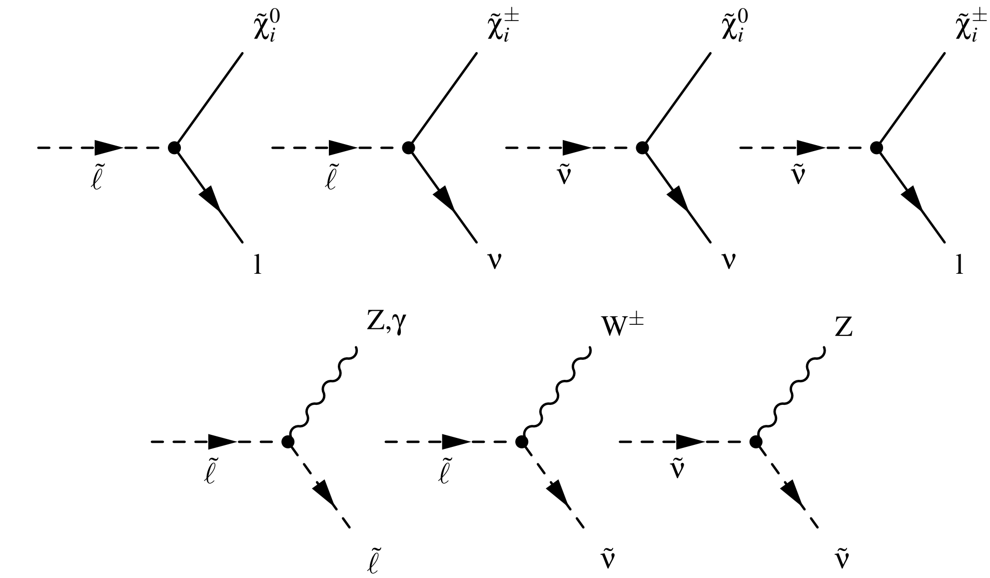

Figure 1.15: The interaction vertices of sleptons, excluding those with the Higgs bosons.

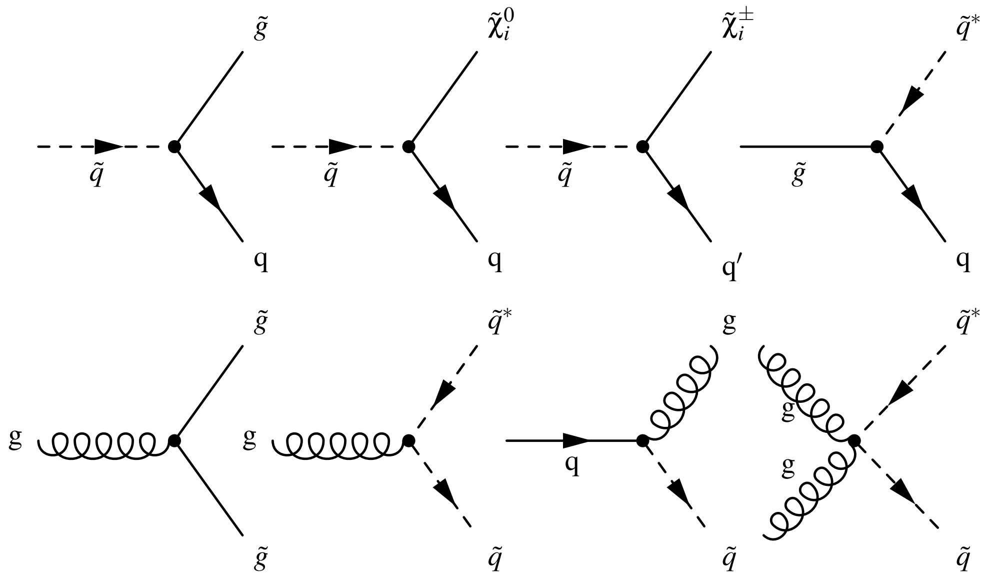

Figure 1.16: A selection of the interaction vertices of squarks and gluinos.

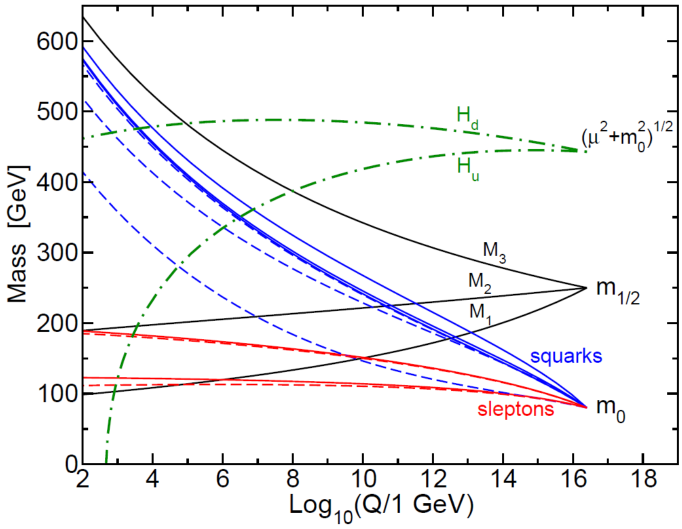

Figure 1.17: An example of the evolution of scalar and gaugino masses from their unified values down to low energy effective masses based on mSUGRA boundary conditions ($m_0 = 80$ GeV, $m_{1/2} = 250$ GeV, $A_0 = -500$ GeV, $sign(\mu) > 0$ and $\tan\beta = 10$) imposed at an energy scale (Q) of 2.5×10^{16} GeV, from [20].

eigenstates and hence which decay channels are kinematically viable and which are favoured.

An illustrative example of the evolution of the scalar and gaugino masses from their GUT values to the EW scale for a particular choice of mSUGRA parameters is shown in Figure 1.17, from [20]. The running gaugino masses are shown as solid lines where the bino mass is given by M_1, the wino mass by M_2 and the gluino mass by M_3. In general the gluino will be heavier than the lightest neutralinos and charginos due to its QCD couplings. A fairly universal prediction of the MSSM is that at the EW scale the mass hierarchy between gauginos should be similar to 6:2:1 [20].

The blue lines show the running squark masses with the solid lines indicating the masses of the first two generations and the dotted lines the third. One line is shown for each of the right handed up and down type quarks and one for the left handed. The masses of the first two generations are usually nearly degenerate and heavier than the third. The slepton masses are shown in red, again with first two generations as solid lines and the third as dashed lines. The mass hierarchy between slepton generations is similar to that of squarks, with the lightest charged slepton often the $\tilde{\tau}_1$. Squarks receive mass corrections from gluino loops and so are generally heavier than sleptons. In addition, left handed squarks and sleptons are likely heavier than their right handed counterparts.

A further general prediction of MSSM is that at least one Higgs boson will be light at the EW scale. This is traditionally chosen to be the h_0 and should have mass < 150 GeV.

Of course all of these generalities are not necessarily realised in nature and it would be a mistake to presume the form of SUSY without any evidence. However, they do serve as useful guidelines for experimental searches.

1.2.4 Experimental Constraints on SUSY

The available SUSY parameter space is heavily constrained both directly and indirectly in order to be consistent with experimental observations.

Indirect constraints include: consistency with cosmological considerations, (primarily that the LSP be compatible with the observed cold dark matter relic density of the universe), limits on rare flavour decay rates, the anomalous magnetic moment of the muon, and on fits to EW observables. WMAP data, in particular, constrains the LSP mass to be less than around 500 GeV, dependent on the other model parameters [24].

Table 1.4: Experimental constraints on direct searches for sparticles from [5]. Δm refers to the mass splitting between the sparticle of interest and the lightest neutralino.

Sparticle	Lower mass limits [GeV]	Notes
$\tilde{\chi}_1^0$	46	
$\tilde{\chi}_2^0$	62.4	$1 <$ tan $\beta < 40$
$\tilde{\chi}_3^0$	99.9	$1 <$ tan $\beta < 40$
$\tilde{\chi}_4^0$	116	$1 <$ tan $\beta < 40$
$\tilde{\chi}_1^\pm$	94	tan $\beta < 40$, $\Delta m > 3$ GeV
$\tilde{g}$	308	any $m_{\tilde{q}}$
	390	$m_{\tilde{q}} = m_{\tilde{g}}$
$\tilde{e}$	73	
$\tilde{\mu}$	94	$1 <$ tan $\beta < 40$, $\Delta m > 10$ GeV
$\tilde{\tau}$	81.9	$\Delta m > 15$ GeV
$\tilde{q}$	379	tan $\beta = 2, \mu < 0, A_0 = 0$
$\tilde{b}$	89	$\Delta m > 8$ GeV
$\tilde{t}$	95.7	$\Delta m > 10$ GeV

Direct constraints from searches for the production and decay of SUSY particles at the LEP and Tevatron colliders have set parameter dependent lower mass limits due to non-observation of SUSY. These constrain the lightest neutralino to be heavier than 46 GeV for all tan β. Table 1.4 summarises the current lower mass limits on SUSY particles from direct searches.

The indirect and direct limits can be combined into exclusion plots which show the available parameter space consistent with all measurements. Figure 1.18, taken from [24], show these limits

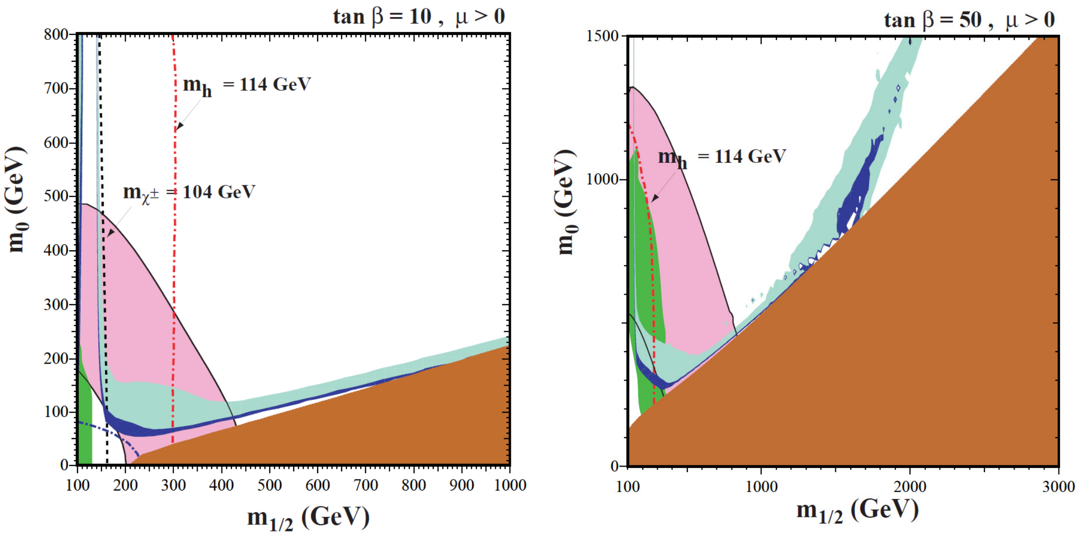

Figure 1.18: The m_0, $m_{1/2}$ mSUGRA parameter space planes for $A_0 = 0$, $|\mu| > 0$ and $\tan\beta = 10$ and 50, from [24]. The blue areas shows the parameter space regions allowed by the dark matter density measurements, where the dark blue areas include WMAP constraints while the light blue areas do not. The pink regions are those favoured by the anomalous magnetic moment of the muon. The brown regions are excluded due to the $\tilde{\tau}_1$ being the LSP, and the green regions are excluded by precision measurements of the $b \to s\gamma$ rates. The lines shows the LEP constraints on the MSSM Higgs mass (red dot-dash) and chargino masses (black dashed).

as imposed on the constrained MSSM parameter space. The allowed regions are shown in blue in the m_0, $m_{1/2}$ plane for two fixed values of $\tan\beta$.

As well as constraining the viable SUSY parameter space, the available experimental data, particularly discrepancies with the SM, can be interpreted as hints to the nature of the SUSY model. These can then be combined to determine which regions of parameter space best fit the observed values. An example of just this approach is detailed in [25]. Figure 1.19 shows the likelihood maps for all six of the two dimensional mSUGRA parameter planes, with the favoured regions identified by high values of the likelihood. The best fit point obtained by such an analysis is:

$$m_0 = 964\ GeV,\ m_{1/2} = 341\ GeV,\ A_0 = 1394\ GeV,\ \tan\beta = 57.9,\ |\mu| > 0, \qquad (1.7)$$

which gives consistent results with all observed limits and constraints. Moreover, these results indicates that the entire favoured mSUGRA parameter space should lie within the sensitivity reach of the LHC. However, as it stands, the current experimental information is too vague to do any more than weakly constrain the available parameter space. SUSY observation, or non observation is expected to be one of the most intriguing areas of study at the LHC.

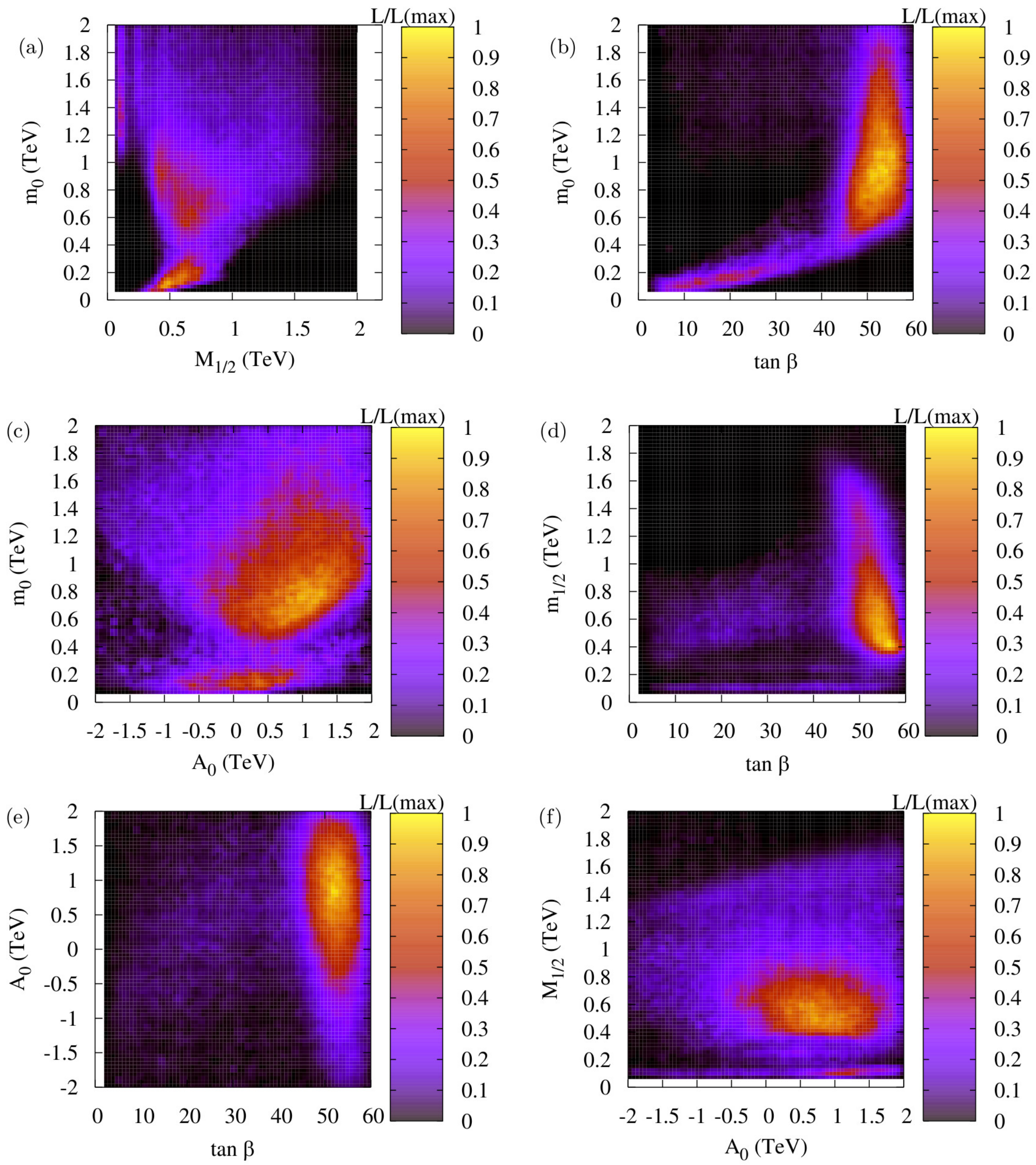

Figure 1.19: Likelihood maps of mSUGRA parameter space, based on fits to $b \to s\gamma$ rates, the anomalous magnetic moment of the muon and dark matter constraints, from [25]. The graphs show the likelihood distributions, relative to the highest bin, from the full parameter space integrated down to two dimensions.

1.2.5 SUSY Searches

In order to assess the potential of collider experiments to discover SUSY, two complementary methods of study are often pursued. The first involves detailed studies of a few benchmark points in SUSY parameter space. The second involves more generalised studies of a large number of points over scans of parameter space. The following section will introduce the mSUGRA benchmark points and parameter space scans that are studied in the following chapters of this thesis. These studies will focus on the leptonic signatures of SUSY and so this section pays particular attention to the origins of leptonic final states.

Benchmark Points

The mSUGRA benchmark points studied in this thesis are two of those studied as part of the ATLAS Computer System Commissioning (CSC) exercise [27]. These points were chosen to be compatible with the WMAP cold dark matter constraints, and to be easily accessible with relatively small amounts of data. The points are: SU3 (the *bulk region*) and SU4 (the *low mass point*).

SU3 has GUT scale parameters of:

$$m_0 = 100\,GeV,\; m_{1/2} = 300\,GeV,\; A_0 = -300\,GeV,\; \tan\beta = 6,\; |\mu| > 0. \qquad (1.8)$$

The sparticle mass spectrum, as calculated by Isajet 7.64 [28], can be seen in Figure 1.20.

SU4 has GUT scale parameters of:

$$m_0 = 200\,GeV,\; m_{1/2} = 160\,GeV,\; A_0 = -400\,GeV,\; \tan\beta = 10,\; |\mu| > 0. \qquad (1.9)$$

The SU4 sparticle mass spectrum, as calculated by Isajet 7.71 [28], can be seen in Figure 1.21. Both SU3 and SU4 are relatively low mass points, whose entire sparticle spectrum lies with the energy reach of the LHC. This is reflected in their proportionately large cross sections.

The favoured mechanisms for the production of sparticles at collider experiments and the subsequent sparticles decay modes are both strongly dependent on the parameters of the point under study. The dominant production mechanisms for SU3 and SU4 sparticles at a proton-proton collider, such as the LHC, is via pairs of coloured sparticles, such as: $\tilde{q}+\tilde{g}$, $\tilde{q}+\tilde{q}$ or $\tilde{g}+\tilde{g}$. The next-to-leading order (NLO) cross-section for production of sparticles at an LHC centre-of-mass energy of 10 TeV, as calculated by the PROSPINO 2.0.6 program [29], is 8.16 pb for SU3 and 171 pb for SU4. The produced sparticles then typically decay through long chains, or cascades, of lighter SUSY particles to the LSP, which at both points is the lightest neutralino.

At the SU4 point, leptonic final states generally arise from the leptonic decays of EW $W^{\pm}$ or

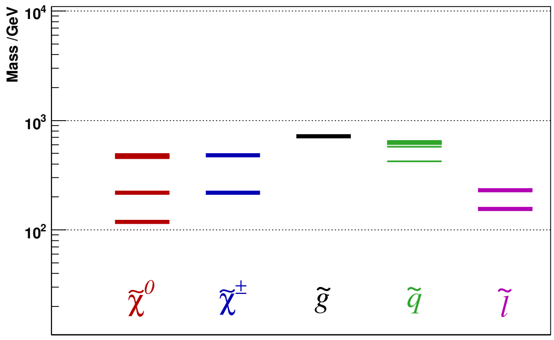

	Mass [GeV]		Mass [GeV]
$\tilde{g}$	717		
$\tilde{u}_L$	632	$\tilde{u}_R$	612
$\tilde{d}_L$	636	$\tilde{d}_R$	611
$\tilde{b}_1$	575	$\tilde{b}_2$	611
$\tilde{t}_1$	424	$\tilde{t}_2$	651
$\tilde{\ell}_L$	230	$\tilde{\ell}_R$	155
$\tilde{\tau}_1$	150	$\tilde{\tau}_2$	232
$\tilde{\nu}_L$	217	$\tilde{\nu}_\tau$	216
$\tilde{\chi}_1^0$	118	$\tilde{\chi}_2^0$	219
$\tilde{\chi}_3^0$	464	$\tilde{\chi}_4^0$	481
$\tilde{\chi}_1^\pm$	218	$\tilde{\chi}_2^\pm$	480

Figure 1.20: SU3 sparticle mass hierarchy, from [26].

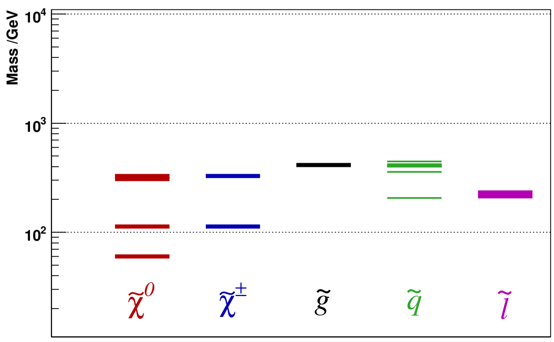

	Mass [GeV]		Mass [GeV]
$\tilde{g}$	413		
$\tilde{u}_L$	412	$\tilde{u}_R$	405
$\tilde{d}_L$	420	$\tilde{d}_R$	406
$\tilde{b}_1$	358	$\tilde{b}_2$	399
$\tilde{t}_1$	206	$\tilde{t}_2$	445
$\tilde{\ell}_L$	232	$\tilde{\ell}_R$	213
$\tilde{\tau}_1$	201	$\tilde{\tau}_2$	236
$\tilde{\nu}_L$	218	$\tilde{\nu}_\tau$	216
$\tilde{\chi}_1^0$	60	$\tilde{\chi}_2^0$	113
$\tilde{\chi}_3^0$	309	$\tilde{\chi}_4^0$	328
$\tilde{\chi}_1^\pm$	113	$\tilde{\chi}_2^\pm$	327

Figure 1.21: SU4 sparticle mass hierarchy, from [26].

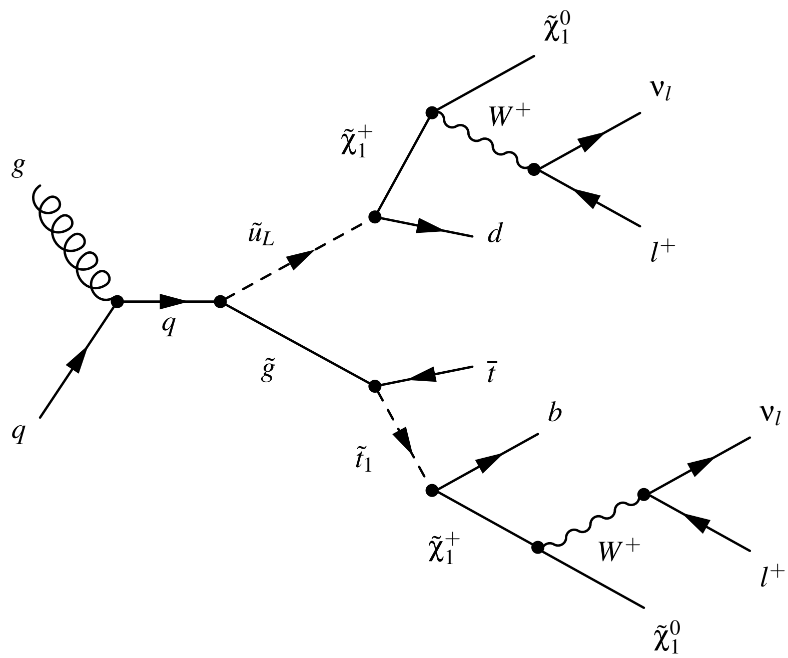

Figure 1.22: An example Feynman diagram of a SU4 SUSY process which results in a leptonic final state.

Z bosons produced when left-handed squarks or gluinos decay to gauginos and these gauginos subsequently decay to the LSP and an EW-boson. Similarly, the majority of SU3 leptonic final states arise through squark or gluino decays to gauginos. Although, unlike SU4, at SU3 sleptons are lighter than the heavier gauginos, and as a result gauginos commonly decay to a slepton rather than directly to the LSP, producing a lepton in the process. In general, due to the long decay chains involving coloured sparticles as well as leptons, the leptonic signatures of SUSY are expected to be very different from the clean final states of processes such as $Z \rightarrow e^+e^-$, with leptons often produced in environments dense with highly energetic objects. Figure 1.22 shows an example of a typical leptonic SU4 SUSY signature.

The studies in [27] indicate that both SU3 and SU4 could be discovered unambiguously at ATLAS in any of the leptonic modes with only a small amount of well understood data. As such, SU3 and SU4 present excellent benchmark models of typical SUSY events for an early physics programme at the LHC.

Parameter Space Scans

Benchmark points are selected in order to present a range of phenomenological signatures accesible with relatively little LHC data. However, these will not necessarily be representative of how SUSY manifests itself in nature. Studies of parameter space scans have the advantage of covering a wide range of parameter space and hence a wide variety of possible SUSY phenomenologies. Such studies can be used to optimise the search strategies developed on benchmark points in order to cover as broad a range of SUSY signatures as possible.

Table 1.5: The parameters of the m_0 and $m_{1/2}$ mSUGRA grid planes, all planes have $\mu > 0$.

$\tan\beta$	A_0
10	0
30	-400
30	0
30	400
50	-400
50	400

The parameter space scans, or *grids*, studied in this thesis consist of a large number of points in mSUGRA parameter space located in radial coordinates in m_0 and $m_{1/2}$. Six planes in $\tan\beta$, A_0, are studied, all with $\mu > 0$. The remaining parameters of the grids studied are summarised in Table 1.5. Each point in each grid was required to have the masses of the first two generation squarks and the gluino less than 1 TeV, in order for each point to be accessible with relatively little LHC data. The only theoretical constraints used in the choice of which points to choose was that the lightest neutralino be the LSP, EW symmetry breaking be preserved and that no particles be tachyonic. The WMAP dark matter and other experimental constraints were ignored. Whilst any realistic model must, of course, obey all constraints, it is possible to alter the SUSY breaking model such that these constraints can be satisfied at most points without significantly altering the phenomenology of the point. Therefore, each point in these grids could still be representative of a plausible SUSY scenario. For each point the low energy sparticle mass spectrum and decays were computed from the GUT scale parameters by Isajet. The general view is that these grids should not be viewed as complete theories, rather as possible patterns of LHC signatures.

This thesis will focus on two representative grids of the six studied. The first is in the $\tan\beta = 10$, $A_0 = 0$, $\mu > 0$ plane, and the second is in the $\tan\beta = 50$, $A_0 = -400$, $\mu > 0$ plane. Figure 1.23 shows the NLO cross sections of the two studied grids as calculated using PROSPINO 2.1. Cross sections are seen to decrease logarithmically with increasing m_0 and $m_{1/2}$. Previous studies have indicated that the discovery potential of SUSY at collider experiments is highest in the low m_0 and $m_{1/2}$ regions, primarily due to the increased SUSY cross section.

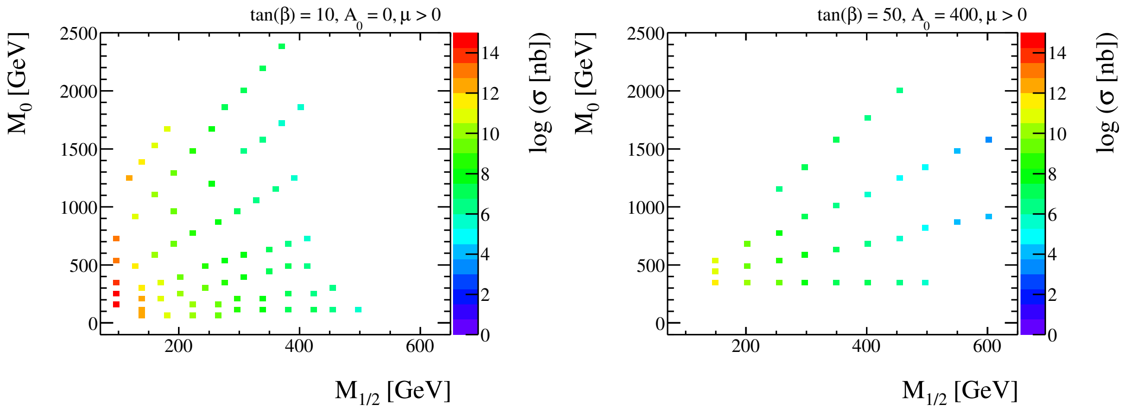

Figure 1.23: The NLO cross sections of SUSY grid points at an LHC centre-of-mass energy of 10 TeV, as computed by PROSPINO.

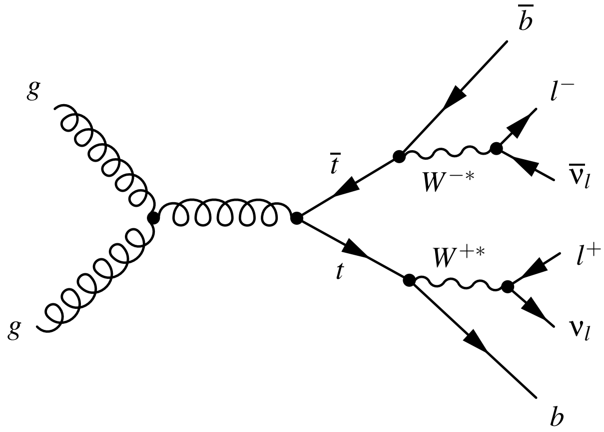

Figure 1.24: An example Feynman diagram of top quark pair production which can results in a leptonic final state.

SM top-quark production and SUSY

A common background to many leptonic SUSY searches is that of top quark pair production. Top quarks will be copiously produced at the LHC and will typically decay to a *b*-jet and a W-boson. The W-boson will then subsequently decay to either a lepton and a neutrino or to two quarks. The resultant final state is one that is rich in hadronic activity and may contain multiple leptons and the missing energy carried away by the escaping neutrinos. In short, exactly the sort of final state predicted by many SUSY models. Figure 1.24 shows an example Feynman diagram of top quark production and decay.

Understanding top decays will be an important part of many SUSY search strategies. In addition, the similarity of the top event topology to SUSY events provides a convenient SM benchmark within which the performance of the particle detectors in a SUSY like environment can be established.

1.3 Neutral BSM Resonances

SUSY is not the only viable extension of the SM. Many other theories exist, some of which address the issues of the hierarchy problem and cold dark matter and others which postulate extensions to the SM gauge groups, possible grand unification schemes, and even additional spatial dimensions. A common feature of many of these models is the inclusion of new, neutral, heavy particles. Two such models will be discussed in this thesis: one which predicts the existence of an additional EW gauge boson, the Z' , and another predicting the existence of a heavy graviton. The decays of these resonances will be exemplified by pairs of extremely energetic, opposite sign leptons, for example electron-positron pairs. These models have been studied to evaluate the effect to evaluate the effect on triggering of modified shower shapes for highly energetic electrons. However, as these processes are not the main subject of this thesis, only a very brief overview is given here.

1.3.1 Heavy Gauge Bosons

In 1974 Georgi and Glashow showed that the number of neutral gauge bosons associated with a theory is given by the *rank* of the gauge group [30]. Therefore Z' resonances are typically predicted by models proposing alternative or extended SM gauge groups which result in higher rank theories [31]. An especially compelling example is that of a grand unified theory based on a higher order symmetry which includes the SM group $\mathrm{SU}(3)_c \times \mathrm{SU}(2)_L \times \mathrm{U}(1)_Y$ as a subgroup. Within these models the mass of the Z' is generally not constrained and therefore the new Z' could exist anywhere between the EW and Planck scales. In SUSY versions of these theories the mass of the Z' is typically tied to the SUSY mass scale and so it should be in the TeV range.

A great variety of Z' models exist and studying them each individually would be impractical. Instead studies typically focus on the Sequential Standard Model (SSM) where the new Z' resonance simply has the same couplings as the SM Z but is heavier. Rather than being a realistic Z' model, the SSM is a commonly used benchmark to evaluate the discovery potential of experimental searches.

Currently no evidence for a Z' exists. Direct searches for the signatures of the production and decay of a Z' are limited by the available centre of mass energy of the collider. As such, LEP and the Tevatron have set lower mass limits due to non-observations [32, 33]. Additionally, indirect searches can look for interference effects where the existence of a Z' would alter the SM prediction for a given process. These result in the strictest experimental limits on the lower Z'_{SSM} mass from precision fits to EW data, and constrain the Z' mass to be above 1.5 TeV. Table 1.6 summarises the current experimental bounds.

Table 1.6: Experimental constrains on the SSM Z' and the RS graviton from [5].

Model	Search method	Lower mass bound [GeV]
Z'_{SSM}	Precision EW fits	1,500
	LEP e^+e^-	1,305
	CDF $p^+p^- \to e^+e^-$	923
Graviton, $k/M_P = 0.1$	CDF $p^+p^- \to e^+e^-, \gamma\gamma$	889
Graviton, $k/M_P = 0.05$	CDF $p^+p^- \to e^+e^-$	694
Graviton, $k/M_P = 0.01$	CDF $p^+p^- \to \ell^+\ell^-, \gamma\gamma$	250

1.3.2 Randall-Sundrum Gravitons

The second example of a heavy neutral resonance considered in this thesis is the graviton [34, 35]. This hypothesised spin-two particle is the quanta of gravity and is predicted by any quantum theory of gravity. Many such theories include the existence of extra spatial dimensions and are often proposed in an attempt to unify gravity with the SM, and, in the process, explain gravity's relative weakness when compared to the other forces. One example of a theory predicting a graviton resonance is the Randall-Sundrum (RS) model [36]. Within this model the SM particles exist localised on a four dimensional brane which is in turn embedded in a five dimensional space. The boundaries of this space consist of the SM brane and the so called *Planck* brane, separated from each other via an additional spatial dimension known as the *bulk*. As the SM particles are contained within only four dimensions, the fifth dimension does not affect their interactions and therefore the standard four dimensional field theories hold. Gravity, uniquely, is localised on the Plank brane and its force carriers, gravitons, are allowed to propagate in the bulk. Any gravitational interaction must therefore communicate with the SM across the separation between the branes. In this theory, the natural strength of gravity is comparable to the other forces. The apparent weakness observed on our brane arises as warped geometry in the bulk results in an exponential decay in the gravitational coupling strength. Such theories allow for the existence of *towers* of Kaluza-Klein excitations of massive gravitons within the bulk, which could be produced as resonant states at colliders.

Experimental bounds for RS graviton searches at colliders depend not only on the mass of the graviton, but also on the warp parameter, k, which governs the curvature of the bulk and hence the couplings at the SM brane. These limits are summarised in Table 1.6 for different values of k/M_{P}, from [5].

*

In conclusion, although the SM provides an excellent description of three of the four fundamental forces of nature it is an incomplete theory, failing to offer a description of gravity, a solution to the hierarchy problem or a candidate particle for cold dark matter. Both SUSY and theories which predict new resonance particles offer solutions to some of these outstanding issues and provide observable phenomenology in the TeV energy range. The Large Hadron Collider at CERN is dedicated to exploring the TeV energy regime and may soon discover the signatures of SUSY, the Higgs Bosons or new neutral resonances.

Chapter 2

The ATLAS Experiment at the Large Hadron Collider

2.1 The Large Hadron Collider

The Large Hadron Collider (LHC) [37, 38] is a next generation particle accelerator, constructed at CERN (European Organisation for Nuclear Research) in a 27 km, near circular tunnel, 100 m underneath the Franco-Swiss border. The LHC is designed to collide two counter-rotating beams of protons at a centre of mass energy ($\sqrt{s}$) of 14 TeV at four interaction points around the ring. Situated at each of these interaction points are detectors designed to record and study the results of the collisions. The four detectors are:

- ALICE (**A** **L**arge **I**on **C**ollider **E**xperiment) [39],
- ATLAS (**A** **T**oroidal **L**HC **A**pparatu**S**) [40],
- CMS (**C**ompact **M**uon **S**olenoid) [41],
- LHCb (**LHC** **b**eauty) [42].

ATLAS and CMS are general purpose detectors designed to search for new physics beyond the Standard Model, whilst ALICE and LHCb are more specialised experiments. LHCb will study CP violation using the decays of b-hadrons. ALICE, uniquely, has been designed to study the heavy ion collisions that will be produced by the LHC during periods of dedicated running each year. In addition, two smaller experiments, TOTEM [43] and LHCf [44], are situated along the beam line around 100 m away from the CMS and ATLAS interaction points respectively. TOTEM will perform luminosity studies and LHCf will study neutral particles produce in the forward region. Figure 2.1 shows the schematic layout of the LHC machine and the major experiments.

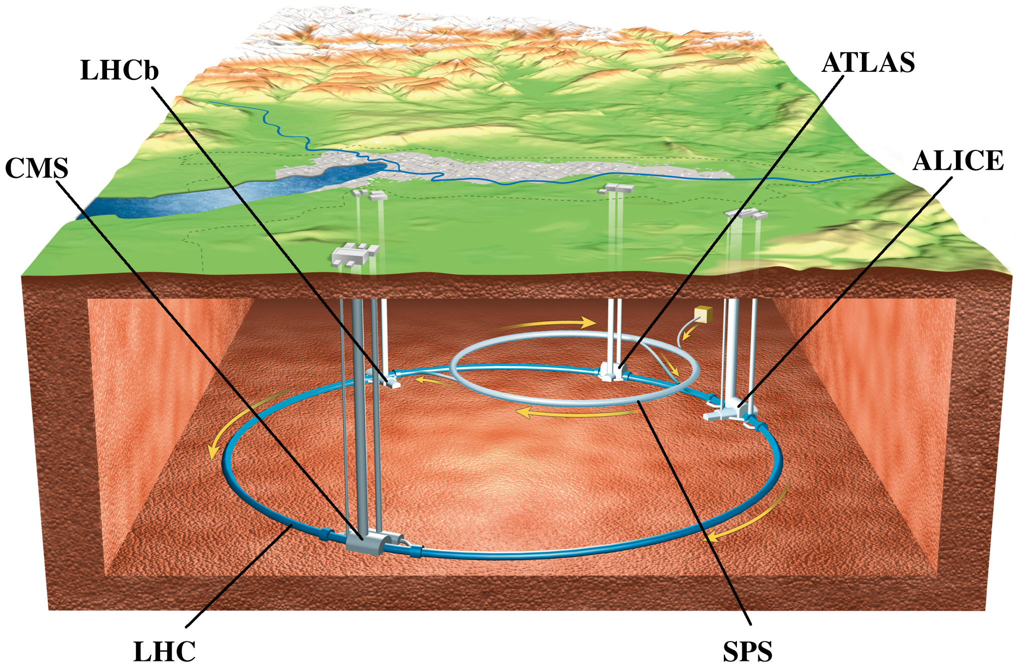

Figure 2.1: A schematic representation of the LHC and the four major experiments (adapted from [45]).

The LHC proton beams begin the acceleration process in a series of pre-accelerators. The first stage is a small linear accelerator, in which protons reach energies of 50 MeV. This is followed by a proton synchrotron booster and the Proton Synchrotron (PS), where the beams are accelerated to 1.4 GeV and 26 GeV respectively. The final pre-accelerator is the Super Proton Synchrotron (SPS), in which beams are accelerated to 450 GeV before their final injection into the main LHC ring. The LHC further accelerates these beams up to 7 TeV before bringing them into head-on collisions at each of the four interaction points. A nominal beam consists of a train of 2,808 packets or *bunches* of around 10^{11} protons, spaced 25 ns apart. These bunches cross at the interaction points at a rate of 40 MHz. Table 2.1 show a selection of important LHC design parameters from [38].

A proton-proton interaction resulting from beam collisions is known as an *event*. The number of events per unit time is the event rate, R, which is proportional to the instantaneous *luminosity* $\mathcal{L}$. Luminosity is a figure of merit of an accelerator and is determined by the beam intensities and other machine parameters. It is equal to the flux of particles per unit area, per unit time, and is usually expressed in units of $cm^{-2}s^{-1}$. The nominal LHC luminosity is 10^{34} cm^{-2} s^{-1}. The total number of collisions produced by an accelerator is often given in terms of *integrated luminosity* over time, which is expressed in units of inverse area. The rate (i.e.the expected number of events per unit time) of any given process is determined by:

Table 2.1: Some important parameters of the LHC [38].

LHC Parameter	
Beam injection energy	450 GeV
Design collision energy	14 TeV
Bunches per beam	2,808
Protons per bunch	1.15×10^{11}
Stored energy per beam	362 MJ
Bunch crossing rate	40 MHz
Time between bunches	25 ns
RMS bunch length	7.55 cm
RMS bunch width	16.7 μm
Interactions per bunch crossing	$O(20)$
Beam lifetime	22 h

$$R = \mathcal{L}\sigma, \tag{2.1}$$

where σ is the cross section, or the probability of the considered process to occur. Cross sections are purely based on the physics of the process of interest, and are expressed in units of area, commonly in barns, where 1 barn is $10^{-28}\,\mathrm{m}^2$. The total cross section for all inelastic proton-proton collisions at $\sqrt{s} = 14\,\mathrm{TeV}$ is expected to be around 79 mb [38]. This translates into an expected average of 25 interactions per bunch crossing. The majority of events will be *soft* interactions, in which the momentum transferred between protons is small. Multiple soft interactions occuring in a single bunch crossing are referred to as *pileup*.

The first beams were circulated in the LHC on the 10th of September 2008. Unfortunately, shortly afterwards, damage caused by an electrical fault lead to the suspension of collisions for over a year, whilst repairs were undertaken and additional safety features installed. On the 20th of November 2009, the beam was resumed. This was followed three days later by the first collision at the injection energy of $\sqrt{s} = 900\,\mathrm{GeV}$, and the first high energy collisions at $\sqrt{s} = 2.36\,\mathrm{TeV}$ on 30 November. Following a planned shut-down of one month, the LHC resumed in early 2010 and achieved collisions at $\sqrt{s} = 7$ TeV, half the design energy, on the 20th of March. At the time of writing, the LHC schedule was to aim for the collection of $\sim 1\,\mathrm{fb}^{-1}$ of integrated luminosity at $\sqrt{s} = 7\,\mathrm{TeV}$ over 2010/2011. This schedule was chosen in order to maximise the early potential for physics studies, whilst at the same time protecting the safety of the machine. A year long shut-down and consolidation work will follow, after which collisions will be resumed, this time, it is expected, at the $\sqrt{s} = 14\,\text{TeV}$ design energy.

2.2 A Toroidal LHC ApparatuS

The ATLAS detector [40, 46] is a general purpose detector. It was designed to study the LHC collisions in order to determine the origin of electroweak symmetry breaking and to search for new physics beyond the SM. ATLAS resembles a symmetric cylinder, 42 m long and 11 m in radius. It is aligned coaxially with the beam line and centred about the nominal interaction point. ATLAS consists of a cylindrical barrel section and two circular endcaps, each comprised of concentric layers of highly granular and hermetic subdetectors. Figure 2.2, from [40], shows the ATLAS detector with the major components labelled. The innermost section of ATLAS is the inner detector, this is designed to track the progress of charged particles as they propagate out from the interaction point. Surrounding the inner detector are the calorimeters, these serve to contain and measure the energies and positions of electrons, photons and hadrons. The outermost subdetector, surrounding the calorimeters, is the muon system. The muon system will measure the position and momenta of muons which penetrate through both the inner detector and the calorimeters. Not all of the collisions produced by the LHC will be recorded to storage by ATLAS. The *trigger* system is the system used by ATLAS to decide which events to store, and which to discard.

The following sections introduce some coordinates and conventions, then discuss the various subdetector systems sequentially, starting with the innermost and moving radially outwards. Following this, a brief introduction to the trigger system will be given. The trigger is explained in more detail in the following chapter.

2.2.1 Nomenclature

The ATLAS coordinate system is defined with its origin at the nominal interaction point. The x-axis points towards the centre of the LHC ring, the y-axis points upwards and the z-axis points along the beam line towards the LHCb experiment to form a right handed coordinate system. The transverse radius from the beamline is denoted as r. The azimuthal angle ϕ is measured from the positive x-axis clockwise around the beam axis when facing in the positive z-direction. The polar angle θ is the angle measured from the beamline. Instead of θ, the polar angle is often denoted in terms of the pseudo-rapidity η. This is a dimensionless measure of θ which for massless particles is invariant under longitudinal, z, boosts. It is defined as:

$$\eta = -\ln\left(\tan\frac{\theta}{2}\right). \tag{2.2}$$

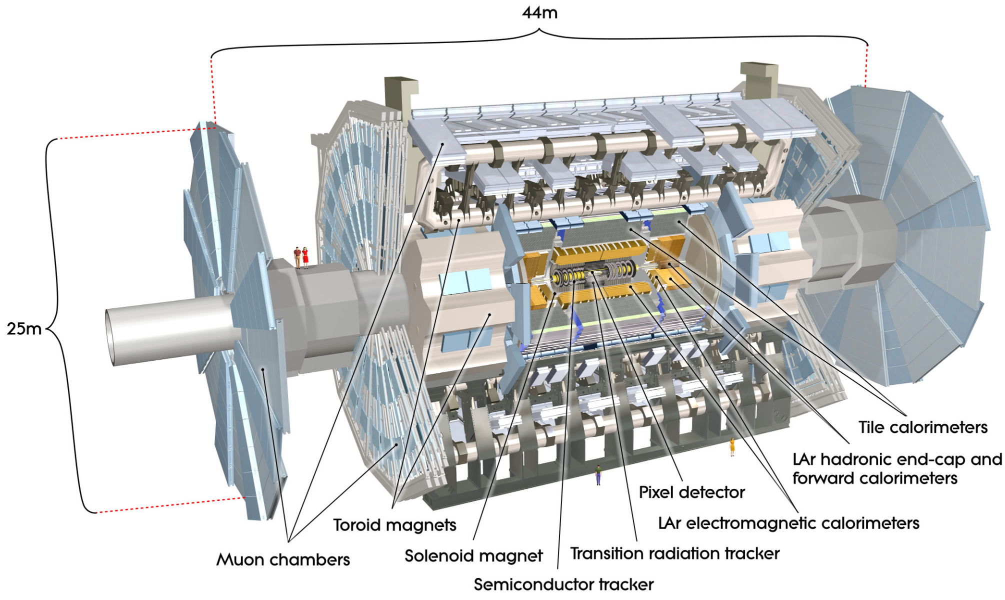

Figure 2.2: A cut-away view of the ATLAS detector, from [40].

The ATLAS coordinate system uses pseudo-rapidity and azimuthal angle as generic spatial coordinates. The distance ΔR in pseudo-rapidity-azimuthal angle space is defined as:

$$\Delta R = \sqrt{\Delta\eta^2 + \Delta\phi^2}. \tag{2.3}$$

Small angles to the beamline, at large $|\eta|$, are generically refered to as the *forward* region, whilst the low $|\eta|$ region, perpendicular to the beamline, is refered to as the *central* region. The *transverse momentum*, p_T, and *transverse energy*, E_T of particles, are defined in the xy-plane to be:

$$p_T = \sqrt{p_x^2 + p_y^2}, \tag{2.4}$$

$$E_T = \sqrt{E^2 - p_z^2}, \tag{2.5}$$

where E is the total energy of the particle and p_x, p_y and p_z are the x, y and z components of momentum. Missing transverse energy, E_T^{miss}, is indicative of exclusively weakly interacting particles, such as neutrinos or neutralinos, escaping ATLAS undetected.

2.2.2 Magnet System

In order to enable momentum measurements, ATLAS is equipped with a large magnet system. Charged particles travelling through a magnetic field experience a deflecting force whose magnitude is related to the strength of the magnetic field and the charge of the particle. Such particles will then bend with a radius of curvature proportional to their momentum. The ATLAS magnet system consists of a central solenoid surrounding the inner detector, and three large air-core toroids outside the calorimeters. Figure 2.3 shows the layout of the magnets system.

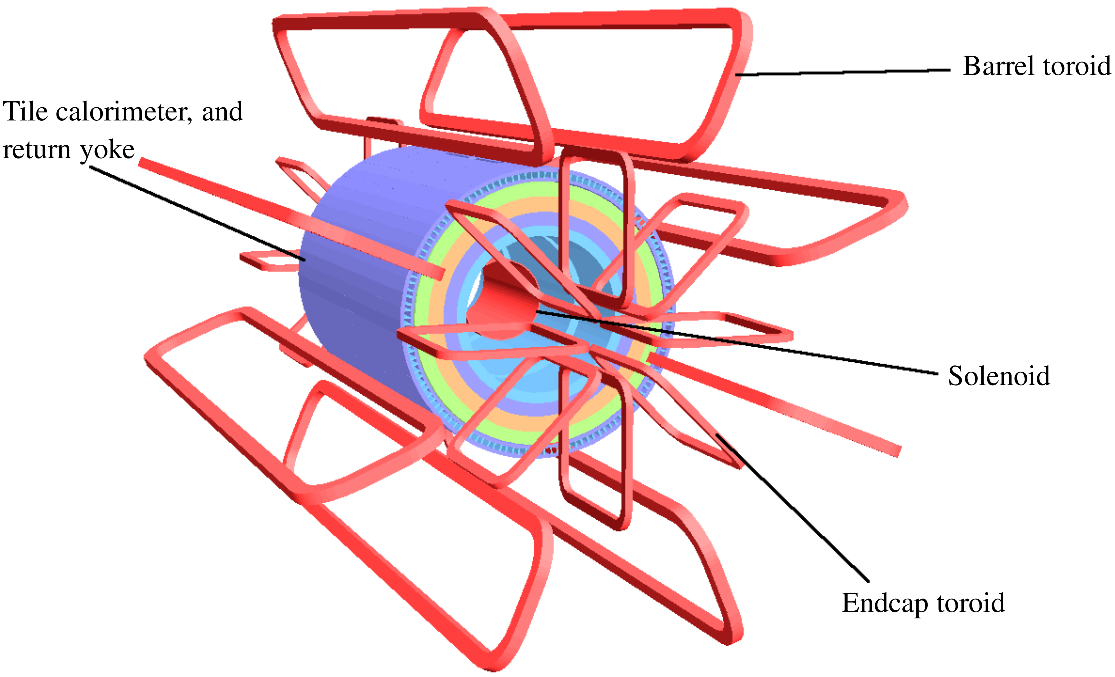

Figure 2.3: The layout of the ATLAS magnet systems, from [40].

The central solenoid provides an axial 2 T magnetic field across the inner detector volume. This provides sufficient bending power to allow for accurate momentum measurements for particles with momentum up to 100 GeV. It is 5.3 m in length and 2.44 m in diameter. In order to minimise the amount of material in front of the calorimeters, the central solenoid is only 44 mm thick and shares a cryostat with the electromagnetic calorimeter barrel. The magnetic flux is returned in the steel of the hadronic calorimeter and its support structure.

The toroid system consists of the barrel toroid and two endcaps. These provide a tangential magnetic field, which is mostly orthogonal to muon trajectories over the entire muon system. They are designed with an open structure to minimise any multiple scattering of muons which would degrade the momentum resolution. Both the barrel toroid and the endcaps consists of eight coils assembled radially around the beam axis. The barrel section is 25.3 m long, with an inner and outer diameter of 9.4 m and 20.1 m respectively. It provides a magnetic field with a bending power of between 1.5 Tm and 5.5 Tm across the range $|\eta| < 1.4$. The two endcaps are inserted inside the barrel toroid on either side of the central solenoid, these are rotated by 22.5° with respect to the barrel system to provide a radial overlap and to optimise bending power in the interface between the barrel and the endcaps. These provide a bending power of between 1 Tm and 7.5 Tm over the

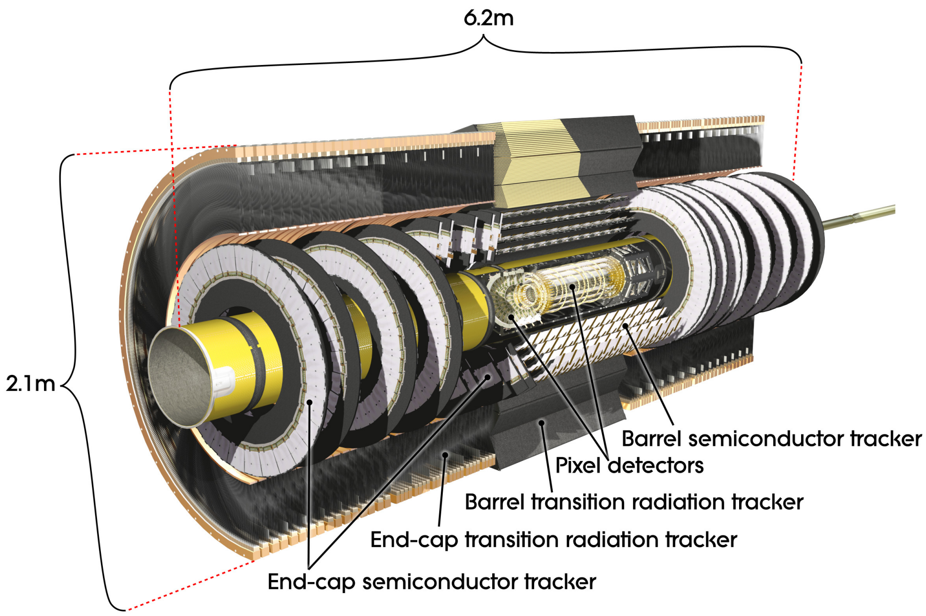

Figure 2.4: A cut away view of the ATLAS inner detector, from [40].

range $1.6 < |\eta| < 2.7$. The interface region between the two systems spans $1.4 < |\eta| < 1.6$ and is termed the *transition region*, over which the bending power is lower.

2.2.3 Inner Detectors

At design specifications the LHC will collide proton bunches at the ATLAS interaction point every 25 ns. On average each collision is expected to produce over 1,000 particles. The ATLAS inner detector (ID) makes use of discrete, high resolution measurements of charged particle positions to track the progress of each particle as it propagates out from the interaction point. The entire ID volume is immersed in a 2 T axial magnetic field provided by the central solenoid magnet. This will bend the trajectories of charged particles propagating from the interaction point in the azimuthal plane. By measuring the curvature of each particle's path the ID is able to precisely determine its momentum. Furthermore, such precise tracking allows for the identification of both the primary interaction vertex, and any secondary vertices created during decays of unstable particles. The inner detector covers the region $|\eta| < 2.5$ and is comprised of three concentric systems. The spatial information provided by these three subdetectors is combined into *tracks*. The innermost ID subdetector, closest to the interaction point, is the *pixel* detector. Surrounding this is the *semiconductor tracker* (SCT), and outside both of these is the *transition radiation tracker* (TRT). Figure 2.4 shows a cut-away view of the ATLAS ID.

Pixel Detector

The pixel detector records the passage of charged particles using semiconducting silicon pixels. A charged particle passing through a pixel will create electron-hole pairs, a voltage bias then causes these to drift towards a readout cathode. If the resultant electrical signal exceeds a preset threshold value, then a *hit* is recorded. Individual pixels have a minimum size of $50 \times 400\mu$m and are segmented in $r-\phi$, and z. Pixel layers are made up of 2×6cm rectangular wafers, each comprised of 46,080 pixels. These are arranged in three concentric barrels layers of radii 50.5 mm, 88.5 mm and 122.5 mm, with wafers mounted parallel to the beam axis. Similarly, two identical endcaps with five disk layers each, are made up of wafers mounted perpendicular to the beam axis. Any track is ensured to pass through at least three layers. The intrinsic resolution of the pixels is 10μm in $r-\phi$ and 115μm in z for the barrel, or r for the endcaps. The pixel detector has around 80.4 million readout channels.

The high resolution of the pixel detector is at the limit of current technology. Its performance is crucial in the identification of secondary vertices, and therefore in the identification, or *tagging*, of b-quarks and τ-leptons. Being close to the interaction point, the pixel detector will be exposed to exceeding high levels of radiation. This will eventually degrade the performance of the detector. To counter this, and to allow the performance of ATLAS to be maintained, the design allows for the replacement of the innermost, or b-layer every few years.

SCT

The middle subdetector of the ID, the SCT, uses semiconducting silicon microstrip layers to record charged particle tracks based on the same principles as the pixel detector. The reduced particle densities expected at higher radii allows the SCT to maintain the required levels of performance yet use significantly fewer readout channels than the pixel detector. The SCT is comprised of modules made of sets of two back-to-back silicon wafers. Each wafer is comprised of 768 61.6 mm strips. One set of wafers is arranged parallel to the beam direction, whilst the other is rotated by 40 mrad in order to provide a measurement in the z-direction. The SCT modules are arranged in four barrel layers with radii ranging from 299 mm to 514 mm, and nine endcap disks. Each charged particle will pass through at least eight silicon layers, providing four positional measurements, or *space points*. The spatial resolution of the SCT is 17μm in $r-\phi$, 580μm in z, in the barrel and 17μm in $r-\phi$, 580μm in r in the endcaps. The total number of readout channels in the SCT is approximately 6.3 million.

TRT

The TRT is the outermost component of the ID. It is both a straw drift-tube tracker and a transition radiation detector. The TRT is constructed from 4 mm diameter *straws* with a 30μm anode wire in the centre. The straws are filled with a xenon, carbon dioxide, oxygen gas mixture. A charged particle traversing a straw will leave a trail of electron-ion pairs in its wake. These will then cascade towards the anode and be registered as an electrical signal, or *hit*. The straws of the TRT are interweaved with sheets or fibres of polypropylene. Polypropylene has a different dielectric constant to the straws themselves. Therefore, when a relativistic particle passes from one medium into the other, it will emit transition radiation, which will contribute to the amount of ionisation that the particle causes. The intensity of produced radiation is roughly proportional to γ, where:

$$\gamma = \frac{E}{m}. \tag{2.6}$$

This means that, for a given energy, the TRT is able to offer some discrimination between light particles, such as electrons, and heavy ones, such as hadrons, by the energy of the transition radiation generated and hence the amount of charge collected. TRT hits are categorised as either low threshold hits or high threshold hits.

The barrel section of the TRT consists of three nested cylindrical layers, each containing a number of 144 cm long straws arranged parallel to the beam direction, interspersed with polypropylene fibres. The endcaps consist of two wheels of 37 cm radially aligned straws interleaved with layers of polypropylene foil. A typical track will pass through 36 TRT layers. The TRT only covers the region $|\eta| < 2.0$ and only provides information on position in the $r-\phi$ plane. Its spatial resolution is 130μm.

The TRT is designed to be complementary to the silicon pixels and SCT. Its lower precision compared to silicon is compensated for by the large number of measurements per track and a larger track length, which significantly contributes to the p_T resolution of the ID.

2.2.4 Calorimeters

The ATLAS calorimeter system is positioned outside the ID and central solenoid. It is designed to contain, and measure the energies of, electrons, photons and hadrons. This is achieved by causing these particles to *shower* in layers of a dense, *absorber* medium and then measuring the energies of the produced showers in interleaved *sampling* regions. Such calorimeters are referred to as sampling calorimeters, as they periodically sample the energy contained in showers. The total amount of energy sampled will be roughly proportional to the energy of the incident particle.

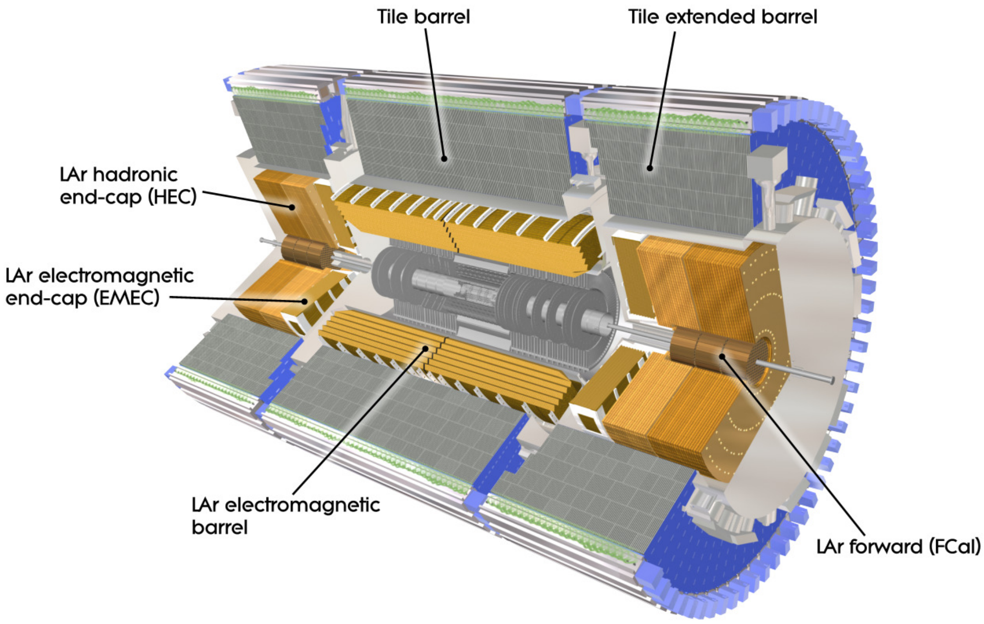

Figure 2.5: A cut-away view of the ATLAS calorimeters, from [40]

The calorimeter system can be divided into two sections, the electromagnetic calorimeter, and the hadronic calorimeter. These use a variety of different techniques suited to the varying physics requirements of each subsystem. Combined, these cover the region $|\eta| < 4.9$. Figure 2.5 shows a cut-away view of the ATLAS calorimeter system.

A high energy electron or photon in a dense medium will initiate an *electromagnetic shower* via a series of alternating pair production ($\gamma \to e^+e^-$) and bremsstrahlung ($e \to \gamma e$) processes [47]. The length scale of electromagnetic showers in a given material is described by its *radiation length*, X_0. This is defined as the mean distance over which a high energy electron will lose all but $1/e$ of its energy by bremsstrahlung. It also corresponds to 7/9 of the mean free path for pair-production by a high energy photon. The shower depth of an EM shower is proportional to the logarithm of the energy of the initial particle. A typical shower produced by a 30 GeV electron will require between fourteen and sixteen radiation lengths for complete containment. The lateral shape of an EM shower is characterised by the Molière radius of a material. This defines that width over which 90% of a shower energy will be contained and is independent of the energy of the initial particle.

Any energetic strongly interacting parton produced at the interaction vertex will *hadronise*, resulting in a *jet* of hadrons visible in the detector. Both charged and neutral hadrons primarily lose energy via inelastic interactions with atoms in which secondary strongly interacting particles are produced. Via this repeated process *hadronic showers* are formed [47]. The depth of hadronic showers is characterised by the *interaction length*, λ, of a material. Similarly to an EM shower, the shower depth of a hadronic shower is proportional to the logarithm of the initial energy. In most materials λ is much greater than X_0 and therefore a typical hadronic shower will be longer and wider than an EM shower. In addition, unlike EM showers, up to 30% of the incident energy of a hadronic shower may avoid detection by being absorbed during the break up of nuclei or by escaping the detector as undetectable secondary particles.

The *energy scale* of the calorimeters relates the observed energy deposited by a particle shower to the energy of the original particle. Due to the nature of their respective showers, defining the energy scale correction is more difficult for hadronic showers than for EM showers.

The ATLAS calorimeter system has been designed to be as hermetic as possible, as this will allow the measurement of any imbalanced or *missing transverse energy*, E_T^{miss}, which is indicative of neutrinos or other weakly interacting particles that escape the detector without interacting.

Electromagnetic Calorimeters

The electromagnetic calorimeter (ECAL) is a sampling calorimeter composed of alternating layers of lead and liquid argon (LAr). The dense lead ($X_0 = 0.56\,\mathrm{cm}$) initiates EM showers, which in turn ionise the LAr in the gaps. An applied voltage across the LAr then allows this signal to be read out via copper electrodes. The lead and LAr layers are folded into an accordion geometry, which allows for complete ϕ coverage.

The ECAL is divided into two endcaps, and two identical barrel sections separated by a small, 4 mm, gap at $z = 0$. The barrel has an inner radius of 1.4 m and an outer radius of 2 m. The endcaps extend radially from 33 cm to 2 m. Each section of the ECAL is subdivided into concentric layers, or samplings, and further segmented into $\eta \times \phi$ cells which are projective with respect to the nominal interaction point. The number of sampling layers varies with η, as does the cell granularity, with the majority of the ECAL having three samplings. The precision region, of highest granularity, covers $|\eta| < 2.5$, matching the coverage of the ID. Figure 2.6 shows the accordion geometry and samplings at $\eta = 0$.

The first, innermost, sampling consists of narrow cell strips of size 0.0031×0.1 in $\eta \times \phi$ at $\eta = 0$[1]. The fine η granularity serves to provide a precise position measurement to complement that made by the ID. In addition, it enables studies of the substructure of showers, which in turn allows for the identification of $\pi^0 \to \gamma\gamma$ decays. Including upstream material, the thickness of the first sampling is $\sim 7\ X_0$, and of this the calorimeter itself constitutes around $3\ X_0$. The second sampling is considerably thicker than the first at around $17\ X_0$. This is the main sampling of

[1] All quoted cell granularities vary across the η range as detailed in [40].

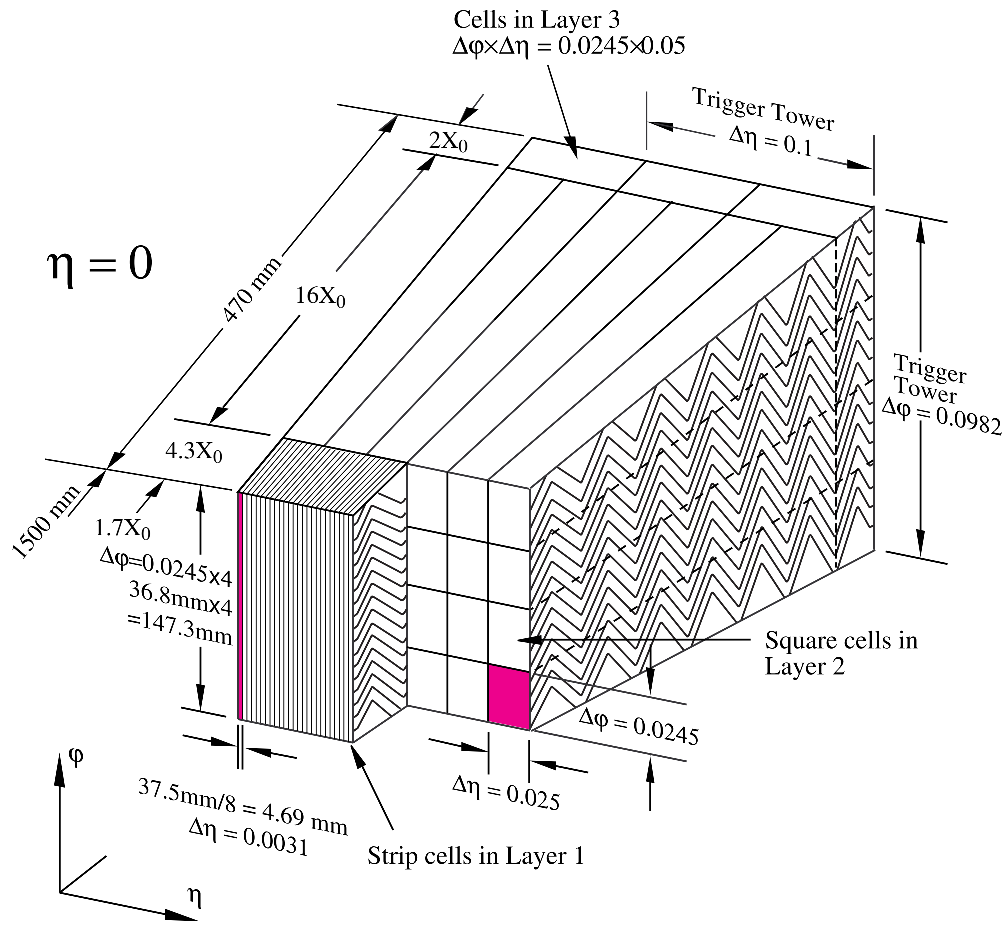

Figure 2.6: The accordion geometry and samplings of the electromagnetic calorimeter, from [40]

the ECAL. It is divided into projective 0.025×0.025 $\eta \times \phi$ cells, which is about 4×4 cm at $\eta = 0$. The chosen size of the cells is derived from the Molière radius of the calorimeter, which is around 2.5 cm in the barrel [48]. This granularity allows for good containment of an EM shower within a relatively small number of cells and therefore minimises any electronic or pile-up noise. Moreover, this size allows for discrimination between EM showers and those produced by pions and other hadrons. A typical EM shower will deposit more than 70% of its energy in the second layer alone [49]. The third and final sampling has a coarser granularity of around 0.05×0.025 in $\eta \times \phi$ and varies in thickness from between 2 to 12 X_0. In the range $|\eta| < 1.8$ a zeroth layer, or *presampler*, consisting of a single LAr layer, is fitted inside the inner solenoid. The purpose of the presampler is to correct for energy losses in the material upstream of the calorimeter. The region $1.37 < |\eta| < 1.52$ at the junction between the barrel and endcap is not used for precision physics measurements due to the large amount of material situated in front of the ECAL. This region is often termed the *crack* region.

The total thickness of the ECAL is around 26 X_0 in the barrel and 30 X_0 in the endcap. In total there are around 170,000 readout channels. Test beams have measured the energy resolution of

ECAL barrel modules to be [40]:

$$\frac{\sigma_E}{E} = \frac{10.1\%}{\sqrt{E}} \oplus 0.2\%, \tag{2.7}$$

which is in accordance with the strict design specifications of the ECAL. These required that the ECAL must have sufficient energy resolution to be able to determine the mass of a low mass Higgs boson ($m_H = 90 - 180\,\mathrm{GeV}$) to within 1% using the decay channels H→ $\gamma\gamma$ and H→ZZ* [40].

Hadronic Calorimeters

The hadronic calorimeter (HCAL) is a sampling calorimeter designed to initiate hadronic showers and measure their energies. In addition, to facilitate measurements of E_T^{miss}, the HCAL must also ensure the containment of these showers and prevent the leakage into the muon system. The HCAL is made up of a number of complementary technologies composing the barrel, the endcaps and the forward calorimeters.

The barrel region is a *tile calorimeter* and is composed of a central barrel covering the range $|\eta| < 1.0$ and two extended barrels covering the regions $0.8 < |\eta| < 1.7$. It has an inner radius of 2.28 m and an outer radius of 4.23 m. The tile calorimeter is constructed from alternating layers of steel absorbers and plastic scintillating tiles. Hadronic showers initiated in the steel absorbers produce scintillation light as they pass through the sampling tiles. This is then read out to photomultiplier tubes and converted into an electrical signal. The total thickness of the material in front of the tile calorimeter is 2.3 λ at $\eta = 0$. The tile calorimeter itself is longitudinally segmented into three samplings, which are 1.5, 4.1 and 1.8 λ deep in the central barrel and 1.5, 2.6 and 3.3 λ deep in the extended barrel. The cell granularity is 0.1×0.1 in $\eta \times \phi$ in the first two layers and 0.1×0.2 in $\eta \times \phi$ in the last layer. There are a total of around 10,000 readout channels.

The two hadronic endcaps are LAr sampling calorimeters which use copper as an absorbing material. They are each composed of two disks and cover the range $1.5 < |\eta| < 3.2$. Each HCAL disk is segmented into 4 layers and has a cell granularity of 0.1×0.1 in $\eta \times \phi$ over the range $1.5 < |\eta| < 2.5$ and 0.2×0.2 in $\eta \times \phi$ over $2.5 < |\eta| < 3.2$. In total the endcaps are around 10 λ thick and have a total of around 5,600 readout channels.

The final component of the HCAL is the forward calorimeter. This consists of two endcaps which covers the range $3.1 < |\eta| < 4.9$. The forward calorimeters are LAr sampling calorimeters constructed of a matrix of metal absorbers containing thin LAr filled sampling gaps. The forward calorimeter is approximately 10 λ deep, and consists of three layers. The first layer, made of copper, is optimised for EM measurements, while the other two, made of tungsten, predominantly measure the energy of hadronic interactions. The granularity varies over η but is generally coarser than the other components of the HCAL. There are a total of approximately 3,500 readout channels.

The overall depth of the HCAL has been shown by both measurements and simulations to be sufficient to reduce over-penetration of hadronic showers (or punch through) into the muon system [40] well below the irreducibly level of prompt or decay muons. The energy resolution of the HCAL as measured using pion test beams [40] is:

$$\frac{\sigma_E}{E} = \frac{70.6\%}{\sqrt{E}} \oplus 5.8\%, \tag{2.8}$$

and similarly the forward calorimeter energy resolution is measured to be:

$$\frac{\sigma_E}{E} = \frac{70\%}{\sqrt{E}} \oplus 3\%. \tag{2.9}$$

2.2.5 Muon Spectrometer

Although muons are unstable, the relativistic muons produced during LHC collisions will, on average, live for a much longer time than it takes to traverse a volume the size of ATLAS. Being heavy, muons are not as sharply accelerated as electrons in magnetic fields and as a result do not lose as much energy through bremsstrahlung. For this reason muons are some of the most penetrating particles, and energetic muons will be capable of passing through the entire detector. The muon spectrometer is situated outside the calorimeters, in and around the toroidal magnet system. It is designed to provide precision position and momentum measurements for high energy muons, and any other charged particles, which may not have been well measured in the ID. It is the largest of the ATLAS subdetectors and its geometry defines the size of ATLAS itself. The muon system is comprised of four complementary types of projective muon chamber. Two of these provide precision position measurements and the remaining two provide triggering capability and provide secondary coordinates. The toroidal magnets provide a magnetic field which will bend the trajectories of muons propagating from the interaction point in the pseudo-rapidity plane. Figure 2.7 shows a cut-away view of the ATLAS muon spectrometer.

The muon system is divided into a barrel and two endcaps. The three concentric barrel layers, containing both precision and trigger chambers, are positioned at radii of 5 m, 7.5 m and 10 m and cover the range $|\eta| < 1.0$. The two endcaps are each comprised of four layers, again containing both precision and trigger chambers. They are positioned at $|z|$ of 7.4 m, 10.8 m, 14 m and 21.5 m, and cover the range $1.0 < |\eta| < 2.7$. There exists a small gap at $|z| = 0$ which allows services access to the ID, calorimeter and solenoid magnet. In addition there are two gaps in acceptance at $\phi \sim 1.2$ and $\phi \sim 2.2$ due to the detector support structure. A muon will typically pass through

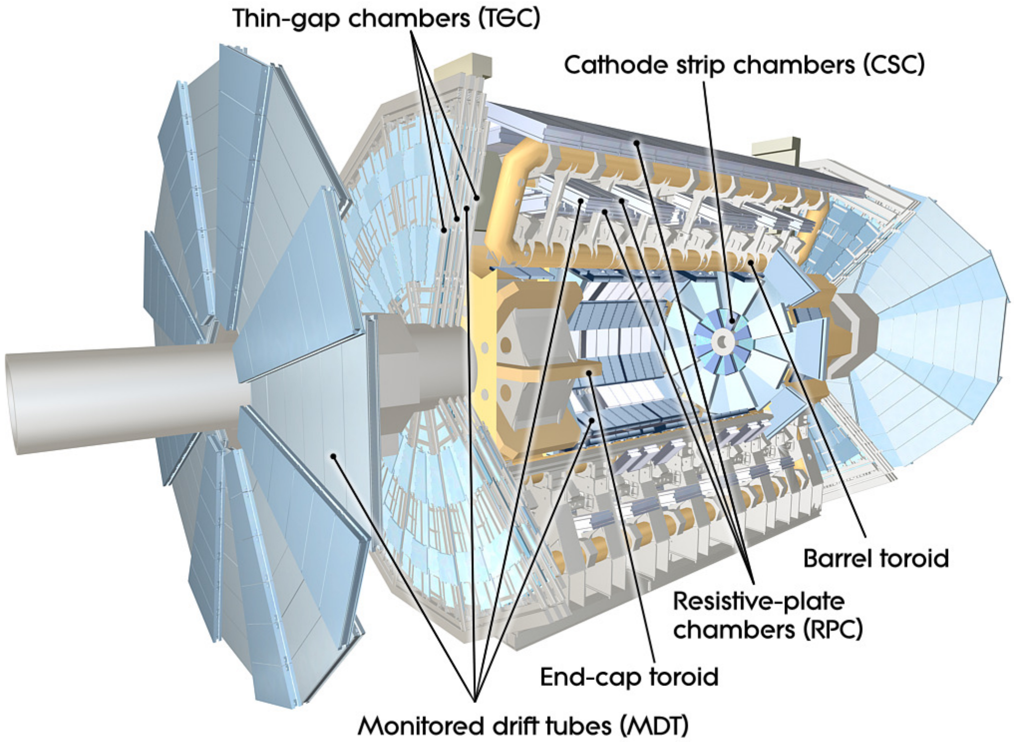

Figure 2.7: A cut-away view of the ATLAS muon system, from [40].

three layers of chambers.

Precision Chambers

The two types of *precision chambers* are the Monitored Drift Tubes (MDTs), and the Cathode Strip Chambers, (CSCs).

MDT chambers cover the range $|\eta| < 2.7$. Each chamber is constructed from three to eight layers of aluminium tubes, 30 mm in diameter, varying in length from 85 cm to 650 cm. The tubes are filled with argon and carbon dioxide gas and contain a central tungsten wire. A charged particle passing through such a tube will leave a trail of ions in the gas which are collected on the wire. The spatial resolution of the MDTs is around 80 μm per tube or 35 μm per chamber.

In the forward region, $2.0 < |\eta| < 2.7$, CSCs are used in the innermost tracking layer due to their higher rate capability and time resolution. CSCs are multi-wire proportional chambers, filled with a gas mixture of Argon, CO_2 and CF_4 and closely spaced anode wires. Placed perpendicular to the wires are cathode strips. A charged particle will initiate an ion shower in the gas which will be detected at both the cathode and the anode, allowing the measurement of both r and ϕ coordinates. The resolution of the CSCs is 40 μm in r and 5 mm in ϕ.

Trigger Chambers

The ATLAS trigger system is introduced in Section 2.2.7 and described in detail in Chapter 3. An essential criterion of the trigger system is to be able to identify potentially interesting events within a very short space of time and associate these unambiguously to a given bunch crossing. However, the time resolution of the precision chambers exceeds the stringent constraints of the trigger system. In order to provide the capability to trigger on muons, dedicated chambers are used which are capable of recording and providing information with microsecond latency and nanosecond timing resolution required. There are two types of muon trigger chambers: Resistive Plate Chambers, (RPCs), and Thin Gap Chambers, (TGCs).

RPCs are used in the barrel region over the range $|\eta| < 1.05$. RPCs are made from two parallel resistive plates, separated by 2 mm, with a potential difference between them. The gap is filled by a $C_2H_2F_4$, Iso-C_4H_10, SF_6 gas mixture. A charged particle will initiate an ion shower in the gas which will be read out by metallic strips on the outer faces of the resistive plates. The resolution of the RPCs are 10 mm in z and ϕ.

TGCs cover the range $1.05 < |\eta| < 2.4$ and are multi-wire proportional chambers, similar to the CSCs. TGCs get their name as the gap between the wires and the cathode is smaller than the gap between wires. TGCs have higher granularity than the RPCs at $2-6$ mm in r and $3-7$ mm in ϕ. The time resolution of the trigger chambers is 1.5 ns for the RPCs and 4 ns for the TGCs, well within the limits for triggering. In addition to triggering, these chambers also provide a complementary measure of the muon coordinate in the direction orthogonal to that determined by the MDT precision-tracking chambers.

The muon system provides momentum measurements and charge identification for muons with p_T greater than 3 GeV and up to $\sim$ 3 TeV. At 1 TeV the momentum resolution for muons is:

$$\frac{\sigma_{p_T}}{p_T} = 10\%, \tag{2.10}$$

and closer to 2-3% at lower energies of around 20 GeV.

2.2.6 Minimum Bias Trigger Scintillators

In order to understand the soft p-p collisions which comprise the vast majority of the LHC event rate, ATLAS must be able to select events typical of these very soft interactions. The Minimum Bias Trigger Scintillator (MBTS) disks [50] provides ATLAS with the ability to select collisions as inclusively as possible, or synonymously, with the "minimum of bias". The MBTS system consists of two disks of sixteen scintillation counters installed on the inner faces of the hadronic endcap calorimeter cryostats $\pm 3.56\,\mathrm{m}$ from the nominal interaction point. Each MBTS disk is divided into an inner and an outer ring, each of which is further divided into eight units in ϕ. These cover the regions $2.82 < |\eta| < 3.84$ and $2.09 < |\eta| < 2.82$ respectively. Individual MBTS units consist of a 2 cm thick layer of polystyrene-based scintillating material. Any charged particle traversing the scintillator will leave a trail of scintillation light which will then be read out by wavelength shifting fibres to external photo-multiplier tubes and registered as a signal. Candidate collision events are identified based on coincidences of signals in both MBTS systems.

Unlike the majority of ATLAS, the MBTS system is not particularly resistant to radiation damage and is expected to exhibit a significant degradation in performance after only three to four months of running at luminosity of $10^{33}\ \mathrm{cm}^{-2}\ \mathrm{s}^{-1}$.

2.2.7 The Trigger and Data Acquisition System

The ATLAS Trigger and Data Acquisition (TDAQ), system is dedicated to selecting which events should be recorded for later study, and for handling the transfer of the data corresponding to these events to permanent storage. The TDAQ software runs in real time, that is, as the detector is recording information, and is referred to as *online* software. This is to be contrasted with the software used to examine events after they have been recorded which is known as *offline* software. The TDAQ is subdivided into two systems, the *trigger*, which is responsible for the selection of events, and the *Data Acquisition* system (DAQ) which handles the flow of data. Comprehensive descriptions of these can be found in [40, 51, 52]. The TDAQ system is described in detail in the following chapter.

*

The ATLAS detector is composed of a combination of precision tracking detectors, hermetic calorimeters and a large dedicated muon system. This design should ensure that if new physics is produced by the LHC, then ATLAS will be in an excellent position to witness it, no matter how it manifests itself.

Chapter 3

The ATLAS Trigger System

At the LHC design luminosity of $\mathcal{L} = 10^{34}$ cm^{-2}s^{-1}, the event rate witnessed at ATLAS is expected to be around 1 GHz. Figure 3.1, from [53], shows the cross sections and event rates at $\mathcal{L} = 10^{34}$ cm^{-2}s^{-1} extrapolated from Tevatron observations, along with those expected at the LHC. The overwhelming majority of the expected event rate is observed to consist of SM QCD interactions, whilst the physics processes of interest often have cross sections several orders of magnitude smaller than this *background*. In theory, an ideal experiment should be capable of recording each and every event, and thus ensuring the complete acceptance of any interesting processes. However, in reality, technological constraints limit the amount of data that can be recorded to around 300 MBs^{-1}. As an average collision is expected to be around 1.3 MB in size this, therefore, limits the rate at which collisions can be stored to approximately 200 Hz. The system for deciding which events to store the information on and which to discard is made by the *trigger* system. In order to abide by the bandwidth constraints, the trigger is required to achieve an overall rejection factor of around $O(10^5)$, and, at the same time, it must sustain an excellent selection efficiency for the rare processes of interest. The trigger system is therefore at the cornerstone of the ATLAS physics programme, as it is this which dictates which processes can be fully explored and which cannot.

When discussing trigger selections, the term *event* is often used interchangeably to describe bunch crossings as well as specific interactions. Thus the selected *event rate* relates to the rate at which bunch crossings are stored.

The ATLAS trigger system functions by identifying features which distinguish interesting or new physics from the overwhelming bulk of SM processes. Such features include: high p_T leptons, photons, or jets; large E_T^{miss}; large total amounts of energy and combinations thereof. The usefulness of such features in identifying interesting events from potential backgrounds is further enhanced if they are *isolated*, (produced far from any other particles). In addition, ATLAS

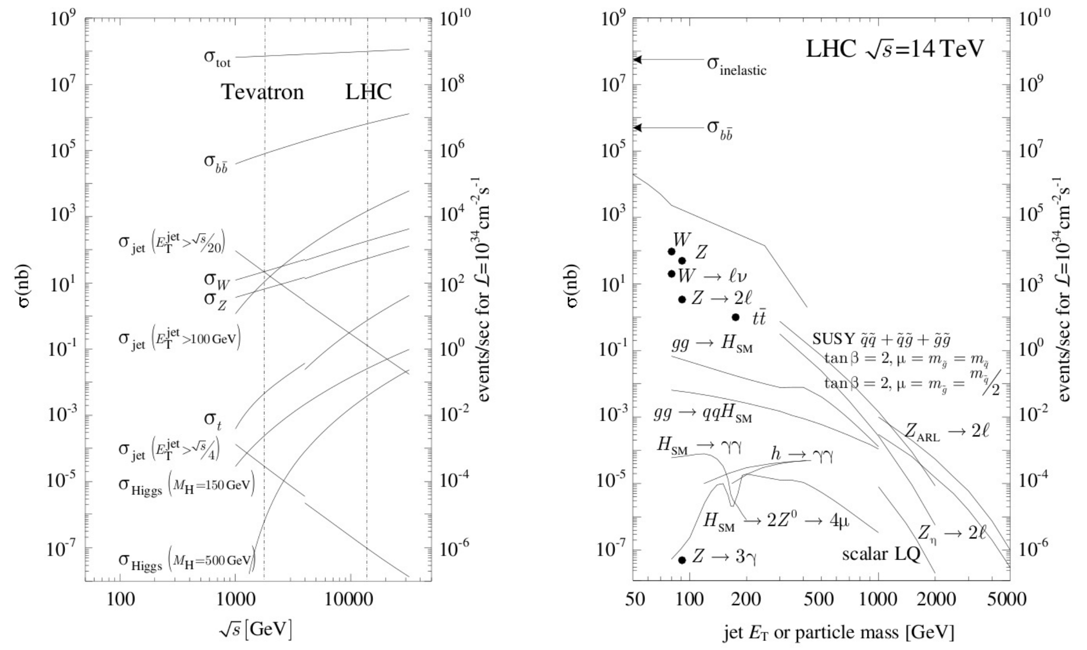

Figure 3.1: Cross-sections and event rates for proton proton collisions. The left-hand figure shows expected cross section as a function of the centre of mass energy at the Tevatron ($p-\bar{p}$ collision), and at the LHC ($p-p$ collision) energy scales. The right-hand figure shows expected event rates as a function of the produced particle mass or the highest jet transverse energy for $\sqrt{s}=14\ TeV$. From [52, 53, 54].

possesses the capability to trigger on very minimal detector activity, using the MBTS system, and thereby select events with so called *minimum bias*.

A particular set of requirements which an event must meet to in order to be selected by the trigger is known as a *trigger signature*. Such signatures typically consist of a minimum multiplicity for a certain object type to exceed an E_T threshold. These are discussed further in Section 3.3. Events which meet these requirements are said to have *passed* the trigger. The entire information on these is then passed from the DAQ system to mass storage. It is only these events which will be available for later analysis. The information on any events which *fail* the trigger will be lost.

The ATLAS trigger system, shown schematically in Figure 3.2, is comprised of three sequential levels: *Level 1* (L1), which runs on very fast custom hardware, and the software-based *High Level Trigger* (HLT), comprised of *Level 2* (L2), and the *Event Filter* (EF), which are run on large, dedicated computing farms. These levels impose increasingly refined selections designed to identify events containing interesting features. They function in a seeded and step-wise manner in order to enable the identification of uninteresting events as quickly as possible. Such events are then rejected, freeing up resources to study as many collisions in as much detail as possible.

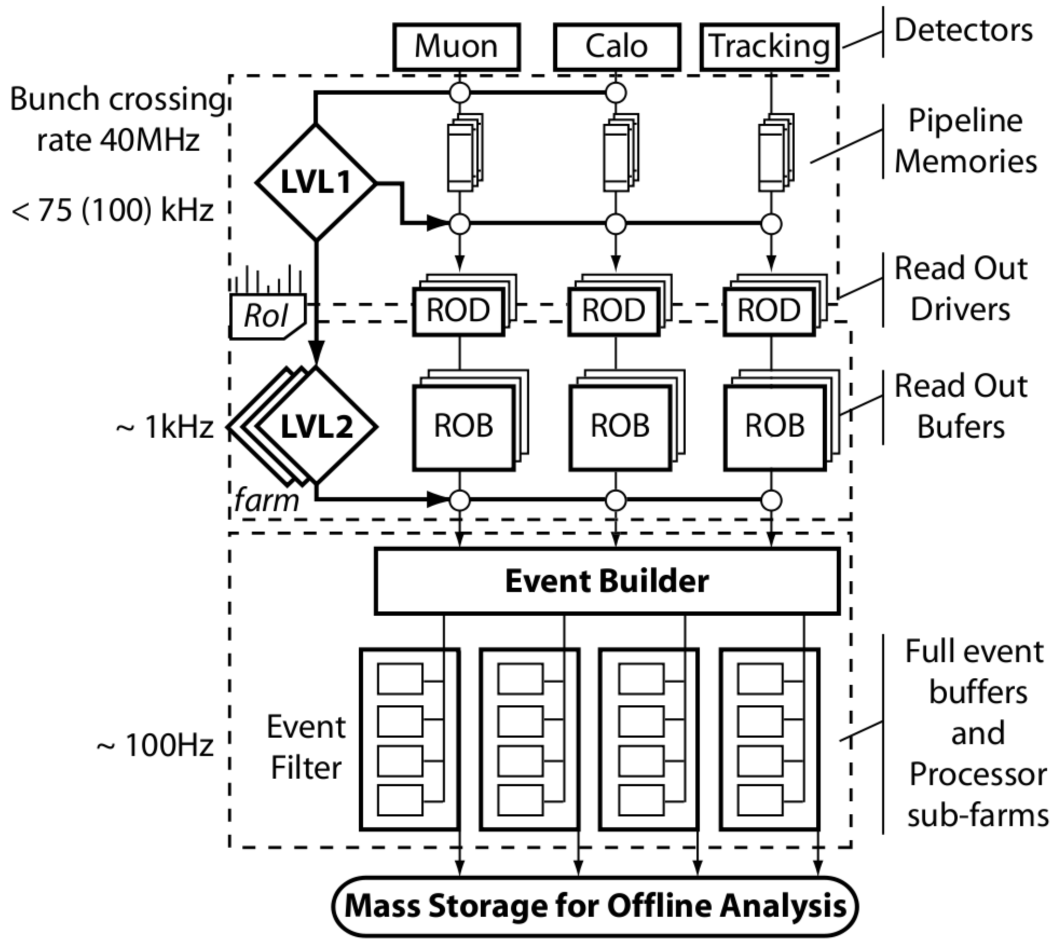

Figure 3.2: Schematic representation of the ATLAS trigger system, from [55].

3.1 The Level-1 Trigger

The L1 trigger scrutinises each collision at the 40 MHz bunch crossing rate, utilising dedicated, custom built electronics and pipelined memories. It searches for the signatures of highly energetic electrons, photons, muons, jets and hadronically decaying tau leptons, as well as events which contain large E_T^{miss} or total transverse energy. L1 uses reduced granularity information from a sub-set of detectors: so called *trigger towers* from the calorimeter, and RPCs and TGCs within the muon spectrometer.

Figure 3.3 shows a block diagram representation of the L1 trigger. Following the identification of interesting features by the L1 calorimeter and muon systems, information on the energy thresholds and multiplicities of these features is passed onto the central trigger processor (CTP). The CTP combines the information from the various subsystems and compares this to pre-configured trigger signatures in order to make an overall L1 decision. The result of this decision along with the LHC clock and other input signals are then passed to the detector front-end readout systems via

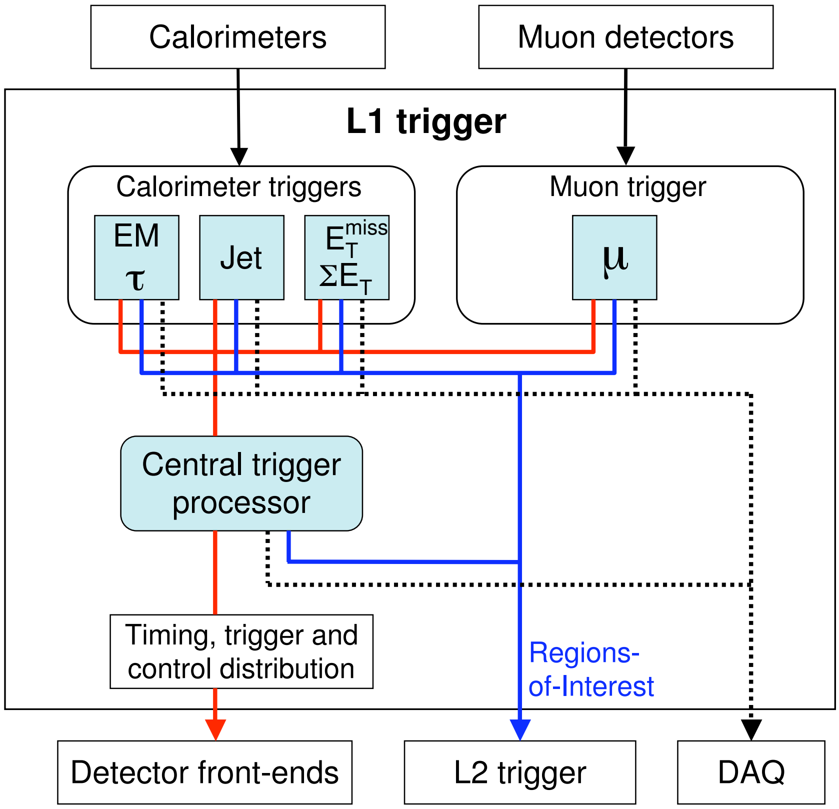

Figure 3.3: A schematic diagram of the L1 trigger, from [40].

the timing, trigger and control system. During the L1 trigger processing, the data from multiple bunch-crossings are held in pipeline memories. If the CTP has passed a given bunch crossing, then the corresponding information on the location and threshold energies of the interesting features are passed as *Regions of Interest* (RoIs) to L2, where they are used to *seed* the selection performed by the HLT. Otherwise this information is discarded.

The maximum L1 accept rate is 75 kHz, with a latency for decision making of 2.5 μs following the associated bunch crossing. The L1 trigger achieves an overall rejection factor of around 400.

3.1.1 The Calorimeter Trigger

The L1 calorimeter trigger system is based on trigger towers formed by the summation of adjoining cells in all samplings in each of the EM and hadronic calorimeters. Trigger towers have a granularity of 0.1×0.1 in $\eta \times \phi$ in most parts of the calorimeter, although this increases at large $|\eta|$. Figure 2.6, from the previous chapter, shows the trigger towers of the EM calorimeter at $\eta = 0$. Energy signals picked up in trigger towers are sent to pre-processors where they are associated with a specific bunch crossing and converted into transverse energy via a calibrated look up table. The L1 calorimeter is capable of measuring transverse energy, in discrete units of around

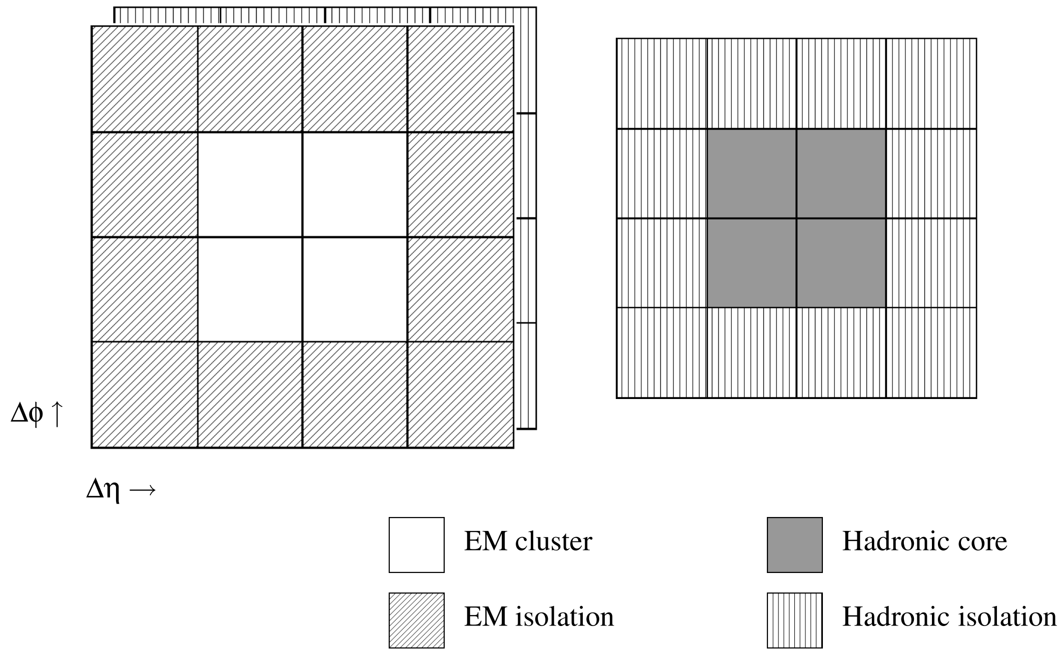

Figure 3.4: The ATLAS L1 EM trigger system. EM objects are required to have E_T contained in the central EM cluster (white) above a threshold. For isolated signatures it is also required that not too much energy is deposited into the surrounding ring of EM trigger towers (diagonally hatched), the hadronic calorimeter directly behind the central cluster (grey) or the surrounding ring (vertically hatched).

1 GeV, up to 255 GeV, above which the signal saturates. Energy information is transmitted to both the Cluster Processor (CP), and to the Jet Energy-sum Processor (JEM).

The CP searches for electrons, photons and hadronically decaying taus in an overlapping, 2×2, sliding window of EM trigger towers. EM trigger towers are present across the entire EM calorimeter, $|\eta| < 2.5$. EM candidates are identified as a window containing an E_T maxima exceeding a trigger threshold in a 1×2 or 2×1 trigger tower region. Tau candidates also include, in addition to the EM tower energies, the energy deposited in the 2×2 hadronic trigger towers directly behind the EM window. Both EM and tau candidates are either just required to have transverse energy above threshold or, optionally, to be isolated as well as sufficiently energetic. The *isolation* requirements at L1 serve to reject non-EM or tau like showers as well as EM/tau showers produced close to other detector activity. Figure 3.4 shows an overview of the CP trigger tower selections.

Isolated EM objects generally leave a narrow energy deposit in the EM calorimeter, with limited leakage into the hadronic calorimeter. The width of the EM candidate is restricted by a measurement of the energy in a ring of twelve EM trigger towers surrounding the central 2×2 window containing the candidate maxima. This is known as the *EM isolation ring*. Energy leakage into the hadronic calorimeter is measured as the energy in the four hadronic trigger towers directly behind the central EM window, known as the *hadronic core*, and in the twelve hadronic trigger towers around the central hadronic region, known as the *hadronic isolation ring*. Isolated EM candidates are required to have less than 5 GeV, 3 GeV and 4 GeV, deposited in the EM isolation ring, the hadronic core and the hadronic isolation ring respectively. Isolated tau candidates are required to have both the hadronic and EM isolation rings below the thresholds.

Up to sixteen CP thresholds can be simultaneous defined as the L1 stages of various trigger signatures. Of these, eight are reserved for EM thresholds and the other eight available for either EM or taus.

The JEM utilises *jet elements* formed from the energy sum of 2×2 trigger towers in both the EM and the hadronic calorimeters. Jet candidates are identified by energy depositions exceeding a minimum energy threshold in either a 2×2, 3×3 or 4×4 jet elements region. At the same time as searching for jet candidates, the JEM implements an energy summation algorithm which produces total sums of E_T, E_x and E_y. These are used to identify events with large missing transverse energy or large sums of transverse energy. Up to eight independent combinations of E_T threshold and jet element window size can be simultaneous defined as well as four total E_T and eight E_T^{miss} thresholds. The jet calorimeter trigger covers the range $|\eta| < 3.2$.

3.1.2 The Muon Trigger

The L1 muon trigger system is comprised of the dedicated RPCs and TGCs, as introduced in Section 2.2.5. These cover the range $|\eta| < 2.4$, and aim to identify muon candidates. Unlike the precision muon chambers, trigger chambers have sufficient timing resolution to be able to provide unambiguous identification of which bunch crossing gave rise to each muon of interest.

Figure 3.5 shows the schematic setup of the L1 muon trigger. Candidate muons are first registered as hits in the *pivot plane* of trigger chambers, which is the either the second RPC plane or the fourth TGC plane. A coincidence of further hits is then required to be contained within a *road* which points from the nominal interaction point. The width of the road corresponds to the p_T threshold required. A total of six programmable trigger thresholds can be simultaneously configured. Of these, three correspond to low p_T thresholds, of between six and nine GeV, and three to high p_T thresholds of between nine and thirty five GeV. Unlike the calorimeter thresholds, muon thresholds are exclusive, meaning a muon candidate only passes the highest p_T threshold which it satisfies.

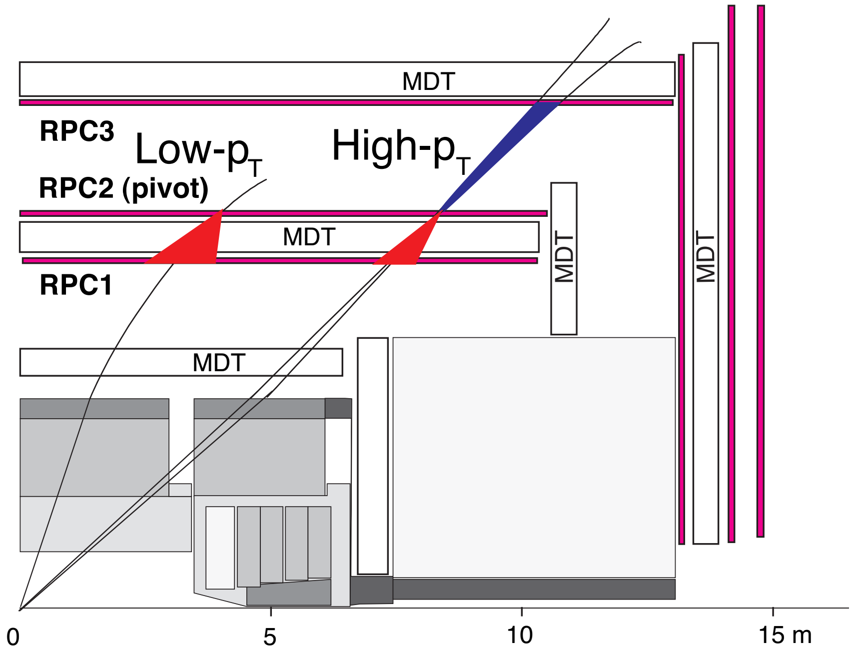

Figure 3.5: A schematic diagram of the L1 muon RPC trigger, from [40].

3.2 The High Level Trigger

The ATLAS HLT is a software based system which runs almost entirely on commercially available computers and network hardware. The HLT implements guided algorithms which run in a step-wise manner to validate or invalidate specific trigger hypotheses. Unlike L1, information from all subdetectors, including the ID, is available. The decision making components of the HLT are the Level-2 trigger and the Event Filter.

3.2.1 The Level-2 Trigger

Following selection by the L1 trigger, event data is transferred to the HLT DAQ system. For each event, the L1 calorimeter, muon and CPT subsystems provide RoI information to the RoI builder, as shown in Figure 3.2, which assembles this into a single data structure to be forwarded to the L2 system. Using the RoI locations, the L2 requests the appropriate data from the readout subsystems, which is then processed in order to arrive at the decision to accept or reject the event. In this way L1 is said to *seed* the HLT. The L2 system is designed to reduce the selected event rate from $\sim 75\,$kHz to $\sim 3.5\,$kHz, providing a rejection factor of about 30. The L2 trigger benefits from improved, though not final, detector calibrations and thresholds.

The principal component of the L2 trigger is the processing farm, where event selection is performed. L2 generally only uses information within RoIs to make its decision, although certain algorithms reconstruct the full event. Within RoIs the detector information with full granularity is available. The use of RoIs restricts the amount of data required to only around 1-2% of the total event size, and hence minimises the CPU and bandwidth usage needed to reach a decision. Starting from each RoI, L2 applies simple, robust, hypothesis selections in a series of steps, each refining the existing selection via the acquisition of additional data from increasingly more detectors. Depending upon the trigger signature, different stages of event reconstruction, termed feature extraction, are performed. These typically request detector data within an RoI and attempt to identify physical features such as tracks or calorimeter energy clusters. A hypothesis algorithm then tests to determine if the located features meet the trigger selection criteria. Criteria are hypothesis specific, and include variables such as calorimeter shower shapes, E_T thresholds and track to cluster matchings. As soon as a hypothesis test is failed the RoI is rejected. This further limits the amount of processing by rejecting an uninteresting events as early as possible. Only events which pass the full L2 trigger selection criteria are passed onto the EF.

3.2.2 The Event Filter

Each event accepted by L2 is forwarded to an event builder node, as shown in Figure 3.2, which builds the entire event data with the full detector granularity and sends this to the final selection stage of the trigger, the EF. Due to the high available latency of around 4 s, the EF, unlike L2, can afford to apply more sophisticated event reconstruction algorithms. As much as possible, the EF uses the standard ATLAS analysis and event reconstruction applications developed for offline analysis, as well as final calibrations. In addition, the EF is able to access the information on the entire event, rather than just within RoIs. The EF applies refined hypotheses algorithms to identify leptons, jets and photons as well as generalised E_T^{miss} and b-physics objects. The EF trigger reduces the event selection rate from $\sim 3.5\,\text{kHz}$ to the final $\sim 200\,\text{Hz}$ able to be written to storage, achieving a rejection factor of about 15.

In addition to selection, the EF also classifies events into *trigger streams* according to the type of candidate object which causes them to pass the trigger. Any events passing the EF are subsequently transferred to CERN's central data recording facility where they are stored for future offline analysis.

3.2.3 Electron HLT Selection

The electron trigger selection is designed to identify events which contain energetic transverse electrons. An electron will be characterised by an energy deposit, or cluster, contained within the EM calorimeter with an associated pointing ID track whose p_T should be similar to the E_T of the cluster. The majority of the background that contributes to the electron trigger rate comes from QCD processes which deposit significant energy in the EM calorimeter.

At the HLT the electron selection process is guided by the RoI mechanism, as described previously, where the RoI is the detector region surrounding a triggered L1 EM candidate. The L2 then implements *feature extraction algorithms* (FEXs), designed to first identify calorimeter clusters and then ID tracks. Following each FEX, a hypothesis algorithm tests if the identified features are consistent with an electron like signature.

The L2 calorimeter FEX reconstructs energy clusters in a region of 0.075×0.175 in $\eta \times \phi$. The calorimeter hypothesis algorithm then applies cuts based upon: the cluster E_T; the E_T in the first layer of the hadronic calorimeter (often refered to as the hadronic leakage); the shower shape in the η plane in the second sampling of the EM calorimeter R_η; and on the ratio of the first and second energy maxima found within the first sampling of the EM calorimeter E_{ratio}. Due to the energy dependence of the cross section, jet backgrounds are mainly rejected by the E_T cut. Further cuts on the η shape and leakage into the hadronic calorimeter provide increased jet-electron discrimination as EM showers are typically more contained in pseudo-rapidity and deposit most of their energy in the EM calorimeter. The final cut variable E_{ratio} will take values close to unity for isolated electrons, but not for diffuse hadronic showers or $\pi^0 \rightarrow \gamma\gamma$ decays, as the multiple particles contained within these can create many local maxima that may carry significant fractions of the shower energy.

Assuming the candidate cluster passes the calorimeter hypothesis, the L2 ID FEX then reconstructs tracks in the ID region corresponding to the RoI, as described in [56]. A combined ID-calorimeter hypothesis algorithm then tests for an energetic track, closely matched in $\Delta\eta \times \Delta\phi$ to the calorimeter cluster.

The electron selection at EF uses offline algorithms as much as possible along with more precise calibration and alignment constants than are available at L2. Electron reconstruction takes place within RoIs seeded by the improved direction found at L2. The EF selection then follows the same scheme as L2, although the looser timing constraints allow more sophisticated reconstruction algorithms to be used. As at L2, the selection is based on the calorimeter, ID and combined ID-calorimeter information, although more shower shape and track quality cuts are applied. The EF algorithms, in common with offline, can apply varying degrees of electron selection, ranging from *loose* to *tight*. A tight cut will have high purity but lower electron identification efficiency, whereas a loose cut will have lower purity but higher efficiency. The offline and EF electron hypothesis cuts are often referred to as `isEM` and are described in detail in [57], and in Section 4.2.1. The electron and photon trigger is further described in [58].

3.2.4 Muon HLT Selection

The L2 muon trigger consists of several complementary algorithms, each acting to identify muons in different ATLAS subdetectors. Muon reconstruction takes place in a region of 0.2×0.2 in $\eta \times \phi$ surrounding the initial RoI. Muons are firstly reconstructed as *standalone* muons in the muon spectrometer using information from both the precision chambers and from the trigger chambers. This is then combined with ID track information within the RoI to produce *combined* muons. Combined muons possess an improved measure of η, ϕ and transverse momentum, especially in the low p_T range. This increased p_T resolution serves to provide increased rejection against very low momentum muons, such as those produced by in-flight decays of pions and kaons.

EF reconstruction is seeded by L2 RoIs. Due to the larger admissible latency, the EF uses adapted versions of the offline reconstruction algorithms. The EF muon selection consists of two complementary algorithms. The first starts at the muon system and extrapolates back to the ID, and the second begins from the ID and carries on muon identification outwards. These each consists of four FEX algorithms. Starting from the outside and working in, these: identify MDT track segments; build tracks from these; extrapolate them back to the interaction point; they then find ID tracks and combine these with the muon tracks. The hypothesis algorithm then simply cuts on the p_T of any identified muon candidate. The muon trigger is described fully in [59, 60].

3.3 Trigger Signatures

A trigger signature is the total set of requirements that an event must meet in order to pass the trigger. Each signature has a L1, a L2 and an EF stage, with each of these stages composed of one, or more, alternating FEX algorithms and trigger hypotheses. Figure 3.6 shows a schematic overview of an electron trigger signature. Many individual signatures will be configured simultaneously and each bunch crossing will have the potential to pass one or more signatures.

Trigger signature naming conventions are based on the hypotheses algorithms applied. Each stage of each signature is identified using a notation where a symbol representing the candidate particle type is preceded by a multiplicity value and followed by a E_T or p_T threshold value. The symbol *e* indicates an electron candidate, γ a photon, *mu* a muon, *j* a jet, *tau* a tau and `XE` E_T^{miss}. For example, the signature `2e5` corresponds to a requirement of two or more electrons, each with E_T above 5 GeV. `EF 2e5` is the EF stage of such a signature and will be seeded by the L2 stage `L2 2e5`, which was in turn seeded by the L1 `L1 2EM3`. L1 E_T thresholds are generally slightly lower than at the HLT to account for the poorer L1 E_T resolution. A `i` suffix on a trigger indicates that an isolation requirement has been made, usually at the L1 stage. Furthermore, electron triggers are

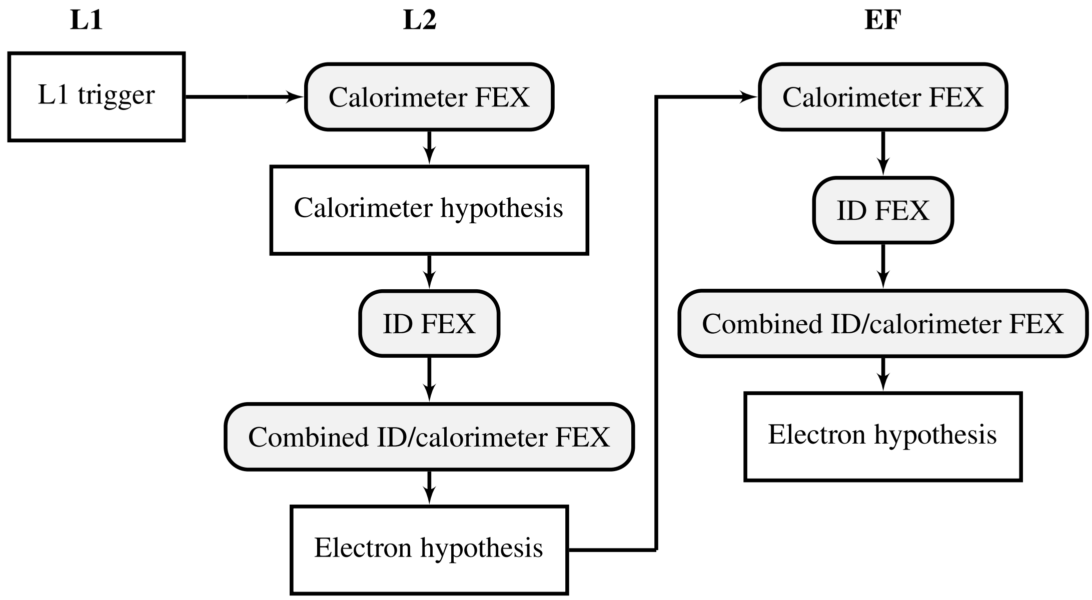

Figure 3.6: A schematic flow diagram of an electron trigger chain.

often suffixed by *loose*, *medium* or *tight*, indicating tightness of the `isEM` selection required at EF. The rejection power of individual signatures can be adjusted by tuning the lower transverse energy threshold, the object multiplicities and the tightness of the object selection criteria. In addition, some signatures can be *prescaled*, meaning that only a fraction of events meeting the signature will be written to storage.

3.4 Trigger Menus

In order to control the overall trigger rate, lists of potential signatures are compiled into a *trigger menu*. Such menus are selected in order to maintain a 200 Hz pass rate regardless of the LHC operating conditions. The process of deciding which signatures compose a trigger menu must take into account the intended LHC conditions. As well as an assessment of the rejection capabilities of each signature at each selection stage, and the rate capabilities of each level of the trigger and the computing system. This procedure is iterative, and the formation of any trigger menu will be heavily influenced by earlier trigger studies. Menus will doubtless evolve as knowledge of the ATLAS detector, and of the physics cross sections progresses. Further details on the construction and validation of trigger menus can be found in [51, 52].

The trigger menu is divided into *slices* depending upon the final state hypothesised: minimum bias events; electrons or photons, *egamma*; hadronically decaying taus; muons; jets; *b*-jets; *b*-physics; missing energy and or total energy; and finally, events for the calibration of the detector.

Each slice is assigned a portion of the overall 200 Hz bandwidth. Table 3.1 shows a subset of triggers from an example trigger menu proposed for use at an early luminosity of $\sim 10^{31}\text{cm}^{-2}\text{s}^{-1}$.

At the initial luminosity of $\sim 10^{31}\,\text{cm}^{-2}\text{s}^{-1}$ event rates are expected to be low enough that triggers will not have to require particularly strict selection criteria or very high thresholds. This will allow time to commission the trigger system and to validate the harsher cuts that will be required as instantaneous luminosity increases.

Table 3.2 shows a subset of triggers from an example menu proposed for use at a higher luminosity of $\sim 2 \times 10^{33}\text{cm}^{-2}\text{s}^{-1}$. The signatures foreseen for use in this menu have higher energy thresholds when compared to those intended for lower instantaneous luminosities. Furthermore, the selection of candidate objects within given signatures is expected to be more stringent and isolation is increasingly relied upon. For example, whilst at low luminosity the primary single electron signature is `e10`, which is expected to implement a *medium* `isEM` cut at EF, and no isolation. At high luminosity, the corresponding single electron signature is expected to be `e22i`. Which not only implements a higher energy threshold, but also a *tight* `isEM` cut and L1 isolation. It is often undesirable to increase the minimum thresholds or object multiplicities of triggers too much, as this can severely limit the ability of the trigger to select many interesting processes. As a result, isolation requirements and the tightness of object selection criteria are expected to become increasingly important if rates are to be controlled. Therefore, a good understanding of these will be crucial to any studies at ATLAS. This is especially true at higher instantaneous luminosities, where the need for harsher selection criteria will make the selection of interesting physics processes increasingly difficult.

The studies presented in this thesis took place over a period of time during which the proposed initial energy and luminosity of the LHC varied greatly. As a result a number of different trigger menus and signatures are studied throughout this work. The exact nature of each signature and the menu in which it is situated will be introduced as appropriate.

Table 3.1: A subset of trigger signatures from an illustrative trigger menu for $\mathcal{L} = 10^{31}$ cm^{-2}s^{-1}, adapted from [40].

Signature	L1 rate (Hz)	HLT rate (Hz)	Intended Physics Processes
Minimum Bias	up to 10,000	10	All, but will be prescaled
e10	5,000	21	$b, c \rightarrow e$, W, Z, Drell-Yan, $t\bar{t}$
2e5	6,500	6	Drell-Yan, J/ψ, Υ, Z
γ20	370	6	Direct photons, γ-jet balance
2γ15	100	< 1	Photon pairs
mu10	360	19	W, Z, $t\bar{t}$
2mu4	70	3	B-physics, Drell-Yan, J/ψ, Υ, Z
j120	9	9	QCD and other high-p_T jet final states
4j23	8	5	Multi-jet final states
tau20i + XE30	5,000	10	W,$t\bar{t}$

Table 3.2: A subset of trigger signatures from an illustrative trigger menu for $\mathcal{L} = 2 \times 10^{33}$ cm^{-2}s^{-1}, adapted from [61].

Signature	L1 rate (Hz)	HLT rate (Hz)	Intended Physics Processes
e22i	12,000	40	$b, c \rightarrow e$, W, Z, Drell-Yan, $t\bar{t}$
2e12i	4,000	< 1	Drell-Yan, J/ψ, Υ, Z
γ55i	12,000	25	Direct photons, γ-jet balance
2γ17i	4,000	2	Photon pairs
mu20i	800	40	W, Z, $t\bar{t}$
2mu10	200	10	B-physics, Drell-Yan, J/ψ, Υ, Z
j370	200	10	QCD and other high-p_T jet final states
4j90	200	10	Multi-jet final states
tau35i + XE45	2,000	5	W,$t\bar{t}$

Chapter 4

Event Simulation and Reconstruction at ATLAS

The following chapter will describe the process by which simulated data is produced at ATLAS, and how signals observed in the ATLAS subdetectors are reconstructed into meaningful representations of particles. The reconstruction stage is common both to simulated and real data. All event simulation and reconstruction takes place within the ATLAS computing framework, ATHENA, which is detailed in [62].

4.1 Event Simulation

In the absence of data, complex *Monte Carlo* (MC), computer simulations are used to simulate the responses of the ATLAS detector to the various signals expected of physical processes. MC methods use random number generators to model processes and interactions based on the underlying, probabilistic, physical laws. Typically the MC simulations used at ATLAS have been extensively tested and tuned at previous experiments [63] and using data collected at dedicated ATLAS test beams [40].

The ATLAS MC process is subdivided into three steps: firstly, the generation of the primary event from the p-p interaction, including any immediate, unstable particle decays; secondly, the simulation of the interactions of the produced particles with the detector; and finally, the conversion of any energy deposited in sensitive regions of the detector into currents and voltages to be read out as signals. The format of simulated data has been devised such that its output is identical to that of real data as recorded by the actual detector. Using the same methods for MC as for actual data the raw detector outputs are then reconstructed into meaningful representations of physical objects ready for analysis. Figure 4.1 illustrates the stages involved in both the simulation process

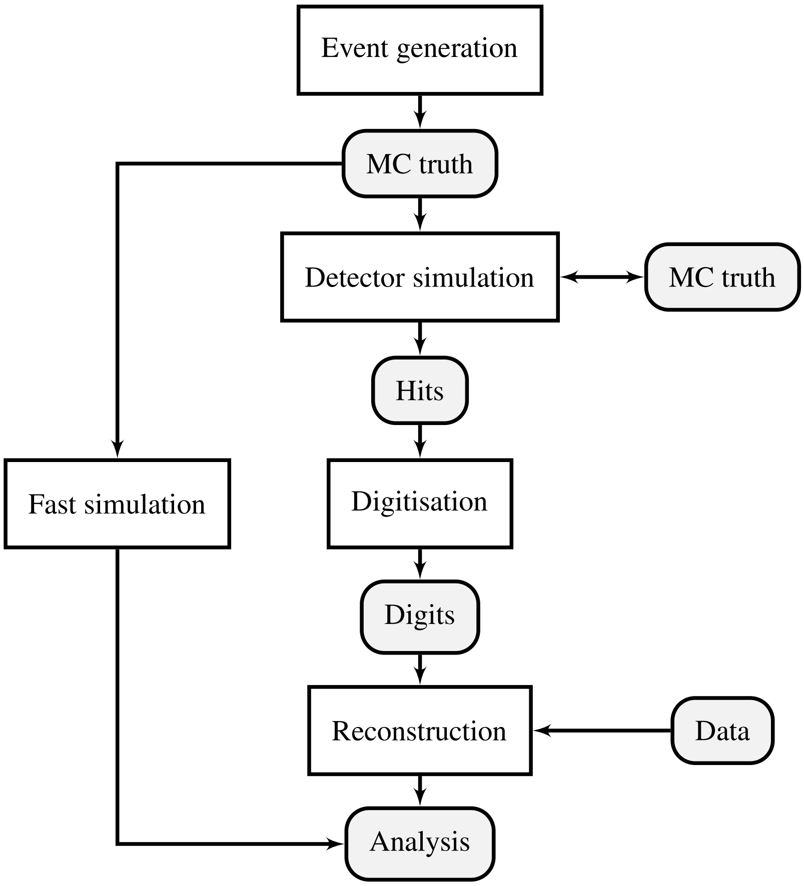

Figure 4.1: A block diagram overview of the ATLAS data taking and Monte Carlo simulation setups. Processing stages are shown in white, data formats in grey.

and in data taking. A detailed description of the ATLAS MC project can be found in [64]. The following sections will describe the important parts of the MC process at ATLAS.

4.1.1 Event Generation

Event Generation involves the use of MC *generators* to produce examples of specific particle-particle interactions. Such generators start from a set of initial conditions and then compute the kinematics of any stable, *final state*, particles produced via a desired interaction and decay process. Particles are considered stable by the generator if their proper lifetime is sufficient to allow them to propagate a significant distance, ($>$ 10 mm), at relativistic speeds within the detector before decaying. The decays of longer lived particles are handled by the detector simulation.

At the LHC, the initial conditions will consist of two beams of protons with a given energy. The protons themselves are each modelled in terms of their contents, *partons*, by a *parton distribution function* (PDF). PDFs describe the probability density for finding a particular parton with a particular fraction of the total proton momentum. These vary depending on the parton type and the

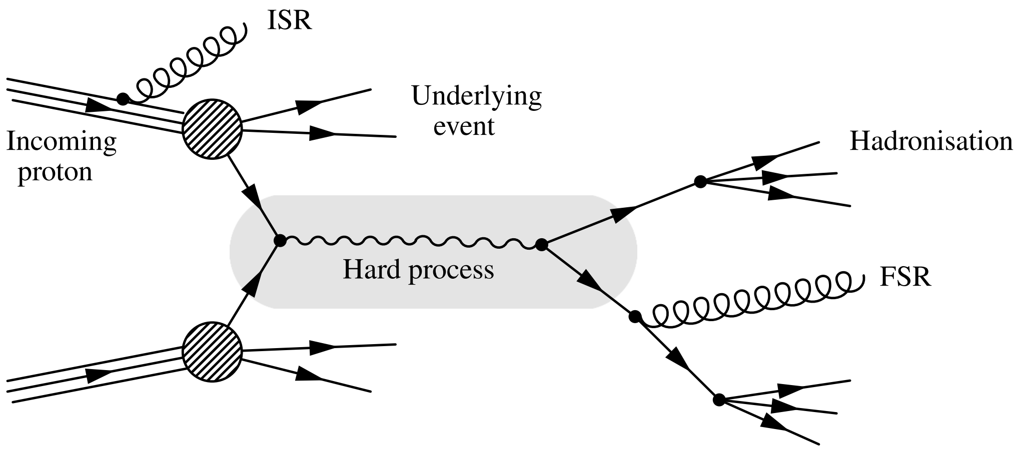

Figure 4.2: A schematic illustration of the stages involved in the generation of a Monte Carlo event. Time runs from left to right (see text).

overall energy of the proton. The PDFs used at ATLAS are CTEQ6L and CTEQ6M, as described in [65].

Event generation begins by first modelling any initial state radiation (ISR), via emission from the initial partons. Following this is the main interaction itself, whereby one parton from either proton is involved in the desired high energy transfer, or *hard*, process. This process will result in the production of final state particles, either directly, or via the decay of an intermediate resonance particle. Particles in the final state can then emit radiation, in a similar way to initial particles, as final state radiation (FSR). Any final state parton will then fragment to colour-neutral hadrons, which may in turn decay further. This process is referred to as *hadronisation*. In addition to the hard process, the underlying event is modelled including any secondary interactions between the colliding protons and the subsequent hadronisation of the proton remnants. Figure 4.2 shows a schematic overview of the event generation process.

Any particle produced by the event generation is referred to as a *prompt* particle. The kinematics of the each particle in an event is determined by the Monte Carlo method, that is, by random number selections and the appropriate probability distribution functions. The details of the event generation are stored and are available to the end user as so-called *truth* information. Two classes of generators; general purpose and specialised, are used at ATLAS. General purpose generators produce complete descriptions of events starting from the proton-proton initial states, through to the final state particles. Specialised generators are used to augment general purpose generators, by providing improved descriptions of specific decays or final states.

The general purpose generators used in this thesis are PYTHIA [66] and HERWIG [67], complemented by the specialist generators Isajet [28], MC@NLO [68] and AcerMC [69]. In addition, some single-particle generators are used to produce individual particles with which the detector response can be studied. The majority of the samples studied in this thesis were generated by PYTHIA. PYTHIA is a widely used generator, tested and validated over many years at both e^+e^- and hadron colliders. PYTHIA provides a complete description of an event including ISR, FSR and hadronisation. The SUSY samples studied in this thesis were generated using the HERWIG generator with the Jimmy [70] implementation of the underlying event. For these events Isajet was used to providing the relevant weak scale masses and decay modes from the GUT scale model parameters. Top-quark samples were produced using either AcerMC or MC@NLO, supplemented by PYTHIA. All of the these generators, with the exception of MC@NLO, compute processes to leading order (LO). MC@NLO, as the name suggests, provides full next to leading order (NLO) corrections. All the samples studied in this thesis, except where noted, were produced centrally by the ATLAS collaboration.

4.1.2 Detector Simulation

Particles produced by the event generators are passed on to the detector simulator. This then simulates their interactions with the detector. Detector simulation can either be a so-called *full simulation*, which is based on the modelling program *GEANT4* [71]; or a *fast simulation*, which is based on a parametrisation of the detector response, or a combination of the two.

The full simulation mechanism involves the propagation of each particle through a detailed virtual model of the detector, whilst modelling their interactions along the way. This is achieved via the GEANT4 "toolkit". The particle showers and interactions produced during the simulation are included in the truth information. Any energy deposited in sensitive portions of the detector is collected as so called *hits*. These hits are later digitised in such a way as to simulate the output of the detector and stored as *digits*. Digits are formatted such that they are identical to the signals expected to be produced by the actual detector. This then allows simulated data to use the same reconstruction algorithms as real data. Full simulation has been extensively validated and has been shown to reproduce existing real data to a high degree of accuracy.

Although full simulation produces the most accurate description of events, it demands a very large amount of computing power. It is not always possible to afford the computing resources to simulate enough data for certain signals, or to simulate enough events for particularly detailed studies. In order to address this issue, several versions of *fast* simulation exist which aim at reducing the computing time needed per event via a simplification of the detector simulation. The full blown fast simulation, known as ATLFAST-I [72] dispenses with the GEANT4 stage altogether and instead parametrises the detector response using smearing functions relating to detector resolutions. This does not include any detailed simulation of particle identification efficiencies or of particles being falsely reconstructed as different particles, or *fakes*. The resultant data consists of only four-vectors corresponding to each particle, which can then be analysed by the user. ATLFAST-I is around 10^4 times faster than full simulation.

The program ATLFAST-II [73] sits somewhere in between full simulation and ATLFAST-I. It provides full GEANT4 based tracking and muon simulation, whilst relying on a parametrisation of calorimeter shower profiles based on a large sample of presimulated, full simulation showers. The output of ATLFAST-II is in such a form that the standard reconstruction algorithms can be used in common with full simulation and real data. ATLFAST-II offers a factor of ten improvement in computing time over full simulation. Whilst the resultant data is not in complete agreement with full simulation, for most physics observables the agreement is within 10%. However, some notable exceptions include the inability of the fast simulation to describe fakes, and the unsatisfactory modelling of calorimeter punch through. Neither ATLFAST-I nor ATLFAST-II include simulations of the trigger system.

4.2 Particle Reconstruction

Before any analysis of the signals observed during an event can begin, they must first be assembled into a coherent, simplified data structure. This process, known as reconstruction, condenses the information contained in the raw subdetector signals, combines this with various calibrations and alignments and finally identifies individual particles and event level quantities. The result is a data format that only includes abstract physical *objects*, overall event variables, such as E_T^{miss}, and a reduced set of detector information. The reconstruction process reduces the event size from an average of 1.5 MB to around 100 kB.

Reconstructed objects correspond to detector signals that are consistent with those expected as various particles interact with the detector. The types of reconstructed object include: electrons, photons, muons, hadronic tau decays and jets. The majority of these objects are composed from tracks in the ID and muon spectrometer, along with energy deposits, or *clusters* in the calorimeters. Tracks themselves are formed by linking SCT and pixel hits into track seeds in the inner four ID layers, and then extending these to include measurements from the outer layers and form complete tracks. Clusters are formed from contiguous groups of calorimeter cells which contain significant energy deposits.

Reconstruction aims to achieve a one-to-one correspondence between truth level particles and jets and the correct type of reconstructed object. However, this is not always possible with physics, detector and software effects sometimes resulting in objects being reconstructed as the wrong type of object, or not being reconstructed at all. The *efficiency* of reconstruction, ε, is defined as the probability, P, that a certain particle or jet will be reconstructed as a particular type of object, given the conditions, I, that describe the object. For example, the electron reconstruction efficiency, ε_e, is given by:

$$\varepsilon_e = P(\text{object is reconstructed as an electron} \mid I, \text{object is an electron}). \quad (4.1)$$

In this case I may include the transverse energy and η of the electron, as well the topology of the event in which it is present. Similarly, the efficiency of a jet to be falsely reconstructed as an electron, ε_{jet}, is given by:

$$\varepsilon_{jet} = P(\text{object is reconstructed as an electron} \mid I', \text{object is a jet}). \quad (4.2)$$

Such falsely reconstruction objects are termed *fakes*. The inherently random nature of particle interactions mean that complete separation between different object types is not always achievable. The sources of fakes depend on the type of object being reconstructed. For example, the overwhelming majority of fake electrons arise from jets. Jets typically contain around a third of their energy as neutral pions, which decay to photons and can result in electron-like calorimeter clusters. In addition, the remaining jet constituents, mainly charged hadrons, can leave tracks which maybe mistaken for the track due to an electron. An important measure of the performance of reconstruction is *purity*, p. Purity is defined as the probability that an object reconstructed as a certain type of object is, indeed, that type of object. The purity, p_e, of the electron reconstruction is:

$$p_e = P(\text{object is an electron} \mid \text{object is reconstructed as an electron}). \quad (4.3)$$

If the only source of fake electrons are jets, then the electron purity will be given by:

$$p_e = \frac{\varepsilon_e \pi_e}{\varepsilon_e \pi_e + \varepsilon_{jet} \pi_{jet}}, \quad (4.4)$$

where π_e is the prior probability for the existence of electrons and π_{jet} is the prior probability for the existence of jets. This is often described in terms of *rejection factor*, f, defined as the ratio of the efficiency of the correct object reconstruction to the fake efficiency:

$$f = \frac{\varepsilon_e}{\varepsilon_{jet}}. \quad (4.5)$$

In practice the optimisation of reconstruction techniques are driven by the need to balance efficiencies with rejection factors.

The object defining cuts specified here, and used throughout this thesis, correspond to those used in the CSC exercise [27]. In the following, the reconstruction of the objects relevant to this thesis is described.

4.2.1 Electrons

The identification of electrons above the overwhelming jet backgrounds will prove quite a challenge at ATLAS. In the moderate energy range, between 20 and 50 GeV, the ratio between the rate of isolated electrons and the rate of QCD jets is expected to be $\sim 10^5$ [74]. Therefore a jet rejection factor exceeding 10^5 will be needed in order to reduce the backgrounds of jets faking electrons to a level well below that of real electrons. This, however, rapidly falls off with energy. Such that, in the TeV range, an equivalent electron purity can be obtained with a rejection factor of only 10^3.

Electron reconstruction at ATLAS is performed using a combination of calorimeter clusters and ID tracks. There are two procedures for electron reconstruction. The first, standard method is optimised for the identification of isolated energetic electrons. This starts from a calorimeter cluster and searches for an appropriate matching track. The second more specialised method, is designed to look for non-isolated low p_T electrons. This starts from tracks before searching for matching clusters. The studies in this thesis will primarily use only the standard reconstruction algorithm.

Standard electron candidates are seeded by an EM cluster, found within a $\eta \times \phi$ sliding window in the EM calorimeter containing an E_T deposit of above 3 GeV in the sum of all longitudinal samplings. The size of the window in $\eta \times \phi$ is defined in the second calorimeter sampling and varies from 3×7 cells in the barrel to 5×5 cells in the endcaps. The increased size in ϕ accounts for the bending of electrons in the magnetic field, which will cause them to radiate soft bremsstrahlung photons along a range in ϕ.

Following the identification of a seed EM cluster, a matching track is searched in the ID within a $\Delta\eta \times \Delta\phi$ window of 0.05×0.10. If such a track is found, then the ratio of the cluster energy to the track momentum is required to be less than ten. Any candidates that fulfil these three criteria are said to have passed the electron preselection. The efficiency of preselection has been shown to be $\sim 93\%$ for simulated single electron samples with $E_T > 20$ GeV and $|\eta| < 2.5$ [74].

Further electron identification criteria are made based upon a series of E_T and $|\eta|$ dependent cuts; cuts are made in seven bins in $|\eta|$ and six bins in E_T. These cuts are grouped into a series of increasingly stringent electron selection criteria, termed `isEM`. The `isEM` selection can be required to be *loose*, *medium*, or *tight*, depending on the desired background rejection and selection efficiency. The loose, medium and tight cuts are summarised in Tables 4.1, 4.2 and 4.3 respectively. The indicated cut values show the range of cuts made across all bins. Further details on `isEM` can be found in [74].

In addition to the preselection, a loose `isEM` cut places requirements on the hadronic leakage and on the shower shape in the second layer of the EM calorimeter. These cuts reject hadronic showers which tend to be wider and deposit more energy in the hadronic calorimeter. A loose cut provides an electron identification efficiency of around 90%, but only a limited jet rejection factor of around 560 [74].

A medium `isEM` cut, in addition to the loose cuts, places further requirements on the energy deposited in the strips of the first layer of the ECAL and on the quality of the associated track. The cuts on the ECAL strips serve to reject diffuse hadronic and pion showers, within which secondary particles can carry a significant fraction of the total shower energy. The medium cuts increase the jet rejection by a factor of three to four to around 2,000, although electron identification efficiency drops by around 10% with respect to the loose cuts to around 80% [74].

The final level of selection, a tight `isEM` cut, uses all the available information to further increase the purity of the selected electrons. In addition to the medium and loose requirements, a tight selection also: cuts on the track to cluster matching, requires a b-layer hit in the pixels, cuts on the ratio of high threshold TRT hits to low threshold hits, tightens the ratio of the cluster energy to the track momentum, and cuts on the isolation of the electron. These cuts serve to increase the rejection of jets by a factor of around 400 to around 10^5 [74]. This is at the cost of a 15% reduction in electron identification efficiency relative to medium cuts to around 65%. Figure 4.3, from [74], shows the electron identification efficiencies of the `isEM` cuts as functions of E_T and $|\eta|$.

The electron selection used in this thesis only includes electrons with E_T above 10 GeV, which

Table 4.1: Loose `isEM` cuts [74].

Variable	Symbol	Description	Cut
Acceptance			$|\eta| < 2.47$
Hadronic Leakage	R_{had}	Ratio of the E_T in the 1^{st} sampling of the hadronic calorimeter to the E_T of the EM cluster.	$<$ 0.015-0.045
2^{nd} layer of ECAL	R_η	The Ratio of the energy in a 3×7 to a 7×7 $\eta \times \phi$ cell window.	$>$ 0.60-0.91
	w_2	Lateral width of the shower.	$<$ 0.0125-0.0200

Table 4.2: Medium `isEM` cuts [74].

Variable	Symbol	Description	Cut
		All loose `isEM` cuts.	
1^{st} layer of ECAL	ΔE_s	Difference between the energy associated with the second energy maxima and the energy associated with the minimal value between the 1^{st} and 2^{nd} maxima.	$<$ 0.10-0.30 [GeV]
	R_{max2}	Second largest energy deposit normalised to the cluster energy.	$<$ 0.25-0.53
	w_{stot}	Total shower width.	$<$ 1.40-4.00
	w_{s3}	Shower width for the three strips around the maximum strip.	$<$ 0.60-0.80
	F_{side}	Fraction of energy outside the core of three central strips, within seven strips.	$<$ 0.20-0.48
Track Quality	N_{pixels}	Number of hits in the pixel detector.	$\geq$ 1
	N_{si}	Number of hits in the pixels and SCT.	$\geq$ 9
	d_0	Transverse impact parameter.	$<$ 1 mm

Table 4.3: Tight `isEM` cuts [74].

Variable	Symbol	Description	Cut
		All medium `isEM` cuts.	
Isolation		The ratio of E_T in a hollow cone of $\Delta R < 0.2$ surrounding the cluster to the cluster E_T.	$\leq$ 0.20-0.80
Track Matching	$\Delta\eta$	$\Delta\eta$ between the cluster and track.	$<$ 0.005
	$\Delta\phi$	$\Delta\phi$ between the cluster and track.	$<$ 0.02
	E/p	Ratio of the cluster energy to the track momentum.	$>$ 0.9 $<$ 2.5-3.5
Vertexing Layer		Number of hits in the vertexing-layer	$\geq$ 1
TRT		Ratio of high threshold hits to total hits.	$>$ 0.1-0.13

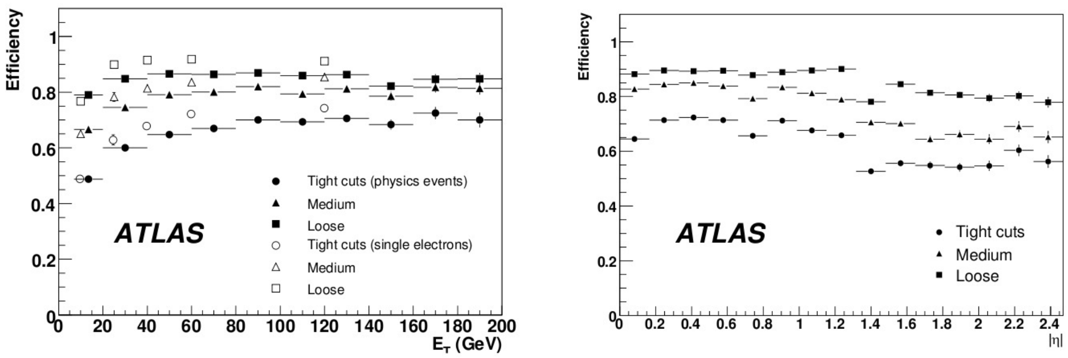

Figure 4.3: Electron identification efficiency as a function of E_T (left) and $|\eta|$ (right). The full symbols correspond to electrons in SUSY events and the open ones to single electrons. The efficiencies as a function of $|\eta|$ are shown only for electrons with $E_T > 17$ GeV, from [74].

pass the medium `isEM` selection and that have less than 10 GeV of energy in the calorimeters in a ΔR cone of 0.2 surrounding them. The transverse energy cut serves to reduce contamination of the electron sample by soft secondary electrons (which are not produced as part of the primary decay process) whilst, at the same time, coming to a compromise with the acceptance of low energy primary electrons. The ΔR cut is an isolation cut, designed to reject non-isolated electrons with large amounts of energy deposited nearby by other energetic particles. Furthermore, electrons contained within the crack region, $1.32 < |\eta| < 1.52$, are rejected because of the degraded calorimeter coverage in this region.

4.2.2 Muons

Muons are identified as tracks both in the muon spectrometer and in the ID. ATLAS implements three methods by which muons can be reconstructed: *standalone* muons are identified in the muon spectrometer alone; *combined* muons are first identified as standalone muons and are subsequently matched to an ID track; and *tagged* muons, are identified as ID tracks which have been extrapolated out to match track segments in the innermost muon stations. These methods are complementary, and the muons identified by the reconstruction include non-overlapping muons found by all three methods. There are two ATLAS algorithms to reconstruct muons, each using slightly differing mechanisms to implement the three methods of muon reconstruction. These are: the statistic combination algorithm (STACO) and MuID [75]. The default algorithm used during the CSC exercise, and in this thesis, is STACO.

STACO constructs standalone muons by first building track segments, identified as straight lines of hits in a muon station, and then linking these to form tracks. The tracks are then extrapolated back to the interaction point, whilst accounting for multiple scattering effects and parametris-

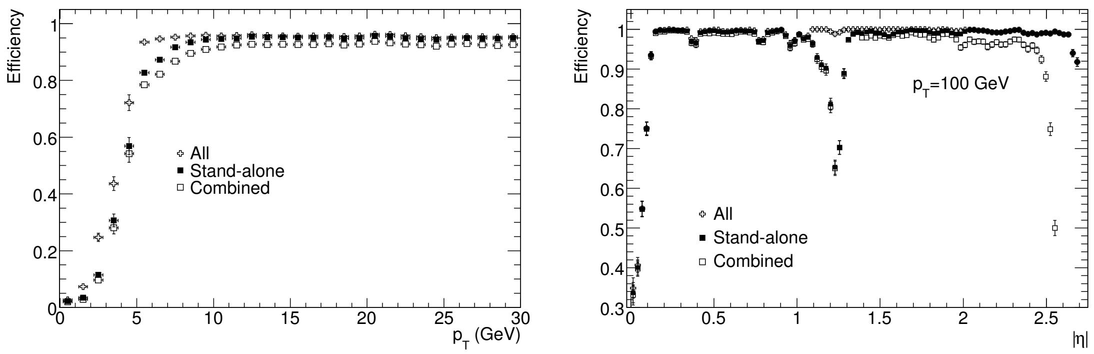

Figure 4.4: Muon identification efficiency as a function of p_T (left) and $|\eta|$ (right). The efficiencies as a function of $|\eta|$ are shown for muons with a fixed p_T of 100 GeV, from [40].

ing for energy loss based on the amount of material traversed in the calorimeters. Standalone muons can be identified across the coverage of the muon system $|\eta| < 2.7$. Gaps in the coverage degrade the performance at $\eta = 0$ where the detector support structure is located, and at the transition region $1.1 < |\eta| < 1.7$, where some muon stations are missing. Standalone tracks provide the best momentum resolution for high momentum muons.

Combined muons are formed across the coverage of the ID, $|\eta| < 2.5$. ID tracks are associated to standalone tracks using a χ^2 match between the two track vectors. Combined tracks are then formed using a statistical combination of the two tracks. Combined muons provide a much improved momentum resolution for muons with $p_T < 100$ GeV.

Tagged muons are formed by extrapolation from ID tracks to track segments in the inner muon stations. The tracks are again matched using a χ^2 function. Tagged muons significantly improve the overall muon reconstruction efficiency by identifying low p_T muons, typically below 6 GeV, which may not reach the middle or outer muon stations. Additionally, tagged muons considerably improve the performance where muon stations are absent. Figure 4.4, from [40], shows the muon identification efficiency as functions of p_T and $|\eta|$.

In this thesis, muons are selected to be STACO muons, with $p_T > 10$ GeV, and $|\eta| < 2.5$. In addition, they are required to be combined muons with track combination χ^2 of less than 100. Furthermore, muons are selected to be isolated, by requiring the amount of energy deposited in the calorimeters in a hollow ΔR cone of 0.2 around the muon to be less than 10 GeV.

4.2.3 Jets

The production of energetic partons will result in *jets* consisting of a large number of collimated hadrons. These will leave energy deposits in both the EM and hadronic calorimeters as well as a number of charged tracks in the ID. Jets are reconstructed across the entire calorimeter coverage, $|\eta| < 4.9$, using only information provided by the calorimeters. Jets are generally built up of clusters either formed from *towers* or *topological clusters* of cells. Towers are formed from summations of cells within a projective $\eta \times \phi$ grid of size 0.1×0.1. Cells fully contained within a grid square contribute their entire energy to the tower, while those partially contained contribute a weighted fraction.

Topological clusters are seeded from individual calorimeter cells with E_T above four times the cell noise standard deviation. These cells are then amalgamated with their direct neighbours, in three dimensions, which contain energies greater than twice the noise standard deviation. This merging procedure continues for all direct neighbours until no more cells with energies above threshold are found.

A number of jet finding algorithms exist. These include; cone jets, sequential recombination jets, seedless infra-red safe jets, track jets, and particle flow jets. During the CSC exercise, and in this thesis, only cone jets, based on towers of cells were considered.

Cone-based jet finding algorithms are formed around a seed tower with the highest local E_T. These are then combined with all towers in a ΔR region of 0.4 around the seed. The combination of towers is used to compute the jet four momentum, which is then used to define a new centre around which the cone is redefined. The four momentum is then recomputed and the centre redefined again. This combination and re-computation process is repeated until a stable cone is found. Overlaps between cones are resolved using a split and merge procedure [76].

Jets in this thesis are required to have $p_T > 10$ GeV and $|\eta| < 2.5$.

4.2.4 Overlap Removal

In the reconstruction strategy adopted by ATLAS, reconstruction and identification of objects belonging to one of the categories detailed above is not exclusive. This means, for example, that it is possible to have a electron within a jet reconstructed as both an electron and a jet. In order to remove these overlaps, and therefore any ambiguity, the following overlap removals are applied:

- Jets within $\Delta R < 0.2$ of electrons are removed, and the electrons kept, thus giving precedence to reconstruct objects as electrons.

- Electrons and muons within $\Delta R < 0.4$ of the remaining jets are removed. This serves to remove the contributions of non-primary leptons originating within jets.

4.2.5 Missing Transverse Energy

Exclusively weakly interacting particles, such as neutrinos or neutralinos, are likely to traverse the entire detector without leaving any signals, rendering direct detection impossible. However, the presence of such non-interacting particles can be inferred by an imbalance in the observed transverse momentum in an event.

Total transverse energy, and hence missing transverse energy, is measured at ATLAS by the summation of all energy observed in the calorimeter and muon systems in the transverse plane. This is done either using topological cells or using reconstructed physics objects. In the CSC exercise, and in this thesis, the object based method is used. In this method E_T^{miss} is measured as the imbalance in the combined total energies of electrons, photons, muons and jets along with any additional low p_T objects that may not have been reconstructed as physics objects. This energy sum includes calibrations and corrections for energy loss in non-active materials such as the cryostats.

Measuring E_T^{miss} is difficult, and there are a number of sources of fake missing energy. These include instrumental effects such as noisy or dead calorimeter cells, badly reconstructed or fake muons, and acceptance effects due to lack of coverage over certain regions [77].

4.3 Data Samples and Software Versions

The simulated data samples used in this thesis are listed in Appendix A. These samples were produced centrally by the ATLAS collaboration over the period of four years during which the work in this thesis was undertaken. As a result, samples simulated at several different centre of mass energies, (14 TeV, 10 TeV and 900 GeV), are studied. These corresponds to the perceived ATLAS physics programme at the time of study. In addition, this thesis follows the evolution of the ATLAS offline reconstruction and trigger software and menus, which have been updated and improved regularly over the years. Consequently, different ATHENA software versions (v13, v14 and v15) have been used to produce the results presented. Throughout this thesis, details of the specific datasets will be introduced where relevant and any pertinent differences in software, or trigger menu, to versions studied previously will be discussed.

Chapter 5

The Efficiency of the Single Electron Trigger

This chapter introduces the concept of trigger efficiency and its uncertainty. This is followed by a study of the efficiency of two representative electron trigger signatures to select electrons in fully simulated MC samples of single electrons and the $Z \rightarrow e^+e^-$ process. Finally, a method is introduced to measure the efficiency of the electron trigger directly from data.

5.1 Trigger Efficiency

In order for a measurement of the number of electrons observed at ATLAS to be related to a physical parameter such as a cross-section, the efficiency of ATLAS to select and reconstruct these electrons needs to be known. This efficiency will consist of a convolution of the geometric acceptance of the detector, the efficiency of the trigger system and the efficiency of the offline reconstruction. The studies in this thesis will focus on a particular aspect of this; the efficiency of the trigger. In particular, on the efficiency of the single electron trigger to select electrons within events of varying topology.

The efficiency of the single electron trigger, ε, is interpreted as the probability, P, that an electron, e, will pass the trigger given certain conditions, I, that describe the electron and the event it is present within.

$$\varepsilon = P(\text{pass the electron trigger} \mid I, e). \tag{5.1}$$

Being a probability, the actual value of this efficiency cannot be directly determined. Instead it must be estimated with the available data. This estimation is done assuming that the true efficiency,

ε, is a real number between zero and one, to which the measured probability of selection tends in the limit of an infinite number of measurements. In a binomial model of efficiency, the measured probability, or efficiency *estimator*, $\hat{\varepsilon}$, is given by:

$$\hat{\varepsilon} = \frac{k}{n}, \tag{5.2}$$

where n is the total number of electrons, and k is the number of electrons which pass the trigger. The estimator of the variance on this efficiency estimator, $\hat{V}[\hat{\varepsilon}]$, is then defined by:

$$\hat{V}[\hat{\varepsilon}] = \frac{\hat{\varepsilon}(1-\hat{\varepsilon})}{n}. \tag{5.3}$$

This formualation is considered to describe variance well for the majority of scenarios. However, it also results in a variance which tends to zero when efficiency tends to zero or one, even if n is low. As a result, in this limit, the binomial model is not considered to constitute an accurate expression of uncertainty. An alternative method is to determine the efficiency using *Bayes' theorem* as described in [78]. In this formulation, the modal value of the efficiency estimator is again given by Equation 5.2, with the variance estimator now given by:

$$\hat{V}[\hat{\varepsilon}] = \frac{(k+1)(n-k+1)}{(n+2)^2(n+3)}. \tag{5.4}$$

This, similarly to Equation 5.3, is a function of n^{-1}. However, in this formulation, the variance estimator now also displays the desired behaviour at $k = 0$ or n, of not tending to zero. These two methods can be shown to give compatible results for the variance on efficiencies when not in the extreme limits. As a consequence, the majority of the studies in this thesis use the binomial model and only cases where the discussed limits are approached will use the Bayesian formulation. Where Bayesian methods are used this will be clearly indicated in the text.

Standard deviation is defined as:

$$\sigma = \sqrt{V}, \tag{5.5}$$

and is used to define the uncertainties on efficiencies. These uncertainties are statistical only; systematic sources of error are not discussed in this thesis.

Differential trigger efficiency, as a function of a given variable, can be measured by simply binning k and n in the appropriate variable and then computing the $\hat{\varepsilon}$ and $\hat{V}[\hat{\varepsilon}]$ for each bin. For example, the *1-Dimensional* (1-D) efficiency estimator as a function of transverse energy is defined in each bin i of transverse energy as:

$$\hat{\varepsilon}_i = \frac{k(E_T^i)}{n(E_T^i)}. \tag{5.6}$$

Here $k(E_T^i)$ is the number of electrons with transverse energy in the i-th E_T bin that pass the trigger, and $n(E_T^i)$ is the total number of electrons with transverse energy in the same bin. This concept of differential efficiency can be easily extended to higher dimensions than one. For example, to 2-D efficiency defined as a function of E_T and η.

When considering any measure of efficiency it is crucial to keep in mind the conditions in which this efficiency is assessed. For example, efficiency for electrons in $Z \rightarrow e^+e^-$ events quoted as a single number implicitly includes information on the kinematics of these electrons and on the underlying event topology, as both of these factors will influence the measured efficiency. Similarly, efficiency differential in E_T in the same sample will include information on all such conditions except E_T. Later sections of this thesis will deal with identifying which conditions are important when describing efficiency.

Trigger efficiency in this thesis is usually defined with respect to offline selection criteria as detailed in Section 4.2.1. That is to say, n is defined as the number of offline reconstructed electrons. Such a normalisation should, to first order, disentangle any offline reconstruction effects and leave the overall efficiency to describe only effects of trigger behaviour.

5.2 Trigger Signature Definitions

In this chapter, two examples of single electron trigger signatures are studied. These are `e15 loose` and `e25i medium`. The trigger `e15 loose` is an example of a relatively low-threshold, unisolated trigger signature. A trigger of this form is intended for use during low luminosity running periods of $\mathcal{L} \sim 10^{31}$ cm^{-2}s^{-1} up until $\sim 10^{32}$ cm^{-2}s^{-1}. Above this luminosity, the rate for this trigger is expected to become unsustainably high. The trigger `e25i medium` is an example of a medium-threshold, isolated trigger signature. A trigger of this form is intended for use at higher luminosities of $\mathcal{L} \sim 10^{32}$ cm^{-2}s^{-1} and above. The higher E_T threshold, tighter EF cuts and isolation requirement mean that the rate expected for this signature is much lower than that for `e15 loose`. Table 5.1 shows an overview of the cuts implemented by these triggers [79].

5.2.1 Performance with Single Electrons

In order to evaluate the efficiency of the single electron trigger, a MC sample containing only single electrons is studied. Within this sample, each event contains only a single generated electron, with η and E_T uniformly distributed across the ranges of -2.5 to 2.5, and 10 GeV to 120 GeV

Table 5.1: An overview of the cuts applied by the `e15 loose` and `e25i medium` triggers [79].

Variable	`e15 loose` cuts	`e25i medium` cuts
L1		
E_T threshold	$>$ 13 GeV	$>$ 18 GeV
Isolation	No	Yes
L2		
Cluster E_T threshold	$>$ 15 GeV	$>$ 25 GeV
Hadronic leakage	$<$ 3 GeV	$<$ 3 GeV
R_η	$>$ 0.87	$>$ 0.89
E_{ratio}	$>$ 0.6	$>$ 0.85
Track p_T	$>$ 2 GeV	$>$ 3 GeV
Track-cluster $\Delta\eta$	$<$ 0.03	$<$ 0.03
Track-cluster $\Delta\phi$	$<$ 0.15	$<$ 0.15
EF		
E_T threshold	$>$ 15 GeV	$>$ 25 GeV
`isEM` selection	*loose*	*medium*

respectively. The lack of additional particles enables the intrinsic electron selection efficiency of the trigger to be studied. Trigger efficiencies as functions of E_T, η and ϕ are calculated from Equation 5.6, and shown for `e15 loose` and `e25i medium`. Efficiencies for all trigger levels can be seen for `e15 loose` in Figures 5.1 and 5.2 and for `e25i medium` in Figures 5.3 and 5.4. These are discussed in more detail below.

The `e15 loose` trigger efficiency as a function of electron E_T is shown in Figure 5.1. Below the E_T thresholds of the various trigger levels, there is a negligible probability for electrons to pass the trigger. As the electron E_T reaches the energy thresholds, the efficiency is observed to increase sharply from zero to nearly one over the space of only a few GeV. This is the *turn-on* region. The slope of the turn-on curve is determined by the energy resolutions of each trigger level and, as such, is steeper at L2 and EF than at L1. Above the turn-on, efficiency is observed to be very high and almost flat. This is known as the *plateau* region. Efficiencies dependent on variables other than E_T are usually shown only for electrons in this region in order to remove effects from the turn-on curve. In this thesis, the plateau region is defined to be 10 GeV above the EF energy threshold.

The `e15 loose` trigger efficiencies as functions of electron η and ϕ are shown in Figure 5.2.

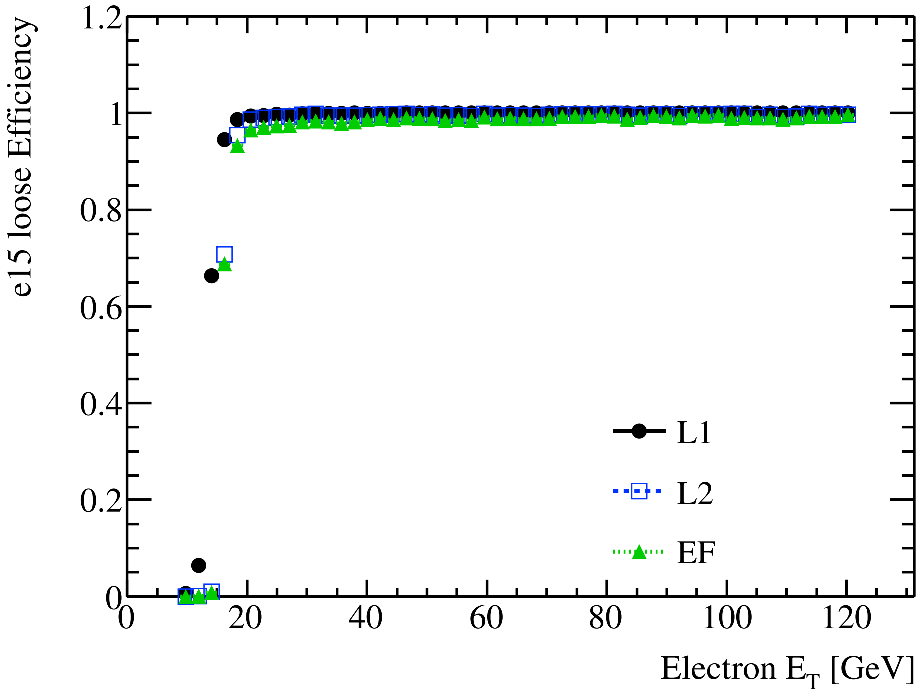

Figure 5.1: The `e15 loose` trigger efficiency with respect to the offline selection in a single electron sample. L1 (black circles), L2 (blue open squares), and EF (green triangles), as a function of electron, E_T.

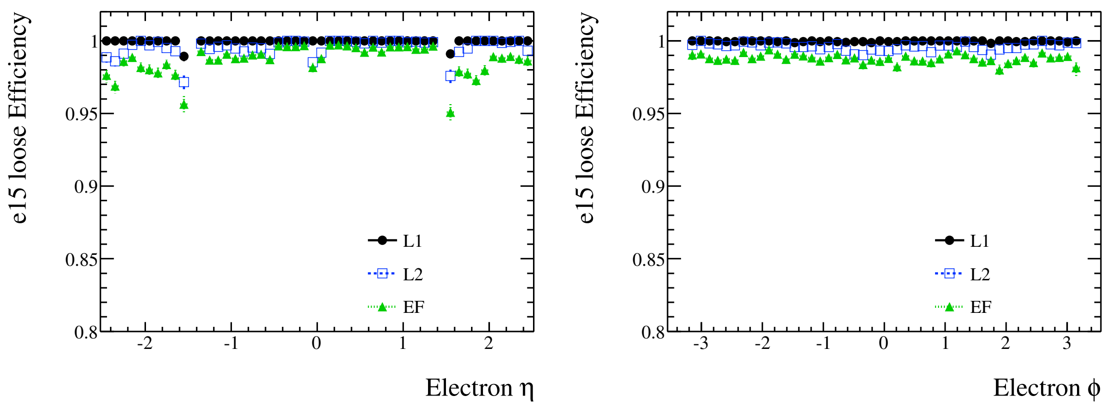

Figure 5.2: The `e15 loose` trigger efficiency with respect to the offline selection in a single electron sample. L1 (black circles), L2 (blue open squares), and EF (green triangles), as a function of electron, η (left) and ϕ (right). The efficiencies are shown only for electrons with $E_T > 25$ GeV.

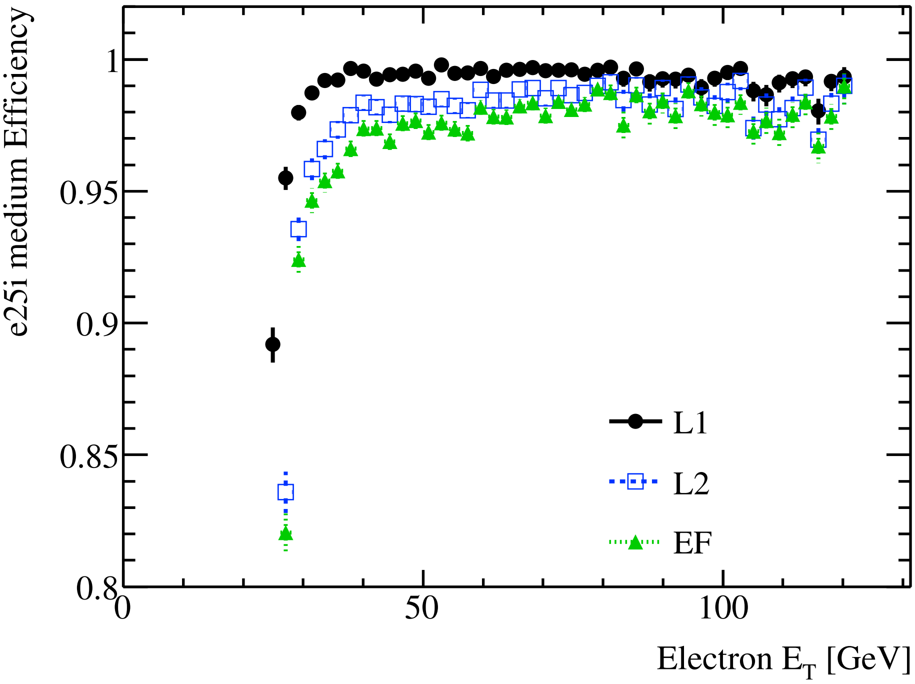

Figure 5.3: The `e25i medium` trigger efficiency with respect to the offline selection in a single electron sample. L1 (black circles), L2 (blue open squares), and EF (green triangles), as a function of electron E_T.

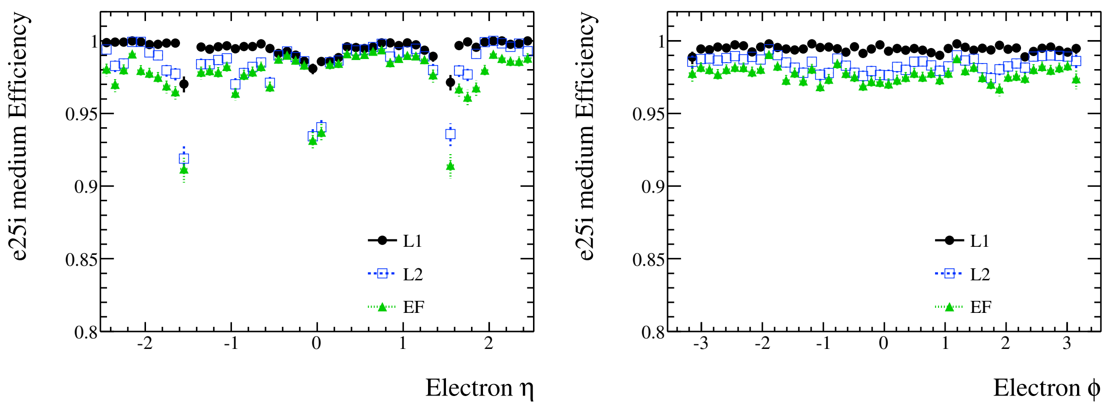

Figure 5.4: The `e25i medium` trigger efficiency with respect to the offline selection in a single electron sample. L1 (black circles), L2 (blue open squares), and EF (green triangles), as a function of electron, η (left) and ϕ (right). The efficiencies are shown only for electrons with $E_T > 35$ GeV.

Table 5.2: Integrated trigger efficiencies with respect to the offline selection in % for plateau electrons in the single electron sample (errors are statistical only).

Trigger	L1 efficiency	L2 efficiency	EF efficiency
`e15 loose` (cumulative)	99.97 ± 0.01	99.61 ± 0.02	98.79 ± 0.04
`e15 loose` (relative to above level)		99.64 ± 0.02	99.18 ± 0.03
`e25i medium` (cumulative)	99.44 ± 0.03	98.41 ± 0.05	97.74 ± 0.06
`e25i medium` (relative to above level)		98.97 ± 0.04	99.31 ± 0.03

In both these figures only electrons in the plateau region have been included. Efficiency is seen to be high and fairly uniform across the η and ϕ ranges. Small dips of a few percent are observed near the crack region and at $\eta \sim 0$ where calorimeter coverage is known to be degraded. The EF efficiency in the endcaps is seen to be slightly lower than in the barrel due to inhomogeneities in the online and offline cuts in the endcap regions. Trigger efficiency for all electrons above 25 GeV is summarised in Table 5.2.

The `e25i medium` trigger efficiency as a function of electron E_T is shown in Figure 5.3. The plateauing behaviour is observed to be slower than for `e15 loose`, with efficiency above the turn-on gradually increasing by a few percent over the E_T range of around 40 to 80 GeV. The trigger efficiencies as functions of electron η and ϕ are shown in Figure 5.4. Again, here, only plateau electrons are included. Efficiency is seen to be slightly lower than for `e15 loose`, and with more pronounced η and ϕ variations. The observed differences between this and Figure 5.2 are due to the tighter selection requirements applied by this trigger. The trigger efficiency for all electrons above 35 GeV is also summarised in Table 5.2.

Electrons present in a single electron samples are, by definition, completely isolated with no other objects present in the detector environment. Therefore, the trigger efficiency is expected to be very high and, indeed, this is what is observed. The overall `e15 loose` and `e25i medium` efficiencies above the turn-on regions are observed to be $\sim 98\%$ across the E_T, η and ϕ ranges. The `e15 loose` trigger is observed to be slightly more efficient than `e25i medium`, due to slight, 0.5% and 0.7% drops in efficiency observed at the L1 and L2 stages respectively of `e25i medium`. The EF efficiencies, relative to L1 and L2, are observed to remain extremely high and similar for both triggers. These results indicate that not only is the electron trigger selection efficiency very high for the single electron sample, but that it is robust against both the tightening of selection criteria, and the imposition of isolation requirements at L1.

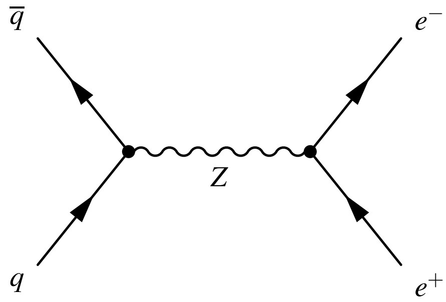

Figure 5.5: An example Feynman diagram of the Z→e^+e^- process.

5.2.2 Performance with Z→ *ee* Events

Whilst single electron events provide a good description of the behaviour of the trigger for well isolated electrons, they are not representative of electrons in actual events, and lack descriptions of the underlying event and of the large particle multiplicities that would be expected in real events. The process Z→ e^+e^-, as shown in Figure 5.5, is an example of a well understood SM process expected to result in energetic, isolated electrons. The next-to-leading order cross section for the Z→e^+e^- process at an LHC centre of mass energy of 14 TeV is expected to be around 2,069 pb [80]. This would result in the production of around 206,900 events within only $\int \mathcal{L}dt = 100$ pb^{-1} of data. The relative abundance and simple topology of the Z→e^+e^- process mean that it represents an excellent benchmark process for the evaluation of trigger efficiencies in a realistic detector environment. This section will study the trigger efficiency for electrons in a simulated MC dataset of Z→e^+e^- events and compare the obtained results to those observed in single electron events.

Table 5.3: Selection cut flow for MC analyses of the Z→e^+e^- sample. All efficiencies are quoted with respect to the number of all offline electrons.

Electron selection	Efficiency of selection (%)
All offline electrons	100.0
Reconstructed by the standard algorithm	86.7
`isEM` *medium*	71.5
E_T >10 GeV	55.3
$\lvert\eta\rvert < 2.5$	54.8
E_T in $\Delta R < 0.2$ <10 GeV	54.6
Overlap removal with jets	54.4
Exclude crack region ($1.37 < \lvert\eta\rvert < 1.52$)	51.3
Truth matched	51.2

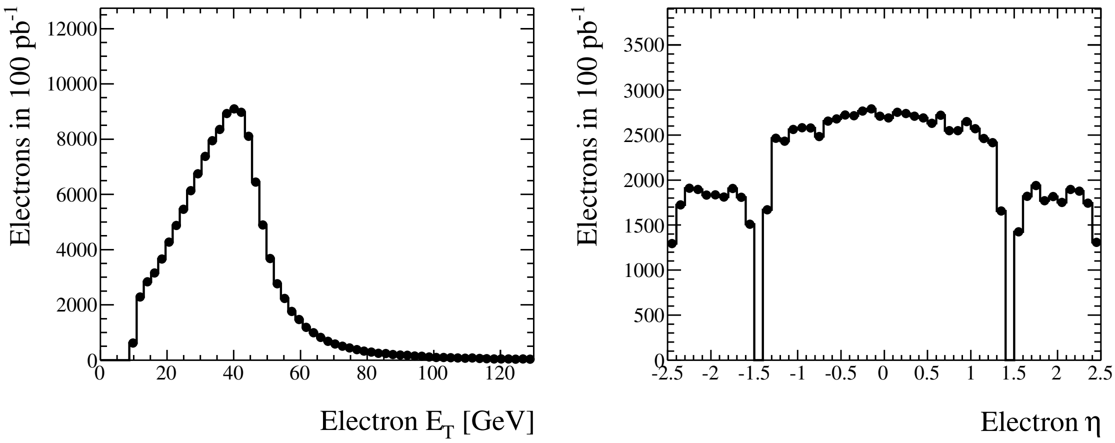

Figure 5.6: The E_T (left) and η (right) distributions of electrons in the Z→e^+e^- sample.

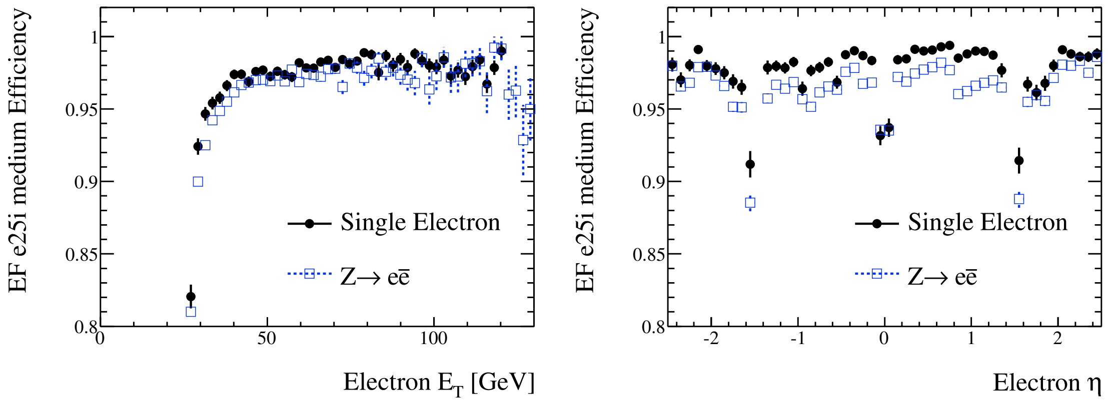

Figure 5.7: The `e25i medium` trigger efficiency with respect to the offline selection in the Z→e^+e^- (blue open squares) and single electron sample (black circles), as a function of electron, E_T (left) and η (right). The η efficiencies are shown only for electrons with $E_T > 35$ GeV.

In the following, electrons in the Z→e^+e^- sample are reconstructed using the standard electron selection. In addition, they are further required to be within $\Delta R < 0.1$ of a truth electron identified as coming from the decay of the Z-boson itself. This is done in order to remove the effects of non-electrons faking electrons. The efficiency of electron selection cut flow with respect to the total number of electrons selected offline within the Z sample is shown in Table 5.3. The E_T and η distributions of the selected electrons are shown in Figure 5.6. The E_T distribution is observed to be peaked around half the mass of the Z boson, due to the nature of the process, and the η distribution is observed to be concentrated in the barrel. The reduction in the number of electrons observed in the endcaps is primarily due to a degradation in the tracking efficiency at high $|\eta|$ and the lack of TRT coverage above $|\eta| = 2.0$.

The `EF e25i medium` efficiencies for the electrons in the Z→e^+e^- sample are shown in Figure 5.7 and compared to those observed in the single electron sample. The Z→e^+e^- trigger efficiency for plateau electrons is summarised in Table 5.4. Efficiency is observed to be high

Table 5.4: Integrated trigger efficiencies with respect to the offline selection in % for plateau electrons in the Z→e^+e^- sample (errors are statistical only).

Trigger	L1 efficiency	L2 efficiency	EF efficiency
`e15 loose` (cumulative)	99.74 ± 0.01	99.24 ± 0.02	97.94 ± 0.03
`e15 loose` (relative to above level)		99.50 ± 0.01	98.69 ± 0.02
`e25i medium` (cumulative)	98.95 ± 0.02	97.51 ± 0.03	96.49 ± 0.04
`e25i medium` (relative to above level)		98.54 ± 0.03	98.95 ± 0.02

across the studied ranges, with similar structures as functions of E_T and η observed as were in the single electron sample. The trigger efficiency in the Z sample is seen to be consistently 1% to 2% lower than in the single electron sample. This reduction is likely caused by features of the Z event generation which are absent from the single electron sample. Such features include: photons emitted as FSR; the effects of additional particles in the event; and the underlying event itself. Despite these small differences, the efficiency for electrons from Z decays is observed to be high and similar to that observed for single electrons. As such, electrons within this process can be considered almost ideal examples of isolated electrons. A measurement of the trigger efficiencies of these electrons would therefore represent a very good measure of the efficiencies for a single electron to pass the trigger.

5.3 Data Driven Efficiency Measurement

A typical search for new physics at ATLAS will look for an excess in events above that predicted by the SM. The uncertainty on the number of events observed will be determined by a combination of many factors. One of these will be the knowledge of the trigger efficiency. Whilst efficiencies can, in principle, be determined from MC, determining efficiencies from data reduces the reliance upon MC and therefore reduces the associated systematic errors. This section describes the use of the data driven *Tag and Probe* (TP) method to determine trigger efficiencies.

The TP method uses the Z boson resonance to provide a source of electrons. The TP selection implemented in this thesis utilises the common electron definitions detailed in Section 4.2.1. In this case no match is required between the reconstructed electrons and MC truth. Candidate events are first identified by the requirement that they contain an e^+e^- pair with an invariant mass value within 12 GeV of the nominal Z boson mass [5]. One of the electrons is then randomly selected to be the *tag* electron, and is required to have passed the trigger. The trigger used in this context is `EF e25i medium`. Provided that the event and the tag electron satisfy these selection criteria, the

Table 5.5: Selection cut flow for TP analyses on the $Z \to e^+e^-$ sample.

Event selection	Efficiency of selection (%)
All events	100
Good opposite charge pair	30.5
Z mass window (79→103 GeV)	26.6
Tag electron passes `EF e25i medium`	22.5

event is selected and the remaining electron, the *probe*, can be used to measure trigger efficiencies. The overall trigger efficiency estimator, as computed by the TP method, is defined as the number of probes that pass the trigger selection, k^p, divided by the total number of probes, n^p:

$$\hat{\varepsilon} = \frac{k^p}{n^p}. \tag{5.7}$$

This efficiency can also be measured as a function of one or more kinematic variable by binning in the appropriate variable of the probe.

Previously studies have extensively investigated the TP method [74, 81]. These have shown that the electron selection criteria and Z boson mass window requirement serve to reduce background contamination of the probe sample to negligible levels, meaning consistent results can be obtained from the Z sample alone as well as with the inclusion of background effects. As such, the studies in this thesis do not deal with the treatment of backgrounds or their effects on the TP method.

The cut flow efficiency of the TP selection criteria relative to all events in the $Z \to e^+e^-$ sample is shown in Table 5.5. Unsurprisingly, the additional TP requirements reduce the statistics considerably. For an integrated luminosity of 100 pb^{-1} a sample of approximately 46,600 electrons could be obtained using the TP method.

The reconstructed invariant Z mass peak is shown in Figure 5.8(a), with the shadowed area defining the Z mass window cuts. It can be seen from the cut flow in Table 5.5 that after the dielectron requirement, the invariant mass cut rejects around 13% of the remaining events. The electron kinematical variables: E_T; η; and energy in a hollow cone of $\Delta R < 0.4$ around the electron, before and after the requirement of the TP cuts are shown in Figures 5.8(b), (c) and (d) respectively. The shapes of these distributions indicates that the TP selection preferentially selects electrons in the central η region and with E_T peaked around half the Z mass.

The efficiency of each level of the `e25i medium` trigger can be seen in Figure 5.9 for the full MC sample and the TP method. A comparison between the efficiencies obtained by each method

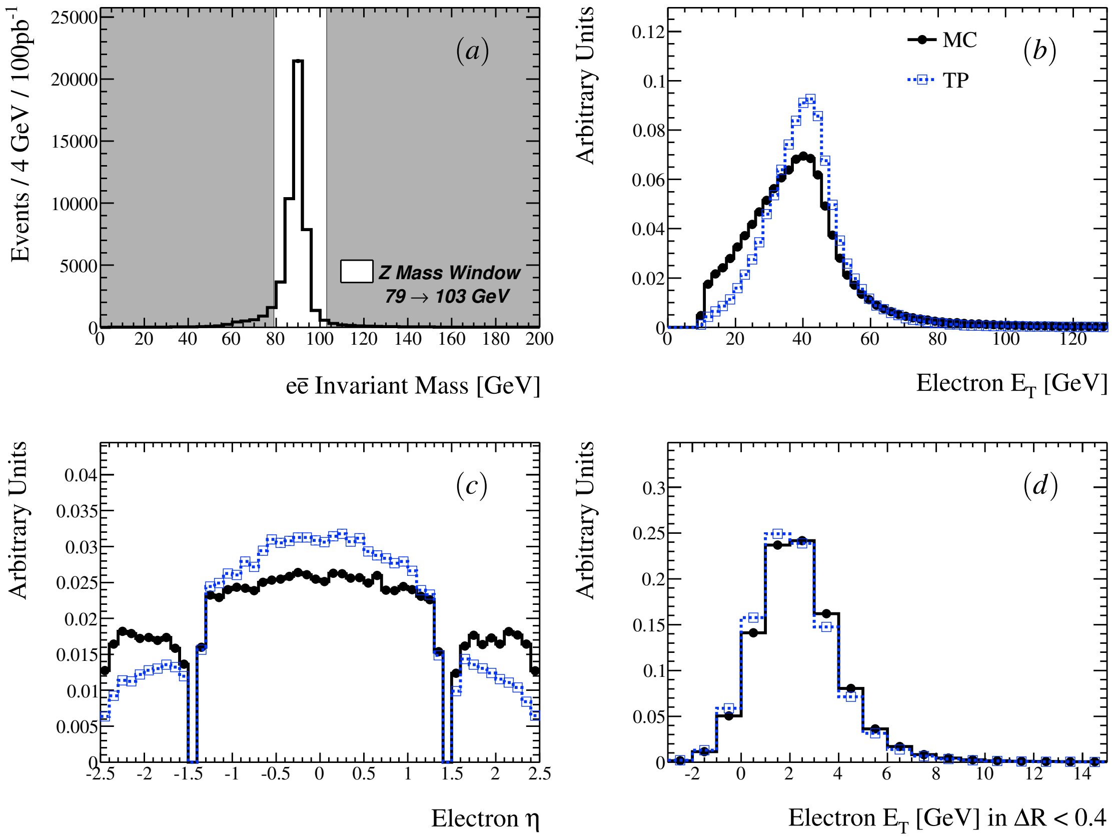

Figure 5.8: (a) Offline reconstructed dielectron invariant mass for the $Z \to e^+e^-$ MC sample (the shadowed area defines the mass window cuts). Reconstructed electron spectrum as a function of (b) electron E_T, (c) $|\eta|$ and (d) E_T in a hollow cone of $\Delta R < 0.4$ around the electron, for the full MC sample (black circles) and for the probe electrons in events that pass the TP selection criteria (blue open squares). For comparison purposes these plots are normalised to a nominal area of 1.

can be seen in Figure 5.10. The efficiencies from the TP method for all probes in the plateau region are summarised in Table 5.6.

The TP method is seen to show good agreement with MC across the E_T and $|\eta|$ spectra. Furthermore, the overall efficiencies are consistent to within $\sim 0.2\%$. These results shows that, to the accuracy of this study, the TP method is a reliable method for measuring trigger efficiencies.

The following chapter of this thesis will study how the efficiency observed in the $Z \to e^+e^-$ sample compares to the efficiency in MC simulations of other physics processes with different event topologies.

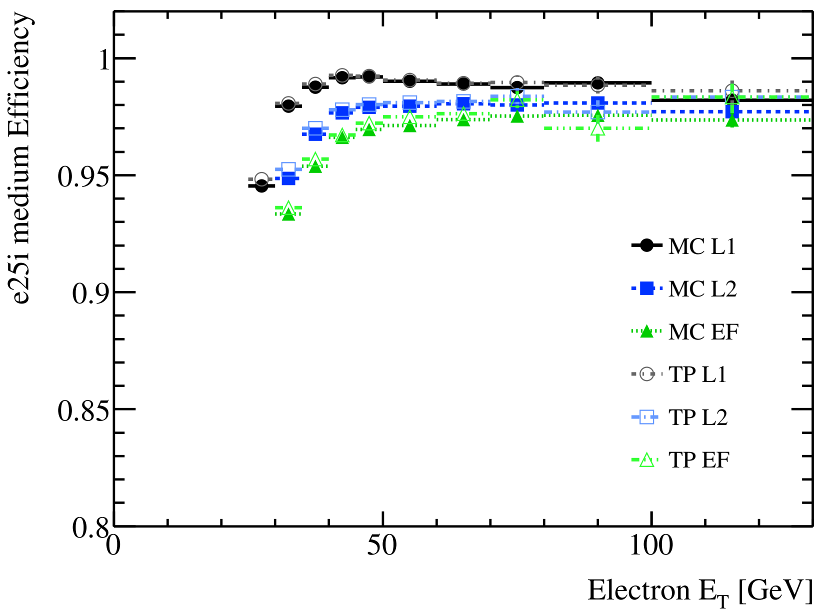

Figure 5.9: `e25i medium` efficiency as a function of electron E_T for all trigger levels as obtained from full MC simulation (filled) and TP (hollow) applied to Z→e^+e^- events.

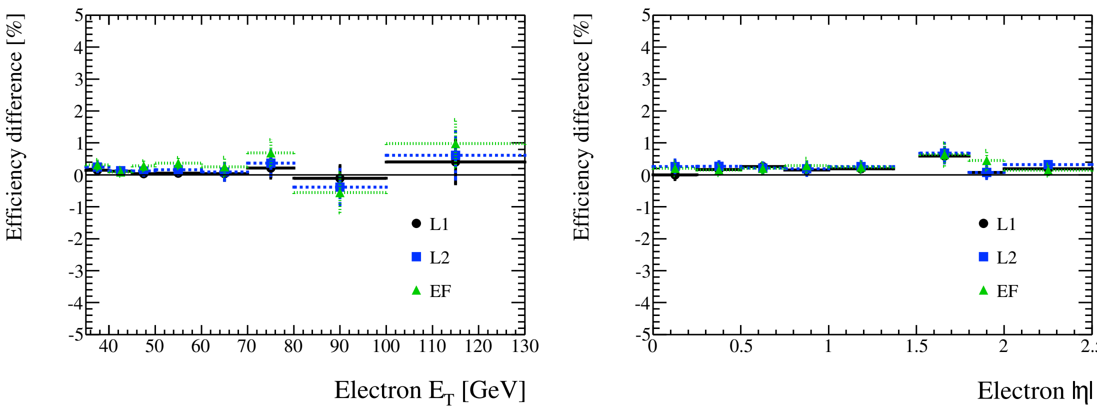

Figure 5.10: Efficiency difference in Z→e^+e^- events between the MC and TP methods for (black circles) L1, (blue squares) L2 and (green triangles) EF as a function of electron E_T (left) and |η| (right).

Table 5.6: Integrated trigger efficiencies from the Tag and Probe method shown with respect to the offline selection in % for plateau electrons in the Z→e^+e^- sample (errors are statistical only).

Trigger	L1 efficiency	L2 efficiency	EF efficiency
`e15 loose` (cumulative)	99.79 ± 0.01	99.38 ± 0.02	98.17 ± 0.04
`e15 loose` (relative to above level)		99.59 ± 0.02	98.79 ± 0.03
`e25i medium` (cumulative)	99.09 ± 0.03	97.68 ± 0.05	96.72 ± 0.06
`e25i medium` (relative to above level)		98.58 ± 0.04	99.02 ± 0.04

Chapter 6

Electron Triggers for Hadron Rich Environments

This chapter studies the efficiency of the electron trigger to select electrons in hadron rich environments. The opening section describes the efficiency of two representative electron trigger signatures when selecting prompt electrons in fully simulated MC samples of the SU3 and SU4 SUSY benchmark points and of top-quark pair production. Following this, a method is introduced that models trigger efficiency in a manner appropriate for all the studied samples. Such a technique could be used with the TP method to enable the measurement of trigger efficiency representative of busy events from data. The final section studies the effects of non-prompt and fake electrons on trigger efficiency and on the data driven measurement techniques.

6.1 Trigger Efficiency

The most important function of the trigger system is to select the rare events characteristic of interesting physical processes. This section will study the efficiency of the electron trigger to select electrons in the busy environments typical of SUSY events and the $t\bar{t}$ process. Specifically, the efficiency of the triggers `e25i medium` and `e15 loose` to select electrons in fully simulated MC SU3, SU4, and $t\bar{t}$ events. These efficiencies will be contrasted to those observed in the Z$\rightarrow e^+e^-$ process as discussed in the previous chapter.

The SUSY MC samples studied here are inclusive, and are comprised of all possible sparticle production and decay modes. The $t\bar{t}$ MC sample contains only events within which at least one of the top-quarks decays leptonically. Details of the MC samples used for this study can be found in Appendix A.1.

Offline reconstructed objects in each sample are identified using the standard reconstruction

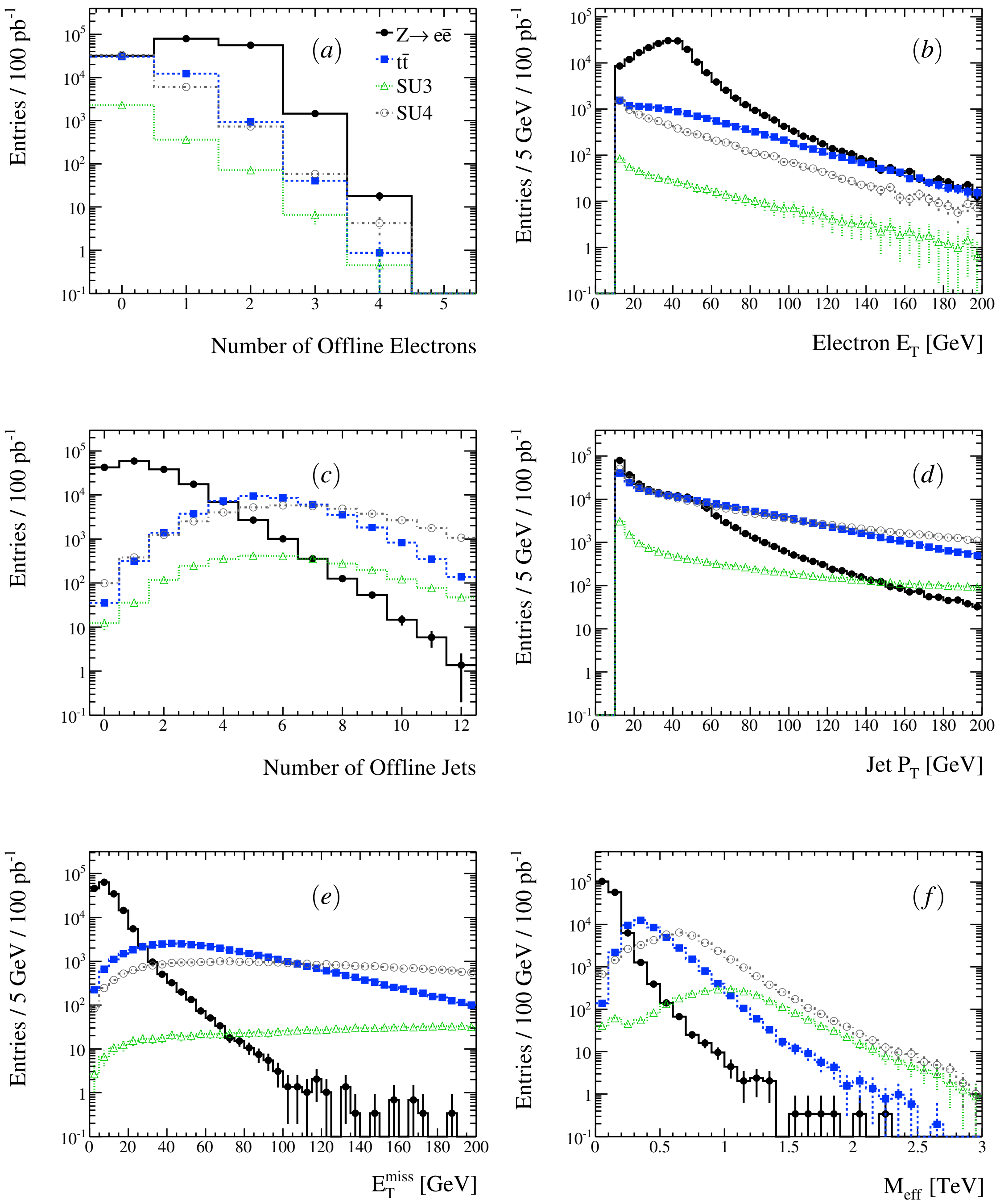

Figure 6.1: Kinematic variables in SUSY and SM events. The (a) number of electrons and the (b) jet E_T; the (c) number of jets and the (d) jet p_T; the (e) E_T^{miss} and (f) M_{eff} present in events. All variables are offline reconstructed values in MC samples of $Z \to e^+e^-$ (black circles), $t\bar{t}$ (blue squares), SU3 (green open triangles) and SU4 (grey open circles). Distributions are normalised to $100\,\mathrm{pb}^{-1}$ of integrated luminosity.

methods detailed in Section 4.2. In addition, electrons are required to be within $\Delta R < 0.1$ of a MC truth electron which has been identified as part of the hard process. Such electrons are defined as prompt electrons coming from Z-boson, t-quark or SUSY particle decays.

Some kinematic quantities for the processes studied are shown in Figure 6.1. Both SUSY and $t\bar{t}$ environments are seen to be rich in high-P_T jets, as shown by Figures 6.1(c)-6.1(d). A further measure of the activity in events, the effective mass, M_{eff} (defined here as the scalar sum of the transverse energy of the E_T^{miss} and of all electrons, muons and jets with $p_T > 10$ GeV present in the event) is seen in Figure 6.1(f) to be very high in SUSY events. Furthermore, both SUSY and $t\bar{t}$ events contain significant amounts of E_T^{miss} (see Figure 6.1(e)). Conversely, the $Z\rightarrow e^+e^-$ sample is seen to contain low amounts of hadronic activity and on average a low E_T^{miss}.

The `EF e25i medium` trigger efficiency as a function of offline E_T is shown in Figure 6.2, and the differences between the efficiencies seen in the SUSY and $t\bar{t}$ process and those in the $Z\rightarrow e^+e^-$ process are shown in Figure 6.3. The overall efficiency for electrons in the plateau region of these samples is summarised in Table 6.1. Similarly, the `EF e15 loose` trigger efficiency is shown in Figure 6.4 and summarised in Table 6.2.

Trigger efficiencies are seen to be above 90% in both $t\bar{t}$ events and at the SUSY benchmark points. This indicates that the ATLAS electron triggers are well optimised to select electrons in these events. However, it is also clear that trigger efficiency, globally and as a function of either E_T or $|\eta|$, differs significantly dependent upon the process studied. Electrons in $Z\rightarrow e^+e^-$ events are selected with a high efficiency by both the isolated and unisolated triggers. The overall L1+L2+EF efficiency in these events is ~97% for both `EF e25i medium` and `EF e15 loose`. On the other hand, electrons in SU3 events are seen be selected with a reduced overall efficiency of ~92% by `EF e25i medium`, as well as a slightly reduced ~96% efficiency by `EF e15 loose`. Electrons in the $t\bar{t}$ and SU4 samples are seen to be selected with efficiencies in between these extremes of ~94% and

Table 6.1: `e25i medium` trigger efficiencies in the plateau region ($E_T > 35$ GeV), expressed in %, as obtained from MC.

Sample	L1 Efficiency	L2 Efficiency	EF Efficiency
$t\bar{t}$ (cumulative)	95.85 ± 0.07	94.56 ± 0.09	93.94 ± 0.09
$t\bar{t}$ (relative to above level)		98.66 ± 0.04	99.34 ± 0.03
SU3 (cumulative)	93.64 ± 0.26	92.50 ± 0.29	91.97 ± 0.29
SU3 (relative to above level)		98.78 ± 0.12	99.43 ± 0.09
SU4 (cumulative)	94.09 ± 0.19	92.88 ± 0.21	92.60 ± 0.22
SU4 (relative to above level)		98.71 ± 0.10	99.71 ± 0.05

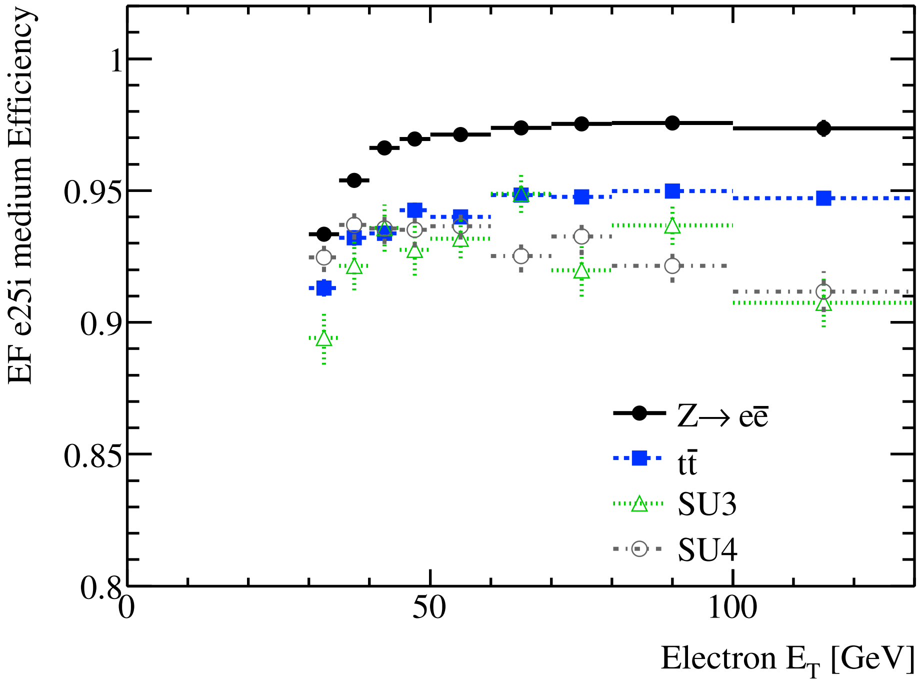

Figure 6.2: `EF e25i medium` efficiency for all offline electrons as a function of offline E_T in MC samples of Z$\rightarrow e^+e^-$ (black circles), $t\bar{t}$ (blue squares), SU3 (green open triangles) and SU4 (grey open circles).

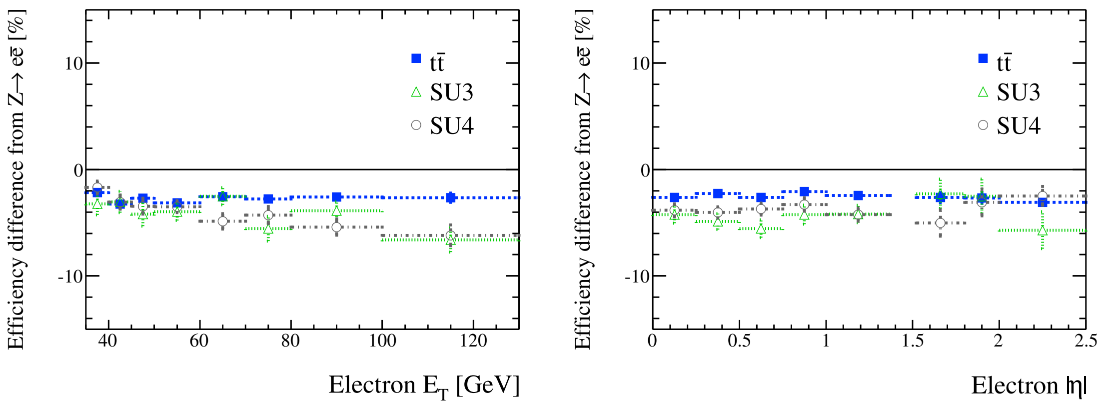

Figure 6.3: The difference in `EF e25i medium` efficiency between the Z$\rightarrow e^+e^-$ sample and $t\bar{t}$ (blue squares), SU3 (green open triangles) and SU4 (grey open circles), as a function of offline (left) E_T and (right) $|\eta|$. The $|\eta|$ efficiencies are shown only for electrons with $E_T > 35$ GeV.

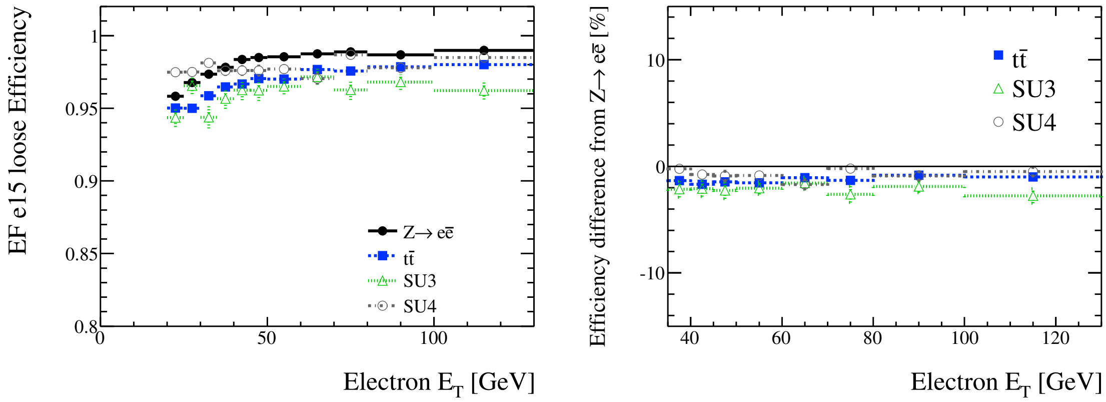

Figure 6.4: `EF e15 loose` efficiency for all offline electrons as a function of offline (left) E_T in MC samples of Z→e^+e^- (black circles), $t\bar{t}$ (blue squares), SU3 (green open triangles) and SU4 (grey open circles) and (right) the difference between the $t\bar{t}$, SU3 and SU4 efficiencies and that observed in the Z→e^+e^- sample.

Table 6.2: `e15 loose` trigger efficiencies in the plateau region ($E_T > 25$ GeV), expressed in %, as obtained from MC.

Sample	L1 Efficiency	L2 Efficiency	EF Efficiency
$t\bar{t}$ (cumulative)	99.03 ± 0.03	97.97 ± 0.05	97.02 ± 0.06
$t\bar{t}$ (relative to above level)		98.93 ± 0.04	99.03 ± 0.03
SU3 (cumulative)	98.77 ± 0.11	96.99 ± 0.17	96.19 ± 0.19
SU3 (relative to above level)		98.20 ± 0.13	99.17 ± 0.09
SU4 (cumulative)	98.88 ± 0.08	98.18 ± 0.10	97.77 ± 0.11
SU4 (relative to above level)		99.29 ± 0.06	99.59 ± 0.05

$\sim$93% respectively by `EF e25i medium`, and of $\sim$97% by `EF e15 loose`. A considerably larger discrepancy is observed for the isolated signature than for the unisolated one. Table 6.1 reveals that the majority of this difference is due to L1, whilst the HLT efficiencies, when normalised to the above levels, are observed to be roughly equivalent between samples.

Whilst the observed differences are only a few percent, it is important to understand the origin of these differences in order to have a complete understanding of the impact of the trigger on the selected SUSY events. Furthermore, it should be recalled that the TP method has been shown to be able to determine the $Z \rightarrow e^+e^-$ trigger efficiency from data, therefore an understanding of the origins of differences between $Z \rightarrow e^+e^-$ and SUSY efficiencies is vital in order to be able to correctly determine the efficiency of the trigger in SUSY events from data. The following sections will focus on the origin of these differences.

6.1.1 Kinematic Effects

In this section the effect of the electron kinematics, namely E_T and η, on trigger efficiencies will be discussed, focusing on the isolated trigger `EF e25i medium`.

As seen in previous chapters, trigger efficiency is a multidimensional function depending on at least E_T and η. When 1-D efficiencies as functions of only E_T or η are shown, then it is implicit that an integration has been performed over all other variables. Similarly, when showing numbers, such as those in Table 6.1, an integral across all variables has been performed to leave only a single number. When performing such integration the information contained within the integrated dimensions is lost. This process could lead to differences in the observed trigger efficiency, due to a loss of information about the electron kinematics contained within the integrated dimensions, rather than an intrinsic difference in the performance of the trigger. For example, if two samples have different electron kinematics in E_T and η, and trigger efficiency depends on both E_T and η, then in order for trigger efficiency to agree between samples, it would have to be compared in appropriately sized $E_T \times \eta$ bins. Alternatively, different kinematics can be accounted for before comparing lower dimensional efficiency.

The electron E_T and η distributions in each sample are compared in Figure 6.5, clearly illustrating differences between each of them. The $t\bar{t}$ and SUSY points have electron η distributions that are more peaked in the barrel than $Z \rightarrow e^+e^-$. The $Z \rightarrow e^+e^-$ sample also has an E_T spectrum which is strongly peaked, with only a small tail to high E_T, whilst the other samples have less of a peak and much larger tails at high E_T. These kinematical differences should be accounted for when comparing efficiencies.

The `EF e25i medium` efficiency for electrons as a function of offline $E_T \times |\eta|$ is shown in

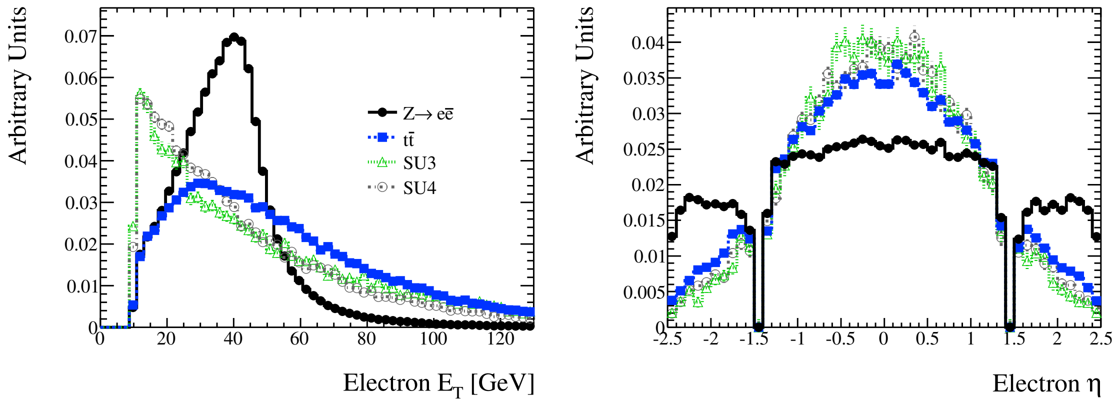

Figure 6.5: The (a) E_T and (b) η distributions of electrons in MC samples of Z→e^+e^- (black circles), $t\bar{t}$ (blue squares), SU3 (green open triangles) and SU4 (grey open circles). For comparison purposes these plots are normalised to a nominal area of 1.

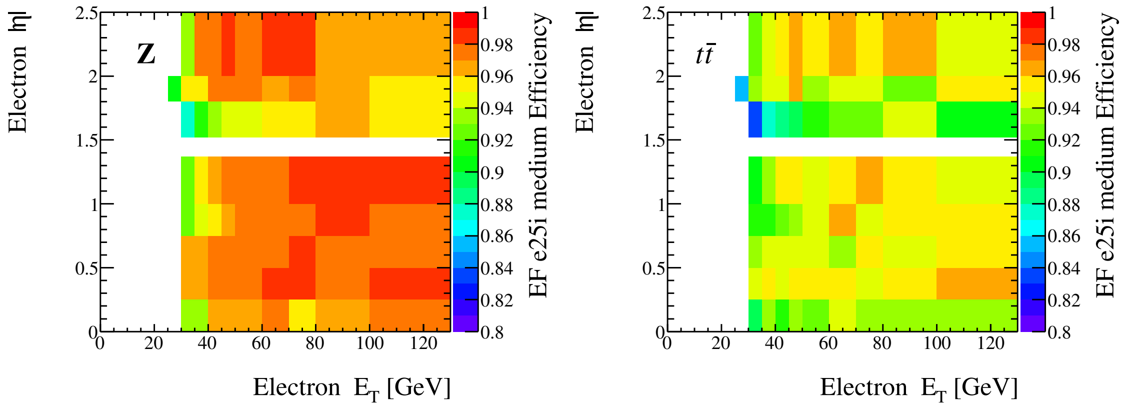

Figure 6.6: `EF e25i medium` efficiency for electrons as a function of E_T and |η| for MC samples Z→e^+e^- (left) and $t\bar{t}$ (right).

Figure 6.6 for Z→e^+e^- and $t\bar{t}$. Whilst it is difficult to quantitatively compare these plots, it is clear that the 2-D efficiency distributions are not the same in the different samples. Z→e^+e^- events are observed to show a consistently higher efficiency across the parameter space than $t\bar{t}$. Therefore, it becomes apparent that kinematics in terms of $E_T \times |\eta|$ alone will not be sufficient to explain the observed discrepancies in efficiency. This conclusion is further illustrated in Section 6.2.

6.1.2 Isolation Effects

The SUSY and $t\bar{t}$ samples have been observed to contain significant amounts of hadronic activity. In such busy environments it would not be uncommon for electrons to be produced in proximity to jets and other high-p_T objects. This proximity could cause electrons to fail the L1 isolation criteria or other trigger selections, and thus lead to the observed differences in $E_T \times |\eta|$ efficiency between samples. This section will explore electron isolation as a cause of this difference.

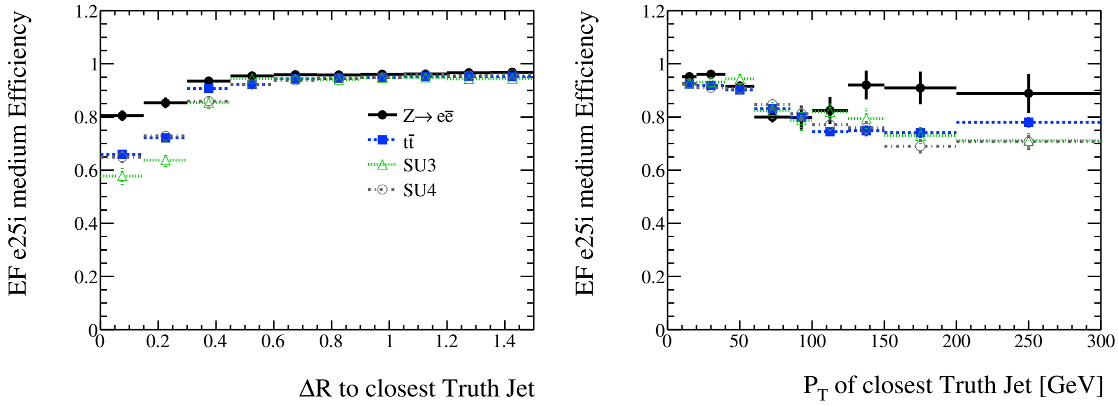

Figure 6.7: `EF e25i medium` efficiency for electrons as a function of the distance to the nearest truth jet (left) and the p_T of this truth jet if such a jet is within $\Delta R < 0.6$ (right), for MC samples of $Z \to e^+e^-$ (black circles), $t\bar{t}$ (blue squares), SU3 (green open triangles) and SU4 (grey open circles).

Isolation can be studied in a number of ways. For example, the `EF e25i medium` trigger efficiency as a function of the ΔR between the electron and the nearest truth jet with $E_T > 10$ GeV, is shown in the left-hand plot of Figure 6.7. Here truth jets are defined as cone jets of radius 0.4, constructed from all particle in the MC truth record. It can be seen that when no truth jet is present with $\Delta R < 0.6$, then the efficiency is high, flat and in seemingly good agreement between samples. On the other-hand, when a truth jet is nearby then the efficiency is observed to decrease and differences emerge between samples. The efficiency as a function of the p_T of the nearest truth jet when this jet is within $\Delta R < 0.6$ of an electron is shown in the right-hand plot of Figure 6.7. It can be seen that, for all samples, efficiency falls as a function of the increasing p_T. From this, it can be concluded that nearby objects depositing energy in close proximity to electrons are leading to trigger inefficiency, and that the p_T of these objects is related to the magnitude of the efficiency drop.

In order to study the effect that nearby objects have on trigger efficiency in a way that is reproducible without truth information, electron offline variables are studied. The $E_T cone$ variable is defined as the amount of energy contained in a hollow cone of $\Delta R < 0.4$ around a central cone that defines the electron object (which in this study has size $\Delta\eta \times \Delta\phi = 0.075 \times 0.125$). The origin of energy contained in this cone can be due to: energy leakage from the central electron cone; detector noise; or from overlap with nearby objects. The amount of energy leakage is related to the shower width and length and hence energy of the electron. Therefore, in addition to $E_T cone$, $E_T cone$ divided by E_T, ($E_T cone$ / E_T), is also studied. $E_T cone$ is very similar to the variables used by L1 to define particle isolation as described previously. The `EF e25i medium` efficiency as a

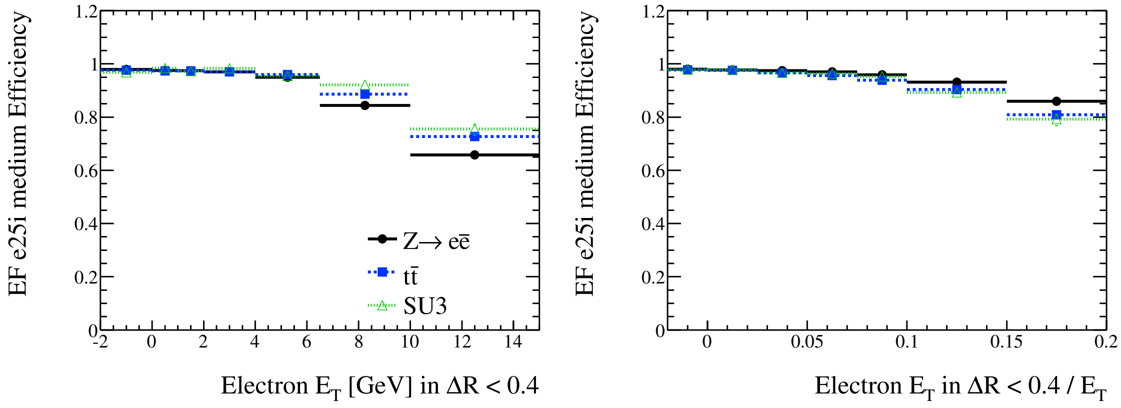

Figure 6.8: EF e25i medium efficiency for electrons as a function of $E_T cone$ (left) and this energy divided by the E_T of the electron, for MC samples of $Z \to e^+e^-$ (black circles), $t\bar{t}$ (blue squares), and SU3 (green open triangles).

function of $E_T cone$ and as $E_T cone$ / E_T for the $Z \to e^+e^-$, $t\bar{t}$ and the SUSY benchmark point SU3 is shown in Figure 6.8. Efficiency is seen to drop sharply as a function of increasing $E_T cone$ and $E_T cone/E_T$.

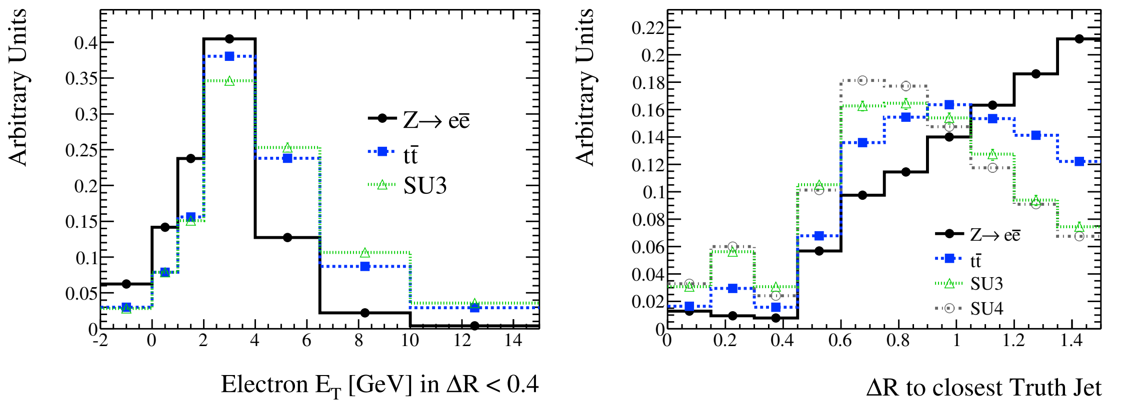

Figure 6.9: The $E_T cone$ (left) and distance to the nearest truth jet (right) distributions for electrons for MC samples of $Z \to e^+e^-$ (black circles), $t\bar{t}$ (blue squares), SU3 (green open triangles) and SU4 (grey open circles). For comparison purposes these plots are normalised to a nominal area of 1.

The distribution for $E_T cone$ and distance to the nearest truth jet for electrons is shown in Figure 6.9. In this, it is seen that the SUSY and $t\bar{t}$ samples have higher proportions of electrons with high values of $E_T cone$ and with nearby truth jets, as was expected.

Trigger efficiency has now been shown to depend not only on $E_T \times |\eta|$, but also on isolation. The EF e25i medium efficiencies for electrons in two $E_T cone$ ranges in the $Z \to e^+e^-$ and $t\bar{t}$ samples are shown in Figure 6.10 in the $E_T \times |\eta|$ plane. By restricting these 2-D figures only to electrons with certain $E_T cone$ values, efficiency can be compared independently of the overall isolation of the samples. In this figure, unlike previous figures, the trigger efficiency now appears to be in agreement between samples; although the large number of bins and low number of electrons

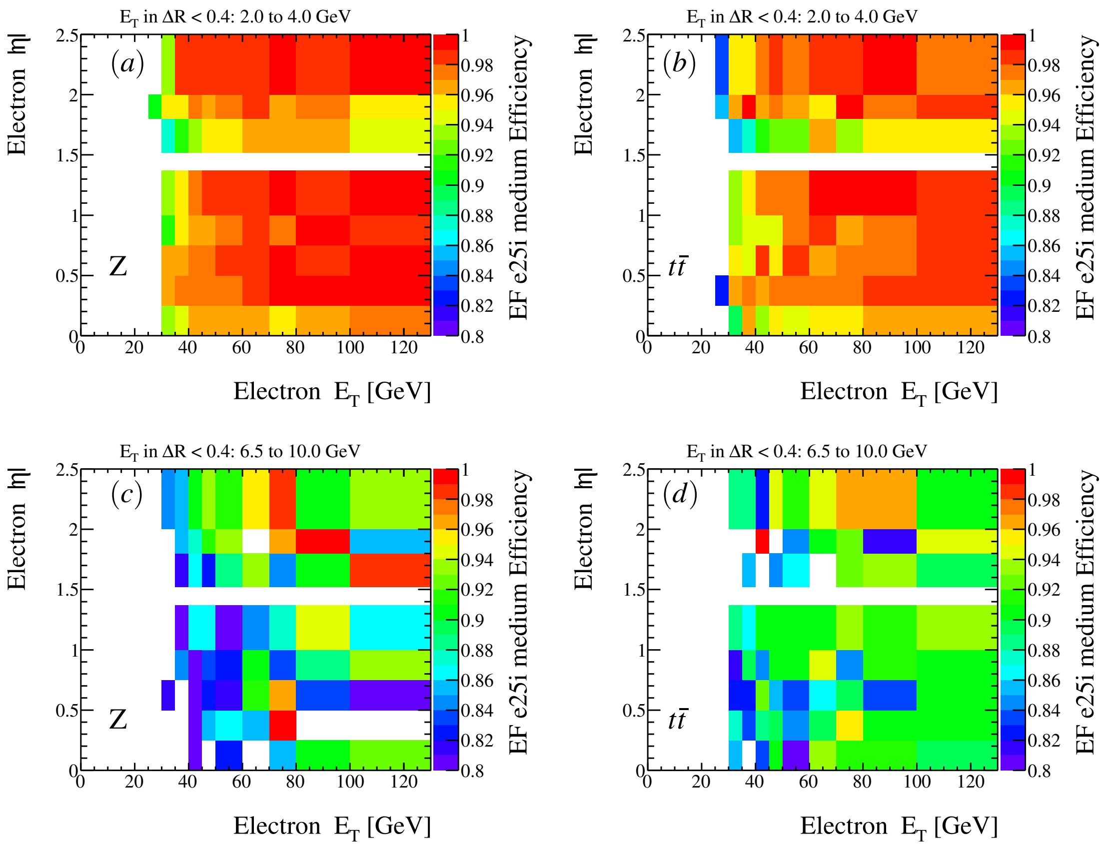

Figure 6.10: `EF e25i medium` efficiency for electrons as a function of E_T and $|\eta|$ only for electrons in two slices of $E_T cone$ in MC samples of $Z \rightarrow e^+e^-$ (left) and $t\bar{t}$ (right). The top plots contain only electrons with $E_T cone$ between 2 GeV and 4 GeV, and the bottom plots only electrons with $E_T cone$ between 6.5 GeV and 10 GeV.

per bin make a quantitative comparison difficult. This result indicates that the observed differences in trigger efficiency between samples when observed in less than 3-D can be explained due to differences in the electron distributions in the same three dimensions. In particular the lower overall efficiencies in the $t\bar{t}$ and SUSY benchmark point samples are due to the increased hadronic activity in these events. When efficiency is compared in 3-D it appears to be sample independent. This result is discussed further as part of the following section.

6.2 Trigger Efficiency Measurement using Weighted Averages

An important aspect of any SUSY search at ATLAS will be a detailed knowledge of the behaviour of the trigger system. In particular, the efficiency to select electrons in SUSY-like events will have to be known to a high degree of accuracy. Previous studies have claimed that trigger efficiency in a SUSY environment can be measured from data, and that with an integrated luminosity of $1\,fb^{-1}$, the uncertainty on this measurement will be less than 1% [27]. However, this result was based upon the principle that efficiency could be determined via the TP method in 0-D. The studies presented in the previous section have shown that if trigger efficiency were to be determined in this way then it would not be representative of efficiency in busy environments, due to differences in the isolation of electrons.

This section will discuss how efficiency can be determined from data such that it is representative of SUSY events. This will be done via a multidimensional weighted average of the `EF e25i medium` efficiency. Efficiency is first measured using $Z\rightarrow e^+e^-$ events, ε^Z, then used to model efficiency in a second sample by constructing a weighted average of efficiency based on the electron kinematics in this sample. For example, an electron in a SUSY sample with values of two kinematical parameters i and j, the trigger efficiency $\varepsilon'_{i,j}$ is given by:

$$\varepsilon'_{i,j} = \varepsilon^Z_{i,j}, \tag{6.1}$$

where $\varepsilon^Z_{i,j}$ is the measured $Z\rightarrow e^+e^-$ efficiency in the bin i, j. Generalising this to the efficiency of all electrons in the SUSY sample, $N_{i,j}$, in bin i, j, we arrive at:

$$\varepsilon'_{i,j} = \frac{\varepsilon^Z_{i,j}.N_{i,j}}{N_{i,j}}. \tag{6.2}$$

This can then be integrated over one of the dimensions, in this case the dimension of j, to get:

$$\varepsilon'_{i} = \frac{\sum_j(\varepsilon^Z_{i,j}.N_{i,j})}{N_i}. \tag{6.3}$$

The resultant efficiency is a weighted average of ε^Z based on the kinematical distributions of SUSY electrons in j. This efficiency can then be compared to the MC efficiency in the same sample, ε^{MC}_i. If the MC efficiency is fully described by the $Z\rightarrow e^+e^-$ efficiency then ε'_i will be equal to ε^{MC}_i. Further details of this method used are given in Appendix B, including a discussion of error propagation. This procedure allows for the comparisons of trigger efficiencies without the need to compare them bin by bin in a multidimensional space. Furthermore, the studies in Chapter 5 have shown that the $Z\rightarrow e^+e^-$ efficiency could be constructed from data using the TP method. Therefore, such a technique could be used with real data to extract a measure of the trigger efficiency in SUSY-like events, and to quantify the error on this efficiency.

It has previously been shown that the trigger efficiency observed in the full $Z\rightarrow e^+e^-$ MC sample is equivalent to that which can be obtained using the TP method. Therefore, in this section, the $Z\rightarrow e^+e^-$ MC efficiency will be studied and it is presumed that equivalent results may be obtained from data.

As a first test, a 2-D efficiency measurement is constructed from $Z\rightarrow e^+e^-$ MC in eleven bins in E_T and eight bins in $|\eta|$. The obtained efficiency is then applied to electrons in the $t\bar{t}$ and

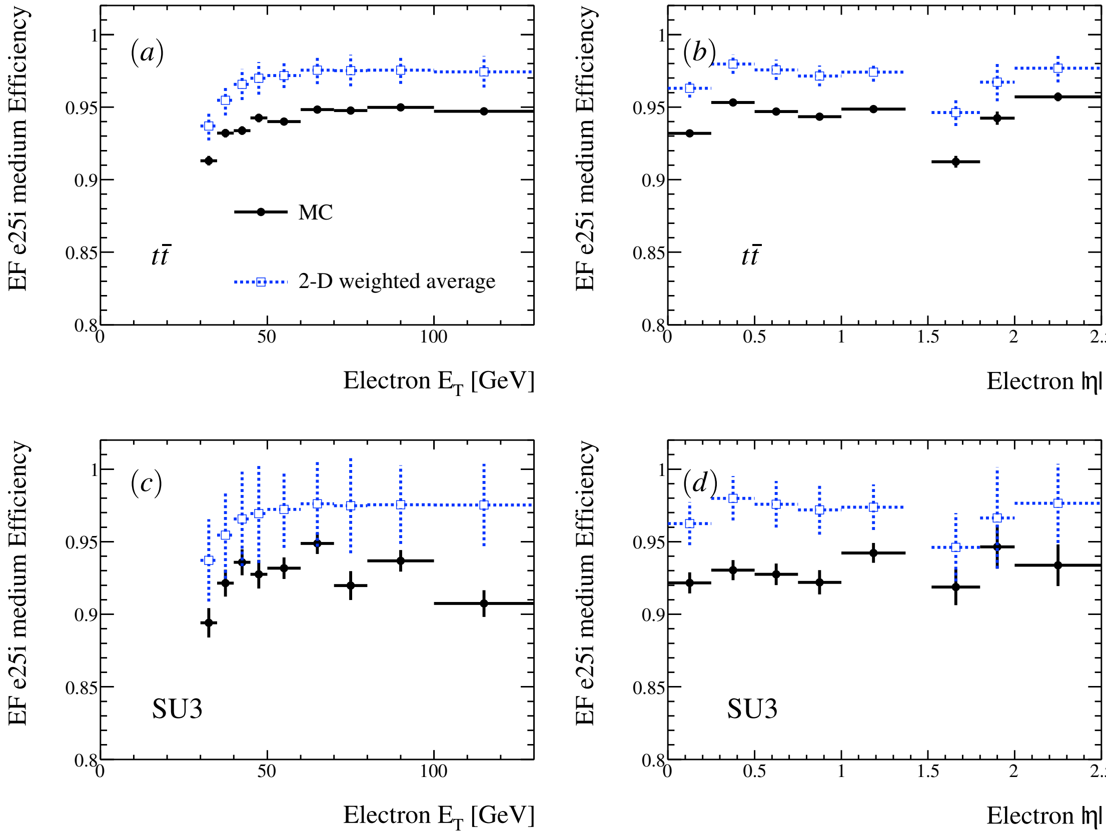

Figure 6.11: The results of using the 2-D $Z\rightarrow e^+e^-$ efficiency (blue open squares) in $E_T \times |\eta|$ of `EF e25i medium` to produce weighted averages of efficiency in the $t\bar{t}$ ((a) and (b)) and SU3 ((c) and (d)) samples as compared to MC efficiency (black circles).

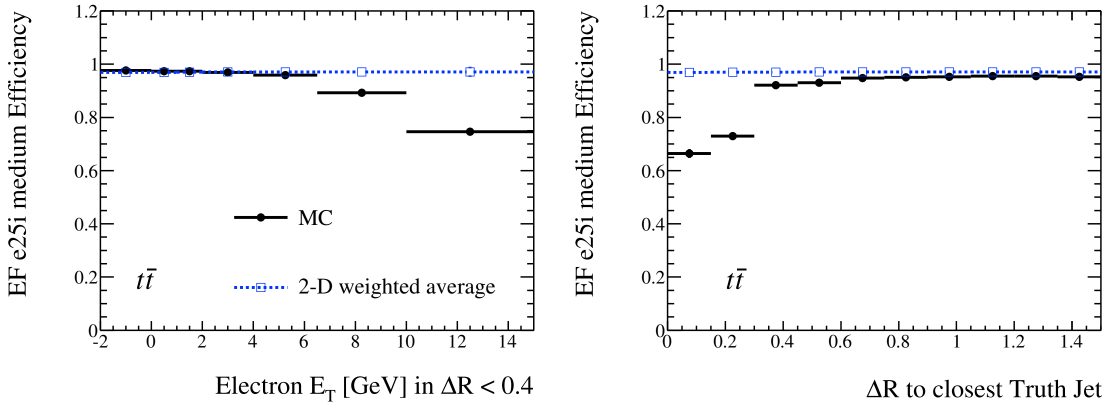

Figure 6.12: The weighted average of the `EF e25i medium` efficiency in $E_T \times |\eta|$ (blue open squares) applied to $t\bar{t}$ as a function of $E_T cone$ (left) and of distance to the nearest truth jet (right), compared to MC efficiency (black circles). The errors shown on the right-hand plot, unlike previous Figures, only take into account errors on the $t\bar{t}$ electron distribution.

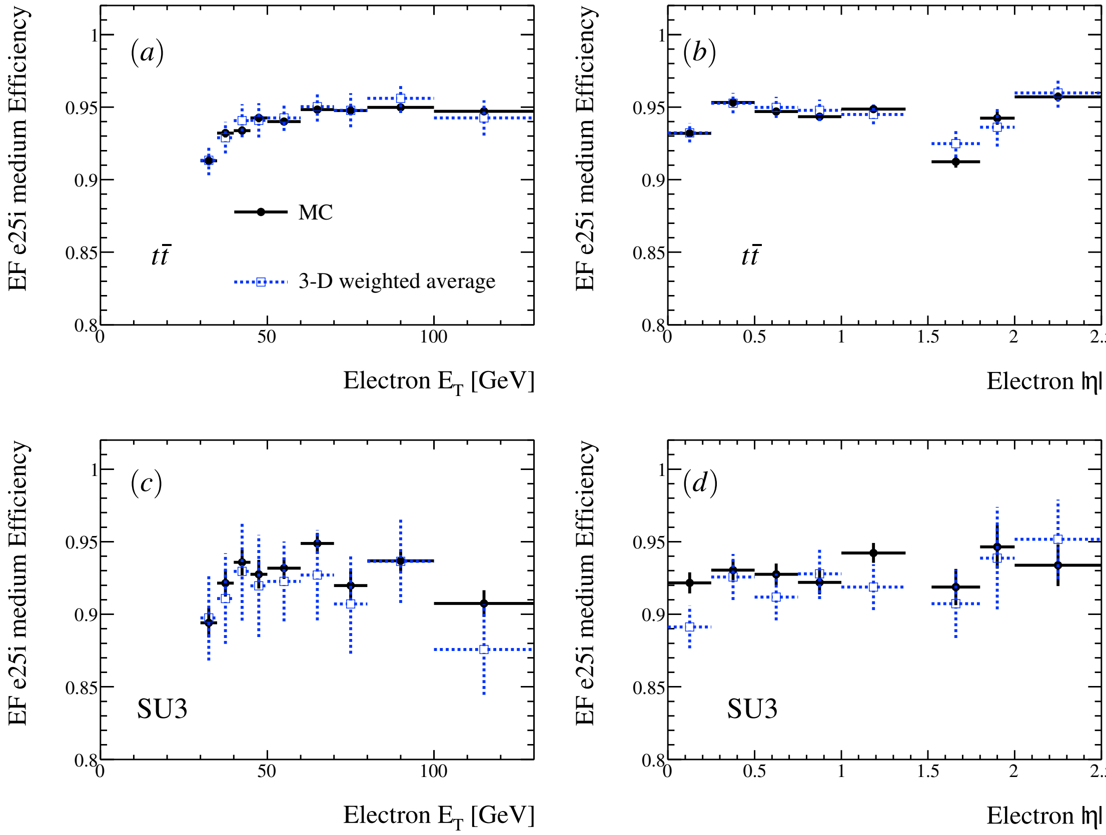

Figure 6.13: The results of using the 3-D Z→e^+e^- efficiency (blue open squares) in $E_T \times |\eta| \times E_T cone$ of `EF e25i medium` to produce weighted averages of efficiency in the $t\bar{t}$ ((a) and (b)) and SU3 ((c) and (d)) samples as compared to MC efficiency (black circles).

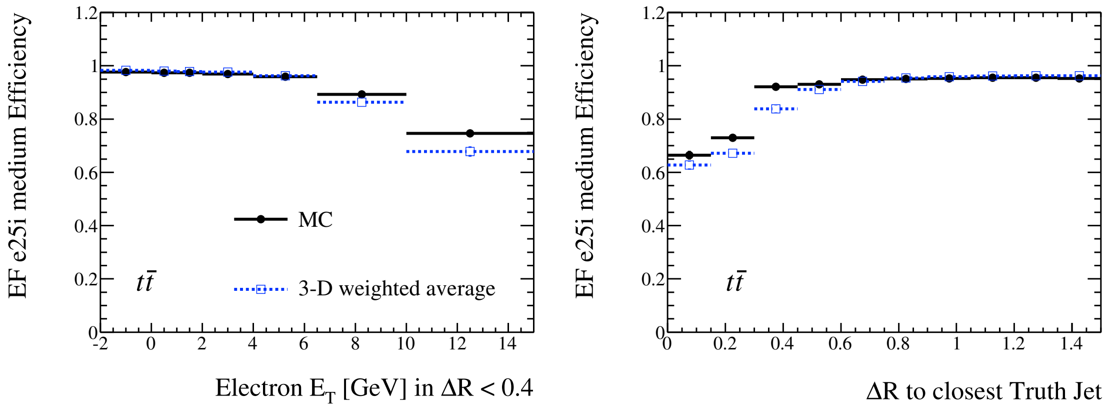

Figure 6.14: The weighted average of the `EF e25i medium` efficiency in $E_T \times |\eta| \times E_T cone$ (blue open squares) applied to $t\bar{t}$ as a function of $E_T cone$ (left) and of distance to the nearest truth jet (right), compared to MC efficiency (black circles). The errors shown on the right-hand plot, unlike previous Figures, only take into account errors on the $t\bar{t}$ electron distribution.

SU3 samples to construct a weighted average of efficiency, and the results compared to MC. The weighted and MC efficiencies as functions of E_T and $|\eta|$ are compared in Figure 6.11 for the $t\bar{t}$ and SU3 samples. In both cases the weighted efficiencies are seen to consistently over-estimate the MC. Therefore, it can be concluded that a 2-D measurement of efficiency is not providing a complete description of trigger efficiency in either the SU3 or the $t\bar{t}$ samples.

The discrepancies remaining after applying the 2-D weighting in the $t\bar{t}$ sample as a function of the isolation variables $E_T cone$ and distance to the nearest truth jet are shown in Figure 6.12. The efficiency as obtained from the weighting is seen to plateau at values close to 98%, whilst efficiencies as obtained from the MC shows the same fall in efficiency as a function of isolation as previously observed in Section 6.1.2.

To account for variation of trigger efficiency as a function of isolation, the efficiency measurement from $Z \rightarrow e^+e^-$ is extended to 3-D using eleven bins in E_T, eight bins in $|\eta|$ and nine bins in $E_T cone$. Again, the obtained efficiency is then applied to electrons in the $t\bar{t}$ and SU3 samples and the results compared to MC. The comparison between efficiencies obtained using this 3-D weighted average and those from MC is shown in Figure 6.13 for the $t\bar{t}$ and SU3 samples. It can be seen that, by also taking into account isolation, the weighted $Z \rightarrow e^+e^-$ efficiencies display a good level of agreement with the SUSY and $t\bar{t}$ MC across the E_T and $|\eta|$ ranges to within statistical errors. This comparison as functions of the isolation variables $E_T cone$ and distance to truth jets is shown in Figure 6.14 for the $t\bar{t}$ sample. Weighted trigger efficiency is now seen to vary as a function of these variables rather than being flat as for the 2-D method.

The trigger efficiency weighted in 3-D, although showing some deviation from MC expectations at high values of $E_T cone$, is seen to provide a good model of the MC trigger efficiency to within statistical errors. As was previously stated, $Z \rightarrow e^+e^-$ suffers from poor statistics in the high $E_T cone$ regime, due to the intrinsically isolated nature of these electrons. This results in higher errors in the measured $Z \rightarrow e^+e^-$ efficiencies in this region and hence higher errors on the weighted SUSY and $t\bar{t}$ results. The weighted $t\bar{t}$ efficiency average for all plateau electrons is seen to be 94.4±0.4%, which agrees well with the MC value of 94.3±0.1%. The same is true in SU3, where the weighted efficiency average for all plateau electrons is seen to be 91.6±1.1%, which agrees within errors with the MC value of 92.9±0.3%.

The results of repeating the measurement and weighting procedure using the unisolated trigger `EF e15 loose` are shown in Figure 6.15 for the $t\bar{t}$ sample. The comparison between trigger efficiency obtained by 3-D $Z \rightarrow e^+e^-$ efficiency and those obtained using the $t\bar{t}$ MC without further corrections is shown in the left-hand plot of Figure 6.15. This result is summarised in the right-hand plot of Figure 6.15 along with results obtained using measures of $Z \rightarrow e^+e^-$ efficiency

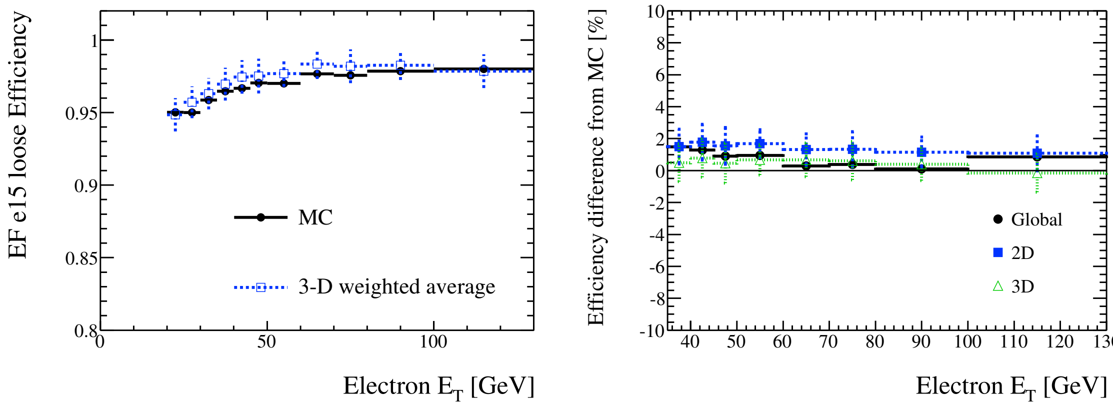

Figure 6.15: The `EF e15 loose` efficiencies in the $t\bar{t}$ sample (left). The weighted average produced using the 3-D $Z \rightarrow e^+e^-$ efficiency in $E_T \times |\eta| \times E_T cone$ (blue open squares) is compared to MC efficiencies (black circles). The efficiency difference between these methods (right).

Table 6.3: Trigger efficiencies in the plateau region (35 GeV $< E_T <$ 130 GeV) for prompt electrons, expressed in % as obtained from MC, and 2-D and 3-D weighted averages of $Z \rightarrow e^+e^-$ efficiency for samples $t\bar{t}$ and SU3.

Sample and method	`EF e25i medium` efficiency	`EF e15 loose` efficiency
$t\bar{t}$ Monte Carlo	94.3 ± 0.1	97.0 ± 0.1
$t\bar{t}$ 3-D weighted average	94.4 ± 0.4	97.5 ± 0.4
$t\bar{t}$ 2-D weighted average	97.1 ± 0.4	98.5 ± 0.4
SU3 Monte Carlo	92.9 ± 0.3	96.2 ± 0.2
SU3 3-D weighted average	91.6 ± 1.1	96.6 ± 1.1
SU3 2-D weighted average	97.1 ± 1.1	98.5 ± 1.1

in other dimensionalities as the efficiency difference between the weighted and MC results. As with unisolated triggers the 2-D $Z \rightarrow e^+e^-$ efficiency consistently overestimates the $t\bar{t}$ MC efficiency, although in this case the magnitude of the observed discrepancy is significantly smaller. The 3-D $Z \rightarrow e^+e^-$ efficiency, on the other-hand, is observed to provide a good description of the MC results. The final summary of results for isolated and non-isolated triggers is given in Table 6.3. These results indicate that a sample independent trigger efficiency measurement can be constructed in these three dimensions. Therefore efficiency in busy events can be measured from data, providing it is measured in 3-D.

6.3 Non-Prompt and Fake Electrons in SUSY Events

The efficiencies shown so far in this chapter only include electrons which have been matched to truth electrons forming part of the hard process. With real data it will not be be possible to perform such a match. This section will study the effects of removing the truth match and thus including *non-prompt* and *fake* electrons in the study of trigger efficiencies. A further section will then investigate the origins of these electrons in SUSY and $t\bar{t}$ events.

Objects reconstructed as electrons but to which no MC generator electron can be associated are fake electrons. The overall rate of fake electrons will depend on the structure and response of the detector as well as on the purity of offline selection criteria. Reconstructed electrons matched to true electrons that do not form part of the hard process are termed non-prompt electrons.

The definition of offline electrons used in this thesis was selected as it provides the required electron purity and background rejection factors for use in SUSY searches. Whilst this selection will reject the majority of backgrounds, it will not have 100% purity. Some of the objects identified in the offline reconstruction as electrons will, in fact, be jets that look like electrons, or non-prompt electrons that do not originate from the primary decay process.

6.3.1 Trigger Efficiency

This section will study the efficiency of the trigger to select any reconstructed electron in the SUSY and $t\bar{t}$ events. These studies use the same MC samples as the preceding sections of this chapter.

The `EF e25i medium` trigger efficiencies for all electrons in the SUSY and $t\bar{t}$ samples is shown in Figure 6.16 along with the prompt electrons from the $Z\rightarrow e^+e^-$ process. The differences in efficiency between the SUSY and $t\bar{t}$ samples and $Z\rightarrow e^+e^-$ is shown in Figure 6.17. Table 6.4 summarises these efficiencies as global numbers. Again, as with truth matched electrons, the efficiencies seen in the SUSY and $t\bar{t}$ samples are consistently lower than those for the $Z\rightarrow e^+e^-$ process. The turn-on behaviour for all samples is observed to be significantly slower than previously seen for only prompt electrons in Figure 6.2, and the efficiency plateau is now not established until higher values of E_T. Overall efficiency in the SU3 sample is now observed to be $\sim$87%, which is around 10% lower than $Z\rightarrow e^+e^-$. This represents almost double the discrepancy as was seen for prompt electrons only. Similarly, the differences between $Z\rightarrow e^+e^-$ and $t\bar{t}$ and SU4 have increased, to $\sim$5% and $\sim$7% respectively. The majority of this difference is seen to be due to the L1 trigger, with the HLT efficiencies observed to be roughly equivalent (to within 1 %) between samples when normalised to the appropriate preceding levels.

The `EF e25i medium` MC efficiency and weighted efficiency average produced using the $Z\rightarrow e^+e^-$ efficiency in 3-D for all electrons in the $t\bar{t}$ sample are compared in the left-hand plot of

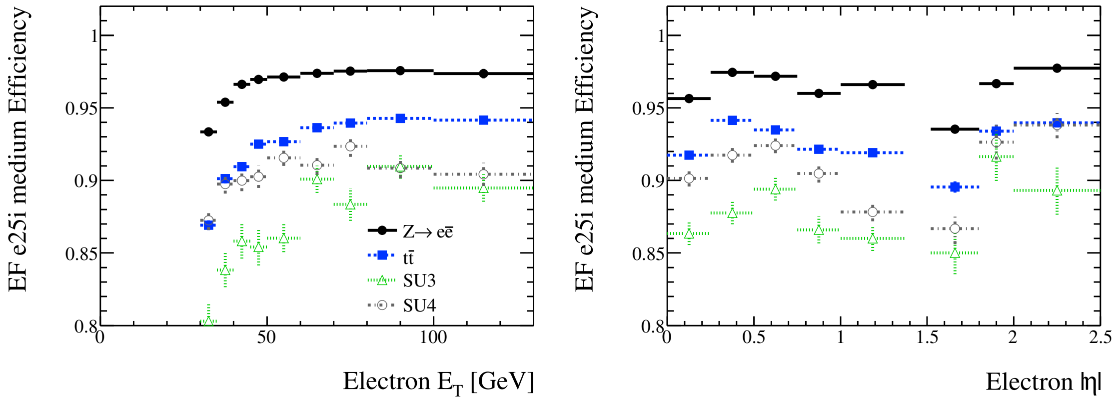

Figure 6.16: The `EF e25i medium` efficiency for all offline electrons as a function of E_T (left) and $|\eta|$ in MC samples of Z$\rightarrow e^+e^-$ (black circles), $t\bar{t}$ (blue squares), SU3 (green open triangles) and SU4 (grey open circles).

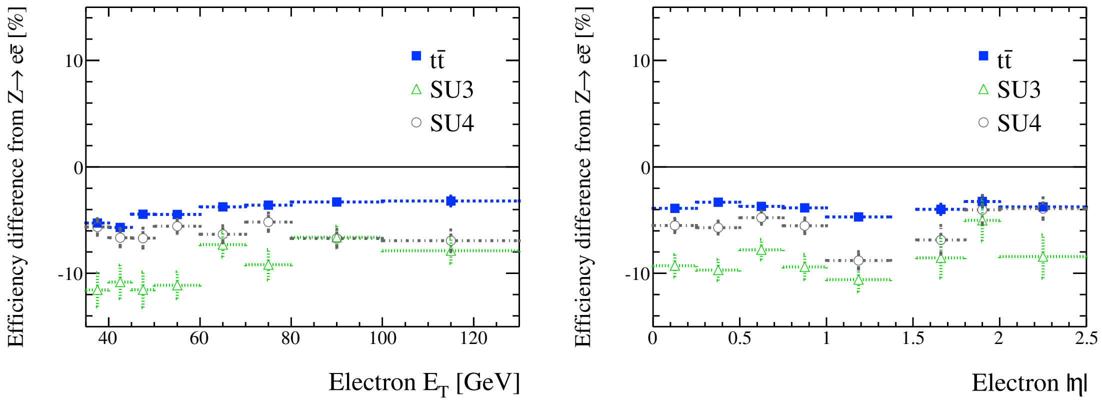

Figure 6.17: The difference in `EF e25i medium` efficiency between the Z$\rightarrow e^+e^-$ sample and $t\bar{t}$ (blue squares), SU3 (green open triangles) and SU4 (grey open circles), as a function of offline (left) E_T and (right) $|\eta|$. The $|\eta|$ efficiencies are shown only for electrons with $E_T > 35$ GeV.

Table 6.4: `e25i medium` trigger efficiencies in the plateau region ($E_T > 35$ GeV) for all reconstructed electrons, expressed in %, as obtained from MC.

Sample	L1 Efficiency	L2 Efficiency	EF Efficiency
$t\bar{t}$ (cumulative)	95.01 ± 0.08	93.35 ± 0.09	92.55 ± 0.09
$t\bar{t}$ (relative to above level)		98.25 ± 0.05	99.14 ± 0.03
SU3 (cumulative)	91.54 ± 0.29	88.64 ± 0.33	87.28 ± 0.35
SU3 (relative to above level)		96.83 ± 0.19	98.47 ± 0.14
SU4 (cumulative)	92.62 ± 0.21	90.82 ± 0.23	90.48 ± 0.24
SU4 (relative to above level)		98.05 ± 0.12	99.63 ± 0.05

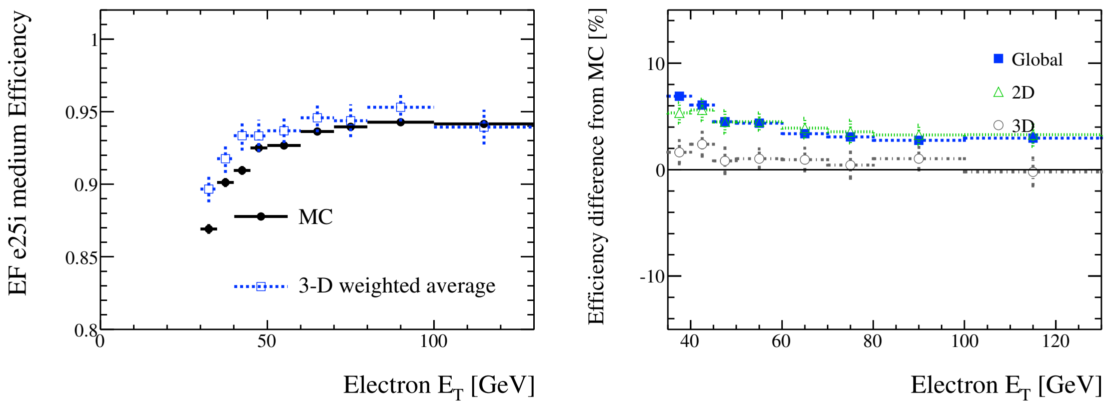

Figure 6.18: The `EF e25i medium` efficiency for all electrons in the $t\bar{t}$ sample (left), as a weighted average of the $Z \rightarrow e^+e^-$ efficiency measured in $E_T \times |\eta| \times E_T cone$ (blue open squares) and the MC efficiency (black circles). The fractional efficiency difference between `EF e25i medium` weighted average and MC efficiencies (right).

Table 6.5: Trigger efficiencies in the plateau regions for all electrons, including non-prompt and fake electrons, expressed in % as obtain from MC, and 2-D and 3-D weighted averages of $Z \rightarrow e^+e^-$ efficiency for samples $t\bar{t}$ and SU3.

Sample and method	`EF e25i medium` efficiency	`EF e15 loose` efficiency
$t\bar{t}$ Monte Carlo	92.8 ± 0.1	95.6 ± 0.1
$t\bar{t}$ 3-D weighted average	93.8 ± 0.3	97.0 ± 0.3
$t\bar{t}$ 2-D weighted average	97.0 ± 0.3	98.4 ± 0.3
SU3 Monte Carlo	87.6 ± 0.4	92.2 ± 0.3
SU3 3-D weighted average	90.6 ± 1.0	96.1 ± 1.0
SU3 2-D weighted average	97.1 ± 1.0	98.5 ± 1.0

Figure 6.18. It is observed that the 3-D Z→e^+e^- efficiency consistently over-estimates the MC result by $\sim$ 1% across the E$_T$ spectrum. The differences between the MC efficiency and weighted average produced using for global, 2-D and 3-D measures of Z→e^+e^- efficiency are shown in the right-hand plot of Figure 6.18. Both global and 2-D Z→e^+e^- efficiencies are seen to over-estimate the MC result by $\sim$ 4% across the spectrum, whilst a 3-D efficiency reduces, but does not entirely remove, the observed discrepancy. Table 6.5 summarises these results along with those obtained for the SU3 sample and using the unisolated `EF e15 loose` trigger. In the SU3 sample it is seen that the 2-D `EF e25i medium` Z→e^+e^- efficiency over estimates the trigger efficiency by $\sim$ 10% and that by extending this efficiency measure to 3-D this discrepancy is reduced to $\sim$ 3%. Comparable results are observed for `EF e15 loose` for both samples, although the magnitude of the observed discrepancies between SUSY and $t\bar{t}$ MC and the weighted average based on Z→e^+e^- efficiency is reduced compared to the isolated trigger.

Clearly, a method to account for the presence of fake electrons will have to be developed in order for any estimation of trigger efficiency to be truly sample independent.

6.3.2 The Origins of Non-Prompt Electrons

It is important to be able to understand the contribution of non-prompt and fake electrons in order to be able quantify the impact these will have on the trigger efficiency. This section will investigate the origins of fake electrons in SUSY and $t\bar{t}$ events and the efficiency of these electrons to pass the `EF e20i loose` trigger. The datasets studied in this section have been simulated at a reduced centre of mass energy of 10 TeV compared to the previous studies in this chapter. In addition they have been reconstructed using a newer version of the ATLAS software. Consequently the optimisation of the offline selection criteria is slightly different to the previous section and a different trigger must be studied. Details of the samples studied can be found in Appendix A.2.

The origin of a reconstructed electron is determined from MC truth record based on the closest truth electron and the record of its production chain. The classification scheme used here is of the form of the standard ATLAS methods detailed in [82]. Truth electrons can either originate from prompt processes or from non-prompt processes such as photon conversions, decays of b/c-quarks or other hadronic decays. Those electrons identified as originating from photons are further classified based on the origin of the photon. If the photon was emitted from an electron then the origin of this electron is considered if it is within ΔR <0.1 of the reconstructed electron of interest. The origin of fake electrons is determined from the closest truth particle.

An overview of the origins of all reconstructed electrons in the SU4 and $t\bar{t}$ samples is shown in Table 6.6. In both cases the majority of electrons are seen to originate from prompt processes,

Table 6.6: The origins of fakes in the SU4 and $t\bar{t}$ samples in 100 pb^{-1} of data for an LHC centre of mass energy of 10 TeV (~17,000 SU4 events and ~21,700 $t\bar{t}$ events).

Electron Origin	Number of electrons (% of all electrons)			
	SU4		$t\bar{t}$	
Prompt	2,415 ± 16	(82.4)	5,628 ± 11	(83.5)
SUSY	1,478 ± 12	(50.4)	–	–
EW boson	711 ± 8	(24.2)	5,107 ± 11	(75.8)
τ-lepton	225 ± 5	(7.7)	521 ± 3	(7.7)
Non-prompt	480 ± 7	(16.4)	1,066 ± 5	(15.8)
γ-conversions (from prompt $e^{\pm}$)	251 ± 5	(8.6)	767 ± 4	(11.4)
γ-conversions (from non-prompt $e^{\pm}$)	85 ± 3	(2.9)	104 ± 2	(1.5)
b/*c*-quarks	121 ± 3	(4.1)	166 ± 2	(2.5)
hadrons	23 ± 2	(0.8)	30 ± 1	(0.5)
Fakes	36 ± 2	(1.2)	42 ± 1	(0.6)
hadrons	34 ± 2	(1.2)	30 ± 1	(0.5)
μ-lepton	2 ± 0	(0.1)	0 ± 0	(0)
undetermined	1 ± 0	(0.0)	1 ± 0	(0.0)
Total	2,931 ± 17		6,739 ± 12	

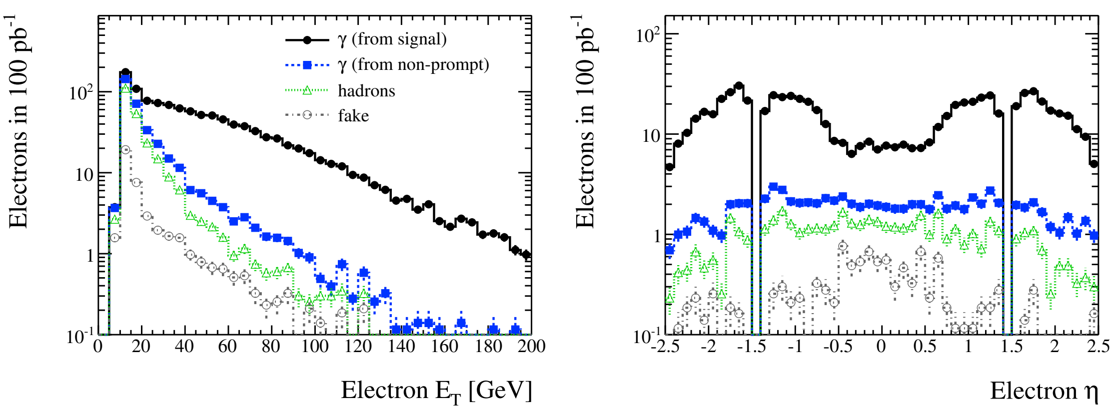

Figure 6.19: The E_T and η distributions of the non-prompt and fake electrons in the $t\bar{t}$ sample. For clarity these distributions are shown cumulatively.

Table 6.7: The efficiency of the `EF e20i loose` trigger to select electrons divided by the origin of the electrons.

Electron Origin	`EF e20i loose` efficiency	
	SU4	$t\bar{t}$
Prompt electrons	97.7 ± 0.1	98.7 ± 0.0
γ (from prompt electrons)	96.5 ± 0.4	98.0 ± 0.1
γ (from non-prompt electrons)	80.6 ± 2.4	84.0 ± 0.9
non-γ, non-prompt electrons	75.6 ± 3.0	76.8 ± 1.1
fakes	75.4 ± 5.2	80.3 ± 1.8

constituting around 82% of the total number of electrons. Around 16% of electrons are of non-prompt origin, and the remaining 1% are fakes. Non-prompt electrons are observed to mostly come from photon conversions with reduced contributions from b/c-quarks and other hadrons. Fake electrons primarily result from hadrons being reconstructed as electrons, although a small contribution is observed to come from muons. The reduced overall numbers of electrons expected in 100 pb^{-1} compared to the earlier studies is due to the decreased SU4 and $t\bar{t}$ cross sections at 10 TeV relative to 14 TeV.

The cumulative E_T and η distributions of the non-prompt and fake electrons in the $t\bar{t}$ sample are shown in Figure 6.19. The dominant contribution of non-prompt and fake electrons is seen to be peaked at high η ranges in the barrel and around the transition region between the barrel and the endcaps.

In the context of the studies in this thesis the primary reason for studying non-prompt and fake electrons is that they exhibit different trigger efficiencies from prompt electrons. The global `EF e20i loose` trigger efficiencies of electrons in the SU4 and $t\bar{t}$ samples subdivided by the origin of the electrons and shown in Table 6.7. The trigger studied, `EF e20i loose`, is a trigger intended for studies of L1 isolation in the early data taking phases when instantaneous luminosity is $\sim 10^{31}\ cm^{-2}s^{-1}$. Prompt electrons are selected with very high efficiency of around 98% in both samples. Similarly, electrons originating from photon conversions where the photon is radiated from a prompt electron are selected with around 97-98% efficiency. However, electrons originating from conversions from non-prompt sources and fake electrons all exhibit significantly reduced trigger efficiencies of between 75% and 84%.

The similarity observed in trigger efficiency between electrons from photons from prompt electrons and for prompt electrons indicates that, from a trigger efficiency point of view, these electrons can considered together. In many cases it may well be that the reconstructed electron

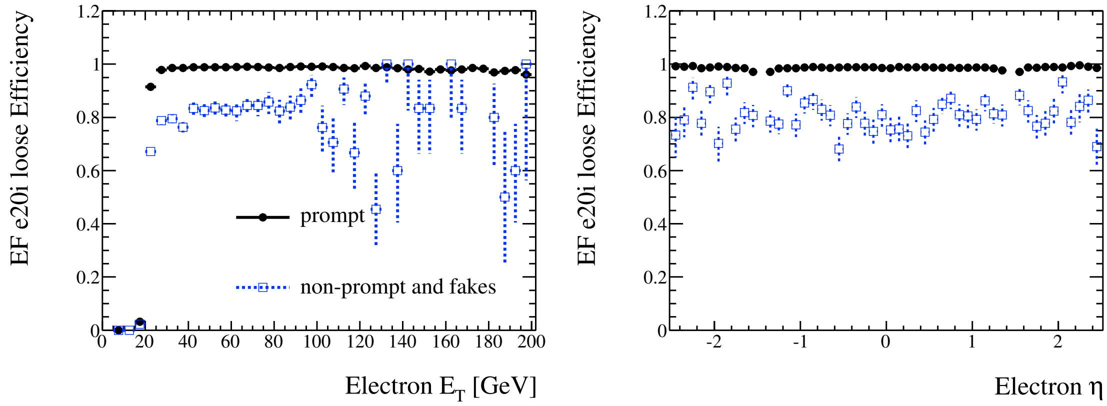

Figure 6.20: The efficiency of the `EF e20i loose` trigger to select prompt and non-prompt or fake electrons in the $t\bar{t}$ sample.

does, indeed, originate directly from a prompt process, but the closest truth particle to the reconstructed electron happens to be an electron produced during the showering of the original prompt electron. Henceforth electrons originating from photons from prompt processes will be considered to be prompt electrons.

The `EF e20i loose` trigger efficiencies for both prompt electrons and for non-prompt and fake electrons across the reconstructed electron E_T and η ranges are shown in Figure 6.20. Similarly to the results presented in Table 6.7 trigger efficiency is seen to be very high for prompt electrons. In addition, very little structure is seen in the patterns of trigger efficiency in either the E_T or η ranges. This represents an improvement from the triggers studied in previous chapters. This improvement is partly due to the looser selection applied by `e20i loose` and partly due to a harmonisation between the trigger and offline electron selection cuts since the previous studies. This figure clearly shows the the trigger efficiency for fake and non-prompt electrons is systematically reduced from that observed for prompt electrons across the studied kinematic ranges. Therefore in order for results such as those expected by the TP method, which have been shown to be applicable to prompt electrons, to be representative of those seen in samples containing additional electrons, then the contribution of these additional electrons will need to be established.

Some preliminary studies, not included in this thesis, have indicated that it is possible to determine the contribution of fake and non-prompt electrons within a sample based on the jet composition of this sample. This combined with a measure of the trigger efficiency of this type of offline electron would enable the contribution to overall trigger efficiency from fake and non-prompt electrons to be quantified. However, such a method would require more extensive study before it would be ready for use on actual data.

6.4 Conclusions

It has been shown that the overall trigger efficiency for prompt electrons is above 90% in both the SUSY and $t\bar{t}$ samples. This efficiency is up to 5% less than that observed in the previous chapter for electrons in Z$\rightarrow e^+e^-$ events when viewed as an overall number or as a 1-D function. The origin of this difference has been attributed to the increased hadronic actively in both SUSY and $t\bar{t}$ events resulting in a decrease in trigger efficiency at L1. Trigger efficiencies were shown to be compatible between samples when compared in a 3-D space comprised of E_T, $|\eta|$ and isolation as this takes into account the varying degrees of isolation in the different samples. It was further demonstrated that a weighted average of the 3-D Z$\rightarrow e^+e^-$ efficiency in terms of kinematics and particle isolation reproduces the MC efficiencies in other samples well. The complementary studies in Section 5.3 have previously shown that the Z$\rightarrow e^+e^-$ efficiency can be determined from data. This means that trigger efficiency can be determined from data in a complete and sample-independent manner for prompt electrons. A caveat to this method is that the contributions of fake and non-prompt electrons have been ignored. The overall trigger efficiency for all electrons, including non-prompt and fake electrons, in the SUSY and $t\bar{t}$ samples is seen to be up to 10% less than that observed for electrons in Z$\rightarrow e^+e^-$ samples. This is due to the increased number of fake and non-prompt electrons in these samples and the lower trigger efficiencies associated with these types of electrons. Without the removal of fake electrons a 3-D weighted average of the Z$\rightarrow e^+e^-$ trigger efficiency still provides a more complete description than a 1-D or 2-D average. However, it is then no longer in full agreement with the MC result. The removal of fakes via the use of MC generator information is not something that could be done with data. Instead the fake rate will have to be estimated based on sample composition and appropriate correction factors deduced and applied.

Chapter 7

Leptonic Triggers for SUSY Parameter Space Scans

This chapter studies the efficiency of the trigger to select leptons in a large number of SUSY points across scans, or grids, of mSUGRA parameter space simulated using ATLFAST-II. This study aims to determine if the trigger selection is appropriate for a large variety of SUSY models.

The first section of this chapter introduces electrons and muons as reconstructed by ATLFAST-II at the SU4 SUSY benchmark point. This is followed by a study of the application of weighted averages of leptonic trigger efficiency, which are then used to evaluate the leptonic trigger efficiency at each of the SUSY grid points. Finally, triggering for a representative SUSY search channel, the trilepton channel, is studied in more detail.

The samples studied in this chapter have been simulated and reconstructed using a later version of the ATLAS software than the bulk of the preceding studies. As a consequence, slightly different optimisations of both the offline and the trigger selection are used. The events studied in this chapter are simulated at a reduced LHC centre of mass energy of 10 TeV, inline with the perceived LHC operational schedule at the time of writing.

7.1 Leptons in ATLFAST-II

Detailed studies of large areas of SUSY parameter space require the simulation of a large number of SUSY points. However, due to limited computing resources, it is not feasible to simulate these using full simulation and yet still produce meaningful event statistics for each point. Therefore the ATLAS strategy in this context is to use the ATLFAST-II fast simulation instead. ATLFAST-II (as previously introduced in Section 4.1.2) provides a factor of ten improvement in computing time relative to full simulation; although this gain is necessarily arrived at by a reduction in the completeness of the detector simulation. In order to have confidence in the validity of ATLFAST-II studies based on leptons, it is important to establish that ATLFAST-II is modelling these leptons well. This section presents a brief comparison of leptons from the SU4 SUSY benchmark point sample as simulated by ATLFAST-II and by full simulation. A more complete study of ATLFAST-II can be found in [73].

Table 7.1: A comparison of the numbers of lepton reconstructed within full simulation and ATLFAST-II simulations of an SU4 sample. These numbers are weighted to an integrated luminosity of 100 pb^{-1}.

Lepton selection	Full simulation	ATLFAST-II
Offline electrons	2,640 $\pm$ 30	2,620 $\pm$ 15
Fraction which are prompt	91.3 %	93.0 %
Fraction which are fake or non-prompt	8.7 %	7.0 %
Offline muons	2,620 $\pm$ 30	2,680 $\pm$ 15
Fraction which are prompt	97.4 %	97.5 %
Fraction which are fake or non-prompt	2.6 %	2.5 %

The overall number of leptons reconstructed within SU4 samples simulated by ATLFAST-II and full simulation weighted to an integrated luminosity of 100pb^{-1} are compared in Table 7.1. The total number of offline electrons within each sample is seen to be in agreement to within the statistical errors. Although the fraction of these electrons classified by their truth origin to be fake or non-prompt is observed to be slightly decreased in the ATLFAST-II sample. Previous studies have indicated that at low E_T ATLFAST-II overestimates the reconstruction efficiency for prompt electrons and, at the same time, underestimates the rate of fake electrons arising from jets. The E_T, η and $\text{E}_T$cone distributions of prompt electrons identified within each of the samples are compared in Figure 7.1. The familiar electron E_T and η distributions are seen to show complete agreement between full and fast simulation. However, some discrepancy is observed between the $\text{E}_T$cone present in each sample, with the ATLFAST-II distribution shifted towards slightly higher values. This discrepancy is not unexpected as $\text{E}_T$cone is a calorimeter based isolation variable, and it is the calorimeter simulation which ATLFAST-II reduces in complexity. Overall it is fair to say that good agreement is seen in the description of electrons by ATLFAST-II and full simulation.

Up to this point the studies in this thesis have focused exclusively on electrons. However, muons are also important to SUSY searches. This chapter expands on the studies of the previous chapters to include studies of muons within SUSY events. As muons are not the main topic of this thesis a detailed treatment is omitted. Muons are reconstructed using the standard muon reconstruction procedure as introduced in Section 4.2.2. Table 7.1 summarises the total number of

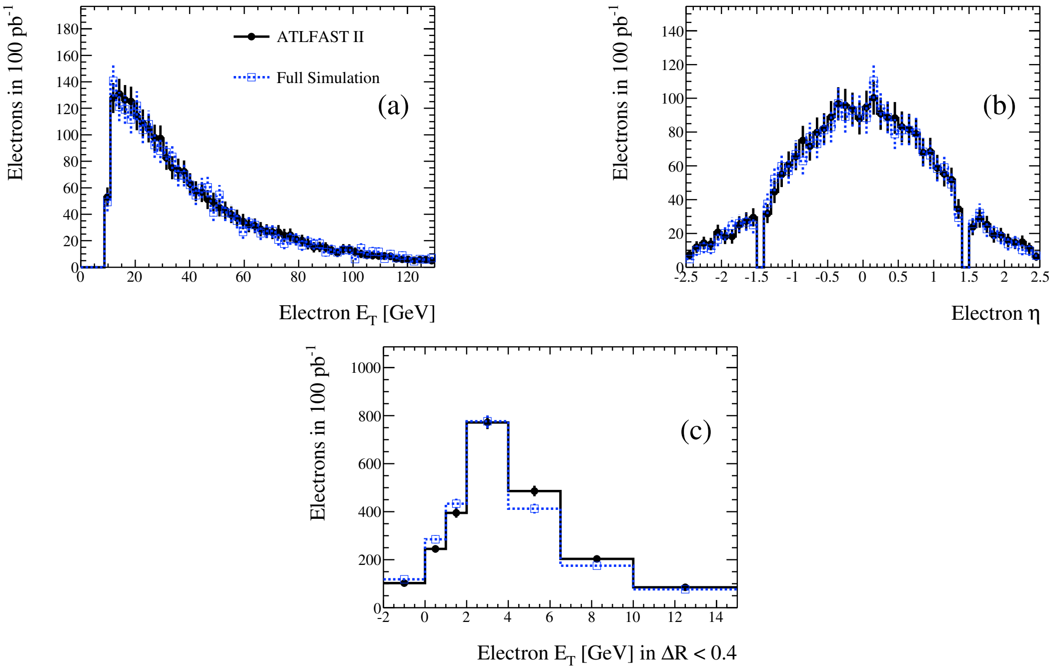

Figure 7.1: Comparisons of the (a) E_T , (b) η and (c) $E_T$cone of electrons in full simulation (blue open squares) and ATLFAST-II (black circles) in an SU4 sample.

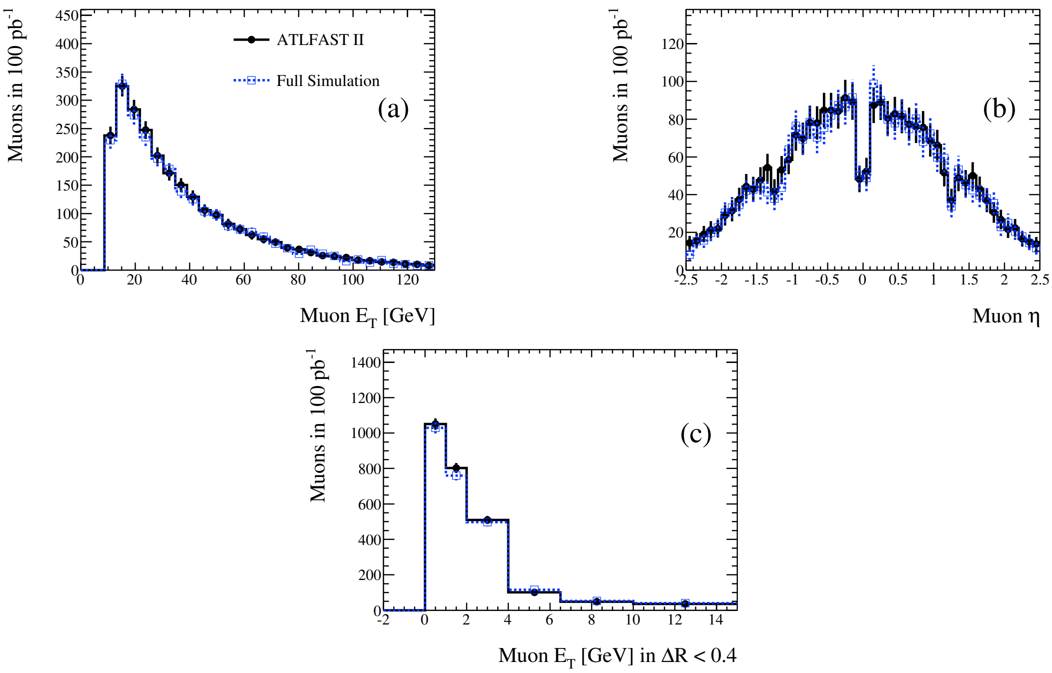

Figure 7.2: Comparisons of the (a) E_T , (b) η and (c) $E_T$cone of muons in full simulation (blue open squares) and ATLFAST-II (black circles) in an SU4 sample.

muons reconstructed in each sample. The studies in [73] have shown that although ATLFAST-II provides a good description of the reconstruction efficiency of muons. Again, the rate of muons arising due to jets is underestimated. This leads to an overall underestimation of the number of muons when compared to full simulation. The muon selection criteria applied in this thesis serves to remove this discrepancy by rejecting the non-isolated muons present in the full simulation due to jets. Overall, slightly more muons are seen to be present in the ATLFAST-II sample than in the full simulation sample. The proportions of muons identified to be of fake or non-prompt origin is seen to be reduced relative to the corresponding electron proportions and to be in agreement between both simulation methods. The E_T, η and $E_T$cone distributions of reconstructed prompt muons in full and ATLFAST-II simulations are compared in Figure 7.2. All studied kinematical variables are observed to be in good agreement between full and fast simulations.

Detailed studies of the ATLFAST-II performance are beyond the scope of this thesis. Previous studies, such as [73], have validated ATLFAST-II extensively against full simulation and shown that it provides a very good description of leptons within ATLAS, which is confirmed by the brief comparison presented here.

7.1.1 Weighted Averages of Leptonic Trigger Efficiencies

ATLFAST-II lacks any simulation of the trigger system. This renders the direct extraction of MC trigger efficiency using fast simulation impossible. However, it is still desirable to know how the trigger will perform in ATLFAST-II events. This section will study the application of the weighted efficiency average methods developed in the previous chapters to the prompt leptons identified within ATLFAST-II samples.

Electrons

As in the previous chapter, electron trigger efficiency is estimated using a 3-D measurement of efficiency in fully simulated $Z \rightarrow e^+e^-$ events. This is then applied to all the prompt electrons identified in both ATLFAST-II and full simulation events to produce a weighted average of efficiency. The weighted efficiencies of the `EF e25i medium` trigger as functions of electron E_T and $|\eta|$, and the full simulation MC efficiencies are compared in Figure 7.3. The global efficiencies obtained from the three methods are summarised in Table 7.2. As expected, the weighted full simulation efficiency is seen to be in agreement, to within statistical errors, with the MC result. The central value of the ATLFAST-II weighted efficiency is seen to be around 1.5% lower than the full simulation MC result and 1% lower than the full simulation weighted result. This reduction in efficiency is most likely to be due to the shift towards higher values of $E_T$cone observed in

Table 7.2: Integrated trigger efficiencies in the plateau region (35 GeV $< E_T <$ 130 GeV) for prompt electrons in SU4 events, expressed in % as obtain from fully simulated MC and 3-D weighted efficiency of both fully simulated and ATLFAST-II samples.

Sample and method	`EF e25i medium` efficiency
SU4 full simulation Monte Carlo	94.5 ± 0.4
SU4 full simulation 3-D weighted average	93.8 ± 1.8
SU4 ATLFAST-II 3-D weighted average	92.9 ± 0.9

the ATLFAST-II sample. However, the large error margins mean that these results are consistent between the weighted full and fast simulation.

Muons

Muon triggers were previously introduced in Section 3.2.4. The lower background rates of muons, when compared to electrons, and the nature of this background, means that the muon trigger can sustain a lower energy thresholds, not require calorimeter isolation, and yet still maintain an acceptable pass rate. This section will study the efficiency of the `EF mu20` trigger to select prompt muons in fully simulated SU4, $t\bar{t}$ and $Z \rightarrow \mu^+\mu^-$ samples, and use the results to construct a weighted average of trigger efficiency analogous to that used for electron triggers previously. Similarly to the electron trigger `EF e25i medium`, the muon trigger `EF mu20` is intended for use at instantaneous luminosities of 10^{32} cm^{-2}s^{-1} and above.

The `EF mu20` trigger efficiency in the $Z \rightarrow \mu^+\mu^-$, $t\bar{t}$ and SU4 samples as functions of the muon E_T and η is shown in Figure 7.4. The differential selection efficiencies within each sample are seen

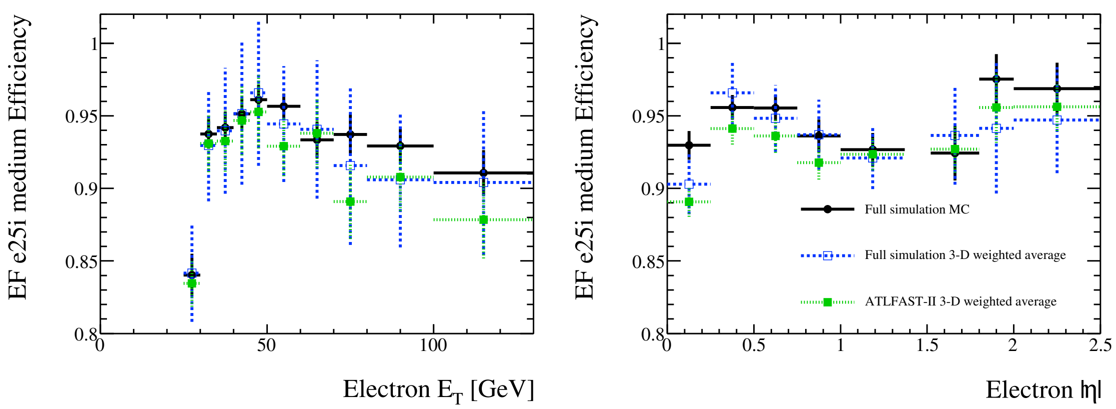

Figure 7.3: The weighted average of the `EF e25i medium` efficiency in $E_T \times |\eta| \times E_T cone$ applied to full (blue open squares) and ATLFAST-II (green triangles) simulations of SU4 events, compared against the full simulation MC efficiency (black circles).

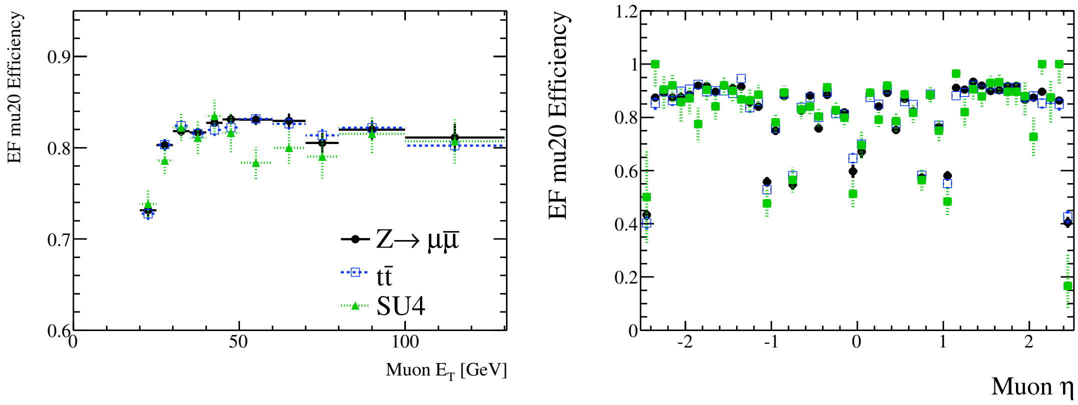

Figure 7.4: The `EF mu20` trigger efficiency in fully simulated samples of $Z\to\mu^+\mu^-$(black circles), $t\bar{t}$ (blue open squares) and SU4 (green triangles) as a function of muon E_T (left) and η (right).

to be in relatively good agreement. Integrated efficiencies are summarised in Table 7.3. For muons in the $t\bar{t}$ and $Z\to\mu^+\mu^-$samples, efficiency is seen to be around 82%, and is in good agreement between samples. For muons within the SU4 sample, the equivalent efficiency is observed to be marginally lower (by about 1%). The lower efficiency of the muon trigger, compared to the electron trigger arises due to to losses in the L1 acceptance from incomplete or degraded trigger chamber coverage. Details of the efficiency of the muon trigger can be found in [59]. Overall the muon trigger efficiency for both muons in $Z\to\mu^+\mu^-$events and in SUSY and $t\bar{t}$ events is seen to be high.

Unlike the `e25i medium` electron trigger, `mu20` does not apply calorimeter isolation requirements to the selected muons. This results in efficiency that is not observed to decrease when selecting muons in busy environments, leading to relatively good agreement in the observed overall trigger efficiencies in each of the studied samples. This lack of dependence on isolation means that the measure of muon trigger efficiency used to construct the weighted average in other events need not include an isolation dimension. To confirm this, a $Z\to\mu^+\mu^-$sample is used to construct a 2-D measure of trigger efficiency in $E_T \times |\eta|$. This is then applied to all muons in full and ATLFAST-II simulations of SU4 events to be contrasted with the MC trigger efficiency in the full

Table 7.3: Integrated `EF mu20` trigger efficiencies in the plateau region (E_T > 30 GeV), expressed in %, as obtained from full simulation MC.

Sample	`EF mu20` efficiency
$Z\to\mu^+\mu^-$	82.3 ± 0.2
$t\bar{t}$	82.1 ± 0.2
SU4	81.0 ± 0.6

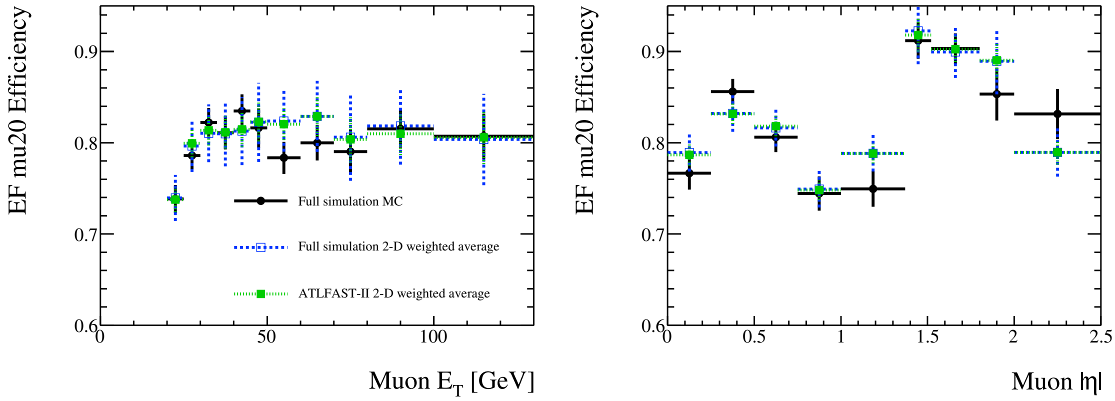

Figure 7.5: The weighted average of the `EF mu20` efficiency (blue open squares) constructed from a 2-D $Z \rightarrow e^+e^-$ efficiency measurement in $E_T \times |\eta|$ applied to full (blue open squares) and ATLFAST-II (green triangles) simulations of SU4 events, compared against the full simulation MC efficiency (black circles).

Table 7.4: Trigger efficiencies in the plateau region (30 GeV $< E_T <$ 130 GeV) for prompt muons, expressed in % as obtain from MC and 2-D weighted efficiency for samples $t\bar{t}$ and SU4.

Sample and method	`EF mu20` efficiency
SU4 full simulation Monte Carlo	80.9 ± 0.7
SU4 full simulation 2-D weighted average	81.6 ± 1.4
SU4 ATLFAST-II 2-D weighted average	81.5 ± 0.7

simulation sample. This comparison between the `EF mu20` MC efficiency and the 2-D weighted efficiency constructed from the full simulation and ATLFAST-II samples is shown in Figure 7.5. As expected, the weighted full simulation efficiency is seen to agree with the MC result. Furthermore, the weighted ATLFAST-II efficiency is seen to agree with both the weighted full simulation and MC efficiencies. The global efficiencies as obtained from these three methods are summarised in Table 7.4.

7.2 SUSY Parameter Space Scans

The previous studies in this thesis have shown that leptons at the SU3 and SU4 SUSY benchmark points are selected with a high efficiency by the lepton trigger. This section will investigate if this is the case over the wider range of SUSY parameter space. In particular, studies will focus on two planes of m_0 by $m_{1/2}$ parameter space, as introduced in Section 1.2.5. These planes are: the ($\tan\beta = 10$, $A_0 = 0$, $\mu > 0$) plane, and the ($\tan\beta = 50$, $A_0 = 400$, $\mu > 0$) plane.

The kinematics of leptons produced at each SUSY point are expected to vary depending on the phenomenology of each point. The mean number of reconstructed prompt leptons (i.e. electrons and muons) per event for each point in the two planes is shown in Figure 7.6. Similarly, the mean prompt lepton E_T and $\mathrm{E}_T$cone at each point are shown in Figures 7.7 and 7.8 respectively. The mean number of leptons per event is seen to be close to 0.3 at each grid point in both grids, although this is typically reduced at very low values of $m_{1/2}$ and increased in other regions. The mean lepton E_T is seen to generally increase with increasing $m_{1/2}$, and to be somewhat reduced at higher values of m_0. Likewise, a similar pattern is seen in the mean lepton $\mathrm{E}_T$cone.

7.2.1 Weighted Average Trigger Efficiencies

In order to extract a measure of the leptonic trigger efficiency at each grid point, the trigger response is constructed as a weighted average of the full simulation $Z \rightarrow \ell^+\ell^-$efficiency based upon the kinematics of the leptons present. Similarly to previous studies, these are based on a 3-D weighted average in $E_T \times |\eta| \times E_T cone$ for electrons, and a 2-D weighted average in $E_T \times |\eta|$ for muons.

The weighted average `EF e25i medium` efficiency for all prompt electrons at each grid point is shown in Figure 7.9. The efficiency is seen to increase from around 30% to around 80% with increasing m_0 and $m_{1/2}$. Relatively low efficiencies are seen at high values m_0 and $m_{1/2}$ and, in the tan $\beta = 10$ grid, at low m_0 for all $m_{1/2}$. The highest efficiencies are concentrated in the moderate m_0 region for high $m_{1/2}$. Similarly, the efficiency for only those electrons with $E_T > 35$ GeV is shown in Figure 7.10. This is seen to be around 90% and consistent for all grid points, indicating that the observed losses in efficiency seen previously for all electrons are due to the contributions of low E_T electrons, rather than intrinsic trigger inefficiencies. This result is further supported as the efficiency losses observed in Figure 7.9 are inline with the observed lepton E_T distribution shown in Figure 7.7.

Similarly, the weighted average `EF mu20` efficiency for prompt muons at each grid point is shown in Figure 7.11 and the efficiency for only those muons with $E_T > 30$ GeV is shown in Figure 7.12. A pattern comparable to that for electrons is observed, with the efficiency for all muons increasing with increasing m_0 and $m_{1/2}$. In this case, from around 20% to around 70%. The efficiency for plateau muons is observed to be consistently around 80% for all grid points.

These results indicate that the leptonic triggers will perform well when selecting leptons in the efficiency plateau regions, regardless of the SUSY scenario. However, drops in efficiency are observed inline with the observed mean lepton E_T and can lead to low average selection efficiencies, especially in the low SUSY mass ranges where the majority of leptons are soft. Generally it is considered undesirable to implement a trigger selection that has a higher E_T threshold than the offline object selection. However, this is unavoidable in cases where analyses are used to study

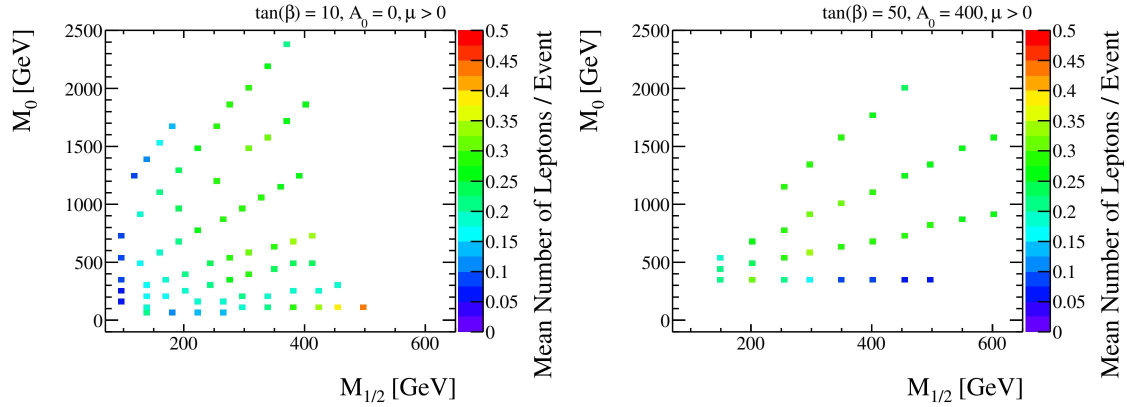

Figure 7.6: The mean number of reconstructed Leptons per event.

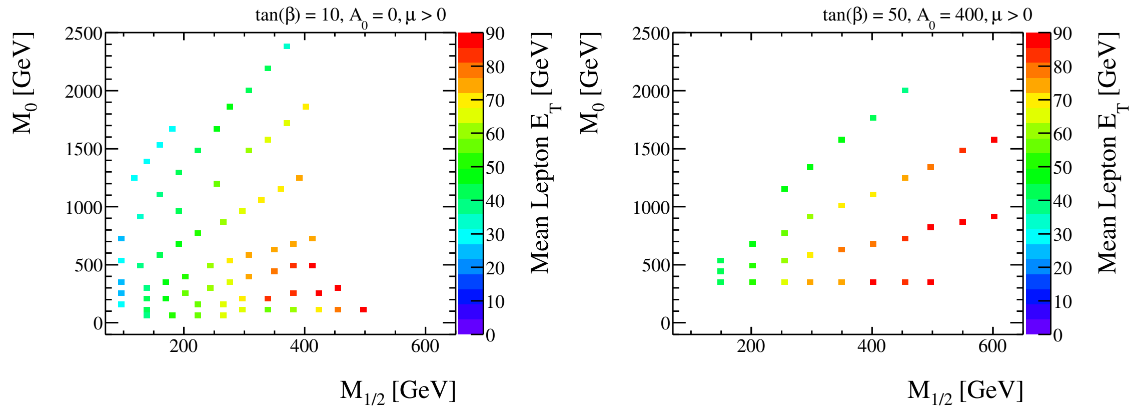

Figure 7.7: The mean E_T of reconstructed leptons.

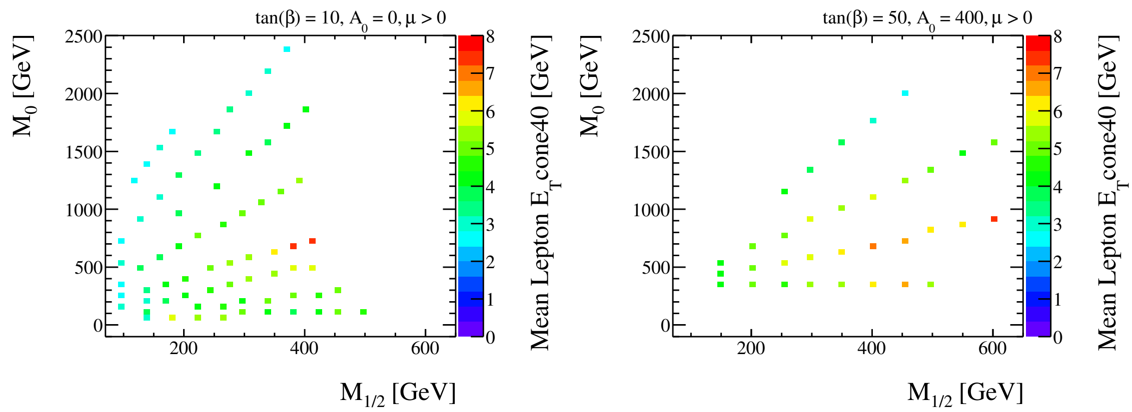

Figure 7.8: The mean $E_T$cone of reconstructed leptons.

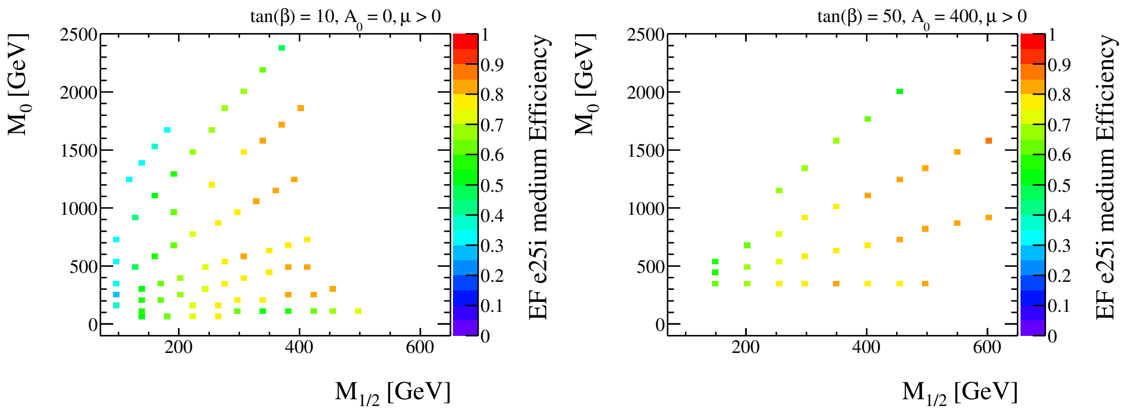

Figure 7.9: The weighted average `EF e25i medium` efficiency, for all prompt electrons.

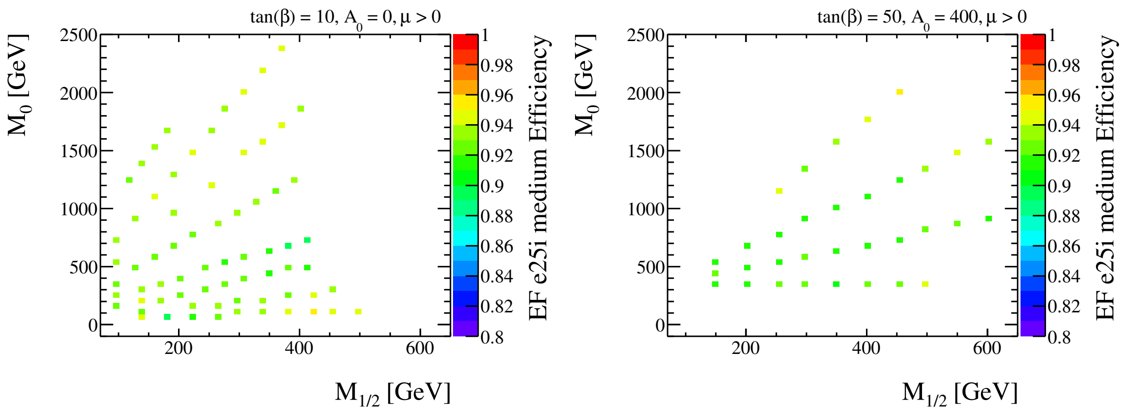

Figure 7.10: The weighted average `EF e25i medium` efficiency, for prompt electrons with $E_T > 35$ GeV.

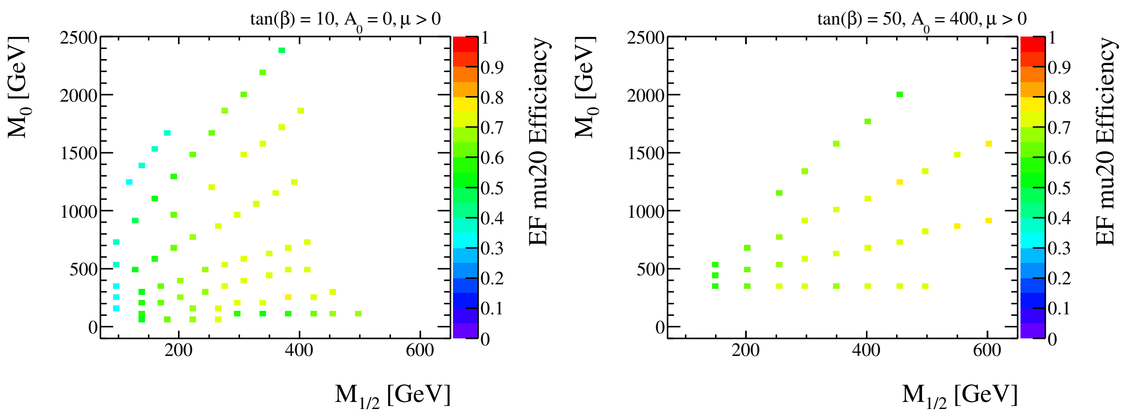

Figure 7.11: The weighted average `EF mu20` efficiency, for all prompt muons.

soft leptons. Although many leptons in SUSY events are observed to be too soft to be selected by the trigger, such events are expected to contain many other features that may enable them to pass the trigger. The following section of this chapter will study events typical of a particular SUSY

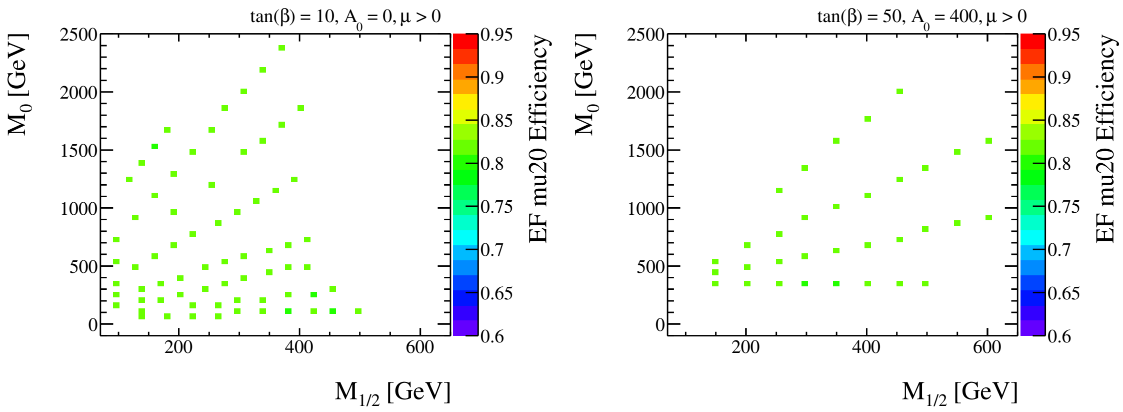

Figure 7.12: The weighted average `EF mu20` efficiency, for prompt muons with E_T >30 GeV.

search channel: the trilepton channel, and the ability of the ATLAS trigger to select these events.

7.2.2 Triggering for Trileptonic Signals

ATLAS has developed several, complementary SUSY search strategies based on simulation studies designed to maximise the discovery potential of ATLAS [83]. Potential SUSY events are selected based on combinations of E_T^{miss}, numerous energetic jets, overall event shapes and a certain number of leptons, meaning electrons or muons. The main search modes are:

- **Zero lepton mode**: This requires the presence of multiple jets along with significant E_T^{miss}. This is the least model-dependent search mode. Typically four or more jets are required in order to reduce the significant backgrounds from QCD jets and W/Z+jets.

- **One-lepton mode**: This requires one lepton in addition to multiple jets and sizeable E_T^{miss}. The lepton requirement greatly reduces the QCD multijet background and also gives better control over the remaining backgrounds ($t\bar{t}$ and W-boson+jets production).

- **Two-lepton mode**: This requires two leptons in addition to multiple jets and sizeable E_T^{miss}. These leptons can either be same-sign (SS), or opposite-sign (OS). Whilst the expected SS dilepton rate from the SM is very small, SS dilepton production can be commonplace in SUSY models.

- **Trilepton mode**: This requires three leptons and either one or more energetic jets or sizeable E_T^{miss}. Trilepton searches are particularly important in SUSY scenarios where coloured sparticles are heavy and therefore signals are dominated by EW signatures.

Additional modes also search for the presence of hadronically decaying τ-leptons and b-jets.

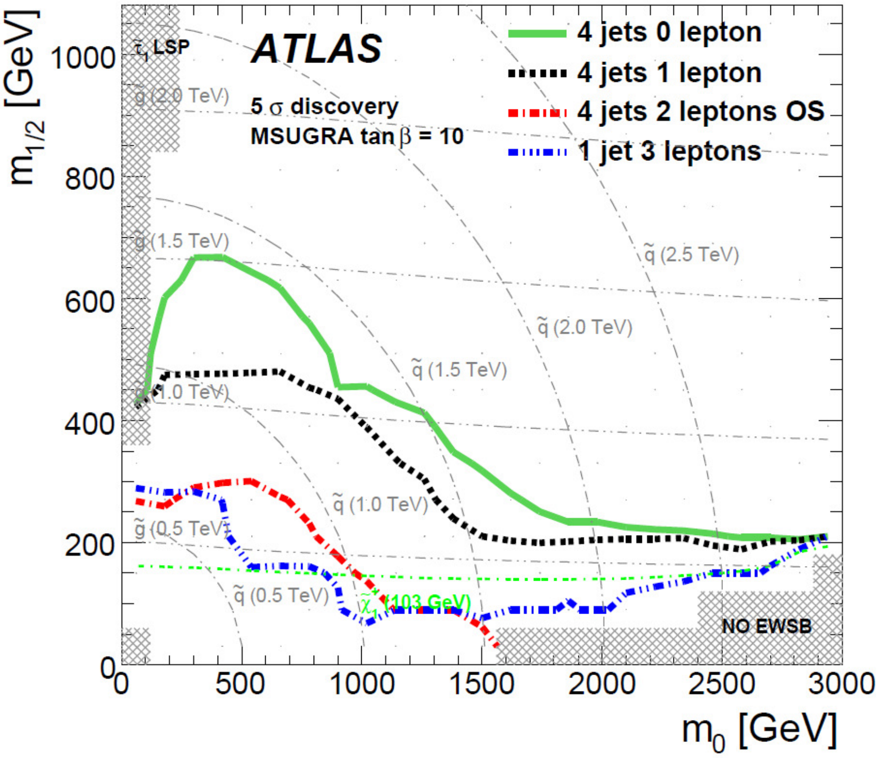

Figure 7.13: The 1 fb^{-1} discovery reach contours for the 4-jet plus E_T^{miss} analyses with various lepton requirements for mSUGRA as a function of m_0 and $m_{1/2}$ in the $A_0 = 0\ GeV$, tan $\beta = 10$, $|\mu| > 0$ plane, The horizontal and curved grey lines indicate gluino and squark mass contours respectively in steps of 500 GeV from [83].

The sensitivity of each search mode varies across the SUSY parameter space. The ATLAS discovery reach with 1 fb^{-1} of data in the $A_0 = 0$ GeV, tan $\beta = 10$, $|\mu| > 0$ plane for the 4-jet plus E_T^{miss} analyses with various lepton requirements for mSUGRA as a function of m_0 and $m_{1/2}$ are shown in Figure 7.13, from [83]. In general the no-lepton mode is the most sensitive. However this must account for large backgrounds and complicated systematic sources of systematic error. Leptonic modes are often more accessible, as the leptons provide a mechanism for triggering on events and for the suppression of backgrounds.

This section will study the trigger efficiency for events within the SUSY grid points identified by a single example search mode with which the author had some involvement: the trilepton mode. Trilepton events are rare, and therefore searches are particularly reliant upon the efficiency of the trigger system. Trilepton studies are discussed in considerably greater detail in [26] and [84].

In these studies, trilepton events are simply identified by the requirement of three well isolated leptons selected in the standard manner. The fraction of all SUSY events which contain three reconstructed leptons is shown in Figure 7.14. This is observed to be typically of the order of 0.8% of all events, with some variation over the studied parameter space. Although trilepton events only represent a small fraction of SUSY events, they only have a few sources of SM background.

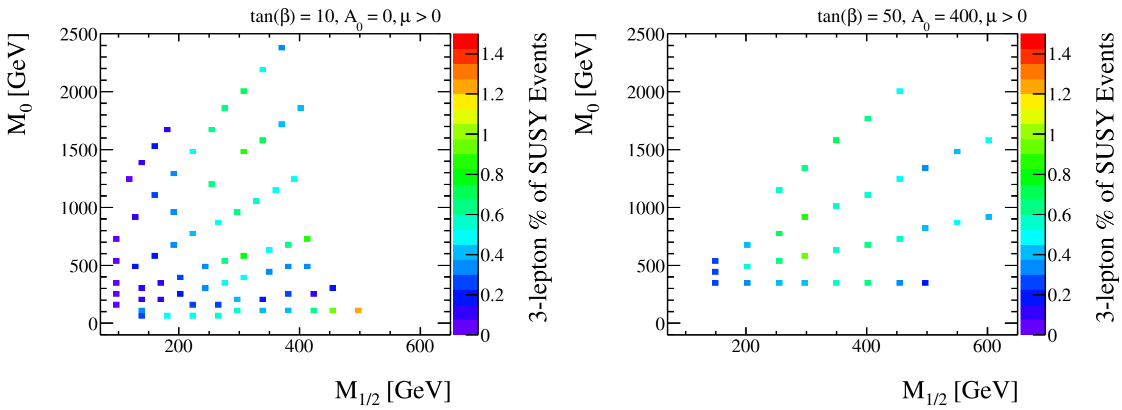

Figure 7.14: The % of all SUSY events which contain three reconstructed leptons.

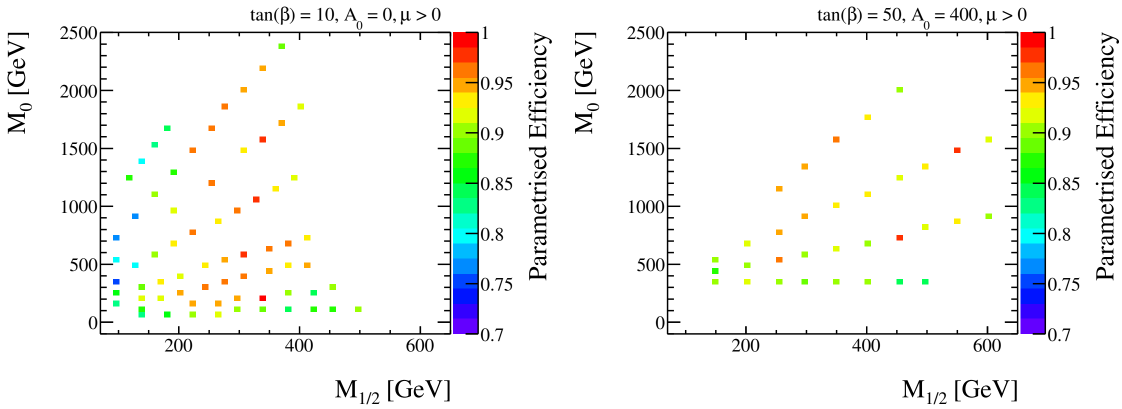

Figure 7.15: Weighted average `EF e25i medium` or `EF mu20` efficiency for trilepton events.

The efficiency of trilepton events to be selected by single leptons triggers is based on a logical `OR` of either single lepton trigger to select any of the leptons in the event. The weighted average efficiency of the `EF e25i medium` and `EF mu20` triggers to select trilepton events is shown in Figure 7.15. This efficiency is seen to vary from around 70% to around 95% across the studied parameter space. Although the thresholds of these triggers exceed that of the offline lepton selection criteria, typically at least one lepton in a trilepton event is expected to possess significant E_T [26]. This, combined with the high lepton multiplicity, results in the selection of the majority of trilepton events by single lepton triggers. The variation in efficiency is observed to follow similar trends to the mean lepton E_T shown previously in Figure 7.7, with the regions of lowest efficiency occurring at low values of m_0 and $m_{1/2}$ and the in highest moderate m_0 region for high $m_{1/2}$.

In addition to single lepton triggers, trilepton events have the potential to be selected by dilepton triggers. Dilepton triggers require that at least two leptons in the event fulfil the lepton selection criteria. This increased multiplicity allows dilepton triggers to use significantly lower energy thresholds than single lepton triggers, yet maintain acceptable pass rates. The dilepton

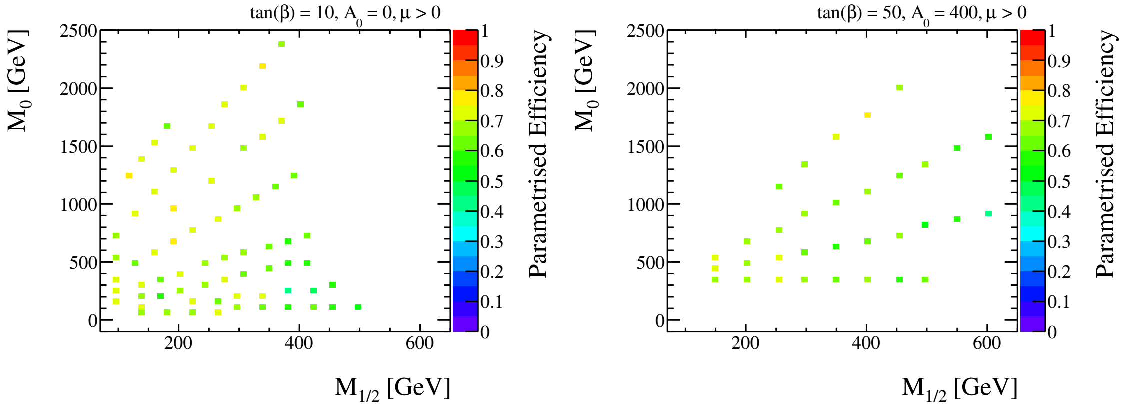

Figure 7.16: Weighted average `EF 2e15i medium` or `EF 2mu10` efficiency for trilepton events.

triggers studied in this section are `EF 2e15i medium` and `EF 2mu10`. As with the single lepton triggers studied previously, these triggers are both intended for use in the trigger menus for $\mathcal{L} \sim 10^{32}\mathrm{cm}^{-2}\mathrm{s}^{-1}$ and above. The weighted average efficiency of the `EF 2e15i medium` and `EF 2mu10` triggers to select trilepton events is shown in Figure 7.16. This efficiency is based on a logical `OR` of any two leptons in each trilepton event to pass either of the dilepton triggers. Efficiency is observed to be around 60% across the studied parameter space, without significant variation between points. The reduced overall efficiency relative to the single lepton triggers is due to the need for an event to satisfy a dilepton trigger requirement.

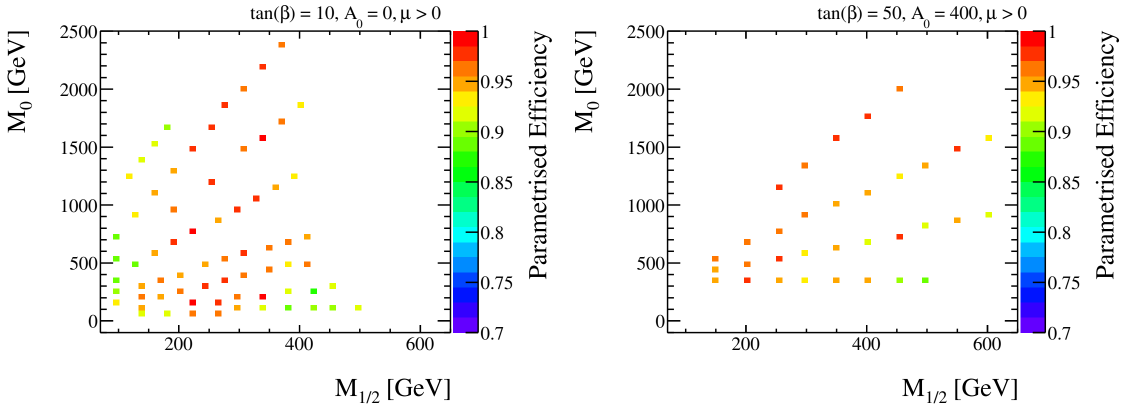

Figure 7.17: Weighted average `EF e25i medium` or `EF mu20` or `EF 2e15i medium` or `EF 2mu10` trigger efficiency for trilepton events

The weighted average efficiency of trilepton event selection by either single or dilepton triggers is shown in Figure 7.17. This is observed to be higher than either set of triggers individually. Trilepton events at all points are seen to be selected by the trigger with an efficiency of above 85%, with the majority of points seen to be selected with an efficiency of above 95%.

Alternative Triggers for Trilepton Events

Leptonic triggers are not the only way that trilepton events could pass the ATLAS trigger. Inline with most SUSY events, trilepton events can also contain energetic jets and considerable E_T^{miss} signatures. The following section will briefly study the *acceptance* of trilepton events by lepton, jet and E_T^{miss} triggers.

Acceptance of a trigger is defined as the fraction of events within a sample which contain offline objects whose kinematics exceed the minimum requirements of the same trigger. For example, an event will be accepted by a `mu20` trigger if it contains at least one offline muon with E_T >20 GeV. This definition can be viewed as an ideal trigger selection, where all events satisfying the minimum requirements pass the trigger. However, as trigger efficiency is not 100%, this definition in fact represents an upper limit for trigger efficiency. In this section, the acceptance of trigger selections are studied to estimate the trigger efficiency of the jet triggers `3j60` and `j260`, and the E_T^{miss} trigger `XE60`. These trigger selections are comparable to those envisaged for use in the trigger menus for $\mathcal{L} \sim 10^{32} cm^{-2} s^{-1}$ and above.

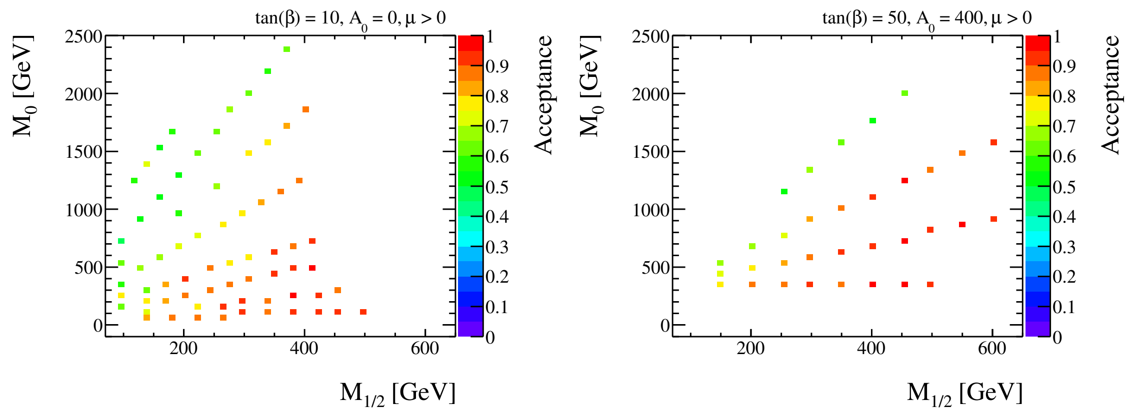

Figure 7.18: The fraction of trilepton events statisfying $E_T^{miss} > 60$ GeV.

The acceptance of trilepton events by an E_T^{miss} minimum threshold cut of 60 GeV is shown in Figure 7.18. This is shown to vary from around 50% at low values of $m_{1/2}$ up to around 100% at high values. Similarly, the acceptance of trilepton events via the requirement of either a single jet with $E_T > 260$ GeV or three jets with $E_T > 60$ GeV is shown in Figure 7.19. This acceptance is observed to vary from around 10% at low values of m_0 and $m_{1/2}$, to around 60% across most of the remainder of the grid.

In practice trilepton events will be selected from those which pass any trigger signature. By combining the acceptance of events by the jet and E_T^{miss} cuts with the weighted average efficiency for the remaining events to satisfy either the single or dilepton triggers, the overall efficiency of

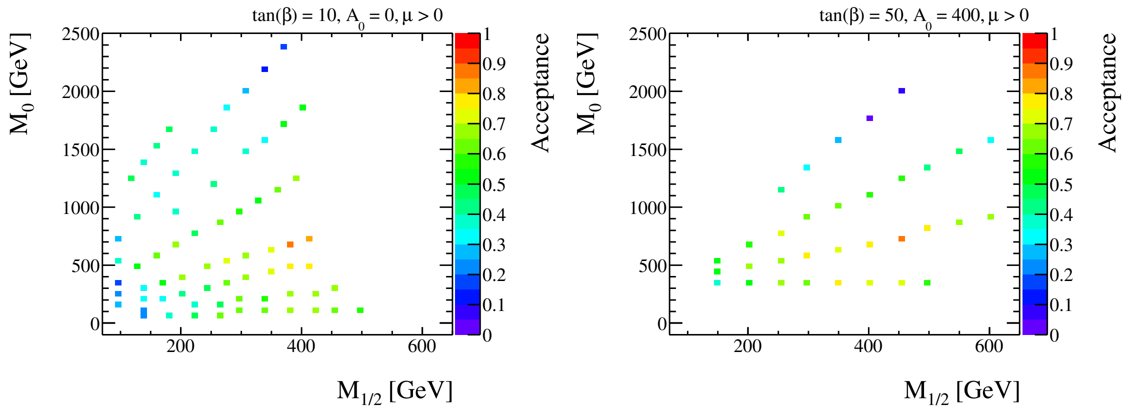

Figure 7.19: The fraction of trilepton events statisfying one jet with $E_T > 260$ GeV or three jets with $E_T > 60$ GeV.

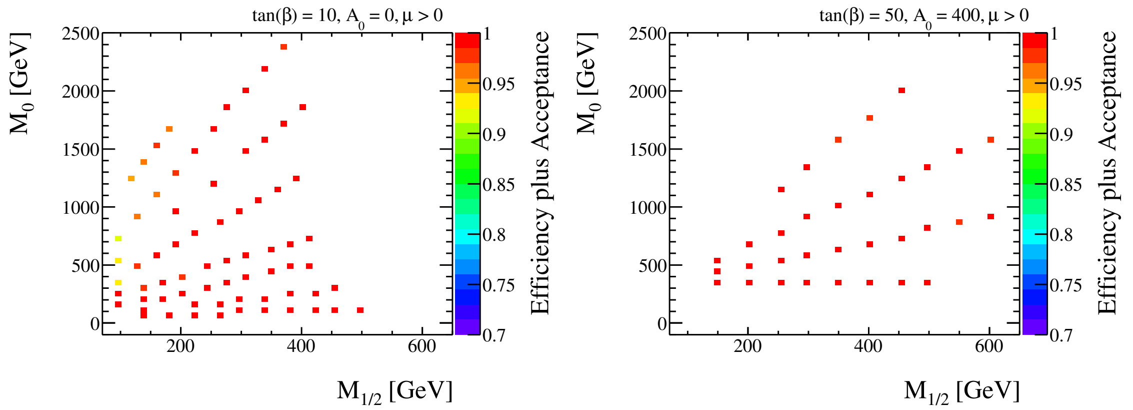

Figure 7.20: The acceptance of trilepton events that satisfy the minimum jet or E_T^{miss} requirements of the trigger combined with a weighted average of efficiency for those that do not.

the trigger can be estimated. The results of this are shown in Figure 7.20. This figure illustrates the potential gain in efficiency over Figure 7.17, by the inclusion of events which satisfy the jet or E_T^{miss} requirements. The overall efficiency is seen to be considerably higher than previously, with efficiency now close to 100% across the entire studied parameter space. The only exceptions are a few low $m_{1/2}$, moderate m_0 points in the $\tan\beta = 10$ grid, where efficiency is seen to be around 90%. This indicates that via the use of jet and E_T^{miss} triggers, as well as leptonic triggers, ATLAS has the potential to trigger on almost every trilepton event expected.

7.3 Conclusions

It has been shown, via the use of weighted average trigger efficiencies, that the ATLAS electron and muon triggers successfully select energetic leptons with a high efficiency in a wide range of SUSY scenarios, with little dependence on the choice of model parameters. However, regions of lower efficiency remain at low SUSY mass scales where the majority of leptons are typically not very energetic and therefore fail to meet the energy threshold requirements of the trigger. The need to maintain acceptable trigger rates means this loss is unavoidable if the triggers are to retain their current tightness of object selection.

As an example of a specific application of leptonic triggering for a SUSY search, the trilepton channel has been studied in more detail. The efficiency for such events to pass either the single or double lepton triggers was shown to be higher than the single lepton triggers alone and around 85% for all points. Yet some events are still seen to fail the trigger, particularly at low SUSY mass scales. A study of the acceptance of trilepton events by the E_T^{miss} and jet trigger thresholds has indicated that the events which fail to pass the leptonic triggers may still be accepted by the other streams. Such studies would need to be performed in more detail, with realistic trigger efficiency measurements in order to confirm this result with high accuracy.

Chapter 8

Electron Triggers for Exotic Dielectron Signatures

This chapter presents a study of the efficiency of the ATLAS electron trigger to select the very energetic electrons characteristic of the decays of new neutral heavy resonance particles. Trigger efficiencies for representative triggers are studied based on fully simulated MC samples of the Standard Model Z$\rightarrow e^+e^-$ and Drell-Yan processes as well as the dilepton decays of a Randall-Sundrum Graviton and the Sequential Standard Model Z'.

8.1 Dielectron Resonances at High Masses

High mass neutral resonances are predicted by many extensions to the SM, including grand unified theories and extra dimensional models. This chapter will consider two examples of well motivated BSM models which predict the existence of resonances within the discovery reach of the LHC. These are the SSM Z' and the RS graviton as introduced in Section 1.3. The decays of these resonances will be typified by pairs of extremely energetic, opposite sign leptons, for example electron-positron pairs. This is a clean, low background process and as such represents a prime candidate for early discovery at the LHC. The potential of ATLAS to discover dielectron resonances has been extensively studied in [85], showing that unambiguous discovery of a 1 TeV SSM Z' can be achieved with as little as 50 pb^{-1} of well understood data. Key to this will be the characterisation of the trigger and detector responses to energetic electrons.

This chapter utilises fully simulated MC samples, produced at an LHC centre of mass energy of 10 TeV. The samples considered here are: a 300 GeV RS graviton, G, with $k/M_{\mathrm{P}} = 0.01$, and a SSM Z' boson of mass 1 TeV and 1.5 TeV. In addition, SM Z and Drell-Yan decays to dielectron final states are also examined to provide well understood SM reference points. The Drell-Yan

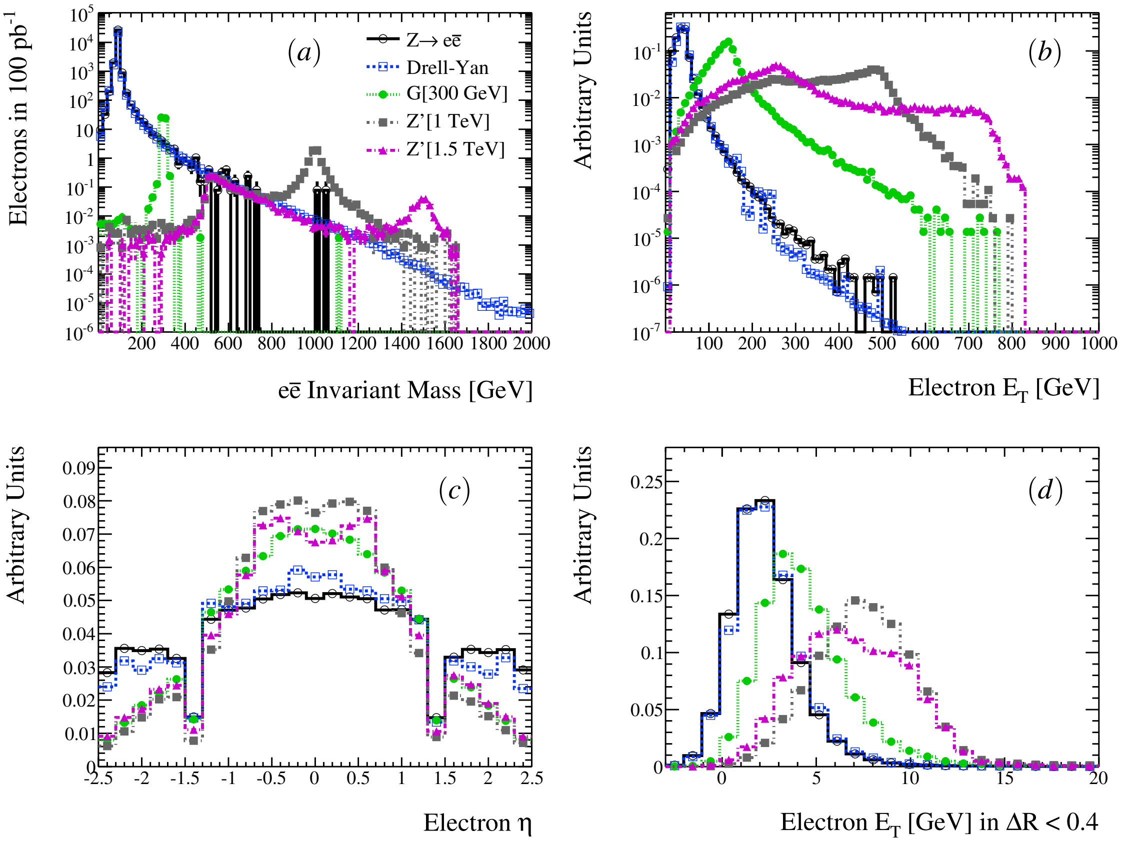

Figure 8.1: Some kinematic distributions for fully simulated Monte Carlo samples of e^+e^- final states from Z-boson decays (black open circles), Drell-Yan (blue open squares), G [300 GeV] decays (green circles), Z' [1 TeV] (grey squares) and Z' [1.5 TeV] (magenta triangles) decays. The variables shown are: (a) the invariant mass of e^+e^- pairs; (b) electron E_T ; (c) electron $|\eta|$ and (d) electron $E_T cone$. For comparison purposes (b), (c) and (d) are normalised to unit area.

process itself constitutes an irreducible background to any dielectron resonance search. As such it must be well understood in order for any confident statements to be made about new physics in the very high mass range at ATLAS. Drell-Yan production also provide a source of highly energetic electrons which can be used for the purpose of determining trigger and detector performance from data. The DY sample studied here has been filtered to only contain events where both electrons have $E_T > 10\,\mathrm{GeV}$ and $|\eta| < 2.7$. Details of the samples studied can be found in Appendix A.3.

Electrons are reconstructed using the common electron selection detailed previously. The expected number of events and reconstructed electrons from each of the considered samples normalised to an integrated luminosity of 100 pb^{-1} are shown in Table 8.1. The increase in the number of electrons reconstructed per event in the DY sample compared to the Z sample, is due to the filters applied at generator level. Some kinematical variables for the selected offline electrons are shown in Figure 8.1. In detail, the invariant mass of dielectron pairs present in each of the samples is shown in Figure 8.1 (a), clearly displaying the exponential tail of the Drell-Yan process

Table 8.1: Expected numbers of events and reconstructed electrons for an integrated luminosity of 100 pb^{-1}. Only decays to e^+e^- are considered for each of the samples listed here. The quoted errors are statistical only.

Sample	Z ($\times 10^3$)	Drell-Yan ($\times 10^3$)	G [300 GeV]	Z' [1 TeV]	Z' [1.5 TeV]
Events	109.8	58.0	83.4	24.9	7.6
Electrons	109.0 ± 0.09	77.6 ± 0.04	129.1 ± 0.5	30.4 ± 0.2	8.08 ± 0.06

and the mass peaks of the resonance processes. The E_T of reconstructed electrons is shown in Figure 8.1 (b). As expected, both the Drell-Yan and Z processes show peaks at relatively low E_T values followed by a long tails towards high E_T values. Conversely, the BSM resonance particles show highly energetic electron spectra. The 300 GeV graviton electron spectrum is seen as a peak at around half the rest mass. Both of the Z' samples include Drell-Yan production above 500 GeV as well as the resonance, and therefore the E_T spectra for these samples are seen to include both the resonance peak at around half the rest mass as well as the exponential fall in E_T. The $|\eta|$ spectrum for reconstructed electrons is shown in Figure 8.1 (c), which is seen to be more central for heavy resonances than for the Z decay or for the Drell-Yan process. The amount of E_T in a hollow cone around the central electron cluster is shown in Figure 8.1 (d). Electrons from the heavy resonances are seen to deposit more energy in the area around the central cluster. This is an effect of the broader showers typical of more energetic electrons. It will be shown later that this has important consequences for triggering and a detailed discussion of the issue is presented in Section 8.2.1.

8.2 Trigger Efficiency

In the following section the efficiency of the trigger to select high-E_T electrons is studied. In particular the triggers `e10 medium`, `e20 loose`, `e105 loose` and `e25i medium` are examined.

The `e10 medium` and `e20 loose` triggers are expected to be the main low threshold triggers for the collection of data at the early luminosity phase of $\mathcal{L} \sim 10^{31}\,\mathrm{cm}^{-2}\mathrm{s}^{-1}$. The low instantaneous luminosity means that these triggers do not have to require particularly strict electron selection criteria. Most early ATLAS electron data is expected to be collected via these triggers, or triggers of this form. Whilst the study of high mass resonances is unlikely to begin in earnest during initial data taking, the evolution of the trigger system will be heavily influenced by the understanding gained during this time. Therefore it is important to study the behaviour of such low luminosity triggers and how this behaviour will evolve towards higher luminosity running.

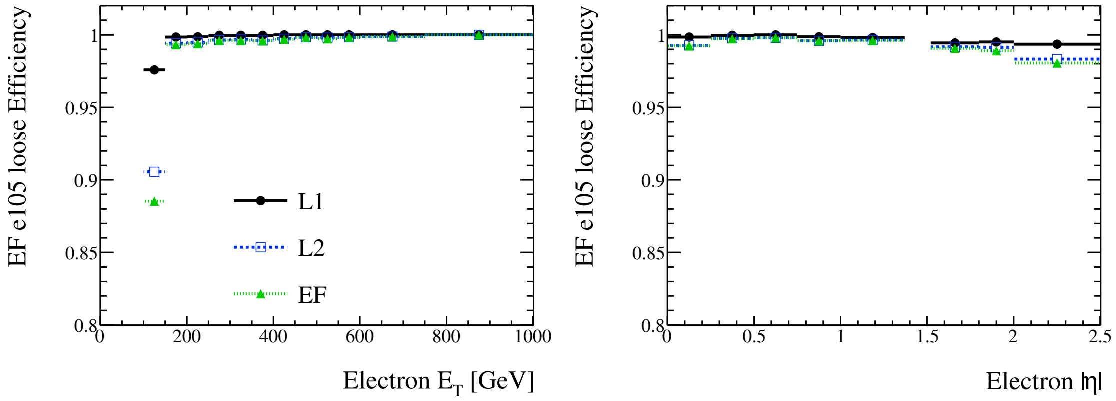

Figure 8.2: The trigger efficiency for L1 (black circles), L2 (blue squares) and EF (green triangles) in MC Drell-Yan decays to e^+e^- , for the trigger `e105 loose` as a function of offline E_T and $|\eta|$.

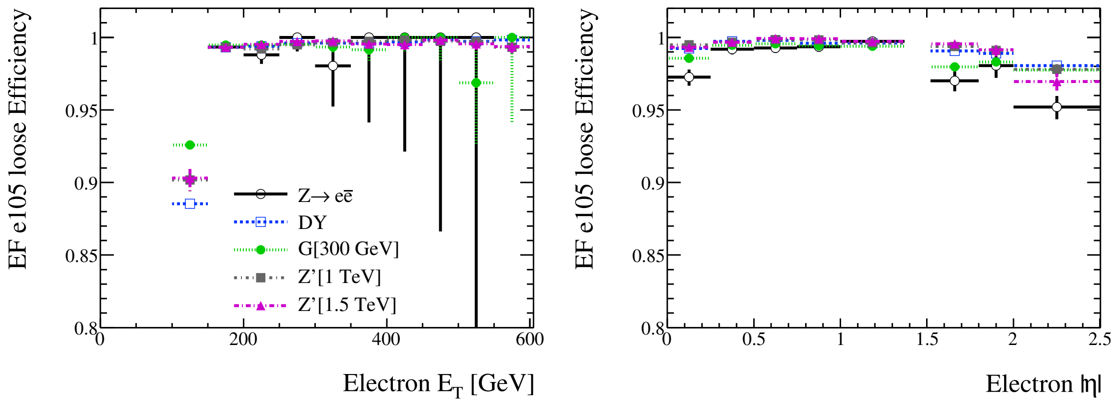

Figure 8.3: The trigger efficiency in the Z (black open circles), Drell-Yan (blue open squares), G [300 GeV] (green circles), Z' [1 TeV] (grey squares) and Z' [1.5 TeV] (magenta triangles) decays to e^+e^- MC samples, for the trigger `EF e105 loose` as a function of offline E_T and $|\eta|$.

Instantaneous luminosity is expected to quickly increase to $10^{32}\text{cm}^{-2}\text{s}^{-1}$, at which point the rates for both `e10 medium` and `e20 loose` are expected to become unacceptably high. As a result the trigger will have to apply more stringent event selection criteria. The simplest way to reduce trigger acceptance rates is by increasing the threshold E_T required. The trigger `e105 loose` is an example of a trigger which relies almost exclusively on a very high minimum energy threshold to control rates and is intended for use at luminosities of $10^{32}\text{cm}^{-2}\text{s}^{-1}$ and above. This trigger will be studied as an example of a trigger that will be used during searches for new high mass resonances.

The trigger efficiency for each trigger level in the Drell-Yan sample as a function of offline E_T and $|\eta|$ for the trigger `e105 loose` is shown in Figure 8.2. The efficiency is seen to be close to 100% for all trigger levels with only a small dependency on either E_T or $|\eta|$. Similarly, the dependence of the EF trigger efficiency on E_T and $|\eta|$ in the Drell-Yan, Z and resonance samples

Table 8.2: Summary of trigger efficiencies (in %) as measured in the E_T plateau region.

Sample	EF e10 medium	EF e20 loose	EF e105 loose
Z→e^+e^-	98.78 ± 0.01	99.52 ± 0.01	98.27 ± 0.17
Drell-Yan	99.21 ± 0.03	99.65 ± 0.02	99.43 ± 0.03
G [300 GeV]	99.41 ± 0.03	99.76 ± 0.02	99.05 ± 0.04
Z' [1 TeV]	99.44 ± 0.04	99.74 ± 0.03	99.56 ± 0.03
Z' [1.5 TeV]	99.39 ± 0.06	99.69 ± 0.04	99.51 ± 0.06

is shown in Figure 8.3. It should be noted that the errors shown on this figure are Bayesian (as introduced in Section 5.1), due to the low Z-statistics and high efficiencies at high values of E_T. All samples are seen to show the same features as the Drell-Yan sample, with high flat efficiency as a function of E_T and $|\eta|$ efficiency that is high in the barrel and drops off slightly in the end-caps. The fact that observed efficiency is high and consistent for all electrons, regardless of their origin, is a good indication that the `e105 loose` trigger is well suited to select energetic electrons.

The EF efficiencies for the `e105 loose`, `e10 medium` and `e20 loose` as measured in the E_T plateau region are summarised in Table 8.2. Similarly to `e105 loose`, the efficiencies for `e10 medium` and `e20 loose` are observed to be very high for all the studied samples. Searches for high mass exotic dielectron resonances are, by definition, interested in very high E_T electrons and it has been shown that the efficiency for unisolated triggers to select these electrons is high with minimal structure as functions of E_T or $|\eta|$.

8.2.1 L1 Isolation

Calorimeter isolation at L1 is an alternative method to raising E_T thresholds in order to control rates as instantaneous luminosity increases. By requiring that the L1 electron candidate cluster is narrow and well contained in the EM calorimeter, further background rejection can be achieved. This allows access to a lower E_T regime than is otherwise available using unisolated triggers alone. Overall L1 isolation is comprised of three separate cuts on as many calorimeter based variables as introduced previously in Section 3.1.1, the definitions are repeated here for clarity: EM ring isolation (`EMIsol`), which requires that the energy deposited in a ring around the central cluster is < 4 GeV; hadronic core (`HadCore`), which requires that the energy in the hadronic calorimeter behind the central cluster is < 2 GeV; hadronic ring isolation (`HadIsol`), which requires that the energy in a ring around the `HadCore` is < 3 GeV. The trigger `e25i medium`, as studied previously, is an example of a trigger which includes L1 isolation. A trigger of this form is foreseen to be included as a primary low threshold trigger for luminosities of $10^{32}cm^{-2}s^{-1}$ and above. This section will study the efficiency of the `e25i medium` trigger to select energetic electrons.

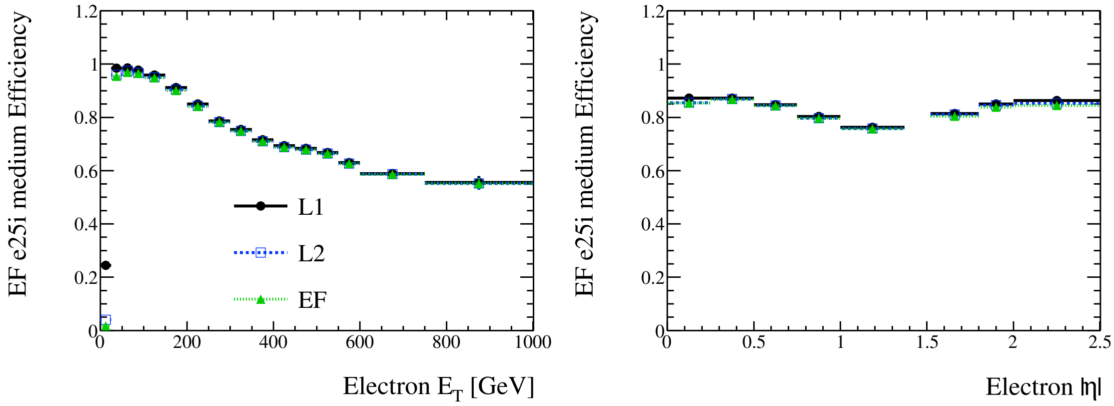

Figure 8.4: The trigger efficiency for L1 (black circles), L2 (blue squares) and EF (green triangles) in MC Drell-Yan decays to e^+e^- , for the trigger `e25i medium` as a function of offline E_T and $|\eta|$.

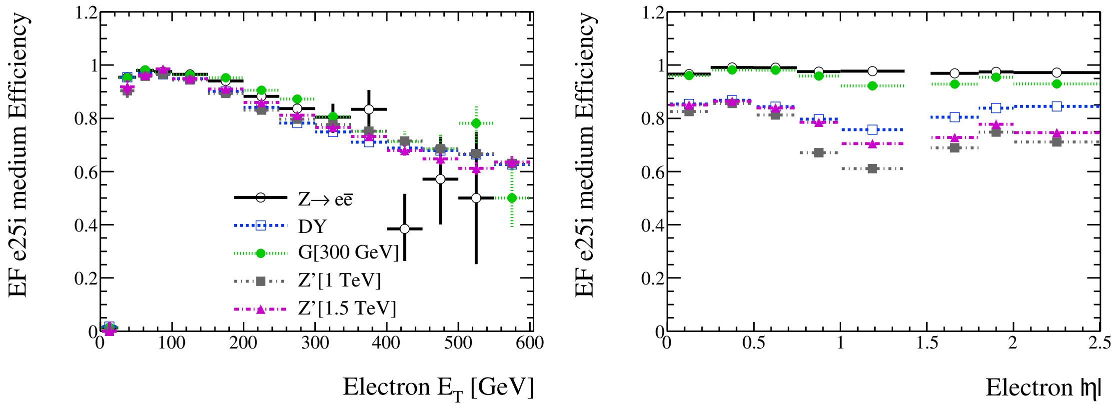

Figure 8.5: The trigger efficiency in the Z (black open circles), Drell-Yan (blue open squares), G [300 GeV] (green circles), Z' [1 TeV] (grey squares) and Z' [1.5 TeV] (magenta triangles) decays to e^+e^- MC samples, for the trigger `EF e25i medium` as a function of offline E_T and $|\eta|$.

The `e25i medium` efficiency as a function of offline E_T for all trigger levels in the Drell-Yan sample is shown in the left-hand plot of Figure 8.4. This figure shows a significant drop in efficiency as E_T increases. This clear downwards trend is seen to occur at L1, where calorimeter isolation is being applied. HLT efficiencies are seen to remain high relative to L1. The efficiency as a function of offline $|\eta|$ is shown in the right-hand plot of Figure 8.4 and is seen to fall around the crack region and rise towards the central barrel and outer endcaps. HLT efficiencies are again shown to remain high relative to L1. The observed fall in efficiency with increasing E_T means that highly energetic electrons are likely to be rejected by this trigger. As such `e25i medium` appears to be not well suited for the collection of high mass physics signals.

Table 8.3: `e25i medium` trigger efficiencies (in %) in the plateau region (E_T <35 GeV).

Sample	L1 Efficiency	L2 Efficiency	EF Efficiency
Z→e^+e^- (cumulative)	99.34 ± 0.01	98.08 ± 0.02	97.70 ± 0.02
Z→e^+e^- (relative to above level)		98.73 ± 0.01	99.61 ± 0.01
DY (cumulative)	83.63 ± 0.12	82.91 ± 0.12	82.73 ± 0.12
DY (relative to above level)		99.14 ± 0.03	99.78 ± 0.02
G[300 GeV] (cumulative)	96.31 ± 0.07	95.73 ± 0.07	95.59 ± 0.08
G[300 GeV] (relative to above level)		99.40 ± 0.03	99.85 ± 0.01
Z' [1 TeV] (cumulative)	76.83 ± 0.22	76.38 ± 0.22	76.25 ± 0.22
Z' [1 TeV] (relative to above level)		99.41 ± 0.05	99.83 ± 0.02
Z' [1.5 TeV] (cumulative)	80.78 ± 0.31	80.27 ± 0.32	80.13 ± 0.32
Z' [1.5 TeV] (relative to above level)		99.38 ± 0.07	99.82 ± 0.04

The `EF e25i medium` efficiencies for the Drell-Yan, Z and resonance samples as a function of offline E_T and $|\eta|$ are shown in Figure 8.5. The same decreasing efficiency trends and $|\eta|$ structures are seen in all samples. Efficiencies are seen to be lower across the $|\eta|$ range for the high mass processes due to the downwards trend in efficiency with increasing E_T resulting in the samples with more energetic electrons having lower overall efficiencies. These results are summarised in Table 8.3. It is clear from this table that the observed efficiency drop is due exclusively to L1 with HLT efficiencies relative to L1 remaining high and comparable between samples.

The behaviour of the L1 calorimeter isolation variables, which are the cause of this efficiency loss, will be investigated in what follows.

In Figure 8.6 four variables that are relevant for isolation are shown for electrons in the Drell-Yan sample: $E_T cone$, as shown previously; `EMIsol`; `HadIsol` and `HadCore`. All isolation variables are shown only for electrons with $E_T > 35$ GeV and, in the case of L1 variables, only if they can be matched to a L1 object. All variables in Figure 8.6 are seen to peak at low energies with exponential drops towards increasing energy, with `EMIsol` showing a slower drop than either `HadCore` or `HadIsol`.

The evolution of the mean value and standard deviation of these variables with offline E_T is shown in Figure 8.7. In Figure 8.7 (a) it is shown that as E_T increases so does the amount of energy in a hollow cone around the electron. This is as the electromagnetic shower produced by the electron becomes broader as the shower becomes more energetic. A similar trend is shown in Figure 8.7 (b) that as E_T increases so does the mean value of `EMIsol`. At E_T of around

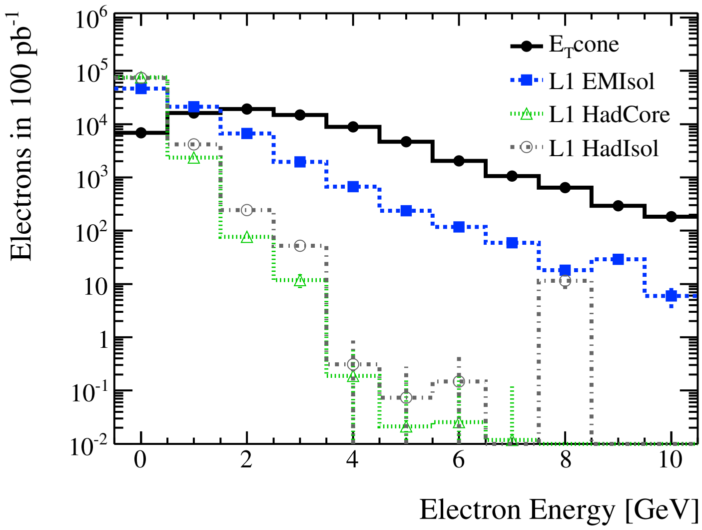

Figure 8.6: Offline isolation variables in the Drell-Yan decay to e^+e^- MC sample. $E_T cone$ (black circles); L1 EMIsol (blue squares); L1 HadCore (green open triangles); L1 HadIsol (grey open circles).

200 GeV the cut value of 4 GeV is seen to fall within one standard deviation of the mean and at E_T $\sim$700 GeV the mean value is compatible with the cut value. A gentle increasing trend is seen for `HadCore` in Figure 8.7 (c). The rise with E_T is seen to be much slower than for `EMIsol`, such that the mean value does not approach the cut value of 2 GeV within the studied E_T range. `HadIsol` shown in Figure 8.7 (d) does not show any clear trend with E_T and as such does not approach the cut value of 3 GeV. From this it is clear that the increasing trend in the amount of energy deposited around the central energy cluster, which is manifest at L1 as an increase in `EMIsol`, is causing isolation cuts to become significantly less efficient at high E_T. Therefore, triggers relying on L1 isolation are clearly not very well suited for the selection of highly energetic electrons.

8.3 Data Driven Efficiency Measurement

The TP method, as introduced previously, has been shown to work well in kinematic regions where there is abundant production of the Z-boson. However, at high-E_T ranges statistics are expected to become a limiting factor. As a result direct, high granularity measurement of efficiency in this range will not be feasible, especially in the low statistics limit of early running.

The previous section, Section 8.2, showed that unisolated trigger efficiencies show a consistent, flat dependence on E_T. Therefore it seems reasonable that a measurement of the plateau efficiency in the medium E_T range could be extrapolated to high E_T. This would allow for a precise measure of efficiency to be made using the copious Z statistics in the medium E_T range. The following section will evaluate the performance of weighted effiency averages for a representative trigger, `EF e10 medium`, using simulated Z MC.

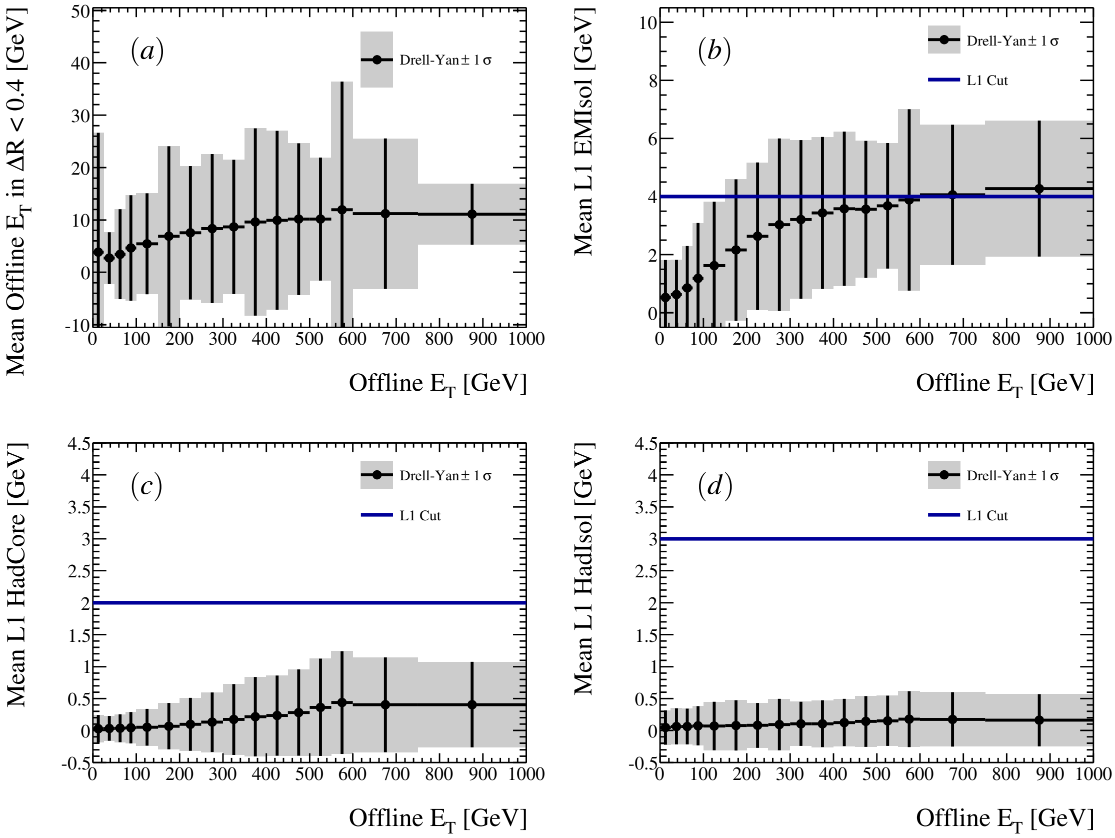

Figure 8.7: The profile of the isolation variables in the Drell-Yan decay to e^+e^- MC sample as a function of offline E_T for: (a) $E_T cone$; (b) L1 EMIsol; (c) L1 HadCore; (d) L1 HadIsol. Corresponding L1 cut values are shown as blue lines.

In order to determine if the efficiency measured using the Z is representative of that seen in the Drell-Yan and BSM resonance samples, a measurement of efficiency is constructed using electrons in the Z sample. The resultant efficiency is then applied to all electrons in the other samples and compared to MC efficiencies.

A 2-D weighted average of the efficiency of `EF e10 medium` is constructed by measuring the $Z \to e^+e^-$ MC efficiency in eight E_T and nine $|\eta|$ bins. More precisely the E_T binning consists of seven bins in the range 0 to 200 GeV and a single bin in the high E_T range above 200 GeV.

A comparison between the `EF e10 medium` weighted average and MC efficiencies in the Drell-Yan sample is shown in Figure 8.8 as a function of (a) E_T and (b) $|\eta|$. Similarly plots for the Z' [1 TeV] sample are shown in Figure 8.8 (c) and (d). It is seen that the weighted average efficiency agrees with the MC result to within errors. Table 8.4 summaries the comparison between the weighted average efficiency and MC for all samples. In all cases these agree to within errors. These show that, to within the available precision, it is valid to determine efficiency in 2-D, and that this can be measured using data driven methods.

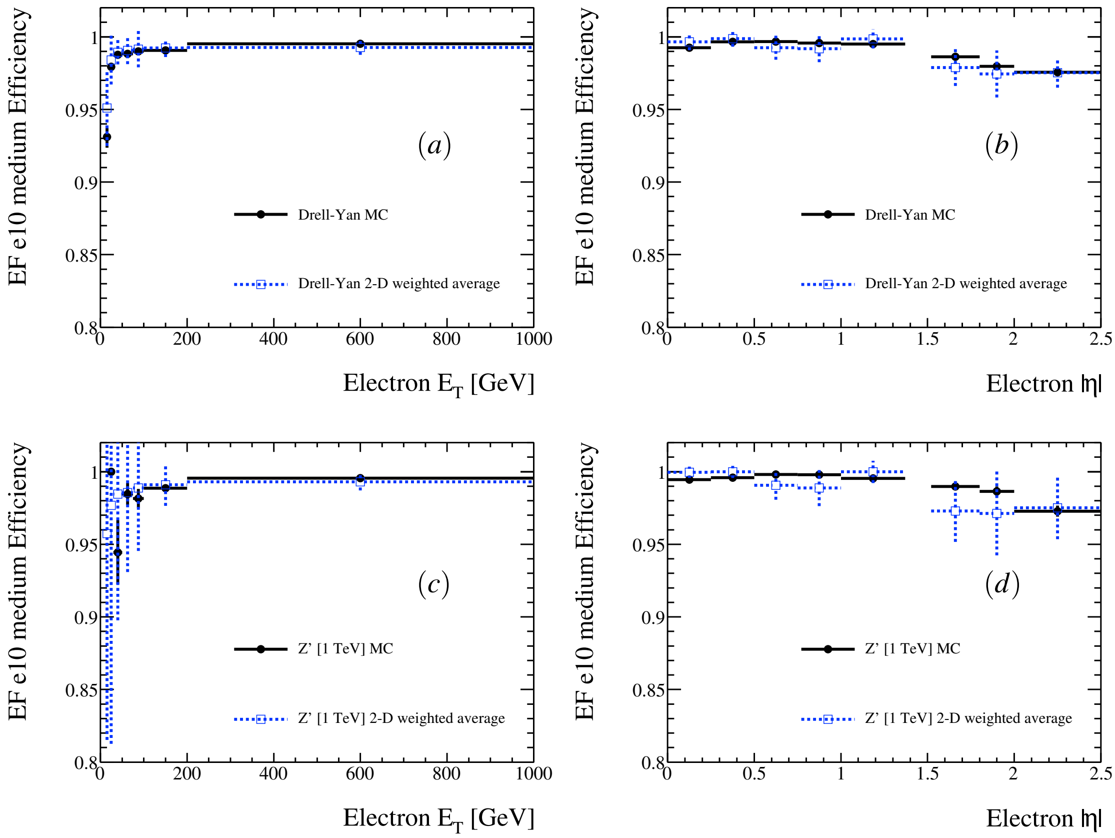

Figure 8.8: Comparisons between `EF e10 medium` MC (black circles) and 2-D weighted average (blue squares) efficiencies for the Drell-Yan sample as a function of offline (a) E_T and (b) $|\eta|$. Analogous distributions are shown for the Z' [1 TeV] in (c) and (d).

It is important to note here that the trigger `e10 medium` will not be used to perform this analysis with real data, as it is only intended for use at very low luminosities. It is very likely that at the higher luminosities, where resonance searches will take place, an unisolated trigger suitable for collection of very energetic electrons will have a very high E_T threshold, such as `e105 loose`. In this case direct measurements of this trigger's efficiency may not be feasible due to the fact that electrons from the Z control sample mainly occupy the intermediate E_T regime in the range of 100 GeV. In this case it is safe to assume that efficiency will either be measured by extrapolation from a lower threshold trigger that is run online but with a prescale factor. Alternatively, an unprescaled trigger that is run offline on data that has already been collected could be used. In either case careful evaluation of how to define the extrapolation region will be crucial. The final choice will depend on the value of E_T at which efficiency reaches a flat plateau and the desired accuracy of the efficiency measurement. Rigorous checks of the evolution of all the trigger variables concerned will be essential to justify any extrapolation of measured trigger efficiencies to the high E_T range.

Table 8.4: Comparisons between `EF e10 medium` efficiencies as obtained from the MC analysis to a 2-D weighted average efficiency.

Sample	MC efficiency	2-D weighted average efficiency
Drell-Yan	99.21 ± 0.03	99.2 ± 0.4
G [300 GeV]	99.41 ± 0.03	99.4 ± 0.4
Z' [1 TeV]	99.44 ± 0.04	99.3 ± 0.6
Z' [1.5 TeV]	99.39 ± 0.06	99.2 ± 0.8

8.4 Conclusions

This chapter has studied the efficiency of the ATLAS electron trigger to select the very energetic electrons characteristic of the decays of new neutral heavy resonance particles. Trigger efficiencies for representative triggers were shown for MC samples of the SM Z and Drell-Yan to dielectron processes and the BSM decays of a 300 GeV RS Graviton, a 1 TeV and a 1.5 TeV SSM Z' . These efficiencies were seen to be consistently high in all samples for unisolated triggers. Conversely, efficiencies were seen to fall off with increasing E_T for isolated triggers. This was established to be due to lack of containment of the EM shower at L1. A 2-D weighted average of the Z$\rightarrow e^+e^-$ trigger efficiency, which can be measured from data using the TP method, was shown to reproduce well the MC efficiencies, but will in practice be limited by statistics. It was shown that, due to the flat dependence of unisolated trigger efficiency on E_T, an extrapolation based on efficiency measured in the intermediate E_T range, where Z statistics are copious, will correctly reproduce the trigger efficiencies for very energetic electrons in a sample independent way.

Chapter 9

Electrons in Early Data

This chapter presents some preliminary results from studies of electrons in early data, performed using the first LHC collisions at a centre of mass energy of 900 GeV.

9.1 Electrons in Early Data

The first LHC collisions were recorded in late 2009. Beams at the SPS injection energy were circulated in the LHC and used to produce collisions at all four interaction points at a centre of mass energy of 900 GeV. Between the 6th and the 15th of December a total of approximately 20 μb^{-1} of collision data (9 μb^{-1} with stable LHC beams and nominal ID voltages) was collected by ATLAS. This chapter will present a brief overview of the first results based on such data and which is relevant for the electron trigger. These results are compared to MC simulations of minimum bias (MB) events. The work in this chapter was produced in collaboration with other members of the relevant ATLAS working groups. In-depth studies of this collision period can be found in [86, 87, 88, 89, 90, 91].

ATLAS data is collected by *run*, defined as a period of uninterrupted data taking. An ideal run will begin with the injection of beam into the LHC and end when the beam is lost or dumped. For the studies in this chapter, events are selected within each run which appear to be produced by LHC collisions and not by cosmic muons or beam related backgrounds; this was achieved by using the requirement that a coincidence of signals be detected in either both MBTSs or both EM endcaps. In addition, only events in a *good runs list* (GRL) are selected. GRLs are defined by periods of data collection during which the detector configuration matches the minimum required state of readiness for a particular analysis. For these studies, in common with those in [91], the GRL requires that the ID and calorimeter systems are operational, and that the solenoidal field is at nominal value.

During this first running period, the maximum instantaneous luminosity was estimated to be around 5×10^{26} cm^{-2}s^{-1} [86]. The low luminosity allowed an acceptable event rate to be maintained by only a very loose L1 MBTS trigger. This trigger selects events which contain at least one above-threshold hit in either MBTS system and is designed to select collision events as inclusively as possible. In addition, although they were not required to maintain an acceptable event rate, L1 EM triggers were also run online, the lowest configured EM threshold being `L1 EM3`. The low luminosity meant that HLT rejection was not required. This allowed the HLT to operate in a *pass-through* mode, whereby objects were reconstructed but no cuts were imposed.

The collected data set contains 903,309 MBTS triggered events. Of these, 383,827 events pass the collision candidate requirements and a total of 453 objects pass the `L1 EM3` trigger. Within this dataset, offline candidate electrons are identified by either the standard or the soft electron algorithms. They are then further required to have deposited more than 30% of their total energy in the second layer of the EM calorimeter. In addition, candidates are excluded in the low rapidity region ($|\eta| < 0.15$) and in the extended crack region between the barrel and the endcap ($1.35 < |\eta| < 1.55$). The low rapidity region was excluded due to known L1 timing problems in the third layer of the EM calorimeter. The extended crack region was excluded as only the endcap calorimeter was connected to the L1 trigger tower system. Both these issues have since been resolved. Only these very loose electron selection criteria were applied due to the limited statistics available. This selection results in the identification of 730 electron candidates. Table A.4 in Appendix A.4 shows a breakdown of the number of MBTS triggered events per run, along with the number of collision candidate events in the GRL.

The total proton-proton cross-section can be divided into elastic and inelastic components and the inelastic component further subdivided into non-diffractive, and diffractive components. Elastic and diffractive interactions do not involve the exchange of any internal quantum numbers between the colliding particles. These are generally soft interactions which result in low multiplicity final states [92]. Non-diffractive interactions, on the other hand, involve the exchange of colour charge between colliding particles and subsequently result in the production of more hadrons in the final state. It is these hard interactions which are likely to give rise to electrons. The electron sample identified within collision data is compared to a fully reconstructed MB MC sample generated using a tuned version of PYTHIA. This MB MC sample consists of one million non-diffractive events and is designed to contain all types of collision events in proportion to the expected cross section.

Within the MC sample, only a small fraction of events include reconstructed electrons. Analysis of the truth origins of these electrons indicates that around two thirds are fake electrons to

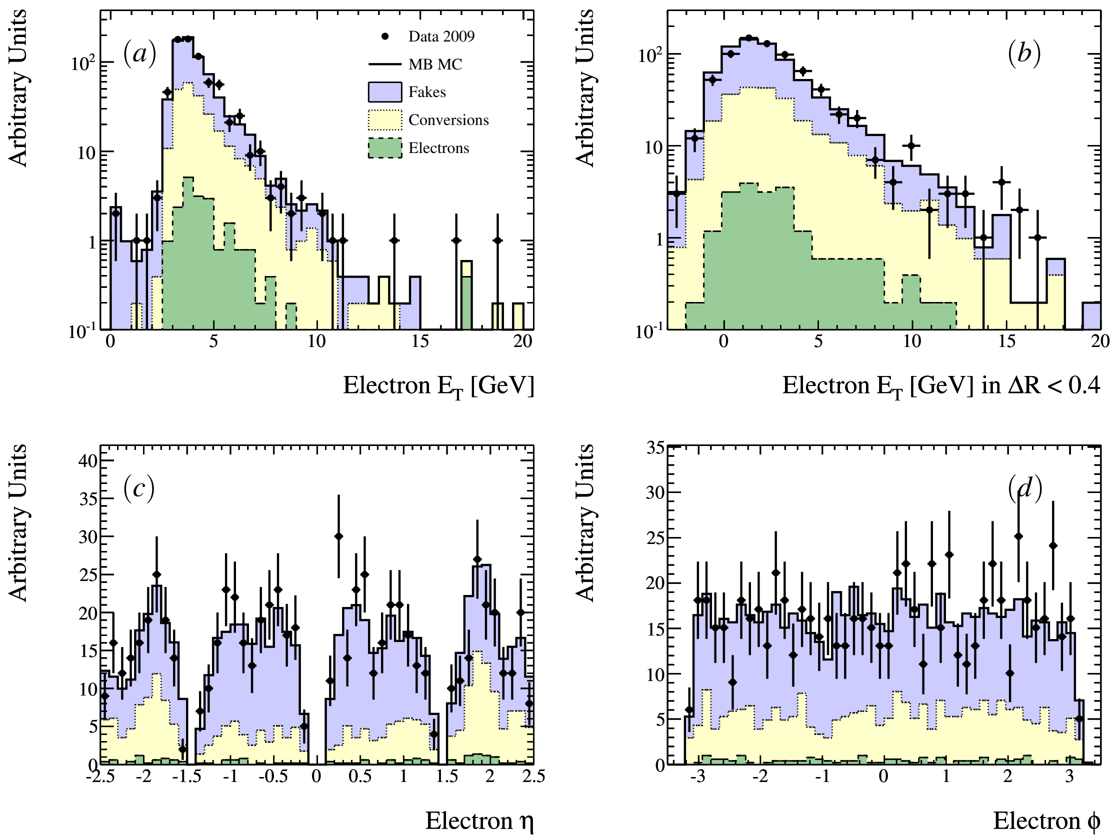

Figure 9.1: Kinematic distributions of electrons from data compared to MB MC. The variables shown are: (a) E_T; (b) $\mathrm{E}_T$cone; (c) η; and (d) ϕ.

which no truth electron can be matched. The majority of the other third are identified as originating from the conversions of photons, and a small remaining fraction ($\sim 4\%$) identified as electrons produced via the decays of light hadrons.

Some kinematic distributions of the 730 electrons found in data are shown in Figure 9.1 and compared to the results obtained from MB MC. The uncertainties shown on the distributions reflect only the statistical uncertainties on the numbers of identified electrons. The MB MC is subdivided by the truth origin of the reconstructed electrons. The MC distributions in this figure, and all subsequent figures is this chapter, have been normalised to the number of data entries in order for shape comparisons to be made. In future, studies such as these will normalise the MC to the measured integrated luminosity. However, at this very early stage such luminosity measures are still poorly understood. The observed electrons, both in data and MC, are seen in Figure 9.1 (a) to be located at very low transverse energies values with an exponential tail towards higher values. The η and ϕ distributions of these electron are shown in Figures 9.1 (c) and (d) respectively to be relatively evenly spread across the entire kinematic range. All three of these MC distributions are seen to be in reasonable agreement with the data, given the large statistical uncertainties. However, the $E_T$cone distribution, as shown in Figure 9.1 (b), observed in the data is seen to be systematically shifted towards slightly higher values than in the MC. Preliminary investigations in [88] have indicated that this can be partially explained by the lack of modelling of cross talk between neighbouring calorimeter cells in the simulation, with the remaining discrepancy explainable by an updated description of the amount of material upstream of the calorimeter in the MC. Overall good agreement is seen between the data and MC.

9.2 Electron Trigger Efficiency

In order to study the performance of the electron trigger with respect to the offline reconstruction, offline electrons were matched to `L1 EM3` trigger RoIs within $\Delta R < 0.15$. Of the 730 electrons identified, only 189 are present in events where the `L1 EM3` trigger was passed. Of these, 164 can be matched to L1 RoIs, and 162 and 160 to L2 and EF RoIs respectively. The low number of electrons matched to L1 objects is primarily due to the low E_T of these electrons, meaning that no `L1 EM3` RoI was created for many of them. The losses observed in the L1 to HLT object flow are due to a small number of HLT RoIs not being created because their extremely low energy resulted in the failure of the cluster seed finding algorithm [91].

MC studies indicate that the MBTS trigger selects non-diffractive MB events with 100 $+0, -2$% efficiency. This is confirmed by the studies seen in [50], which have measured the efficiency of the MBTS trigger from data to be above above 99% for events containing at least one track with p_T above 500 MeV. The inclusiveness of this trigger allows an unbiased extraction of the efficiency of `L1 EM3` to be performed simply by studying all the electrons in events selected by the MBTS trigger and comparing these to the number which are associated to `L1 EM3` RoIs. The efficiency of the trigger is determined by the ratio of the number of electrons which have associated `L1 EM3` RoIs to the total number of electrons.

The efficiency of the `L1 EM3` trigger measured in this way as a function of electron E_T is shown in Figure 9.2. Due to the low statistics the errors shown here are Bayesian. The efficiency curve displays the typical turn-on structure followed by a flat plateau. The plateau efficiency is seen to be above 95%, and for energies higher than 14 GeV to be nearly 100%. Good agreement is seen between the data and MC results. The small “bump” in the MC efficiency curve, observed at very low energies, has been identified as being the result of a small number of offline electrons having additional nearby energy deposits [87]. This additional energy has enabled these electrons to pass the L1 trigger due to the large cluster size utilised at L1. This feature is not expected to be present if more stringent electron selection criteria were to be applied, and not observed in the data due to the small statistics of the considered sample.

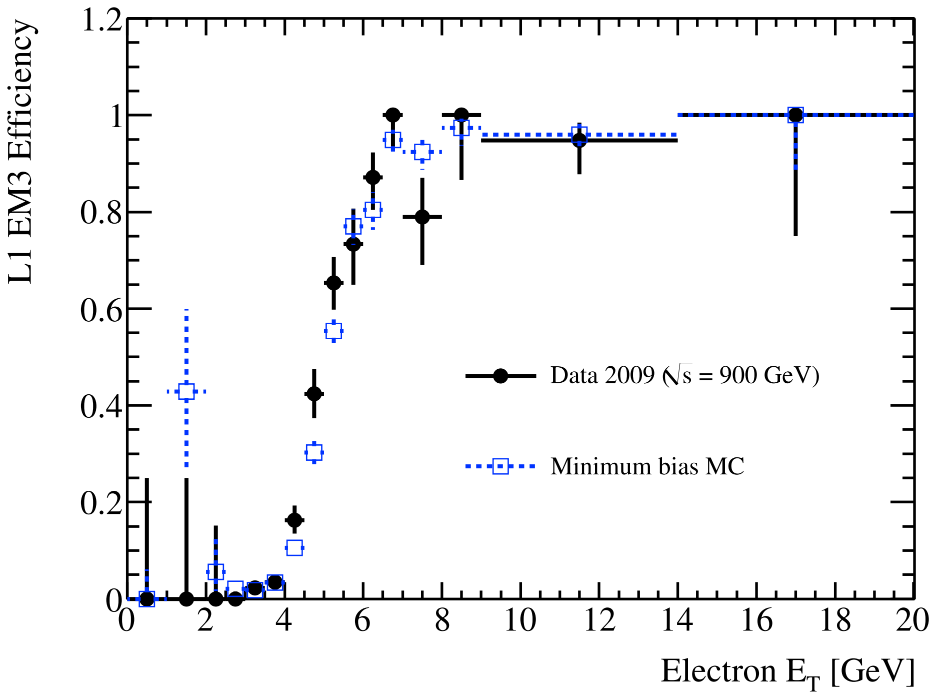

Figure 9.2: The efficiency of the L1 EM3 trigger in $\sqrt{s} = 900$ GeV data.

Table 9.1: The efficiency of the `L1 EM3` trigger to select electrons with $E_T > 7\,\mathrm{GeV}$ as obtained from data and MC.

Sample	`L1 EM3` efficiency (%)
Data	93 ± 5
MC	95 ± 2

Table 9.1 shows the efficiency of the `L1 EM3` trigger in selecting electrons with $E_T > 7\,\mathrm{GeV}$ as obtained from data and MC. As in Figure 9.2, the quoted errors are Bayesian and statistical only. The efficiency from the data is seen to be around 93%, with a large associated error of 5%. Good agreement is seen between this and the MC efficiency of 95$\pm$2%. Overall, the `L1 EM3` efficiency is seen to be high and to be well modelled in the MC.

9.3 Data to MC Comparisons of some Trigger Variables

The following section will examine some properties of electrons reconstructed by the electron trigger. Representative variables as seen at various trigger levels are compared to MC and to the corresponding offline variable. These studies are useful in verifying that the trigger is behaving as expected and that the MC is correctly modelling the real trigger behaviour.

9.3.1 L1 Variables

This section will present a study of some L1 variables important to the electron trigger selection as observed in the data, and will compare these to MC distributions and to the offline reconstruction.

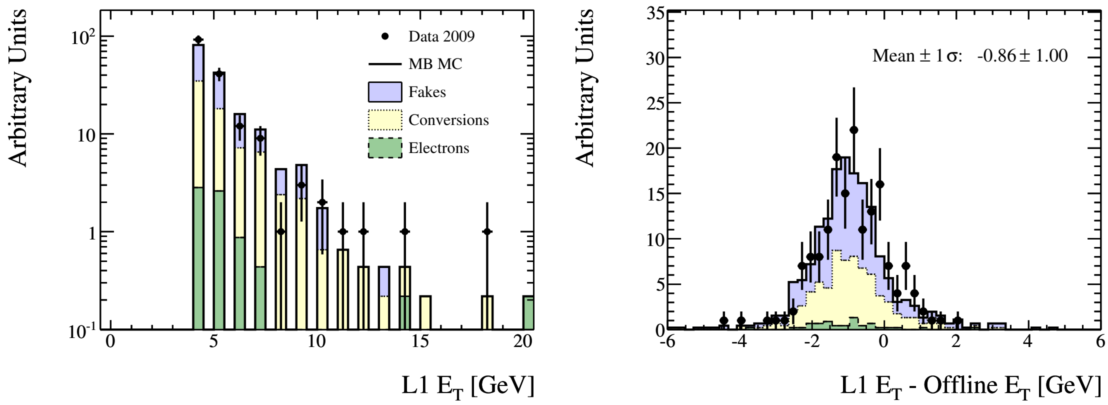

Figure 9.3: Comparisons of the distributions of the L1 E_T (left) and the difference between L1 E_T and offline E_T (right) for electrons in data and MC.

The electron E_T as reconstructed at L1 is shown in the left-hand plot of Figure 9.3 to fall exponentially with increasing E_T. This is inline with the distribution observed previously for all offline electrons. The L1 E_T is always above 3 GeV due to the threshold requirements of the `L1 EM3` trigger. The E_T "resolution", defined as the difference between the energy reconstructed by L1 and the energy reconstructed offline is shown in the right-hand plot of Figure 9.3. The mean value of the data points is at -860 MeV with a standard deviation of around 1 GeV. This indicates that the L1 is systematically underestimating the offline measure of transverse energy. The difference between the online and offline energies can be attributed to several different factors including the reduced granularity of L1, the differences in reconstruction algorithm and cluster size and the calibrations used at the time of processing. Both the observed L1 E_T spectrum and resolution are seen to be well reproduced by the MC to within the statistical errors. The agreement between L1 resolution in data and MC indicates that the observed differences in online and offline energy are well understood and modelled.

In addition to coarse energy resolution, L1 is also restricted in the precision to which the position of objects can be measured. The L1 η and ϕ resolutions, defined as the difference between the L1 and the offline coordinate are shown in Figure 9.4. The L1 η and ϕ coordinates are both observed to be systematically offset with respect to the offline by around 0.03. Such an offset is expected as a result of the methodology used for L1 coordinate determination. Unlike the HLT and offline algorithms, the determination of shower position at L1 is not based on the cluster

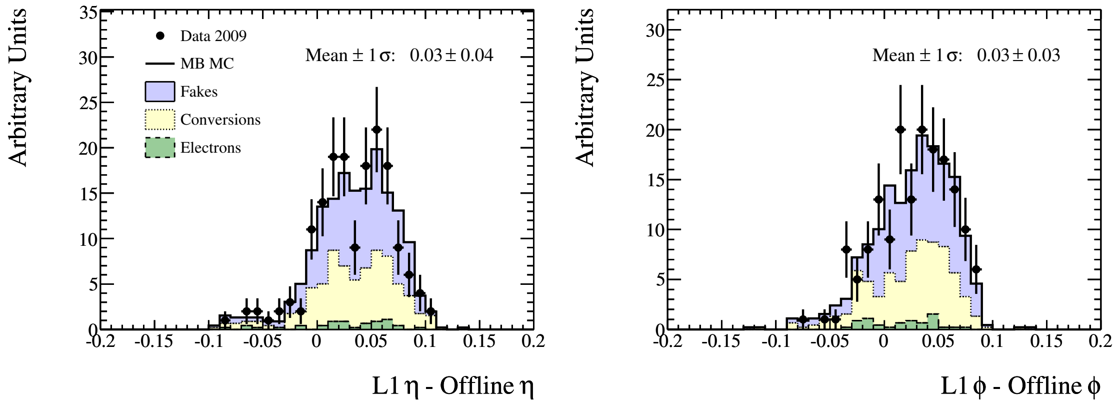

Figure 9.4: Comparisons of the distributions of the L1 η (left) and ϕ (right) resolutions for electrons in data and MC.

barycentre, but rather determined by the centre of the 4×4 window of $\Delta\eta \times \Delta\phi = 0.1 \times 0.1$ trigger towers which form the RoI. For narrow EM clusters, which are often wholly contained in a single trigger tower, this results in a systematic offset in the coordinate, since in this case the active tower will occupy the bottom-left corner of the clustering region. As the electrons studied here are not very energetic, they are expected to have narrow showers and therefore an offset L1 position as observed. The maximum offset between the L1 RoI position and the corresponding offline coordinate is observed to be around 0.1. This indicates that L1 is correctly identifying the cluster barycentre as an offset larger than 0.1 would not be contained in the RoI window. Overall, both the η and ϕ resolutions are seen to be well modelled by the MC.

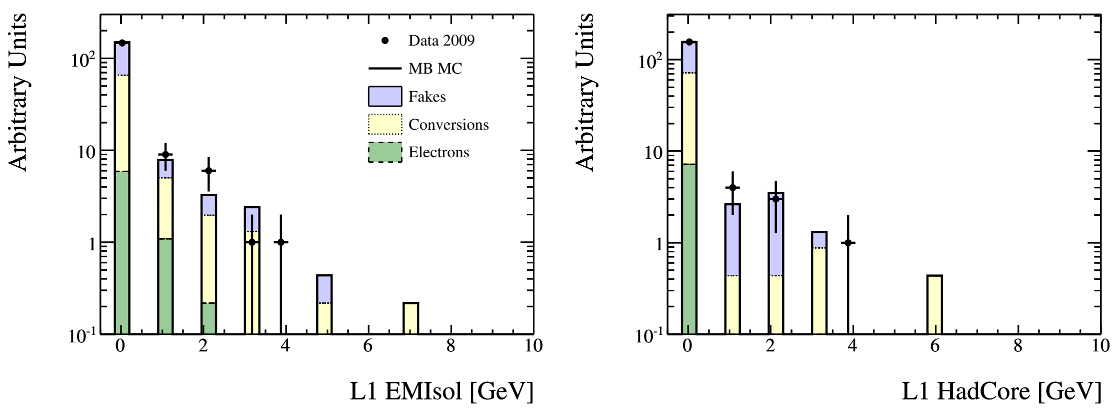

Figure 9.5: Comparisons of the distributions of the L1 isolation variables EMIsol (left) and HadCore (right) for electrons in data and MC.

During data taking phases with low instantaneous luminosity, an E_T cut on L1 EM RoIs alone is expected to be sufficient to control EM trigger rates. However, when instantaneous luminosities becomes higher, isolation variables will become increasingly important as a way to accept lower energy electrons than would otherwise be possible. The distributions of two representative L1 isolation variables, `EMIsol` and `HadCore` are shown in Figure 9.5. Similar to E_T, both isolation variables are seen to peak at low energies with exponential tails towards high values. The `EMIsol` shows a longer tail towards high energies than `HadCore`. For both variables agreement is seen between the data and MC to within the statistical errors. This indicates that, to the limited statistical precision available, the properties of L1 isolation variables are well understood.

9.3.2 HLT Variables

The HLT benefits from looser timing constraints than L1, as a result much more detailed information can be accessed and used to provide additional discrimination between electrons and backgrounds. The following section will present a comparison of some aspects of the HLT reconstruction in data to MC and to offline.

Both L2 and the EF have access to the full calorimeter granularity and refined calibrations, as a result each level calculates an increasingly refined measure of transverse energy. The electron

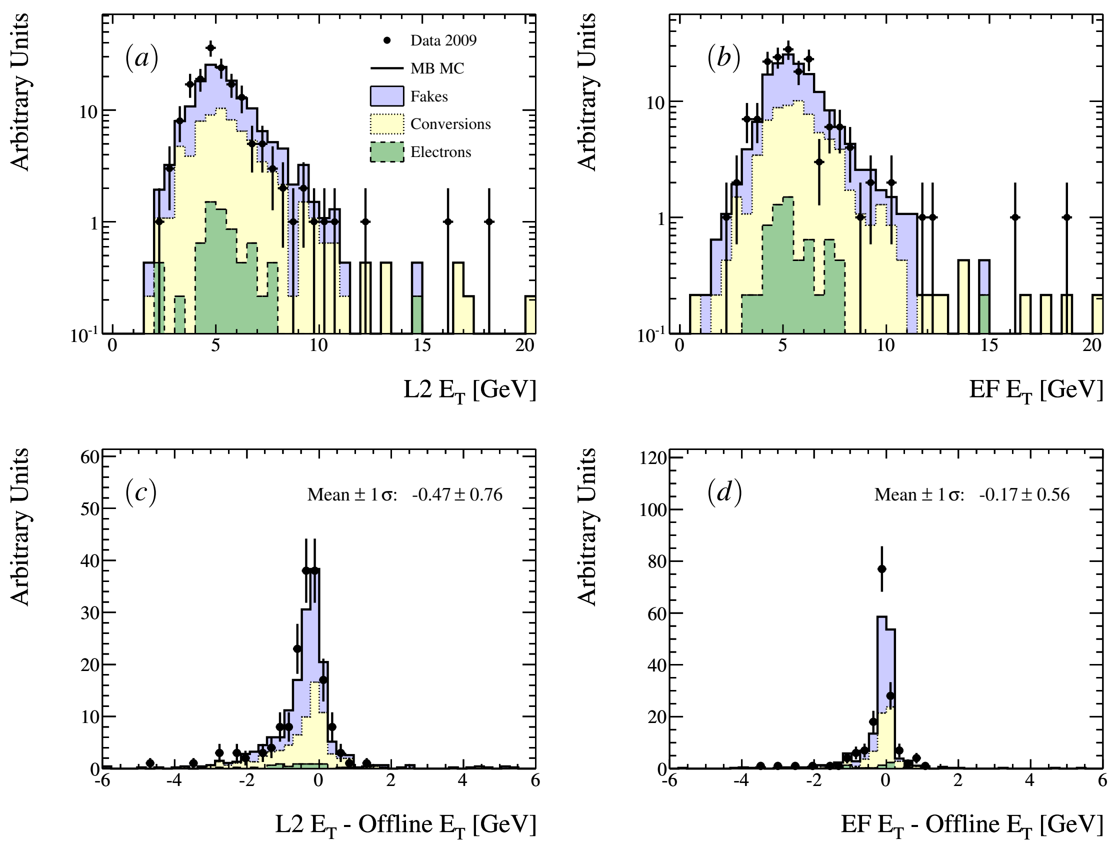

Figure 9.6: Comparisons of the the distributions of electron E_T as calculated by L2 (a) and the EF (b), and the corresponding E_T resolutions relative to offline: L2 (c); EF (d), for electrons in data and MC.

E_T as reconstructed by L2 is shown in Figure 9.6 (a) and as reconstructed by the EF in Figure 9.6 (b). A slight excess in data points is visible in the L2 energy distribution around 5 GeV. Otherwise, fair agreement is seen between data and MC to within the statistical uncertainties.

The difference between the electron energy as calculated at HLT and that calculated offline are shown in Figures 9.6 (c) and (d) for L2 and EF respectively. The L2 energy resolution has a mean value of -470 MeV, with a standard deviation of 760 MeV. This indicates that the L2 is systematically underestimating the offline E_T, although by considerably less than the -860 MeV seen at L1. The EF resolution has a mean value of -170 MeV and a standard deviation of 560 MeV. This is more consistent with the offline result than either of the previous levels. This is unsurprising, as the EF energy measurement reuses the offline methodology, although, unlike the offline reconstruction, the EF cluster size is not allowed to vary. These figures, along with the corresponding L1 distribution, clearly show the incremental improvement in energy measurement by the increasingly sophisticated trigger levels. The residual differences between HLT and offline values can be attributed to differences in calibrations and cluster sizes between online and offline measurements. In most cases the data is well described by the MC, although some slight deviations remain, although the limited statistics both in the data and the MC make it hard to make definite statements.

The η and ϕ resolutions defined as the difference between L2 and EF η and ϕ coordinates and those calculated offline are shown in Figure 9.7. Unlike the corresponding L1 distribution, the HLT angular resolutions are seen to be centred about zero and to show significantly reduced spreads. In all cases the MC resolution is seen to be in reasonably agreement with the data.

In addition to refining the information on the observed electrons, the HLT will reject non-electron candidates based on a series of shower shape and tracking variables. One such selection cut, R_η, is based on the ratio of the energy in the $\Delta\eta \times \Delta\phi = 3 \times 7$ to 7×7 calorimeter cells centred on the shower position. This is a measure of the width of the shower and serves to reject hadronic showers which are typically broader. For electrons, which are commonly well contained in 3×7 cells, this value should peak around one. The distributions of the R_η variable for electrons in data and MC are shown in Figure 9.8 at L2 (left) and EF (right). In both cases R_η is seen to be centred slightly below one, with the shape of the distribution observed to be very similar at L2 and EF. This figure shows general agreement in shape between the data and MC, although a slight shift towards lower values is observed in the data. This shift is also visible in some offline shower shape variables, such as $E_T$cone (as shown in Figure 9.1 (d)) and is believed to have the same cause [88].

Another shower variable that describes hadronic leakage, is defined as the amount of energy

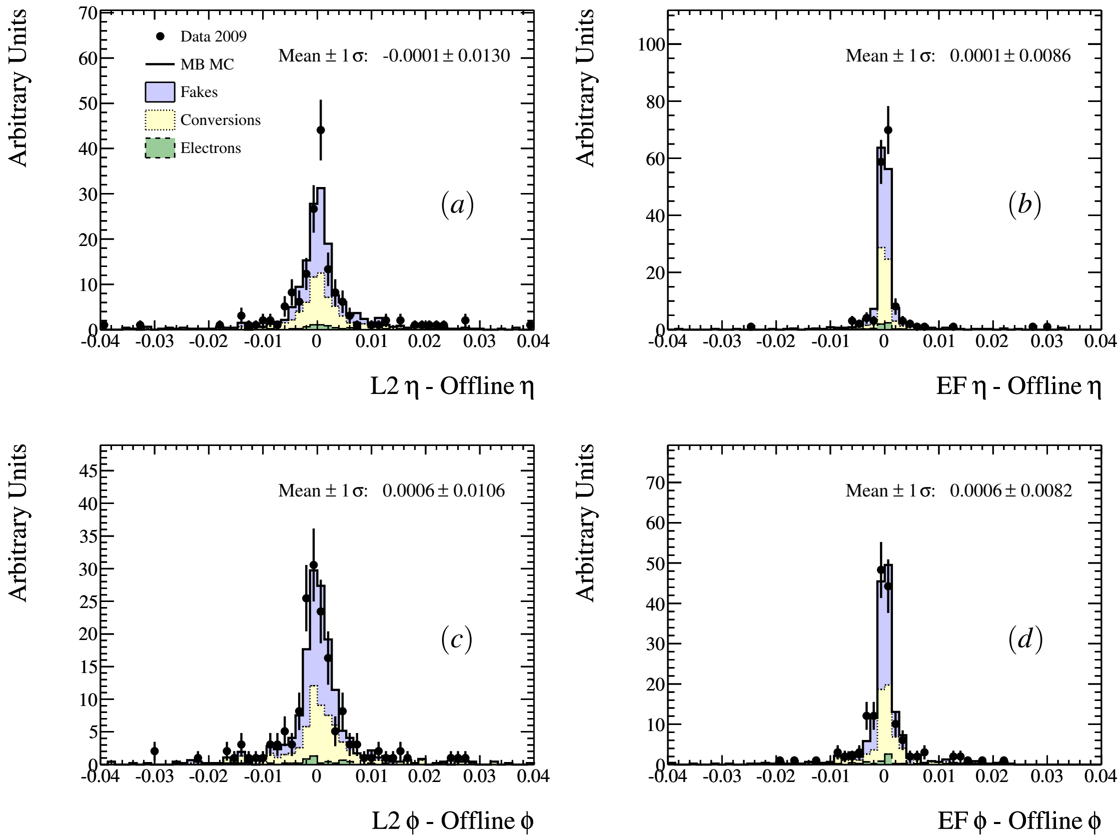

Figure 9.7: Comparisons of the the distributions of the HLT η resolutions relative to offline: L2 (a); EF (b), and the HLT ϕ for resolutions relative to offline: L2 (c), EF (d) for electrons in data and MC.

deposited in the first layer of the hadronic calorimeter directly behind the electron cluster. A typical isolated electron is expected to deposit less than 1% of its energy in this layer [57], whilst hadronic jets will deposit significantly more. The distribution of hadronic leakage for electrons in data and MC are shown in Figure 9.9 at L2 (left) and EF (right). In both cases the hadronic leakage is seen to be peak around zero with exponential tails towards higher values. This figure is seen to show good agreement between data and MC.

As well as calorimeter shower shape variables, the HLT also has access to information on the tracks of charged particle trajectories in the ID. This information can be used to provide additional separation between electrons and jets. One variable which utilises tracking information is the ratio of the cluster E_T to the track p_T (E/p). For isolated electrons E/p is expected to tend to one, as these often consist of a single track pointing to an isolated cluster. Conversely, diffuse hadronic jets will often distribute their p_T between many charged and neutral particles, therefore the E/p of such objects is expected to be lower than one. The distributions of E/p for electrons in data and MC are shown in Figure 9.10 at L2 (left) and EF (right). In both cases E/p is seen to peak slightly lower than one. This is expected, as the majority of reconstructed electrons in this sample

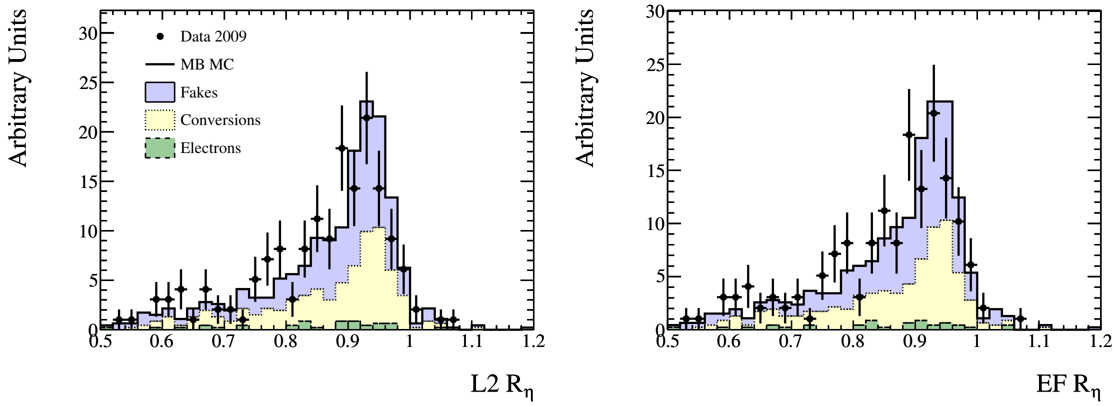

Figure 9.8: Comparisons of the distributions of the shower shapes variables R_η calculated at L2 (left) and EF (right) for electrons in data and MC.

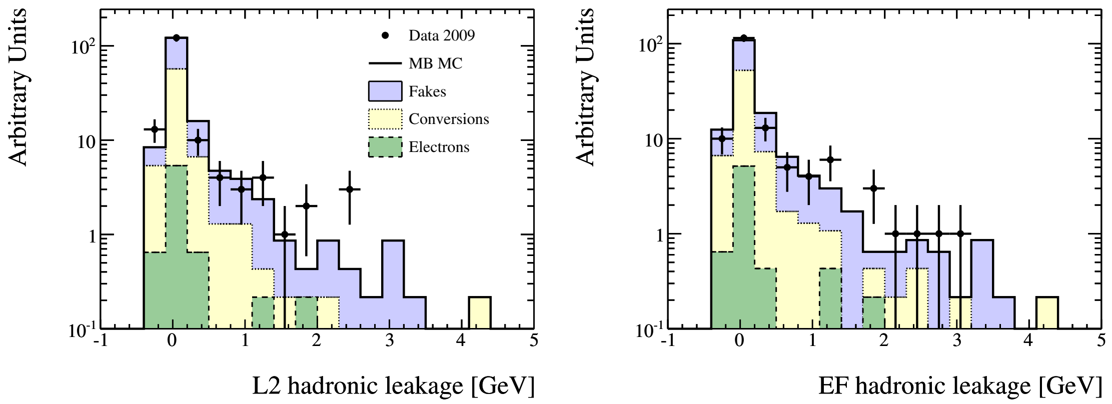

Figure 9.9: Comparisons of the distributions of the energy deposited in the first layer of the Hadronic Calorimeter as calculated at L2 (left) and EF (right) for electrons in data and MC.

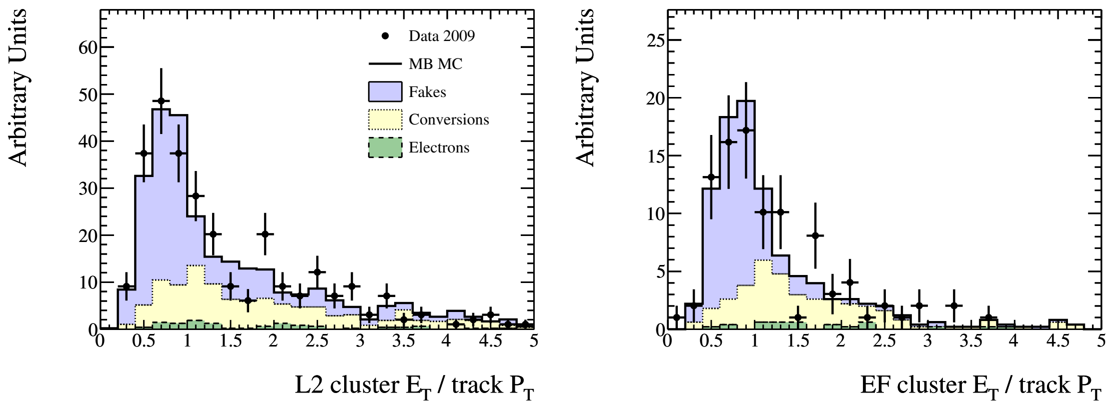

Figure 9.10: Comparisons of the distributions of the ratio of the cluster E_T to track p_T as calculated at L2 (left) and EF (right) for electrons in data and MC.

are not isolated electrons. The L2 peak is expected to be slightly broader than the EF peak due to the reduced L2 energy and momentum resolutions. Overall, reasonable agreement is seen between the data and MC.

9.4 Conclusions

Studies of the electrons in data from collisions at $\sqrt{s} = 900$ GeV indicate that both the detector and the trigger system are functioning well and performing as expected. Electrons identified in the data are seen to be well modelled by the MC, although some small discrepancies are observed in some shower shape variables. Previous studies in [88] have explained these differences via an updated material description and the improvement in the modelling of cross talk in the MC. The turn-on of the lowest threshold EM trigger, `L1 EM3`, has been extracted from data and agrees well with the results in MC. An efficiency plateau is observed above 7 GeV within which the efficiency is similar to 95% and flat as a function of E_T. Preliminary studies of trigger level variables in data have been shown to be in agreement with MC predictions. These results are a good indication that the electron triggers are robust and well optimised, and therefore in good shape to begin the rejection of events in 2010. Overall, the ATLAS detector behaved exceptionally well in this very early phase and the MC simulations are seen to generally be in good agreement with the collected data.

Chapter 10

Conclusions and Outlook

The Standard Model of particle physics provides an excellent description of three of the four fundamental forces of nature. However, it is known to be an incomplete theory, as it fails to offer a description of gravity, a solution to the hierarchy problem or a candidate particle for cold dark matter. SUSY offers solutions to a number of these outstanding issues by proposing a new fundamental symmetry relating bosons to fermions. If SUSY is to resolve these issues then it should also provide observable phenomenology in the TeV energy range accessible at the LHC. If ATLAS is to witness the signatures of SUSY, then the trigger system must be capable of identifying potential SUSY events from the overwhelming SM backgrounds.

This thesis has examined the efficiency of the ATLAS trigger to select leptons in a variety of BSM scenarios, including SUSY and models which propose new neutral resonances. The studies in Chapter 5 determined from Monte Carlo simulations that the single electron trigger has an excellent efficiency of above 96% to select isolated electrons such as those expected from the $Z \rightarrow e^+e^-$ process. A Tag and Probe method has been shown to be capable of determining the efficiencies for these isolated electrons to within a fraction of a percent, both as an overall number and differentially.

Unlike the $Z \rightarrow e^+e^-$ process, SUSY events are typically rich in energetic hadronic activity. In events of this kind it is not uncommon for electrons to be produced in proximity to highly energetic jets. Chapter 6 studied the efficiency of the electron trigger in these busy environments and showed that energy deposited near electrons results in a degradation in the trigger performance, such that prompt electrons in a SU4 SUSY benchmark point are only selected with 93% efficiency. It was shown that the contributions of nearby objects to the efficiency of the electron trigger can be quantified using the $E_T$cone variable which measures the amount of energy in a hollow cone surrounding the electron. This result was used to show that the $Z \rightarrow e^+e^-$ trigger efficiency was representative of electrons in busy events providing the efficiency was modelled differentially in the 3-dimensions of E_T, η, and $E_T$cone. However, the inclusion of non-prompt and fake electrons reduces the accuracy of this description.

Chapter 7 went on to show that both the electron and muon triggers successfully select energetic leptons with a high efficiency across large regions of the model parameter space. However, some slight inefficiencies remain at low SUSY mass scales where the majority of leptons are typically not very energetic and therefore fail to meet the energy threshold requirements of the trigger. It was shown that for trilepton SUSY searches these efficiency losses could be compensated for by orthogonal trigger streams such as jets or E_T^{miss}.

Chapter 8 moved away from SUSY, to study the electron trigger efficiency for the very energetic electrons characteristic of heavy BSM neutral resonances. Electron trigger efficiencies were shown to be consistently high for all studied resonances for triggers that did not require isolation at L1. Conversely, efficiencies were seen to fall off with increasing E_T for isolated triggers due to lack of containment of the EM shower at L1. A 2-dimensional measure of the $Z \rightarrow e^+e^-$ trigger efficiency was shown to well reproduce the efficiencies for non-isolated triggers at high energies, based on an extrapolation from the intermediate E_T range where Z statistics are copious.

The final chapter of this thesis studied the electrons in early ATLAS data from LHC collisions at $\sqrt{s} = 900$ GeV. Electrons identified in the data were generally seen to be well modelled by the MC, although some small discrepancies were observed in some shower shape variables. The turn-on of the lowest threshold EM trigger, `L1 EM3`, was measured from data and seen to agree well with the MC results. An efficiency plateau was observed above 7 GeV within which the efficiency is around 93% and flat as a function of E_T. Preliminary studies of trigger level variables in data have shown these to be in agreement with MC predictions. This indicates that the electron triggers are robust and well optimised, and therefore in good shape to begin the rejection of events in 2010.

The studies in this thesis have shown that the ATLAS electron (and muon) triggers are capable of selecting leptons within SUSY and heavy BSM neutral resonance events with a very high efficiency. In all cases these efficiencies can be measured from data using the Tag and Probe method, thus reducing the consequent reliance on MC. Preliminary studies of the first LHC collisions have indicated that the electron trigger is behaving as expected and that this behaviour is well modelled by MC.

Following the 2009 low energy running period, the LHC was shut down over the winter before restarting in early 2010. Within a few months, collisions had been achieved at 7 TeV, half the design energy of the LHC. The current LHC schedule is to maintain stable running and collisions at 7 TeV throughout 2010 and 2011, with the aim of collecting a total integrated luminosity of $1\,\mathrm{fb}^{-1}$. To date, this plan is proceeding well and the understanding of both the LHC and the ATLAS detector is advancing steadily.

On May 24th 2010, the electron HLT entered rejection mode for the first time. The rate for the lowest threshold L1 trigger `L1 EM2` was observed to be stable at around 300 Hz at an instantaneous luminosity of around 1.7×10^{29} cm^{-2}s^{-1}. The trigger `e3 loose` was then enabled at L2 and EF and was seen to reduce the pass rate to 46 Hz and 17 Hz respectively. On June 3rd 2010 the first ATLAS results were published describing the observation of W and Z bosons in data [93]. These represent just the first of many important milestones on a journey that will culminate in the expansion of the understanding of the the field of particle physics.

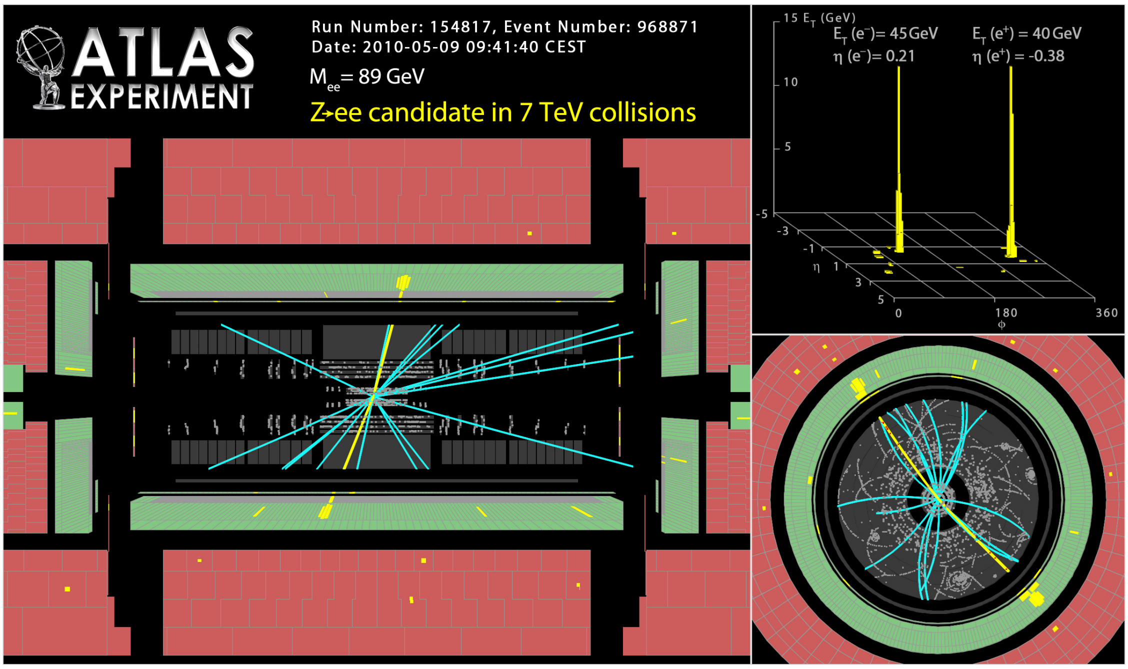

Figure 10.1: A Z→e^+e^- candidate event from $\sqrt{s}$ = 7 TeV running, from [94].

Appendix A

Data Samples

A.1 MC Samples for $\sqrt{s} = 14$ TeV

The following ATLAS MC samples were used for the analysis presented in Chapters 5 and 6 of this thesis:

Table A.1: The logical file names of the Monte Carlo samples studied in Chapters 5 and 6.

Sample	Dataset	σ [pb^{-1}]
Single e	trig1_misal1_mc12.007020.singlepart_e_Et7-80.recon.AOD.v13003003	-
	trig1_misal1_mc13.007023.singlepart_e_Et80-500.recon.AOD.v13003003	-
Z→e^+e^-	trig1_misal1_mc12.005144.PythiaZee.recon.ESD.v13003004	2069
$t\bar{t}$	trig1_misal1_mc12.005205.AcerMCttbar.recon.ESD.v13003004	436
SU3	trig1_misal1_csc11.005403.SU3_jimmy_susy.recon.ESD.v13003003	27.7
SU4	trig1_misal1_mc12.006400.SU4_jimmy_susy.recon.AOD.v13004005	402

These samples were produced centrally by the official ATLAS production team and fully simulated and analysed using Athena version 13 for a nominal LHC centre of mass energy of 14 TeV. The MC generators used were PYTHIA for Z→e^+e^-, AcerMC for $t\bar{t}$ and HERWIG with the Jimmy underlying event modelling for the SU3 and SU4 samples. The quoted cross sections are at NLO and taken from [95].

A.2 MC Samples for $\sqrt{s} = 10$ TeV

The following ATLAS MC samples were used for the analysis presented in Chapters 6 and 7 of this thesis:

Table A.2: The logical file names of the Monte Carlo samples studied in Chapters 6 and 7.

Sample	Dataset	σ [pb^{-1}]
Athena version 14 samples		
$Z \rightarrow e^+e^-$	mc08.106050.PythiaZee_1Lepton.recon.AOD.e347_s462_r604/	1098
$Z \rightarrow \mu^+\mu^-$	mc08.106061.McAtNloZmumu_1Lepton.recon.AOD.e349_s462_r635/	1098
$t\bar{t}$	mc08.105200.T1_McAtNlo_Jimmy.recon.AOD.e357_s462_r635/	217
SU4	mc08.106400.SU4_jimmy_susy.recon.AOD.e352_s462_r635/	171
Athena version 15 samples		
$t\bar{t}$	mc08.105200.T1_McAtNlo_Jimmy.merge.AOD.e357_s462_s520_r809_r838/	217
SU4	mc08.106400.SU4_jimmy_susy.merge.AOD.e352_s462_s520_r808_r838/	171

These samples were produced centrally by the official ATLAS production team and fully simulated, at a nominal LHC centre of mass energy of 10 TeV, and analysed using two different Athena versions: 14 and 15. The MC generators used were PYTHIA for $Z \rightarrow e^+e^-$, MC@NLO for $t\bar{t}$ and $Z \rightarrow \mu^+\mu^-$, and HERWIG with the Jimmy underlying event modelling for the SU4 samples. The studies in Section 6.3.2 of Chapter 6 use the version 15 samples, whilst the studies in Chapter 7 use the version 14 samples. The quoted $t\bar{t}$ and SU4 cross sections are at NLO, whilst the Z cross sections are at LO, all are taken from [95].

In addition, Chapter 7 also studied a large number of SUSY grid points, details of which can be found in [96]. These were generated using HERWIG with the Jimmy modelling of the underlying event and the detector response simulated using ATLFAST-II in Athena version 14.

A.3 Dielectron MC Samples

The following ATLAS MC samples were used for the heavy BSM neutral resonances analysis presented in Chapter 8 of this thesis:

Table A.3: The logical file names of the Monte Carlo samples studied in Chapter 8.

Sample	Dataset	σ [pb^{-1}]
Z	mc08.106050.PythiaZee_1Lepton.recon.AOD.e347_s462_r604	1098
G [300 GeV]	mc08.105616.Pythia_Gee_300.recon.AOD.e355_s462_r604	0.834
Z' [1 TeV]	mc08.105603.Pythia_Zprime_ee_SSM1000.recon.AOD.e352_s462_r604	0.249
Z' [1.5 TeV]	mc08.105624.Pythia_Zprime_ee_SSM1500.recon.AOD.e357_s462_r604	0.076
Drell-Yan	mc08.105417.Pythia_DYee_75M120.merge.AOD.e447_s495_r635_t53/	573
	mc08.105418.Pythia_DYee_120M250.merge.AOD.e447_s495_r635_t53/	7.17
	mc08.105419.Pythia_DYee_250M400.merge.AOD.e447_s495_r635_t53/	0.425
	mc08.105420.Pythia_DYee_400M600.merge.AOD.e447_s495_r635_t53/	8.30×10^{-2}
	mc08.105421.Pythia_DYee_600M800.merge.AOD.e447_s495_r635_t53/	1.62×10^{-2}
	mc08.105422.Pythia_DYee_800M1000.merge.AOD.e447_s495_r635_t53/	4.52×10^{-3}
	mc08.105423.Pythia_DYee_1000M1250.merge.AOD.e447_s495_r635_t53/	1.77×10^{-3}
	mc08.105424.Pythia_DYee_1250M1500.merge.AOD.e447_s495_r635_t53/	5.51×10^{-4}
	mc08.105425.Pythia_DYee_1500M1750.merge.AOD.e447_s495_r635_t53/	1.98×10^{-4}
	mc08.105426.Pythia_DYee_1750M2000.merge.AOD.e447_s495_r635_t53/	7.62×10^{-5}
	mc08.105427.Pythia_DYee_M2000.merge.AOD.e447_s495_r635_t53/	5.59×10^{-5}

These samples were produced centrally by the official ATLAS production team and fully simulated and analysed using Athena version 14 for a nominal LHC centre of mass energy of 10 TeV. The PYTHIA MC generator was used to produce every sample. The quoted cross sections are at LO and taken from [95].

A.4 Data Samples

The following LHC runs were used for the studies of collision data presented in Chapter 9 of this thesis:

Table A.4: The number of events, `L1 EM3` RoIs and reconstructed electrons per run studied in Chapter 9. Only runs in the GRL (as defined in the text), with more than one EM3 object are included.

Run Number	Triggered MB events	GRL	L1 EM3 objects	Electrons
141749	19,317	8,986	4	18
141811	38,941	13,471	14	26
142149	11,009	1,238	1	0
142154	7,827	2,156	4	5
142165	162,192	62,001	66	109
142166	83,111	39,407	50	75
142174	18,654	12,467	17	23
142191	113,553	59,264	73	105
142193	153,499	91,828	123	183
142195	61,662	47,039	46	110
142383	233,544	45,970	55	76
Total	903,309	383,827	453	730

These samples were collected between the 6th and the 15th of December 2009 at a centre of mass energy of 900 GeV. They were reconstructed and analysed using Athena version 15. The MB MC sample to which the data was compared was:

```
mc09_900GeV.105001.pythia_minbias.recon.AOD.e500_s656_s658_d267_r1029/
```

which was produced centrally by the official ATLAS production team using the PYTHIA MC generator at a centre of mass energy of 900 GeV and fully simulated and analysed using Athena version 15.

Appendix B

The Calculation of Errors for Weighted Average Efficiencies

The efficiency for an electron with values of parameters i and j ($\varepsilon'_{i,j}$) is given by:

$$\varepsilon'_{i,j} = \varepsilon_{i,j}, \tag{B.1}$$

where $\varepsilon_{i,j}$ is the measured efficiency in the bin i, j. Generalising this to give the efficiency of all electrons $N_{i,j}$ in bin i, j, we get:

$$\varepsilon'_{i,j} = \frac{\varepsilon_{i,j}.N_{i,j}}{N_{i,j}}. \tag{B.2}$$

If we then integrate over one of the dimensions, in this case the dimension of j, we get:

$$\varepsilon'_{i} = \frac{\sum_j(\varepsilon_{i,j}.N_{i,j})}{N_i}. \tag{B.3}$$

The variance (V) on ε'_i is given by:

$$V[\varepsilon'_i] = \frac{1}{N_i^2}V[\sum_j N_{i,j}\varepsilon_{i,j}], \tag{B.4}$$

which is equivalent to:

$$V[\varepsilon'_i] = \frac{1}{N_i^2}\sum_j V[N_{i,j}\varepsilon_{i,j}], \tag{B.5}$$

where $V[N_{i,j}]$ is given by the binomial distribution across the bins j as shown by:

$$V[N_{i,j}] = \frac{N_{i,j}}{N_i}(1-\frac{N_{i,j}}{N_i})N_i \tag{B.6}$$

and $V[\varepsilon_{i,j}]$ is simply the variance on the efficiency. Finally using error propagation we arrive at the following complete equation for $V[\varepsilon'_i]$:

$$V[\varepsilon'_i] = \frac{1}{N_i^2}\sum_j (N_{i,j}\varepsilon_{i,j})^2 \left[\frac{(1-\frac{N_{i,j}}{N_i})}{N_{i,j}} + \frac{V[\varepsilon_{i,j}]}{\varepsilon_{i,j}^2}\right]. \tag{B.7}$$

Bibliography

[1] D. Griffiths, *Introduction to Elementary Particles*, 2nd Edition, Wiley-VCH, (2009).

[2] F. Halzen, A. D. Martin, *Quarks and Leptons: An Introductory Course in Modern Particle Physics*, John Wiley and Sons, (1984).

[3] C. Kraus *et al.*, *Final results from phase II of the Mainz neutrino mass search in tritium beta decay*, Eur.Phys.J. **C40** (2005) 447–468.

[4] K. Assamagan *et al.*, *Upper limit of the muon-neutrino mass and charged pion mass from momentum analysis of a surface muon beam*, Phys. Rev. **D53** (1996) 6065–6077.

[5] C. Amsler *et al.*, (Particle Data Group), *Review of Particle Physics*, Phys. Lett. **B667** (2008 and 2009 partial update for the 2010 edition).

[6] P. W. Higgs, *Broken Symmetries and the Masses of Gauge Bosons*, Phys. Rev. Lett. **13** (1964) 508–509.

[7] C. Yang, R. Mills, *Conservation of Isotopic Spin and Isotopic Gauge Invariance*, Phys. Rev. **96** (1954) 191–195.

[8] P. Dirac, *The Quantum Theory of the Electron*, Proc. R. Soc. **A117** (1928) 610–624.

[9] S. L. Glashow, *Partial symmetries of weak interactions*, Nucl. Phys. **22** (1961) 579–588.

[10] S. Weinberg, *A model of leptons*, Phys. Rev. Lett. **19** (1967) 1264–1266.

[11] A. Salam, *Weak and electromagnetic interactions*, Proc. of the 8th Nobel Symposium on *Elementary particle theory, relativistic groups and analyticity* (1968) 367–377.

[12] N. Cabibbo, *Unitary Symmetry and Leptonic Decays*, Phys. Rev. Lett. **10** (1963) 531–533.

[13] G. 't Hooft, *Renormalization of massless Yang-Mills fields*, Nucl. Phys. B. **33** (1971) 173–199.

[14] The ALEPH, DELPHI, L3, and OPAL Collaborations, (LEP Working Group for Higgs Boson Searches), *Search for the Standard Model Higgs Boson at LEP*, Phys. Lett. **B565** (2003) 61–75.

[15] H. Aaltonen *et al.*, (CDF and D0 Collaborations), *Combination of Tevatron searches for the standard model Higgs boson in the W^+ W decay mode*, arXiv:hep-ex/1001.4162 (2010).

[16] S. Weinberg, *Implications of dynamical symmetry breaking*, Phys. Rev. **D13** (1976) 974–996.

[17] G. D'Amico, M. Kaminokowski, K. Sigurdson, *Dark Matter Astrophysics*, arXiv:astro-ph/0907.1912v1 (2009).

[18] The WMAP Collaboration, *Seven-Year Wilkinson Microwave Anisotropy Probe (WMAP) Observations: Cosmological Interpretation*, arXiv:astro-ph/1001.4538 (2010).

[19] J. Wess, B. Zumino, *A Lagrangian Model Invariant under Supergauge Transformations*, Phys. Rev. Lett. **B49** (1974) 52–54.

[20] S. P. Martin, *A Supersymmetry Primer*, arXiv:hep-ph/970935v4 (2006).

[21] The Super-Kamiokande Collaboration, *Search for Proton Decay vis $p \to e^+\pi^0$ in a Large Water Cherenkov Detector*, Phys. Rev. Lett. **81** (1998) 3319–3323.

[22] P. Nilles, H, *Dynamically Broken Supergravity and the Hierarchy Problem*, Phys. Rev. Lett. **B115** (1982) 193–196.

[23] F. Giudice, G, R. Rattazzi, *Theories with Gauge-Mediated Supersymmetry Breaking*, Phys. Rev. **322** (1999) 419–499.

[24] J. Ellis *et al.*, *Supersymmetric Dark Matter in Light of WMAP*, arXiv:hep-ph/0303043v1 (2003).

[25] B. Allanach, C. Lester, *Multi-Dimensional mSUGRA Likelihood Maps*, arXiv:hep-ph/0507283v5 (2006).

[26] C. Potter, *The Search for Evidence of Supersymmetry in Trilepton Final States at the LHC*, CERN-THESIS-2009-030.

[27] The ATLAS Collaboration, *Supersymmetry* in *Expected Performance of the ATLAS Experiment - Detector, Trigger and Physics*, CERN-OPEN-2008-020.

[28] H. Baer, F. Paige, S. Protopopescu, *Simulating Supersymmetry with ISAJET 7.0/ISASUSY 1.0*, arXiv:hep-ph/9305342v1 (1993).

[29] W. Beenakker, R. Hoepker, M. Spira, *PROSPINO: A Program for the Production of Supersymmetric Particles in Next-to-leading Order QCD.*, arXiv:hep-ph:9611232v1 (1996).

[30] H. Georgi, S. Glashow, *Unity of All Elementary-Particle Forces*, Phys. Rev. Lett. **32** (1974) 438–441.

[31] P. Langacker, *The Physics of Heavy Z' Gauge Bosons*, arXiv:hep-ph/0801.1345v2 (2008).

[32] The DELPHI Collaboration, *Measurement and interpretation of fermion-pair production at LEP energies above the Z resonance.*, Eur.Phys.J. **C45** (2006) 589–632.

[33] The CDF Collaboration, *Search for new physics in high mass electron-positron events in p anti-p collisions at* $\sqrt{s} = 1.96 TeV$, Phys. Rev. Lett. **99** (2007) 171802.

[34] T. G. Rizzo, *Pedagogical Introduction to Extra Dimensions*, SLAC-PUB-10753 (2004).

[35] A. Perez-Lorenzana, *An Introduction to Extra Dimensions*, arXiv:hep-ph/0503177v2 (2005).

[36] L. Randall, R. Sundrum, *Large Mass Hierarchy from a Small Extra Dimension*, Phys. Rev. Lett. **83** (1999) 3370–3373.

[37] O.S. Bruning *et al.* (eds.), *The LHC design report v.1 : the LHC Main Ring*, CERN-2004-003-V-1; *The LHC design report v.2 : the LHC Infrastructure and General Services*, CERN-2004-003-V-2; M. Benedikt *et al.* (eds.), *The LHC design report v.3 : the LHC Injector Chain*, CERN-2004-003-V-3 (2004).

[38] L. Evans, P. Bryant, *LHC Machine*, Journal of Instrumentation **3**, S08001 (2008).

[39] The ALICE Collaboration, *The ALICE Experiment at the CERN LHC*, Journal of Instrumentation **3**, S08002 (2008).

[40] The ATLAS Collaboration, *The ATLAS Experiment at the CERN Large Hadron Collider*, Journal of Instrumentation **3**, S08003 (2008).

[41] The CMS Collaboration, *The ATLAS Experiment at the CERN LHC*, Journal of Instrumentation **3**, S08004 (2008).

[42] The LHCb Collaboration, *The LHCb Detector at the LHC*, Journal of Instrumentation **3**, S08005 (2008).

[43] The TOTEM Collaboration, *The TOTEM Experiment at the CERN Large Hadron Collider*, Journal of Instrumentation **3**, S08007 (2008).

[44] The LHCf Collaboration, *The LHCf Detector at the CERN Large Hadron Collider*, Journal of Instrumentation **3**, S08006 (2008).

[45] The CERN Document Server: `http://cdsweb.cern.ch`.

[46] The ATLAS Collaboration, *ATLAS Detector and Physics Performance Technical Design Report*, ATLAS-TDR-014 (1999).

[47] C. Grupen, *Particle Detectors*, 1st Edition, Cambridge, (1996).

[48] The ATLAS Collaboration, *ATLAS Calorimeter Performance Technical Design Report*, CERN/LHCC/96-40 (1997).

[49] The ATLAS Collaboration, *ATLAS Trigger Performance: Status Report*, CERN/LHCC/98-15 (1998).

[50] The ATLAS Collaboration, *Performance of the Minimum Bias Trigger in p-p Collisions at $\sqrt{s}$ = 900 GeV*, ATLAS-CONF-2010-025.

[51] The ATLAS Collaboration, *ATLAS First-Level Trigger Technical Design Report*, CERN-LHCC-98-14 (1998).

[52] The ATLAS Collaboration, *ATLAS High-Level Trigger, Data Aquisition and Controls Technical Design Report*, CERN-LHCC-2003-022.

[53] H. P. Beck, *Triggering at High Luminosity Colliders*, New J.Phys. **9** (2007) 334.

[54] The CMS Collaboration, *CMS Collaboration DAQ generic figures gallery*.

[55] A. Gesualdi-Mello *et al.*, *Overview of the High-Level Trigger Electron and Photon Selection for the ATLAS Experiment at the LHC*, IEEE Trans. Nucl. Sci. **5** (2002) 2839–2843.

[56] The ATLAS Collaboration, *HLT Track Reconstruction Performance* in *Expected Performance of the ATLAS Experiment - Detector, Trigger and Physics*, CERN-OPEN-2008-020.

[57] The ATLAS Collaboration, *Reconstruction and Identification of Electrons* in *Expected Performance of the ATLAS Experiment - Detector, Trigger and Physics*, CERN-OPEN-2008-020.

[58] The ATLAS Collaboration, *Physics Performance Studies and Strategy of the Electron and Photon Trigger Selection* in *Expected Performance of the ATLAS Experiment - Detector, Trigger and Physics*, CERN-OPEN-2008-020.

[59] The ATLAS Collaboration, *Performance of the Muon Trigger Slice with Simulated Data* in *Expected Performance of the ATLAS Experiment - Detector, Trigger and Physics*, CERN-OPEN-2008-020.

[60] A. Venture, *The Muon High Level Trigger of the ATLAS Experiment*, ATL-DAQ-PROC-2009-010.

[61] The ATLAS Collaboration, *Trigger for Early Running* in *Expected Performance of the ATLAS Experiment - Detector, Trigger and Physics*, CERN-OPEN-2008-020.

[62] The ATLAS Collaboration, *ATLAS Computing: Technical Design Report*, ATLAS-TDR-017 (2005).

[63] A. Moraes, C. Buttar, I. Dawson, *Prediction for minimum bias and the underlying event at LHC energies*, Eur.Phys.J. **C50** (2007) 435–466.

[64] The ATLAS Collaboration, *The ATLAS Simulation Infrastructure*, arXiv:hep-ph/1005.4568v1 (2010).

[65] W. Tung, H. Lai, J. Pumplin, P. Nadolsky, C. Yuan, *Global QCD Analysis and Collider Phenomenology-CTEQ*, arXiv:hep-ph/0707.0275v1 (2007).

[66] T.Sjöstrand and S.Mrenna and P.Skands, *PYTHIA 6.4 Physics and Manual*, JHEP **0609** (2006) 033.

[67] G. Corcella, *et al.*, *HERWIG 6.5: and event generation for Hadron Emission Reactions With Interfering Gluons (including supersymmetric processes)*, JHEP **0101** (2001) 010.

[68] S. Frixione, P. Nason, B. Webber, *Matching NLO QCD and parton showers in heavy flavour production*, JHEP **0308** (2002) 007.

[69] B. Kersevan, R.-W. E., *The Monte Carlo Event Generator AcerMC 2.0 with Interfaces to PYTHIA 6.2 and HERWIG 6.5*, arXiv:hep-ph/0405247v1 (2004).

[70] J. Butterworth, J. Forshaw, M. Seymour, *Multiparton Interactions in Photoproduction at HERA*, Z. Phys **C72** (1996) 637–646.

[71] S.Agostinelli *et al.*, *Geant4 - a simulation toolkit*, Nucl. Instrum. Meth. **A506** (2003) 250–303.

[72] D. Cavalli *et al.*, *Performance of the ATLAS fast simulation ATLFAST*, ATL-PHYS-INT-2007-005.

[73] D. Adams *et al.*, *The ATLFAST-II performance in release 14 -particle signatures and selected benchmark processes*, ATL-PHYS-INT-2009-110.

[74] The ATLAS Collaboration, *Reconstruction and Identification of Electrons* in *Expected Performance of the ATLAS Experiment - Detector, Trigger and Physics*, CERN-OPEN-2008-020.

[75] The ATLAS Collaboration, *Muon Reconstruction and Identification: Studies with Simulated Monte Carlo Samples* in *Expected Performance of the ATLAS Experiment - Detector, Trigger and Physics*, CERN-OPEN-2008-020.

[76] The ATLAS Collaboration, *Jet Reconstruction Performance* in *Expected Performance of the ATLAS Experiment - Detector, Trigger and Physics*, CERN-OPEN-2008-020.

[77] The ATLAS Collaboration, *Measurement of Missing Transverse Energy* in *Expected Performance of the ATLAS Experiment - Detector, Trigger and Physics*, CERN-OPEN-2008-020.

[78] D. Casadei, *How to measure efficiency*, arXiv:physics.data-an:0908.0130v3 (2009).

[79] The ATLAS Collaboration, *HLT electron hypothesis algorithms* :
`https://twiki.cern.ch/twiki/bin/view/Atlas/TrigHLTelectronHypo`.

[80] The ATLAS Collaboration, *Expected Performance of the ATLAS Experiment - Detector, Trigger and Physics*, CERN-OPEN-2008-020.

[81] L. Di Ciaccio, C. Goy, S. Jezequel, R. Zitoun, *Early extraction of the Zee signal using the Atlas detector*, ATL-PHYS-INT-2007-006.

[82] The ATLAS Collaboration, *MCTruthClassifier*:
`https://twiki.cern.ch/twiki/bin/view/AtlasProtected/MCTruthClassifier`.

[83] The ATLAS Collaboration, *Prospects for Supersymmetry Discovery Based on Inclusive Searches* in *Expected Performance of the ATLAS Experiment - Detector, Trigger and Physics*, CERN-OPEN-2008-020.

[84] The ATLAS Collaboration, *Multi-Lepton Supersymmetry Searches* in *Expected Performance of the ATLAS Experiment - Detector, Trigger and Physics*, CERN-OPEN-2008-020.

[85] The ATLAS Collaboration, *Dilepton Resonances at High Mass* in *Expected Performance of the ATLAS Experiment - Detector, Trigger and Physics*, CERN-OPEN-2008-020.

[86] The ATLAS Collaboration, *Charged-particle multiplicities in pp interactions at* $\sqrt{s} = 900$ *GeV measured with the ATLAS detector at the LHC*, CERN-PH-EP-2010-004.

[87] The ATLAS Collaboration, *Performance of the Electron and Photon Trigger in p-p Collisions at* $\sqrt{s} = 900$ *GeV*, ATLAS-CONF-2010-022.

[88] The ATLAS Collaboration, *Electron and Photon reconstruction and identification in ATLAS: expected performance at high energy and results at* $\sqrt{s} = 900$ *GeV*, ATLAS-CONF-2010-005.

[89] The ATLAS Collaboration, *Performance of the ATLAS Inner Detector Trigger algorithms in p-p collisions at* $\sqrt{s} = 900$ *GeV*, ATLAS-CONF-2010-014.

[90] The ATLAS Collaboration, *ATLAS High Level Trigger Software Performance for First LHC Collision Events*, ATLAS-CONF-2010-030.

[91] D. Damazio, M. Tamsett *et al.*, *Trigger Egamma 2009 Collision Studies*, ATL-COM-DAQ-2010-032.

[92] S. Navin, *Diffraction in PYTHIA*, arXiv:hep-ph:1005.3894v1 (2010).

[93] The ATLAS Collaboration, *Observation of W→lnu and Z→ll production in proton-proton collisions at sqrts* $=$ *7 TeV with the ATLAS detector*, ATLAS-CONF-2010-044.

[94] The ATLAS Collaboration, *ATLAS Event Displays from 2010 Collision Data*: `https://twiki.cern.ch/twiki/bin/view/Atlas/EventDisplayPublicResults`.

[95] The ATLAS Collaboration, *The ATLAS Metadata Interface*: `http://ami.in2p3.fr/opencms/opencms/AMI/www/`.

[96] The ATLAS Collaboration, *Production of SUSY signal grids*: `https://twiki.cern.ch/twiki/bin/view/AtlasProtected/SUSYSignalProduction`.